JETP Letters, Vol. 76, No. 5, 2002, pp. 235–239. From Pis'ma v Zhurnal Éksperimental'noĭ i Teoreticheskoĭ Fiziki, Vol. 76, No. 5, 2002, pp. 291–295.

Trans-Planckian Particle Creation in Cosmology and Ultrahigh Energy Cosmic Rays¶

A. A. Starobinsky[1] and I. I. Tkachev[2]

[1] *Landau Institute for Theoretical Physics, Russian Academy of Sciences, Moscow, 119334 Russia*

[2] *Theory Division, CERN, CH-1211 Geneva 23, Switzerland*

Received July 29, 2002

We consider observational constraints on the creation of particles induced by hypothetical trans-Planckian effects during the current stage of the Universe's expansion. We show that compatibility with the diffuse γ-ray background measured by the EGRET experiment strongly restricts this creation. In particular, it rules out the possibility of detecting signatures of such short-distance effects in anisotropies of the cosmic microwave background radiation. On the other hand, the possibility that some part of ultrahigh-energy cosmic rays originates from new trans-Planckian physics remains open. © *2002 MAIK "Nauka/Interperiodica".*

PACS numbers: 98.80.Cq; 98.70.Vc; 04.62.+v

Recently, much interest was attracted to the study of possible deviations of the dispersion law of quantum ultrarelativistic particles from the standard $\omega(k) = k$ at very large ("trans-Planckian") momenta $k > M$ (presumably, $M \sim M_{\rm P1} = \sqrt{G}$; we put $\hbar = c = 1$ in this paper). This suggestion was previously discussed in the quantum theory of black holes [1] (where it does not lead to any new observable effects), but then it was applied in cosmology [2]. Reasons for the existence of such an effect may follow from an explicit breaking of Lorentz invariance either induced by the existence of additional spatial dimensions (e.g., with "asymmetric warping" of usual 4D curved space–time [3]) or suggested by analogy with quasiparticles in quantum liquids [4]. Nonstandard dispersion laws also arise in noncommutative geometry [5] and κ-Poincare symmetry algebra [6].

Almost all attempts to find observational signatures of this effect in cosmology were related to its influence on the spectra of scalar perturbations and gravitational waves generated during inflation. However, as was emphasized in [7], if any correction to these spectra arises at all, it means creation of real particles with ultrahigh energies (caused by some new trans-Planckian physics) due to *any* expansion of the Universe. In particular, this should also occur at the present time. Note that there is not even a qualitative difference between the type of the Universe's expansion during a de Sitter (inflationary) stage in the early Universe and nowadays: both are accelerating ones. Of course, the present value H_0 of the Hubble parameter $H \equiv \dot{a}/a$, where $a(t)$ is the scale factor of the Friedmann–Robertson–Walker (FRW) cosmological model and H_0 is the Hubble constant, is much less than H during inflation. But, as we will see, it is much easier to detect particles with ultrahigh energies created now than those created long ago during inflation (in spite of the fact discussed below that the number of created particles is second order in the parameter of nonadiabaticity $|\beta(k)|$, while corrections to the spectra of inflationary perturbations are first order in $|\beta(k)|$).

Following the general approach of [7] (see also more recent papers [8]), we will phenomenologically describe the effect of ultrahigh-energy particle creation in cosmology due to unknown trans-Planckian physics in the following way. Expansion of the Universe results in redshifting of spatial momenta: $k = n/a(t)$, $n = \text{const}$, where $k = |\mathbf{k}|$ (in the case of a noncommutative geometry, the quantities which are redshifted $\propto a^{-1}$ are not exactly the usual momenta $\mathbf{k}$, but the difference between them and $\mathbf{k}$ becomes small for $k \ll M$; see [5]). As a result, wave equations for the time-dependent parts of quantum field operators in the Heisenberg representation have the following form in the regime of large momenta $k \gg H$:

$$\ddot{\phi}_k + 3H\dot{\phi}_k + \omega^2(n/a)\phi_k = 0 \qquad (1)$$

for scalar particles, and

$$A_k'' + a^2\omega^2(n/a)A_k = 0 \qquad (2)$$

where the dot denotes the derivative with respect to the time t, the prime denotes the derivative with respect to the conformal time $\eta = \int dt/a(t)$, A_k is some quantity characterizing the electromagnetic field (it is proportional to covariant components of the vector-potential $\mathbf{A}$ in the standard case), and the 3D spatial Fourier expansion is assumed. Note that, in principle, $\omega(k)$ for the

¶This article was submitted by the authors in English.

electromagnetic field may also depend on photon polarization. Deviation of $\omega(k)$ from the standard law $\omega = k$ for $k \gtrsim M$ results in breaking of conformal invariance for photons (and massless neutrinos, too), so photon creation in the FRW metric becomes possible. Below we will argue that massive particles with a rest mass $m \ll M$ must be created as well (even if $m \gg H$) if creation of massless particles is not suppressed.

Let $H \ll M$. Then generic solutions of Eqs. (1) and (2) have the following form in the WKB regime $H \ll k \ll M$ (in the leading WKB approximation):

$$\phi_k = \frac{1}{\sqrt{2\omega a^3}}\left(\alpha_{n,0} e^{-i\int \omega dt} + \beta_{n,0} e^{i\int \omega dt}\right), \quad (3)$$

$$A_k = \frac{1}{\sqrt{2\omega a}}\left(\alpha_{n,1} e^{-i\int \omega dt} + \beta_{n,1} e^{i\int \omega dt}\right), \quad (4)$$

$$|\alpha_{n,s}|^2 - |\beta_{n,s}|^2 = 1, \quad s = 0, 1 \quad (5)$$

(we omit the spin index s below).

Usually, the adiabatic vacuum $\beta_n = 0$ is assumed for all modes of all quantum fields. However, trans-Planckian physics may result in a nonzero β_n (its actual value may be different for quantum fields of different spins and even for different polarizations, but we will not consider the latter possibility). So, supposing that particles with $k \gg M$ do not exist as individual particles or are not observable for other reasons (since we do not see them after all), we arrive at the following observational picture of the effect under consideration: in the course of the Universe's expansion, pairs of particles and antiparticles with superhigh energy M ($\sim M_{\rm P1}$) are spontaneously created at the moment when their momentum $k(t) \equiv n/a(t) = M$ and their occupation number is $|\beta_n|^2$. The corresponding correction coefficient $\mathcal{H}^2(n)$ to the power spectrum of inflationary perturbations is obtained by matching Eq. (3) (or its analogue for gravitational waves) to the exact solution of the massless scalar wave equation in the (approximately) de Sitter background with the Hubble parameter H estimated at the moment of the first Hubble radius crossing $k(t) = H$. It is equal to

$$\mathcal{H}^2(n) = |\alpha_n - \beta_n|^2. \quad (6)$$

We will see below that $|\beta_n|$ should be small. Then α_n can be made unity by a phase rotation, and $\mathcal{H}^2(n) = 1 - 2\,\mathrm{Re}\,\beta_n$. Its difference from unity is first order in $|\beta_n|$.

Our approach is to take α_n and β_n (subject to condition (5)) as phenomenological quantities which should finally follow from a concrete model of nontrivial trans-Planckian physics and investigate how they are limited by present observational data. Thus, we consider only real particle creation (corresponding to an imaginary part of the effective action of quantum fields in a FRW background). This should be contrasted to real, vacuum polarization corrections to the effective action considered, e.g., in [9]. The latter corrections result in a refraction index different from unity for radiation. They can be strongly limited by observations of distant γ bursts [10]. Note also that corrections to the effective volume in phase space leading to "trans-Planckian damping" that were recently proposed in [11] (in particular, they may explain why particles with $k \gg M$ are not observable) can be easily incorporated in the formalism used here by changing the overall time-dependent prefactors in Eqs. (3), (4).

In [7], the first step in this investigation was made by considering the back reaction of created ultrahigh-energy gravitons on the Universe's expansion at present. It was assumed that β_n has the following expansion in terms of the small parameter H_n/M, where $H_n \equiv H(t_n)$ is the Hubble parameter estimated at the moment of the trans-Planckian border crossing $n = Ma(t_n)$ for each Fourier field mode $\mathbf{k}$:

$$\beta_n = \beta_n^{(0)} + \beta_n^{(1)}\frac{H_n}{M} + \ldots \quad (7)$$

Then it was shown that the first term in (15) is very suppressed: $\left|\beta_n^{(0)}\right|^2 \lesssim H_0^2 M_{\rm P1}^2/M^4 = 10^{-122} M_{\rm P1}^4/M^4$, while the second term is bounded by $\left|\beta_n^{(1)}\right|^2 \ll M_{\rm P1}^2/M^2$ (thus, it is also suppressed if $M \sim M_{\rm P1}$). Note that time-translation invariance (which we do not want to abandon) requires $\left|\beta_n^{(0)}\right|^2$ and $\left|\beta_n^{(1)}\right|^2$ to be independent of n, which was noted in [7]. On the other hand, the phase of β_n is n-dependent and may be large. This leads to oscillations in $\mathcal{H}^2(n)$ and results in inflationary perturbation spectra which, however, are unobservable for $H \ll M$ due to their high frequency in $\mathbf{k}$ space [8, 12].

The first, H-independent term in (15) describes "pure" trans-Planckian particle creation, where the Universe's expansion plays a kinematic role only. The second term in (15) is responsible for a mixed effect where both small-scale trans-Planckian physics and large-scale space–time curvature participate. A concrete toy model producing the latter term was proposed in [7], namely, the quantum state of any Fourier field mode $\mathbf{k}$ which has a minimal energy density just at the moment of the trans-Planckian border crossing (this state differs from the adiabatic vacuum in the next term of the WKB expansion). Since the minimal energy state may not appear as a result of the adiabatic evolution in the WKB regime $|\dot{\omega}| \ll \omega^2$ (even for a nonstandard dispersion law), this model implicitly assumes that something radical happens for $k > M$: either no mode exists in this regime at all but is instantaneously "created" at the moment when its momentum falls down to M, or the WKB condition is suddenly violated for $k > M$, e.g., because of $\omega(k)$ becoming very small for $k > M$ (as occurs, e.g., in the model considered in [13]). Then, if $\omega(k) = k$ for $k < M$ exactly, the model leads to $\left|\beta_n^{(1)}\right| = 1/2$

for minimally coupled scalar particles (1) (see [7]; the recent papers [8] arrived at essentially the same result).

To create photons, some deviation from the standard dispersion law $\omega(k) = k$ should exist even for $k \le M$. Let us assume that the quantity to be diagonalized for each Fourier mode $\mathbf{k}$ is $\tilde{\varepsilon}_k = (\hat{A}_k'^2 + a^2\omega^2\hat{A}_k^2)/2a^4$; then equations for α_n and β_n in the representation (4) take the form (cf. [14] for the case of a conformally coupled massive scalar field)

$$\alpha_n' = \frac{\Omega_n'}{2\Omega_n} e^{2i\int\Omega_n d\eta}\beta_n, \quad \Omega_n = a\omega\left(\frac{n}{a}\right) = \frac{n\omega}{k}, \qquad (8)$$

$$\beta_n' = \frac{\Omega_n'}{2\Omega_n} e^{-2i\int\Omega_n d\eta}\alpha_n. \qquad (9)$$

The diagonalization condition at $\eta = \eta_0(n)$ (when $k = M$) is $\beta_n(\eta_0) = 0$. If particle creation is small, $|\beta_n| \ll 1$, then $\beta_n \approx -i(\Omega_n'/\Omega_n^2)_{\eta_0}/4$ (up to a phase factor and an additional strongly oscillating term). Therefore,

$$\left|\beta_n^{(1)}\right| = \frac{M}{4}\left[\frac{k^2}{\omega^2}\left|\frac{d}{dk}\left(\frac{\omega}{k}\right)\right|\right]_{k=M} \sim 1 \qquad (10)$$

for photons.

Note that expression (10) remains valid for conformally coupled massive particles as far as their restmass $m \ll M$. So, this toy model shows that the second term in expansion (15) need not be suppressed for massive particles with $m \gg H$. This remarkable fact may be understood using the following argument: any nonstandard dispersion law $\omega(k)$ is equivalent to the appearance of an effective-mass term $m^2(k) \equiv \omega^2(k) - k^2$ (m^2 may be negative, of course). For $k \sim M$, where a significant deviation from the standard dispersion law occurs, the rest mass $m^2(0)$ is completely irrelevant.

Equations for creation of massive fermions in a FRW background are similar to those in the case of conformally coupled massive scalar particles (with an additional multiplier n/ma in the r.h.s. of Eqs. (8) and (9) for the standard dispersion law $\omega^2 = k^2 + m^2$; see, e.g., [15]). Therefore, if photons are created due to trans-Planckian effects at all, one may expect that massive fermions with $m \ll M$ including leptons are created with a comparable (or even slightly larger) rate due to the present expansion of the Universe.

Now we take the next step and study the limits on trans-Planckian particle creation following from the direct observability of created particles (photons, in particular). Also, we omit the assumption $M \sim M_{\mathrm{P1}}$ and consider the case $M \ll M_{\mathrm{P1}}$. We show that data on high-energy cosmic rays require much more suppression of $\beta_n^{(0)}$ and $\beta_n^{(1)}$ as compared to the results obtained in [7].

The measured flux of ultrahigh-energy cosmic rays (UHECR) extends to energies on the order of $E \sim E_0 \equiv 10^{11}$ GeV only. On the other hand, a typical energy of particles emerging from the trans-Planckian region can be much higher, up to $E \sim 10^{19}$ GeV. Can the highest energy particles pass undetected? The answer is negative. First, measurements place the following constraint on the integral flux of high-energy particles (see, e.g., [16]):

$$F_{E>E_0} \approx 10^{-2}\ \mathrm{km}^{-2}\ \mathrm{yr}^{-1}\ \mathrm{sr}^{-1} \approx 10^{-71}\ \mathrm{GeV}^3\ \mathrm{sr}^{-1}. \qquad (11)$$

Second, the Universe is not transparent to high-energy radiation. Particles which are injected with any $E > E_0$ will rapidly (on the cosmological time scale) migrate into a lower energy range. For our purposes, it is sufficient to consider attenuation of high-energy particles on photons of the cosmic microwave background (CMB) radiation.

Protons lose energy in the process of pion photoproduction. This gives rise to the famous Greisen–Zatsepin–Kuzmin (GZK) cutoff. The attenuation length for this process (that is, the distance over which the energy of a primary particle decreases by one e-fold) is less than 20 Mpc at $E > E_0$. Roughly half of the released energy ends up in the electromagnetic cascade; the rest is carried out by neutrinos. The Universe becomes transparent for protons with $E \approx E_0$. Therefore, the number of protons which could have been produced by trans-Planckian effects (and which conserve) is subject to constraint (11). This can be rewritten as a constraint on the quantum-gravity scale M in a way similar to what follows. However, a somewhat stronger and less model-dependent constraint can be obtained by considering an electromagnetic cascade which migrates to even lower energies. From this point of view, it is unimportant whether the electromagnetic cascade was initiated by the propagation of high-energy protons or by photons (or, for that matter, electrons) which were directly created by trans-Planckian effects. Even neutrino production in the trans-Planckian region is not harmless. Neutrinos create an electromagnetic cascade in interactions with the cosmic background of relic neutrinos. Since about 1% of high-energy neutrinos interact over the horizon scale [17], our final constraint, Eq. (15), would be only an order of magnitude weaker even in the unrealistic case of pure neutrino creation. For these reasons, we concentrate on the constraint imposed by the electromagnetic cascade in what follows.

A high-energy photon cascades to lower energies in the chain of the following reactions. First, it creates e^+e^- pairs in collisions with CMB photons. Secondary electrons recreate photons with energies somewhat lower than the energy of the original photon via the inverse Compton process, and so on. The corresponding attenuation length at $E \gg E_0$ is about 0.1 of the present horizon size, and it is even smaller for smaller energies. Therefore, the cascade migrates to lower energies until

it reaches the sub-TeV scale, which corresponds to the threshold of pair creation on cosmic backgrounds.

Therefore, the integrated energy flux of particles emerging from the trans-Planckian region may not exceed the integrated energy flux in the sub-TeV range, where the diffuse γ-ray background was measured by the EGRET telescope [18]. The measured value of this background is

$$S_0 \approx 10^3 \text{ eV cm}^{-2} \text{ s}^{-1} \text{ sr}^{-1} \sim 10^{-58} \text{ GeV}^4 \text{ sr}^{-1}. \quad (12)$$

Let us relate this flux to the energy-production rate. The rate of growth of energy density in particles emerging from the trans-Planckian region due to the expansion of the Universe is [7]

$$J \equiv \frac{d(a^4\epsilon)}{a^4 dt} = \frac{gNM^4H}{2\pi^2}|\beta_n|^2. \quad (13)$$

In this relation, both particles and antiparticles are counted; $g = 2$ for photons and neutrinos, $g = 4$ for massive fermions. N counts for all particle species which can create the electromagnetic cascade at the end, since one expects that the trans-Planckian creation is "democratic" and insensitive to particle masses as far as $m \ll M$. Omitting the neutrino, $N = 26$ in the standard model. In supersymmetric or Grand Unified models, $N \sim 10^2$–10^3. The integrated flux of energy accumulated during the age of the Universe will be $S_1 \approx JH^{-1}$. Requiring $S_1 < S_0$, we get

$$\left|\beta_n^{(0)}\right|^2 < 10^{-133}\frac{1}{N}\left(\frac{M_{\rm P1}}{M}\right)^4. \quad (14)$$

We see that the constraint on the $\beta_n^{(0)}$ term in the decomposition (15) is very strong. Thus, this term should be practically absent regardless of the value of M. A contribution from the second term is strongly suppressed by the small quantity $H_0^2/M_{\rm P1}^2 \approx 10^{-122}$. As a result, for the $\beta_n^{(1)}$ coefficient we obtain

$$\left|\beta_n^{(1)}\right| < 10^{-6}\frac{1}{\sqrt{N}}\frac{M_{\rm P1}}{M}. \quad (15)$$

In recent literature (see, e.g., [19]), there were optimistic expectations regarding possible imprints of short-distance physics on the spectrum of CMB anisotropies generated in the inflationary scenario of the early Universe. Let us estimate now the impact of the restriction (15) on the possible magnitude of the effect. According to Eqs. (6), (14), and (15), a fractional correction to the power spectrum of inflationary perturbations which arise due to trans-Planckian physics is given by

$$\frac{\delta P}{P} = \beta_n^{(1)}\frac{H_{\rm inf}}{M}, \quad (16)$$

where $H_{\rm inf}$ is the value of the Hubble parameter during the last 60 e-folds of inflation, $H_{\rm inf}/M_{\rm P1} < 10^{-5}$. In view of the constraint (15), we find

$$\frac{\delta P}{P} < 10^{-11}\frac{1}{\sqrt{N}}\left(\frac{M_{\rm P1}}{M}\right)^2. \quad (17)$$

On the other hand, astrophysical data on the constancy of the speed of light yield the lower limit $M > 10^{15}$ GeV [10].[1] This gives $\delta P/P < 10^{-3}$ for the maximum possible magnitude of corrections to the perturbation power spectrum. We conclude that trans-Planckian particle creation is so strongly restricted by observations of UHECR that it will be impossible to detect signatures of short-distance physics in CMB anisotropies, since the allowed contribution is smaller than the cosmic variance at all multipoles of interest, $l < 10^4$.

Returning to UHECR themselves, one may consider the speculative possibility that events observed above the GZK cutoff energy are due to peculiarities of trans-Planckian physics. However, trans-Planckian creation of particles would occur homogeneously in the Universe and therefore should lead to the GZK cutoff in the spectrum of created protons at high energies and to the pileup of protons at $E \sim 4 \times 10^{19}$ eV. Thus, protons cannot explain super-GZK events despite the fact that trans-Planckian creation does occur within the GZK sphere of ~50 Mpc, from where protons can reach us. On the other hand, the attenuation length for photons grows with energy, and therefore photons may produce a spectrum of cosmic rays compatible with the AGASA data [20] at the highest energies. One problem which may arise here is related to an overall normalization. At $E \sim 10^{20}$ eV the attenuation length for photons is about 100 times smaller than the horizon scale. This gives the distance scale to sources which contribute to the flux at ultrahigh energies. On the other hand, byproducts of the electromagnetic cascade pile up at the EGRET energies and are accumulated from the entire Universe. On these grounds, one expects that the ratio of the energy flux in UHECR ($S \sim 10^{-60}$ GeV^4 sr^{-1}, see Eq. (11)) to the diffuse EGRET background cannot be larger than 0.01. This value comfortably fits the data, and the numerical coincidence may indicate that these two backgrounds can indeed be related. However, to maintain this level of the UHECR flux in photons, one should assume

[1] Strictly speaking, this limit was obtained assuming that a correction to the standard dispersion law for $k \longrightarrow 0$ starts with the cubic term, $\omega^2 = k^2(1 \pm (k/M) + \ldots)$. If the cubic term is absent and the correction begins from a larger power of k/M, there is no lower limit on M. However, constraint (15) remains valid. So, even in this specific case, to obtain significant corrections to the perturbation power spectrum generated during inflation, either a specific mechanism for trans-Planckian particle creation producing $\left|\beta_n^{(1)}\right| \gg 1$ should be invented or one has to postulate a low $M \le 10^{-6} M_{\rm P1}$ which is not compatible with the condition $H_{\rm inf} \ll M$ (necessary for general relativistic description of inflation and generation of perturbations) for many inflationary models.

small extragalactic magnetic fields and small universal radio background (cf. [21]). In addition, one would need to fine-tune the rate of trans-Planckian creation to the level of the observed UHECR flux. Also, this mechanism is not favored by the observed angular clustering of UHECR [20, 22]. One should note, however, that the same problems arise in many other models which attempt to explain super-GZK events.

We conclude that at least some cosmic rays with energies beyond the GZK limit may have originate due to new physics in the trans-Planckian region. This striking possibility remains open and deserves further study, while constraint (17) makes the expected contribution of trans-Planckian physics to the CMB anisotropies unobservable.

The authors thank CITA, University of Toronto, where this project was started, for hospitality. A.S. was also partially supported by RFBR, grant no. 02-02-16817, and by the RAS Research Program "Quantum Macrophysics."

REFERENCES

1. W. G. Unruh, Phys. Rev. D **51**, 2827 (1995); R. Brout, S. Massar, R. Parentani, and P. Spindel, Phys. Rev. D **52**, 4559 (1995); S. Corley and T. Jacobson, Phys. Rev. D **54**, 1568 (1996).
2. J. Martin and R. H. Brandenberger, Phys. Rev. D **63**, 123501 (2001); J. C. Niemeyer, Phys. Rev. D **63**, 123502 (2001).
3. C. Csaki, J. Erlich, and C. Grojean, Nucl. Phys. B **604**, 312 (2001); D. J. H. Chung, E. W. Kolb, and A. Riotto, Phys. Rev. D **65**, 083516 (2002).
4. G. E. Volovik, Pis'ma Zh. Éksp. Teor. Fiz. **73**, 182 (2001) [JETP Lett. **73**, 162 (2001)]; G. E. Volovik, Phys. Rep. **351**, 195 (2001).
5. C. S. Chu, B. R. Greene, and G. Shiu, Mod. Phys. Lett. A **16**, 2231 (2001); F. Lizzi, G. Mangano, G. Miele, and M. Peloso, hep-th/0203099 (2002).
6. J. Kowalski-Glikman, Phys. Lett. B **499**, 1 (2001); N. R. Bruno, G. Amelino-Camelia, and J. Kowalski-Glikman, Phys. Lett. B **522**, 133 (2001).
7. A. A. Starobinsky, Pis'ma Zh. Éksp. Teor. Fiz. **73**, 415 (2001) [JETP Lett. **73**, 371 (2001)].
8. U. H. Danielsson, hep-th/0203198 (2002); R. Easter, B. R. Greene, W. H. Kinney, and G. Shiu, hep-th/0204129 (2002).
9. G. Amelino-Camelia, L. Doplicher, S. Nam, and Y.-S. Seo, hep-th/0109191 (2001); N. Kaloper, M. Kleban, A. E. Lawrence, and S. Shenker, hep-th/0201158 (2002).
10. J. R. Ellis, K. Farakos, N. E. Mavromatos, *et al.*, Astrophys. J. **535**, 139 (2000); G. Amelino-Camelia, N. E. Mavromatos, S. Sarkar, *et al.*, Nature **393**, 763 (1998).
11. S. F. Hassan and H. S. Sloth, hep-th/0204110 (2002).
12. S. Shankaranarayanan, gr-qc/0203060 (2002).
13. L. Mersini, M. Bastero-Gil, and P. Kanti, Phys. Rev. D **64**, 043508 (2001).
14. Ya. B. Zeldovich and A. A. Starobinsky, Zh. Éksp. Teor. Fiz. **61**, 2161 (1971) [Sov. Phys. JETP **34**, 1159 (1972)].
15. A. A. Starobinsky, in *Quantum Gravity*, Ed. by M. A. Markov and P. C. West (Plenum, New York, 1984), p. 103.
16. P. Bhattacharjee and G. Sigl, Phys. Rep. **327**, 109 (2000).
17. T. Weiler, Phys. Rev. Lett. **49**, 234 (1982).
18. P. Sreekumar, D. L. Bertsch, B. L. Dingus, *et al.*, Astrophys. J. **494**, 523 (1998).
19. R. H. Brandenberger and J. Martin, hep-th/0202142 (2002).
20. M. Takeda, N. Hayashida, K. Honda, *et al.*, Astrophys. J. **522**, 225 (1999).
21. O. E. Kalashev, V. A. Kuzmin, D. V. Semikoz, and I. I. Tkachev, astro-ph/0107130.
22. P. G. Tinyakov and I. I. Tkachev, Pis'ma Zh. Éksp. Teor. Fiz. **74**, 3 (2001) [JETP Lett. **74**, 1 (2001)]; P. G. Tinyakov and I. I. Tkachev, Pis'ma Zh. Éksp. Teor. Fiz. **74**, 499 (2001) [JETP Lett. **74**, 445 (2001)].

JETP Letters, Vol. 76, No. 5, 2002, pp. 240–244. From Pis'ma v Zhurnal Éksperimental'noĭ i Teoreticheskoĭ Fiziki, Vol. 76, No. 5, 2002, pp. 296–300.

Black-Hole Horizon and Metric Singularity at the Brane Separating Two Sliding Superfluids¶

G. E. Volovik

Low Temperature Laboratory, Helsinki University of Technology, FIN-02015 HUT, Finland
Landau Institute for Theoretical Physics, Russian Academy of Sciences, Moscow, 117940 Russia

Received August 8, 2002

An analogue of a black hole can be realized in the low-temperature laboratory. The horizon can be constructed for "relativistic" ripplons (surface waves) living on the brane. The brane is represented by the interface between two superfluid liquids, ^{3}He-A and ^{3}He-B, sliding along each other without friction. A similar experimental arrangement was recently used for the observation and investigation of the Kelvin–Helmholtz type of instability in superfluids [1]. The shear-flow instability in superfluids is characterized by two critical velocities. The lowest threshold measured in recent experiments [1] corresponds to the appearance of the ergoregion for ripplons. In the modified geometry, this will give rise to the black-hole event horizon in the effective metric experienced by ripplons. In the region behind the horizon, the brane vacuum is unstable due to interaction with the higher-dimensional world of bulk superfluids. The time of the development of instability can be made very long at low temperature. This will allow us to reach and investigate the second critical velocity—the proper Kelvin–Helmholtz instability threshold. The latter corresponds to the singularity inside the black hole, where the determinant of the effective metric becomes infinite. © *2002 MAIK "Nauka/Interperiodica".*

PACS numbers: 04.50.+h; 04.70.Dy; 67.57.De; 47.20.Ft

1. Introduction. The first experimental realization of two superfluid liquids sliding along each other [1] gives us a new tool for the investigation of many physical phenomena related to different areas of physics (classical hydrodynamics, rotating Bose condensates, cosmology, brane physics, etc.). Here we discuss how this experimental arrangement can be modified in order to produce an analogue of the black-hole event horizon and of the singularity in the effective Lorentzian metric experienced by the collective modes (ripplons) living on the brane (the interface separating two different superfluid vacua, ^{3}He-A and ^{3}He-B, which we refer to as the AB brane below).

The idea of the experiment is similar to that discussed by Schützhold and Unruh [2], who suggested using gravity waves on the surface of a liquid flowing in a shallow basin. In the long-wavelength limit, the energy spectrum of the surface modes becomes "relativistic," which allows us to describe the propagating modes in terms of the effective Lorentzian metric. Here we discuss the modification of this idea to the case of ripplons propagating along the membrane between two superfluids.

There are many advantages when one uses the superfluid liquids instead of the conventional ones: (1) The superfluids can slide along each other without any friction until the critical velocity is reached, and thus all the problems related to viscosity disappear. (2) The superfluids represent quantum vacua similar to those in relativistic quantum field theories (RQFT) (see review [3]). That is why the quantum effects related to the vacuum in the presence of an exotic metric can be simulated. (3) The interface between two different superfluid vacua is analogous to the brane in the modern RQFT, and one can study the brane physics, in particular, the interaction between the brane matter and the matter living in the higher dimensional space outside the brane. Here, on example of the AB brane, we show that this interaction leads to vacuum instability in the AB brane behind the event horizon. (4) Reducing the temperature, one can make the time of the development of the instability long enough to experimentally probe the singularity within the black hole (the so-called physical singularity).

2. Effective metric for modes living in the AB brane. Let us consider surface waves—ripplons—propagating along the AB brane in the slab geometry shown in Fig. 1. Two superfluids, ^{3}He-A and ^{3}He-B, separated by the AB brane move along the brane with velocities $\mathbf{v}_1$ and $\mathbf{v}_2$ in the container frame. The normal components of the liquids—the systems of quasiparticles on both sides of the interface—are at rest with respect of the container walls in equilibrium, $\mathbf{v}_n = 0$. The dispersion relation for ripplons can be obtained by modification of the equations obtained in [4] to the slab geometry:

$$M_1(k)(\omega - \mathbf{k}\cdot\mathbf{v}_1)^2 + M_2(k)(\omega - \mathbf{k}\cdot\mathbf{v}_2)^2 = F + k^2\sigma - i\Gamma\omega. \quad (1)$$

¶This article was submitted by the author in English.

0021-3640/02/7605-0240$22.00 © 2002 MAIK "Nauka/Interperiodica"

Here, σ is the surface tension of the AB brane; F is the force stabilizing the position of the brane (in experiment [1] it is an applied magnetic-field gradient); $M_1(k)$ and $M_2(k)$ are the masses of the two liquids involved in the oscillating motion of the brane:

$$M_1(k) = \frac{\rho_1}{k\tanh kh_1}, \quad M_2(k) = \frac{\rho_2}{k\tanh kh_2}; \qquad (2)$$

h_1 and h_2 are the thicknesses of layers of two superfluids; ρ_1 and ρ_2 are mass densities of the liquids, and we assume that the temperature is low enough that the normal fraction of each of the two superfluid liquids is small.

Finally, Γ is the coefficient in front of the friction force experienced by the AB brane when it moves with respect to the 3D environment along the normal $\hat{\mathbf{z}}$ to the brane, $\mathbf{F_{fr}} = -\Gamma(\mathbf{v}_{\rm brane} - \mathbf{v}_n)$ (in the frame of container $\mathbf{v}_n = 0$). The friction term in Eq. (1) containing the parameter Γ is the only term which couples the 2D brane with the 3D environment. If $\Gamma = 0$, the brane subsystem becomes Galilean invariant; the Γ-term violates Galilean invariance in the 2D world of the AB brane.

In a thin slab where $kh_1 \ll 1$ and $kh_2 \ll 1$, one obtains

$$\alpha_1(\omega - \mathbf{k}\cdot\mathbf{v}_1)^2 + \alpha_2(\omega - \mathbf{k}\cdot\mathbf{v}_2)^2 = c^2k^2\left(1 + \frac{k^2}{k_{\rm P}^2}\right) - 2i\tilde{\Gamma}(k)\omega, \qquad (3)$$

where

$$\alpha_1 = \frac{h_2\rho_1}{h_2\rho_1 + h_1\rho_2}, \quad \alpha_2 = 1 - \alpha_1 = \frac{h_1\rho_2}{h_2\rho_1 + h_1\rho_2}, \qquad (4)$$

$$k_{\rm P}^2 = \frac{F}{\sigma}, \quad c^2 = \frac{Fh_1h_2}{h_2\rho_1 + h_1\rho_2}, \qquad \tilde{\Gamma}(k) = \frac{\Gamma}{2}k^2\frac{h_1h_2}{h_2\rho_1 + h_1\rho_2}. \qquad (5)$$

For $k \ll k_{\rm P}$, the main part of Eq. (3) can be rewritten in the Lorentzian form

$$g^{\mu\nu}k_\mu k_\nu = 2i\omega\tilde{\Gamma}(k) - c^2k^4/k_{\rm P}^2, \qquad (6)$$

$$k_\mu = (-\omega, k_x, k_y), \quad k = \sqrt{k_x^2 + k_y^2}, \qquad (7)$$

while the right-hand side of Eq. (6) contains the remaining small terms violating Lorentz invariance—attenuation of ripplons due to the friction and their nonlinear dispersion. Both terms come from physics which is "trans-Planckian" for the ripplons. The quantities $k_{\rm P}$ and $ck_{\rm P}$ play the role of the Planck momentum and Planck energy within the brane: they determine the scales where the Lorentz symmetry is violated. The Planck scales of the 2D physics in the brane are actually much smaller than the "Planck momentum" and "Planck energy" in the 3D superfluids outside the brane. The parameter Γ is determined by the physics of 3D quasiparticles scattering on the brane, and it practically does not depend on velocities $\mathbf{v}_1$ and $\mathbf{v}_2$, which are too small for the 3D world.

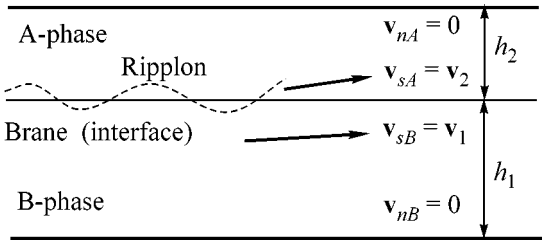

Fig. 1. The brane—interface between two moving superfluids, ^{3}He-A and ^{3}He-B. $\mathbf{v}_{sA}$ and $\mathbf{v}_{sB}$ are the superfluid velocities of two liquids sliding along the brane, while the normal components of the liquids—analogue of the matter living outside the brane—are at rest in the frame of the container, $\mathbf{v}_{nA} = \mathbf{v}_{nB} = 0$. The dashed line demonstrates the propagating surface wave (ripplon) which represents the matter living on the brane.

At sufficiently small k, both non-Lorentzian terms—attenuation and nonlinear dispersion on the right-hand side of Eq. (6)—can be ignored, and the dynamics of ripplons living on the AB-brane are described by the following effective contravariant metric $g^{\mu\nu}$:

$$g^{00} = -1, \quad g^{0i} = -\alpha_1 v_1^i - \alpha_2 v_2^i, \qquad g^{ij} = c^2\delta^{ij} - \alpha_1 v_1^i v_1^j - \alpha_2 v_2^i v_2^j. \qquad (8)$$

Introducing relative velocity U and the mean velocity W of two superfluids,

$$\mathbf{W} = \alpha_1\mathbf{v}_1 + \alpha_2\mathbf{v}_2, \quad \mathbf{U} = \mathbf{v}_1 - \mathbf{v}_2, \qquad (9)$$

one obtains the following expression for the effective contravariant metric:

$$g^{00} = -1, \qquad g^{0i} = -W^i, \quad g^{ij} = c^2\delta^{ij} - W^iW^j - \alpha_1\alpha_2U^iU^j. \qquad (10)$$

3. Horizon and singularity. The original KH instability [5] takes place when the relative velocity U of the motion of the two liquids reaches the critical value $U_c = c/\sqrt{\alpha_1\alpha_2}$. At this velocity, the determinant of the metric tensor

$$g(r) = -\frac{1}{c^2(c^2 - \alpha_1\alpha_2U^2(r))} \qquad (11)$$

has a physical singularity: it crosses the infinite value and changes sign. However, before U reaches U_c, the system reaches the other important thresholds at which analogues of ergosurface and horizon in general relativity appear. To demonstrate this, let us consider the simplest situation, when velocities $\mathbf{U}$ and $\mathbf{W}$ are parallel to

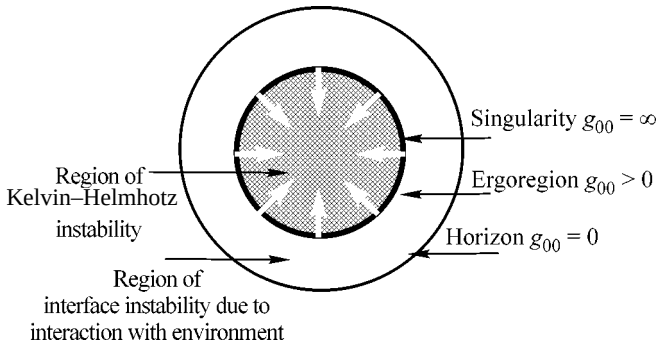

Fig. 2. Horizon and singularity in the effective metric for ripplons on the brane (AB interface). We assume that the A-phase is at rest, while the B phase is radially moving to the center as shown by arrows.

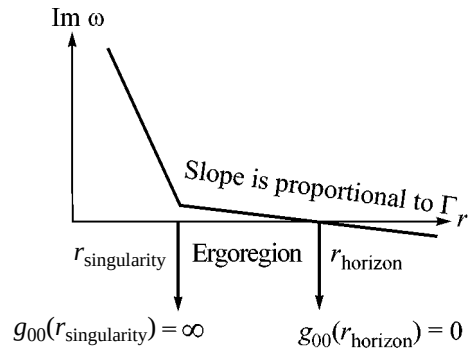

Fig. 3. Imaginary part of the ripplon spectrum due to interaction with the environment in the higher-dimensional space. In the ergoregion, the attenuation transforms to the amplification leading to the instability of the brane world. The time of development of this instability is long at low T, where Γ is small. In contrast, the Kelvin–Helmholtz instability behind the singularity rapidly develops and $r_{singularity} \longrightarrow 0$.

each other (i.e., $\mathbf{v}_1$ and $\mathbf{v}_2$ are parallel) and these velocities are radial and depend only on the radial coordinate r along the flow. Then the interval of the effective 2 + 1 space–time in which ripplons move along the geodesic curves is

$$ds^2 = \frac{-(c^2 - W^2(r) - \alpha_1\alpha_2 U^2(r))dt^2 - 2W(r)dtdr + dr^2}{c^2 - \alpha_1\alpha_2 U^2(r)} + r^2 d\phi^2 \quad (12)$$

$$= -d\tilde{t}^2 \frac{c^2 - W^2(r) - \alpha_1\alpha_2 U^2(r)}{c^2 - \alpha_1\alpha_2 U^2(r)} + \frac{dr^2}{c^2 - W^2(r) - \alpha_1\alpha_2 U^2(r)} + r^2 d\phi^2, \quad (13)$$

$$d\tilde{t} = dt + \frac{W(r)dr}{c^2 - W^2(r) - \alpha_1\alpha_2 U^2(r)}. \quad (14)$$

The circle $r = r_h$, where $g_{00} = 0$, i.e., where $W^2(r_h) - \alpha_1\alpha_2 U^2(r_h) = c^2$, marks the "coordinate singularity" which is the black-hole horizon if the velocity W is inward (see Fig. 2). In such radial-flow geometry, the horizon also represents the ergosurface (ergoline in 2D space dimension) which is determined as the surface bounding the region where the ripplon states can have negative energy. We call the whole region behind the ergosurface the ergoregion. This definition differs from that accepted in general relativity, but we must extend the notion of the ergoregion to the case when Lorentz invariance and general covariance are violated and the absolute reference frame appears. At the ergosurface, the Landau critical velocity for excitations of ripplons is reached. Also, as follows from [4] (see also Section 5 below), the ergoregion coincides with the region where the brane fluctuations become unstable, since both real and imaginary (Fig. 3) parts of the ripplon energy spectrum cross zero at the ergosurface.

4. Brane instability behind the horizon. This means that the brane becomes unstable in the presence of the ergoregion. This instability is caused by the interaction of the 2D ripplons with the 3D quasiparticles in bulk superfluids on both sides of the brane [4]. The interaction of brane with the environment, i.e., with the superfluids on both sides of the brane, is the source of the attenuation of the propagating ripplons: this interaction determines the parameter Γ in the friction force. In the ergoregion, the imaginary part of the spectrum of ripplons becomes positive; i.e., the attenuation transforms to amplification of surface waves with negative ω (see Fig. 3, where the imaginary part of the spectrum crosses zero with the slope proportional to Γ). Since the instability of the interface with respect to exponentially growing surface fluctuations develops in the presence of the shear flow, this instability results in the formation of vortices observed in experiment [1].

In ^{3}He experiments [1] with shear flow along the AB interface, one has $kh_1 \gg 1$ and $kh_2 \gg 1$. Thus, the relativistic description is not applicable. Also, in the rotating cryostat, the superfluids flow in the azimuthal direction instead of the radial. That is why there was no horizon in the experiment. However, the notion of the ergosurface and of the ergoregion behind the ergosurface, where the ripplon energy becomes negative in the container frame [4], is applicable. The instability of the brane inside the ergoregion leads to formation of vortices in the vortex-free ^{3}He-B, which were detected using NMR with single-vortex resolution. The observed threshold velocity for the vortex formation exactly corresponds to the appearance of the ergosurface (ergoline) in the container [1, 4].

There are thus two ingredients which cause the vacuum instability in the ergoregion: (i) the existence of the absolute reference frame of the environment outside

the brane; and (ii) the interaction of the brane with this environment ($\Gamma \neq 0$) which violates Galilean (or Lorentz) invariance within the brane. They lead to attenuation of the ripplon in the region outside the horizon. Behind the horizon, this attenuation transforms to amplification, which destabilizes the vacuum there. This mechanism may have an important consequence for the astronomical black hole. If there is any intrinsic attenuation of, say, photons (either due to superluminal dispersion or due to the interaction with the higher-dimensional environment), this may lead to the catastrophic decay of the black hole due to instability behind the horizon, which we discuss in Section 5.

Let us estimate the time of development of such instability, first in the artificial black hole within the AB brane and then in the astronomical black hole. According to Kopnin [6], the parameter of the friction force experienced by the AB brane due to Andreev scattering of quasiparticles in the bulk superfluid on the A-phase side of the brane is $\Gamma \sim T^3 m^*/\hbar^3 c_\perp c_\parallel$ at $T \ll T_c$. Here, T is the temperature in ^{3}He-A; m^* is the quasiparticle mass in the Fermi liquid; $c_\perp$ and $c_\parallel$ are the "speeds of light" for 3D quasiparticles living in anisotropic ^{3}He-A (these speeds are much larger than the typical "speed of light" c of quasiparticles (ripplons) on the 2D brane); and T_c is the superfluid transition temperature, which also marks the 3D Planck energy scale. Assuming the most pessimistic scenario, in which the instability is caused mainly by the exponential growth of ripplons with the "Planck" wave number k_P, one obtains the following estimation for the time of the development of the instability in the ergoregion far enough from the horizon: $\tau \sim 1/\tilde{\Gamma}(k_P) \sim 10(T_c/T)^3$ s. Thus, at low T, the state with the horizon can live for a long time (minutes or even hours), and this lifetime of the horizon can be made even longer if the threshold is only slightly exceeded.

This provides unique possibility to study the horizon and the region behind the horizon; the physical singularity, where the determinant of the metric is singular, can also be easily constructed and investigated.

At the lower temperature $T < m^* c_\perp^2$, the temperature dependence of Γ changes: $\Gamma \sim T^4/\hbar^3 c_\perp^3 c_\parallel$ [3], and at very low T it becomes temperature-independent: $\Gamma \sim \hbar k^4$, which corresponds to the dynamical Casimir force acting on the 2D brane moving in the 3D vacuum. Such intrinsic attenuation of ripplons transforms to the amplification of the ripplon modes in the ergoregion, which leads to instability of the brane vacuum behind the horizon even at $T = 0$.

5. Instability of the black hole behind the horizon? Now let us suppose that the same situation takes place in our (brane) world; i.e., the modes of our world (photons, or gravitons, or fermionic particles) have finite lifetime due to interaction with, say, the extra-dimensional environment. Then this will lead to the instability of vacuum behind the horizon of astronomical black holes. This can be considered using Eq. (6), which incorporates both terms violating the Lorentz invariance at high energy: the superluminal upturn of the spectrum, which leads to decay of particles, and the intrinsic broadening of the particle spectrum characterized by $\tilde{\Gamma}(k)$. Following the analogy, we can write the intrinsic width as a power law $\tilde{\Gamma}(k) \sim \mu(ck/\mu)^n$, where μ is the energy scale, which is well above the Planck scale E_P of our brane world, $\mu \gg E_P$; and $n = 6$ if the analogy is exact.

We shall use the Painlevé–Gullstrand metric, which together with the superluminal dispersion of the particle spectrum allows us to consider the region behind the horizon:

$$g^{00} = -1, \quad g^{0i} = -W^i,$$
$$g^{ij} = c^2\delta^{ij} - W^i W^j, \quad \mathbf{W} = -\hat{\mathbf{r}}\sqrt{\frac{2GM}{r}}. \tag{15}$$

Here, G is Newton's constant and M is the mass of the black hole. This metric coincides with the 3D generalization of the metric of ripplons on AB brane in Eq. (13) for $\mathbf{v}_1 = \mathbf{v}_2$. Equation (13) gives the following dispersion relation for particles in the brane:

$$(\omega - \mathbf{k}\cdot\mathbf{W})^2 = c^2k^2 - 2i\omega\tilde{\Gamma}(k) + c^2k^4/k_P^2, \tag{16}$$

or

$$\omega(\mathbf{k}) = \mathbf{k}\cdot\mathbf{W} - i\tilde{\Gamma}(k) \pm \sqrt{c^2k^2 + c^2k^4/k_P^2 - \tilde{\Gamma}^2(k) - 2i\mathbf{k}\cdot\mathbf{W}\tilde{\Gamma}(k)}. \tag{17}$$

We are interested in the imaginary part of the spectrum. For small $\tilde{\Gamma}(k) \ll ck$, the imaginary part of the energy spectrum is

$$\mathrm{Im}\,\omega(\mathbf{k}) = -i\tilde{\Gamma}(k)\left(1 \pm \frac{\mathbf{k}\cdot\mathbf{W}}{E(k)}\right),$$
$$E^2(k) = c^2k^2 + c^2k^4/k_P^2. \tag{18}$$

Behind the horizon, where $W > c$, the imaginary part becomes positive for $|\mathbf{k}\cdot\mathbf{W}| > E(k)$ (or $k^2 < k_P^2/(W^2/c^2 - 1)$); i.e., attenuation transforms to amplification of waves with these $\mathbf{k}$. This demonstrates the instability of the vacuum with respect to exponentially growing electromagnetic or other fluctuations in the ergoregion. Such an instability is absent when $\tilde{\Gamma} = 0$, i.e., if there is no interaction with the trans-Planckian or extra-dimensional world(s).

The time of the development of instability within the conventional black hole is determined by the region far from the horizon, where the relevant $k \sim k_P$. Thus, $\tau \sim 1/\tilde{\Gamma}(k_P) \sim \mu^{n-1}/E_P^n$. If μ is of the same order as the brane Planck scale, the time of development of instabil-

ity is determined by the Planck time. That is why the astronomical black hole can exist only if $\mu \gg E_P$, which takes place when the 4D and 3D Planck scales are essentially different, as in the case of the AB brane. The black hole decay due to the quantum process of Hawking evaporation corresponds to $\mu = M$, where M is the black hole mass and $n = 4$.

6. Conclusion. In conclusion, the AB brane—the interface between the two sliding superfluids—can be used to construct an artificial black hole with an ergosurface, horizon, and physical singularity. Using the AB brane, one can also simulate the interaction of particles on the brane with those in the higher-dimensional space outside the brane. This interaction leads to the decay of the brane vacuum in the region behind the horizon. This mechanism can be crucial for astronomical black holes, if this analogy is applicable. If the matter fields in the brane are properly coupled to, say, gravitons in the bulk, this may lead to the fast collapse of the black hole.

I thank V.B. Eltsov, M. Krusius, R. Schützhold, and W.G. Unruh for fruitful discussions. This work was supported by ESF COSLAB Programme and by the Russian Foundation for Basic Research.

REFERENCES

1. R. Blaauwgeers, V. B. Eltsov, G. Eska, *et al.*, Phys. Rev. Lett. **89**, 155301 (2002).
2. R. Schützhold and W. G. Unruh, gr-qc/0205099.
3. G. E. Volovik, Phys. Rep. **351**, 195 (2001); G. E. Volovik, *Universe in a Helium Droplet*, forthcoming book in Oxford University Press, http://ice.hut.fi/Volovik/book.pdf.
4. G. E. Volovik, Pis'ma Zh. Éksp. Teor. Fiz. **75**, 491 (2002) [JETP Lett. **75**, 418 (2002)]; cond-mat/0202445.
5. L. D. Landau and E. M. Lifshitz, *Course of Theoretical Physics*, Vol. 6: *Fluid Mechanics* (Nauka, Moscow, 1986; Pergamon, New York, 1989), Sec. 62, Problem 3, p. 247.
6. N. B. Kopnin, Zh. Éksp. Teor. Fiz. **92**, 2106 (1987) [Sov. Phys. JETP **65**, 1187 (1987)].

JETP Letters, Vol. 76, No. 5, 2002, pp. 245–248. Translated from Pis'ma v Zhurnal Éksperimental'noĭ i Teoreticheskoĭ Fiziki, Vol. 76, No. 5, 2002, pp. 301–305.

Recoil Effect in the β Decay of Molecular Tritium

V. I. Savichev

Department of Physics, Wesleyan University, Middletown, CT 06459-0155, USA

e-mail: vsavichev@wesleyan.edu

Received July 1, 2002; in final form, July 24, 2002

In order to determine the electron (anti)neutrino mass m_ν, a number of precise atomic experiments with gaseous and frozen targets of molecular tritium T_2 have been carried out in the last decade. The nonzero neutrino mass should be manifested in the form of fine features near the upper edge of the β-electron spectrum. The problem of calculating the spectrum of final excitations, which is of crucial importance for determining m_ν, is discussed. An operator approach has been used for an analysis of spectral sums. This allows a number of effects that could not be considered earlier to be discussed, including the recoil effect, which can be of substantial importance in the interpretation of the current and future experiments. © *2002 MAIK "Nauka/Interperiodica".*

PACS numbers: 23.40.Bw; 14.60.Pq; 31.10.+z

In recent atomic experiments, the neutrino mass was determined from the electronic spectrum of the β decay of molecular tritium [1–6]

$$T_2 \longrightarrow T^3He^+ + e^- + \tilde{\nu}_e. \qquad (1)$$

A theoretical spectrum, where the neutrino mass m_ν^2 is a varying parameter, is fitted to the experimental data. The upper edge of the β-electron spectrum is equal to about 18.6 keV and most sensitive to the nonzero neutrino mass. A rich variety of electronic rovibrational states of the T^3He^+ molecule is populated because of the recoil energy and instantaneous change in the charge. The spectrum of final excitations was calculated in [7–13], where it was demonstrated that about 99% of final states were distributed over a 100-eV range near the upper edge. The spectrum consists primarily of comparatively narrow rovibrational multiplets corresponding to bound and resonance adiabatic electronic states, 57.4% of which are in the ground electronic state of the T^3He^+ molecule. The ground rovibrational multiplet consists of several hundred bound and resonance molecular states with the rotational quantum number $J \sim 22$–25 [8]. Although the probability of populating an individual rovibrational state is very sensitive to variations in the recoil momentum (energy) p_β [13], the integral contribution of the multiplet is virtually constant. The statistical processing of most experimental data faces a problem hindering the unambiguous determination of nonzero neutrino mass. Indeed, the best approximation of the β-electron spectrum is reached with negative m_ν^2, i.e., in the nonphysical region. Moreover, the resulting m_ν^2 value depends on the fitting energy range. In the conservative approach, the experiments give an upper limit for neutrino mass $m_\nu \le 2$–3 eV/c^2. The new series of experiments within the plans of the KATRIN collaboration should achieve an accuracy in measuring the neutrino mass in the subelectron-volt range [14]. In this paper, the problem of calculating the spectrum of final excitations is considered. The operator technique of calculating spectral sums provides quantitative estimate of the recoil effect on the spectrum of final excitations. The correction is shown to depend explicitly on the β-electron energy and to be equal to about 1 eV in the energy range below the upper edge by ~100 eV, i.e., in the region of sensitivity of future experiments.

The differential spectrum of β electrons is determined as [10] ($e = m_e = \hbar = 1$)

$$\left|\frac{dN(\epsilon_\beta)}{d\epsilon_\beta}\right| = AF(p_\beta, Z)E_\beta p_\beta \sum_n P_n(p_\beta)\epsilon_n \times (\epsilon_n^2 - m_\nu^2 c^4)^{1/2}\theta(\epsilon_n - m_\nu c^2), \quad \epsilon_n = W_0 - \epsilon_\beta - E_n, \quad \epsilon_\beta = E_\beta - m_e c^2, \qquad (2)$$

where the summation is over all final states of the T^3He^+ molecule; E_β and ϵ_β are the total and kinetic energies, respectively; p_β is the β-electron momentum; and $F(p_\beta, Z)$ is the Fermi factor [15]. The upper edge measured from the ground state is determined as

$$W_0 = (M_t - M_\alpha)c^2 + E_{T_2} - E_g - E_R - m_e c^2, \qquad (3)$$

where E_g is the ground-state energy of the T^3He^+ molecule, E_{T_2} is the ground-state energy of the T_2 molecule, $E_R = p_\beta^2/4M_t$ is the recoil energy of the center of mass of the molecule, and M_t is the triton mass. The proba-

bility of populating final states is expressed in terms of the squared matrix element of the recoil operator:

$$P_n(p_\beta) = \int \frac{d\hat{\mathbf{q}}}{4\pi} \left| \langle n | e^{i(\mathbf{q},\mathbf{R})} | \mathrm{T}_2 \rangle \right|^2, \quad \mathbf{q} = \frac{\mathbf{p}_\beta}{2}, \tag{4}$$

where **R** is the internuclear distance. All available β spectrometers measure the integral spectrum

$$N(\epsilon_\beta) = \frac{A}{3} F(p_\beta, Z) E_\beta p_\beta \sum_n P_n(p_\beta) \times (\epsilon_n^2 - m_\nu^2 c^4)^{3/2} \theta(\epsilon_n - m_\nu c^2). \tag{5}$$

The theoretical spectrum of final excitations is presented as pairs of quantities (E_n, P_n).

The spectrum of final excitations is calculated with inevitable approximations. First, the momentum p_β is taken to be equal to the upper edge. It is difficult to quantitatively estimate variations in recoil operator matrix elements (4). However, the total recoil energy of the molecule must evidently decrease with decreasing β-electron energy. Second, the spectrum of final excitations above the upper edge of the one-electron continuum is calculated in a simplified approach ignoring the nuclear motion. *Ad hoc* corrections to the spectrum are included into the tables published in [12].

An analysis of the above approximations is complicated, because it is necessary to estimate integrals (4) involving fast oscillating functions, where $|qR| \sim 25$. However, experiments can be interpreted by means of integral characteristics given by spectral sums (2) and (5). A similar problem arises in an analysis of the Mössbauer effect [16]. The problem can be solved in the operator formalism leading to the sum rules. Here, a similar approach is proposed for analyzing spectral sums for the β-electron distribution.

Substituting the T^3He^+ molecule Hamiltonian H for E_n in Eq. (5), we remove the summation with respect to n and arrive at the expression

$$N(\epsilon_\beta) = \frac{A}{3} F(p_\beta, Z) E_\beta p_\beta \int \frac{d\hat{\mathbf{q}}}{4\pi} \langle \mathrm{T}_2 | e^{-i(\mathbf{q},\mathbf{R})} \times (\hat{\epsilon}^2 - m_\nu^2 c^4)^{3/2} \theta(\hat{\epsilon} - m_\nu c^2) e^{i(\mathbf{q},\mathbf{R})} | \mathrm{T}_2 \rangle, \tag{6}$$

where $\hat{\epsilon} = W_0 - \epsilon_\beta - H$. Operator expression (6) is transformed by using the relation

$$He^{i(\mathbf{q},\mathbf{R})} = e^{i(\mathbf{q},\mathbf{R})} \left[H + \frac{q^2}{2M} + \frac{(\mathbf{q}, \hat{\mathbf{p}}_\mathbf{R})}{M} \right], \tag{7}$$

which is easily obtained, because the kinetic energy operator has the form $\hat{T}_k = -\frac{1}{2M}\Delta_\mathbf{R}$, where $M = M_t/2$ is the reduced molecular mass. According to Eq. (7), the recoil exponent can be removed from Eq. (6) with the substitution

$$W_0 - \epsilon_\beta - H \longrightarrow W_0 - \epsilon_\beta - \frac{q^2}{2M} - \frac{(\mathbf{q}, \hat{\mathbf{p}}_\mathbf{R})}{M} - H. \tag{8}$$

The term $q^2/2M$ corresponds to the integral rovibrational recoil energy. Adding it to the recoil energy of the molecular center of mass, we obtain

$$E_\mathrm{R} \longrightarrow E_\mathrm{R} + \frac{q^2}{2M} = \frac{p_\beta^2}{2M_t} = \frac{\epsilon_\beta}{M_t}\left(1 + \frac{\epsilon_\beta}{2m_e c^2}\right). \tag{9}$$

Redefining E_R and W_0, we derive the β-electron spectrum in the following form of the expectation of a certain operator in the initial state of the T_2 molecule:

$$N(\epsilon_\beta) = \frac{A}{3} F(p_\beta, Z) \times E_\beta p_\beta \left\langle \mathrm{T}_2 \left| \left(\left(\hat{\epsilon} - \frac{(\mathbf{q}, \hat{\mathbf{p}}_\mathbf{R})}{M} \right)^2 - m_\nu^2 c^4 \right)^{3/2} \times \theta\left(\hat{\epsilon} - \frac{(\mathbf{q}, \hat{\mathbf{p}}_\mathbf{R})}{M} - m_\nu c^2 \right) \right| \mathrm{T}_2 \right\rangle. \tag{10}$$

In Eq. (7), the term linear in the momentum has the magnitude $|(\mathbf{q}, \hat{\mathbf{p}}_\mathbf{R})/M| \sim 10^{-2}$, which corresponds to 0.3 eV. Expanding the θ function in this parameter by using the relation

$$f(\hat{A} + \hat{\varepsilon}) = f(\hat{A}) + f'(\hat{A})\hat{\varepsilon} + \frac{1}{2} f''(\hat{A})[\hat{\varepsilon}, \hat{A}] + O(\hat{\varepsilon}^2, [\hat{A}, [\hat{\varepsilon}, \hat{A}]], \ldots), \tag{11}$$

we arrive at the expression

$$\theta\left(\hat{\epsilon} - m_\nu c^2 - \frac{(\mathbf{q}, \hat{\mathbf{p}}_\mathbf{R})}{M} \right) = \theta(\hat{\epsilon} - m_\nu c^2) - \delta(\hat{\epsilon} - m_\nu c^2) \frac{(\mathbf{q}, \hat{\mathbf{p}}_\mathbf{R})}{M} + \ldots. \tag{12}$$

Generalized functions are, as usual, treated in terms of a convolution with a certain smooth function. For the continuous electron rovibrational spectrum, the convolution arises naturally as the integration over the final states. For the discrete spectrum, the convolution is ensured by the additional averaging with the resolution function of a β spectrometer:

$$N_\mathrm{exp}(\epsilon_\beta) = \int d\epsilon R(\epsilon_\beta - \epsilon) N(\epsilon). \tag{13}$$

In both cases, δ terms in Eq. (12) give rise to energy peaks in the spectral sums. The leading correction is $|(\mathbf{q}, \hat{\mathbf{p}}_\mathbf{R})/M|^2 \sim 10^{-4}$ due to additional averaging over angles $\int d\hat{\mathbf{q}}$. In this paper, only the first term of expansion (12) is taken into account.

The exponential in Eq. (10) is expanded similarly. Upon averaging over the angles, we obtain

$$(\hat{\epsilon}^2 - m_\nu^2 c^4)^{3/2} - \left(\frac{q}{M}\right)^2 \Delta_{\mathbf{R}} \hat{\epsilon} + \hat{C} + O\left(\frac{(m_\nu c^2)^4}{\hat{\epsilon}} \left|\frac{(\mathbf{q}, \hat{\mathbf{p}}_{\mathbf{R}})}{M}\right|^2\right), \tag{14}$$

where

$$\hat{C} = -\frac{1}{3}\left(\frac{q}{M}\right)^2 \left(\left[\left[H, \frac{d}{dR}\right], \frac{d}{dR}\right] - \frac{d}{dR}\left[H, \frac{d}{dR}\right]\right). \tag{15}$$

The spectral contribution of this term is small. In particular, $|\hat{C}| \leq 0.1$ eV^3 for the ground electronic state. The remaining corrections in expansion (14) are of the higher order.

The final operator representation for the β-electron spectrum has the form

$$N(\epsilon_\beta) = \frac{A}{3} F(p_\beta, Z) E_\beta p_\beta \times \left\langle \mathrm{T}_2 \left| \left[(\hat{\epsilon}^2 - m_\nu^2 c^4)^{3/2} - \left(\frac{q}{M}\right)^2 \Delta_{\mathbf{R}} \hat{\epsilon} \right] \theta(\hat{\epsilon} - m_\nu c^2) \right| \mathrm{T}_2 \right\rangle. \tag{16}$$

A similar procedure for the differential spectrum yields

$$\frac{dN(\epsilon_\beta)}{d\epsilon_\beta} = AF(p_\beta, Z) E_\beta p_\beta \times \left\langle \mathrm{T}_2 \left| \left[\hat{\epsilon}(\hat{\epsilon}^2 - m_\nu^2 c^4)^{1/2} - \frac{1}{3}\left(\frac{q}{M}\right)^2 \Delta_{\mathbf{R}} \right] \theta(\hat{\epsilon} - m_\nu c^2) \right| \mathrm{T}_2 \right\rangle. \tag{17}$$

Introducing the unity decomposition $\sum_n |n\rangle\langle n| = 1$ into Eqs. (16) and (17), we obtain operator formulas valuable in practice. For the integral spectrum, it has the form

$$N(\epsilon_\beta) = \frac{A}{3} F(p_\beta, Z) E_\beta p_\beta \sum_n \tilde{P}_n \left[(\epsilon_n^2 - m_\nu^2 c^4)^{3/2} + 2\frac{q^2}{M} \epsilon_n \langle \mathrm{T}_2 | \hat{T}_k | n \rangle \langle n | \mathrm{T}_2 \rangle / \tilde{P}_n \right] \theta(\epsilon_n - m_\nu c^2), \tag{18}$$

$$\tilde{P}_n = |\langle \mathrm{T}_2 | n \rangle|^2.$$

Formulas (16)–(18) are asymptotically exact. Corrections are inversely proportional to the energy interval and are small [see Eq. (14)]. Formula (18) indicates that the pseudo-spectrum of final excitations involves only vibrational modes. Analyzing the simplest classical model, we conclude that the term $q^2/2M = p_\beta^2/4M_\mathrm{t}$ is the integral classical rovibrational energy of molecule recoil. The residual summation over the pseudo-spectrum of vibrational modes corresponds to averaging over the initial vibrational state.

Let us consider the ground electronic state of the T^3He^+ molecule. Only several vibrational states contribute to the pseudo-spectrum of the final excitations:

$$|\langle \mathrm{T}_2 | g, v = 0 \rangle|^2 = 0.522, \quad |\langle \mathrm{T}_2 | g, v = 1 \rangle|^2 = 0.046, \quad |\langle \mathrm{T}_2 | g, v = 2 \rangle|^2 = 0.004, \ldots \tag{19}$$

The integral probability is equal to 0.574 [7] as in the standard approach. Using Eqs. (19), we calculate the mean excitation energy of the ground rovibrational multiplet as

$$\langle E_n \rangle_\mathrm{g} = \frac{q^2}{M} + 1/P_\mathrm{g} \sum_n \tilde{P}_n E_n = 1.69 + 0.03 = 1.72 \text{ eV}. \tag{20}$$

This value coincides with the result of the summation of several tens of rovibrational lines presented in the tables from [9]. Value (20) was obtained with the recoil momentum p_β corresponding to the upper edge of the spectrum and the nonrelativistic relation between the momentum and energy of a β electron. The relativistic formula used in [13] increases the value by 0.03 eV. This result follows from the exact sum rule

$$\sum_n E_n P_n = \sum_n \tilde{P}_n + P_g \frac{q^2}{2M}, \tag{21}$$

which is a particular case of relations used in deriving the operator formulas. The additional shift of the center of rovibrational excitations, which is determined by the second term in Eq. (20), is equal to about 0.1 eV for excited electronic states.

As was mentioned above, the nuclear motion is ignored when calculating high electronic states. According to *ad hoc* corrections made in tables in [12], integral lines are characterized by a shift of 1 eV simulating the rovibrational recoil effect. According to the present analysis, an identical shift of 1.7 eV must be attributed to all lines. A residual uncertainty of about 0.1 eV depends on the properties of a given electronic state. In contrast, a shift of 1.9 eV proposed in [13] is quite large. In addition, the probability distribution of the contribution of electron resonances was taken to be the 3-eV-wide Gaussian, which simulates the rovibrational broadening. According to our concept of the spectrum, the overlap integral can be calculated with the simplest oscillator wave function in the initial state and the semiclassical radial Airy function in the final state. In this case, the resulting distribution is Gaussian-like with the width

$$\delta E = F\sqrt{\ln 2 / M\omega_{\mathrm{T}_2}}, \quad F = Z_\mathrm{eff}/R_0^2, \tag{22}$$

where ω_{T_2} is the oscillation frequency of the T_2 molecule, $R_0 \approx 1.4$ is the equilibrium internuclear distance in

the initial T_2 molecule, and $Z_{\text{eff}} \approx 1.5$–2 is the effective charge determining the slope of the molecular term of the final state at the point R_0. Formula (22) yields $\delta E \approx$ 3–4 eV. According to [12], the fitted neutrino mass is only slightly sensitive to the width of resonance lines.

In conclusion, we discuss the correction of the total molecule recoil energy (9). The spectrum upper edge W_0 is one of free parameters in fitting the β-electron spectrum. The recoil energy is insignificant in this case. However, we revealed that the total recoil energy depends explicitly on energy. This dependence is manifested as both a change in the recoil energy of the molecular center of mass and the integral shift of the centers of rovibrational multiplets. The latter shift is the primary manifestation of the dependence of the recoil-operator matrix elements $P_n(p_\beta)$ on the β-electron energy. The magnitude of the effect is independent of the method of calculating the spectrum.

The correction to the β-electron spectrum given by Eqs. (2) and (5) can be presented as a weak energy dependence of the upper edge W_0:

$$W_0^{(\text{eff})} = W_0 + \delta W_0(\epsilon_\beta),$$
$$\delta W_0 = E_R^{(0)} - E_R \approx \frac{\epsilon_\beta^{(0)} - \epsilon_\beta}{M_t}, \tag{23}$$

where $\epsilon_\beta^{(0)}$ is an arbitrary reference point of the spectrum. The effect is weak. In particular, $\delta W_0 \sim 0.04$ eV for an energy interval of about 200 eV. However, the integral spectrum behaves approximately as $(W_0 - \epsilon_\beta)^3$. Variation in W_0 gives rise to the $\delta W_0(W_0 - \epsilon_\beta)^2$ terms. The dependence on neutrino mass leads to negative contributions on the order of $m_\nu^2 (W_0 - \epsilon_\beta)$ to the spectrum. Thus, the energy interval is responsible for the enhancement of the effect.

Fitting experimental data, we expected that the average W_0 value would be determined primarily by points near the lower edge of the spectrum, where the number of events is several orders of magnitude as large as that near the upper edge. A weak energy dependence leads to a small positive correction to the standard spectrum obtained with a fixed W_0 value. The effect is compensated by taking a negative average value of the free parameter m_ν^2. The farther the lower edge of the spectrum, the lower the effective W_0 value; the higher the effective correction δW_0, the higher the absolute value of the negative parameter m_ν^2. This behavior was pronounced in detailed reports of experiments (see Table 1 in [5]).

The effect was estimated through the simplest numerical simulation. Using the standard tables of the spectrum of final excitations and assuming that the neutrino mass equals zero, we calculated the hypothetical spectra of β electrons with and without the correction δW_0. When W_0 was taken at the lower edge of the fitting interval, these two spectra coincided at two edges of the energy interval. Varying m_ν^2, we fitted the two spectra over the entire interval by the least squares method. As a result, the best fit was reached with $m_\nu^2 \approx -1.9\ \text{eV}^2/\text{c}^4$, which is approximately equal to the values reported in [4, 6]. The inclusion of the correction to the procedure of fitting the experimental spectrum must give the actual effect magnitude.

In summary, operator formalism was applied to analyze the spectral sums. In order to improve the theoretical spectrum of final states, several modernizations were proposed. In particular, the numerical effect of the recoil energy on neutrino mass determined by fitting the theoretical spectrum of β electrons to experimental data was discussed. The numerical estimates, calculations of the spectrum, and detailed analysis of the operator product expansions will be given elsewhere.

This work was supported by the National Science Foundation (USA), grant no. PHY-9984075.

REFERENCES

1. R. G. H. Robertson, T. J. Bowles, G. J. Stephenson, Jr., *et al.*, Phys. Rev. Lett. **67**, 957 (1991).
2. W. Stoeffl and D. J. Decman, Phys. Rev. Lett. **75**, 3237 (1995).
3. C. Weinheimer, M. Przyrembel, H. Backe, *et al.*, Phys. Lett. B **300**, 210 (1993).
4. C. Weinheimer, B. Degenddag, A. Bleile, *et al.*, Phys. Lett. B **460**, 219 (1999).
5. A. I. Belesev, A. I. Bleule, E. V. Geraskin, *et al.*, Phys. Lett. B **350**, 263 (1995).
6. V. M. Lobashev, V. N. Aseev, A. I. Belesev, *et al.*, Phys. Lett. B **460**, 227 (1999).
7. W. Kolos, B. Jeziorski, K. Szalewich, and H. J. Monkhorst, Phys. Rev. A **31**, 551 (1985).
8. W. Kolos, B. Jeziorski, K. Szalewich, and H. J. Monkhorst, Phys. Rev. A **32**, 2573 (1985).
9. O. Fackler, B. Jeziorski, W. Kolos, *et al.*, Phys. Rev. Lett. **55**, 1388 (1985).
10. K. Szalewicz, O. Fackler, B. Jeziorski, *et al.*, Phys. Rev. A **35**, 965 (1987).
11. P. Froelich, B. Jeziorski, W. Kolos, *et al.*, Phys. Rev. Lett. **71**, 2871 (1993).
12. S. Jonsell and H. J. Monkhorst, Phys. Rev. Lett. **76**, 4476 (1996).
13. A. Saenz, S. Jonsell, and P. Froelich, Phys. Rev. Lett. **84**, 242 (2000).
14. http://www-ik1.fzk.de/tritium.
15. E. J. Konopinski, *The Theory of Beta Radioactivity* (Clarendon, Oxford, 1966).
16. H. J. Lipkin, *Quantum Mechanics; New Approaches to Selected Topics* (American Elsevier, New York, 1973).

Translated by R. Tyapaev

JETP Letters, Vol. 76, No. 5, 2002, pp. 249–252. From Pis'ma v Zhurnal Éksperimental'noĭ i Teoreticheskoĭ Fiziki, Vol. 76, No. 5, 2002, pp. 306–309.

High-Energy QCD Asymptotic Behavior of Photon–Photon Collisions¶

S. J. Brodsky[1], V. S. Fadin[2], V. T. Kim[3]*, L. N. Lipatov[3], and G. B. Pivovarov[4]

[1] *SLAC, Stanford, CA 94309, USA*

[2] *Budker Institute for Nuclear Physics, Novosibirsk, 630090 Russia*

* *CERN, CH-1211, Switzerland*

[3] *St. Petersburg Nuclear Physics Institute, Gatchina, 188300 Russia*

[4] *Institute for Nuclear Research, Moscow, 117312 Russia*

Received July 25, 2002

The high-energy behavior of the total cross section for highly virtual photons, as predicted by the BFKL equation at next-to-leading order (NLO) in QCD, is discussed. The NLO BFKL predictions, improved by the BLM optimal scale setting, are in good agreement with recent OPAL and L3 data at CERN LEP2. NLO BFKL predictions for future linear colliders are presented. © *2002 MAIK "Nauka/Interperiodica".*

PACS numbers: 12.38.Cy

Photon–photon collisions, particularly $\gamma^*\gamma^*$ processes, play a special role in QCD [1], since their analysis is under much better control than the calculation of hadronic processes, which require the input of nonperturbative hadronic structure functions or wave functions. In addition, unitarization (screening) corrections due to multiple Pomeron exchange should be less important for the scattering of γ^* of high virtuality than for hadronic collisions.

The high-energy asymptotic behavior of the $\gamma\gamma$ total cross section in QED can be calculated [2] by an all-orders resummation of the leading terms: $\sigma \sim \alpha^4 s^\omega$, $\omega = \frac{11}{32}\pi\alpha^2 \simeq 6 \times 10^{-5}$ (Fig. 1). However, the slowly rising asymptotic behavior of the QED cross section is not apparent, since large contributions come from other sources, such as the cut of the fermion-box contribution: $\sigma \sim \alpha^2(\log s)/s$ [1] (which, although subleading in energy dependence, dominates the rising contributions by powers of the QED coupling constant) and QCD-driven processes (Fig. 2).

The high-energy asymptotic behavior of hard QCD processes is governed by the Balitsky–Fadin–Kuraev–Lipatov (BFKL) formalism [3, 4]. The highest eigenvalue, ω, of the BFKL equation [3] is related to the intercept of the QCD BFKL Pomeron, which in turn governs the high-energy asymptotic behavior of the cross sections: $\sigma \sim s^{\alpha_{IP}-1} = s^\omega$. The BFKL Pomeron intercept in the leading order (LO) turns out to be rather large: $\alpha_{IP} - 1 = \omega_{LO} = 12\ln 2(\alpha_S/\pi) \simeq 0.55$ for $\alpha_S = 0.2$ [3]. The next-to-leading order (NLO) corrections to the BFKL intercept have recently been calculated [5], but the results in the $\overline{\text{MS}}$ scheme have a strong renormalization scale dependence. In Ref. [6] we used the Brodsky–Lepage–Mackenzie (BLM) optimal scale setting procedure [7] to eliminate the renormalization scale ambiguity. (For other approaches to the NLO BFKL predictions, see Refs. [8, 6] and references therein.) The BLM optimal scale setting resums the conformal-violating β_0 terms into the running coupling in all orders of perturbation theory, thus preserving the conformal properties of the theory. The NLO BFKL predictions, as improved by the BLM scale setting, yields $\alpha_{IP} - 1 = \omega_{NLO} = 0.13$–$0.18$ [6]. Strictly speaking, the integral kernel of the BFKL equation at NLO is not conformally invariant, and, hence, one should use a more accurate method for its solution (see [9]). But

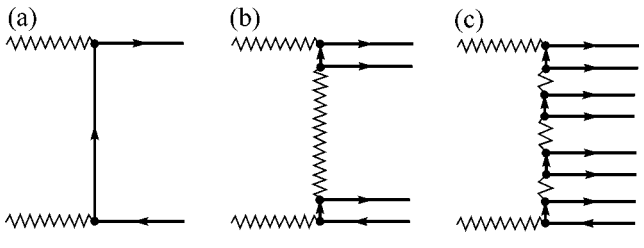

Fig. 1. Photon–photon collisions in QED: (a) electron-box diagram: $\sigma \sim \alpha^2(\log s)/s$; (b) one-photon exchange diagram: $\sigma \sim \alpha^4 s^0$; (c) a typical higher-order diagram, its resummation leads to $\sigma \sim \alpha^4 s^\omega$, $\omega = \frac{11}{32}\pi\alpha^2$ [2].

¶This article was submitted by the authors in English.

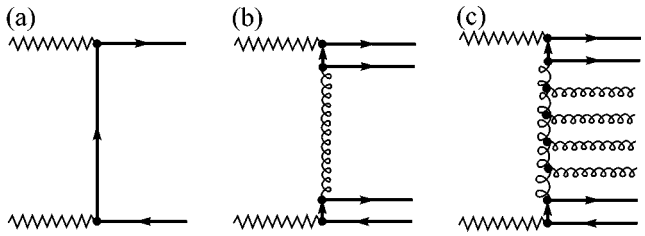

Fig. 2. High-energy photon–photon collisions in QCD: (a) quark-box diagram: $\sigma \sim \alpha^2(\log s)/s$; (b) one-gluon exchange diagram: $\sigma \sim \alpha^2\alpha_S^2 s^0$; (c) a typical higher-order diagram; its resummation leads to $\sigma \sim \alpha^2\alpha_S^2 s^\omega$. $\omega_{LO} = 12\ln 2(\alpha_S/\pi) \simeq 0.55$ [3] and $\omega_{NLO} = 0.13$–0.18 [6].

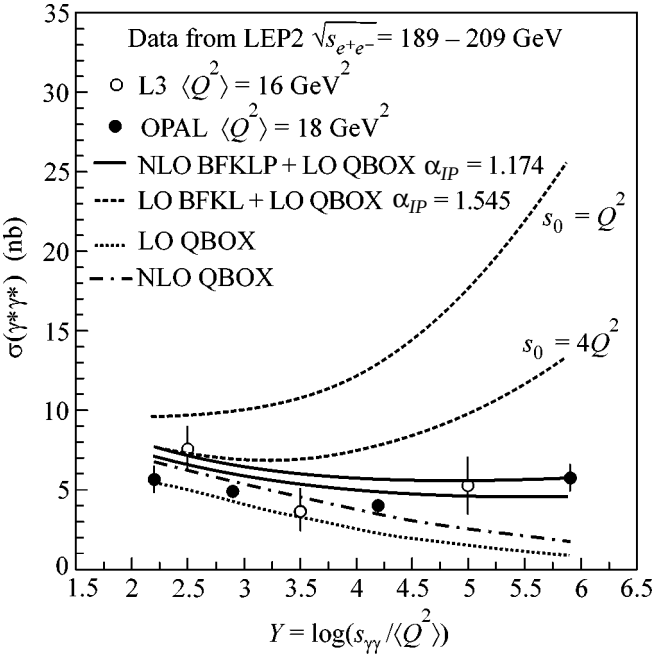

Fig. 3. The energy dependence of the total cross section for highly virtual photon–photon collisions predicted by the BLM scale-fixed NLO BFKL [14, 15, 6] compared with OPAL [16] and L3 [17] data from LEP2 at CERN. The (solid) dashed curves correspond to the (N)LO BFKL predictions for two different choices of the Regge scale: $s_0 = Q^2$ for upper curves and $s_0 = 4Q^2$ for lower curves.

in the BLM approach the dependence of the eigenvalue of the kernel from the gluon virtuality is extremely weak [6] and, therefore, ω_{NLO} coincides basically with the eigenvalue.

The photon–photon cross sections with LO BFKL resummation were considered in Refs. [4, 10–12]. The total cross section of two unpolarized gammas with virtualities Q_A and Q_B in the LO BFKL [4, 11] reads as follows:

$$\sigma(s, Q_A^2, Q_B^2) = \sum_{i,k=T,L} \frac{1}{\pi\sqrt{Q_A^2 Q_B^2}} \times \int_0^\infty \frac{d\nu}{2\pi} \cos\left(\nu \ln\left(\frac{Q_A^2}{Q_B^2}\right)\right) F_i(\nu) F_k(-\nu) \left(\frac{s}{s_0}\right)^{\omega(Q^2,\nu)},$$

with the gamma impact factors in the LO for the transverse and longitudinal polarizations:

$$F_T(\nu) = F_T(-\nu) = \alpha\alpha_S\left(\sum_q e_q^2\right)\frac{\pi}{2} \times \frac{\left[\frac{3}{2} - i\nu\right]\left[\frac{3}{2} + i\nu\right]\Gamma\left(\frac{1}{2} - i\nu\right)^2\Gamma\left(\frac{1}{2} + i\nu\right)^2}{\Gamma(2 - i\nu)\Gamma(2 + i\nu)},$$

$$F_L(\nu) = F_L(-\nu) = \alpha\alpha_S\left(\sum_q e_q^2\right)\pi \times \frac{\Gamma\left(\frac{3}{2} - i\nu\right)\Gamma\left(\frac{3}{2} + i\nu\right)\Gamma\left(\frac{1}{2} - i\nu\right)\Gamma\left(\frac{1}{2} + i\nu\right)}{\Gamma(2 - i\nu)\Gamma(2 + i\nu)},$$

where a Regge scale parameter s_0 is proportional to a hard scale $Q^2 \sim Q_A^2, Q_B^2$; Γ is the Euler Γ function and e_q is the quark electric charge.

Although the NLO impact factor of the virtual photon is not known [13], one can use the LO impact factor of Refs. [2, 11], assuming that the main energy-dependent NLO corrections come from the NLO BFKL subprocess rather than from the photon impact factors [14, 15].

Fig. 3 compares the LO and BLM scale-fixed NLO BFKL predictions $\sigma \sim \alpha^2\alpha_S^2 s^\omega$ [6, 14, 15] with recent CERN LEP2 data from OPAL [16] and L3 [17]. The spread in the curves reflects the uncertainty in the choice of the Regge scale parameter, which defines the beginning of the asymptotic regime: $s_0 = Q^2$ to $4Q^2$ for LO and NLO BFKL, where Q^2 is the mean virtuality of the colliding photons. One can see from Fig. 3 that the agreement of the NLO BFKL predictions [14, 15, 6] with the data is quite good. The sensitivity of the NLO BFKL results to the Regge parameter s_0 is much smaller than in the case of the LO BFKL. The variation of the predictions in the value of s_0 reflects uncertainties from uncalculated subleading terms. The parametric variation of the LO BFKL predictions is so large that it can be, in fact, neither ruled out nor confirmed at the energy range of CERN LEP2.

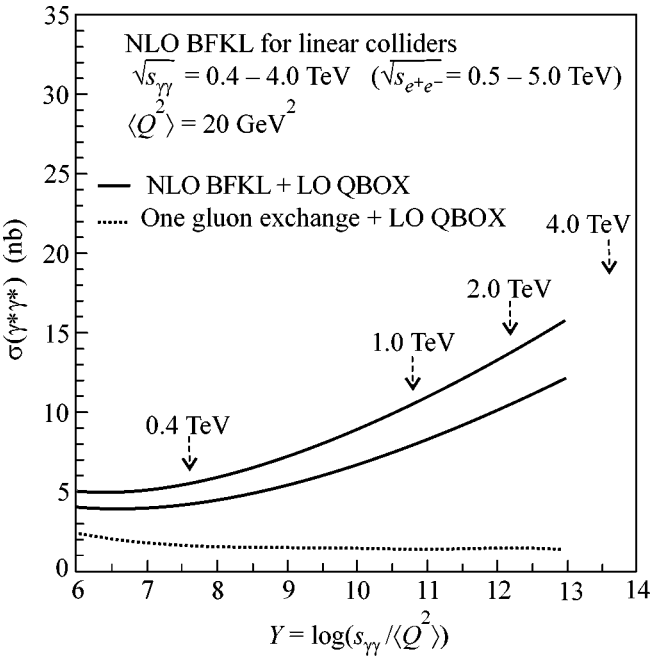

Fig. 4. The energy dependence of the total cross section for virtual photon–photon collisions predicted by the NLO BFKL for future linear colliders. The solid curves correspond to the BLM scale-fixed NLO BFKL predictions with $s_0 = Q^2$ (upper curve) and $s_0 = 4Q^2$ (lower curve). The dotted curve shows the one-gluon exchange contribution.

The double-logarithmic DGLAP asymptotic behavior related with $\log(Q_A^2/Q_B^2)$ terms for the total photon–photon cross section was considered in Ref. [12] and found to be small for the CERN LEP2 kinematical region. The point is that most of the CERN LEP2 data [16–18] are collected at the approximately equal virtualities of the colliding photons: $1/2 < Q_A^2/Q_B^2 < 2$. It should be stressed that the soft Pomeron contribution to the $\gamma^*\gamma^*$ total cross section, if estimated within the vector-dominance model, is proportional to $\sigma_{\gamma^*\gamma^*} \sim (m_V^2/Q^2)^4\sigma_{\gamma\gamma}$ and therefore suppressed for such highly virtual photons as those under consideration.

We also note that the NLO BFKL predictions are consistent [15] with data recently presented by ALEPH [18]. In contrast, the NLO quark-box contribution [19] underestimates the L3 data point at $Y \equiv \log(s_{\gamma\gamma}/\langle Q^2 \rangle) = 6$ by 4 standard deviations. Indeed, the NLO quark-box contribution [19], calculated in massless approximation, can be scaled down from general considerations with the quark masses. For example, at leading order, the inclusion of masses to the quark-box diagram reduces its contribution by 10–15% [19]. Also, the one-gluon exchange added to the (N)LO quark-box contribution is not sufficient to describe the data at $Y = 6$ within (3) 4 standard deviations (see also Fig. 4).

In Fig. 4 the BLM fixed-scale NLO BFKL predictions for a future linear collider with the photon–photon collider option ($\sqrt{s_{\gamma\gamma}} \leq 0.8\sqrt{s_{e^+e^-}}$) under discussion [20] are shown.

The NLO BFKL phenomenology is consistent with the assumption of small unitarization corrections in the photon–photon scattering at large Q^2. Thus, one can accommodate the NLO BFKL Pomeron intercept value 1.13–1.18 [6] predicted by the BLM optimal scale setting. In the case of hadron scattering, the larger unitarization corrections [21] lead to a smaller effective Pomeron intercept value, about 1.10 [22].

In summary, highly virtual photon–photon collisions provide a very unique opportunity to test the high-energy asymptotic behavior of QCD. The NLO BFKL predictions for the $\gamma^*\gamma^*$ total cross section, with the renormalization scale fixed by the BLM procedure, show good agreement with the recent data from OPAL [16] and L3 [17] at CERN LEP2. The results obtained could be very important for future lepton and photon colliders.

The authors thank V.P. Andreev, A. Bohrer, A. De Roeck, J.R. Ellis, J.H. Field, I.M. Ginzburg, A.B. Kaidalov, V.A. Khoze, M. Kienzle-Focacci, M. Krawczyk, C.-N. Lin, V.A. Schegelsky, V.G. Serbo, M. Przybycién, A.A. Vorobyov, and M. Wadhwa for helpful discussions. This work was supported in part by the Russian Foundation for Basic Research, the INTAS Foundation, the U.S. National Science Foundation, and the U.S. Dept. of Energy under contract no. DE-AC03-76SF00515.

REFERENCES

1. V. M. Budnev, I. F. Ginzburg, G. V. Meledin, and V. G. Serbo, Phys. Rep. C **15**, 181 (1975).
2. V. N. Gribov, L. N. Lipatov, and G. V. Frolov, Phys. Lett. B **31B**, 34 (1970); Yad. Fiz. **12**, 994 (1970) [Sov. J. Nucl. Phys. **12**, 543 (1971)]; H. Cheng and T. T. Wu, Phys. Rev. D **1**, 2775 (1970).
3. V. S. Fadin, L. N. Lipatov, and E. A. Kuraev, Phys. Lett. B **60B**, 50 (1975); Zh. Éksp. Teor. Fiz. **71**, 840 (1976) [Sov. Phys. JETP **44**, 443 (1976)]; Zh. Éksp. Teor. Fiz. **72**, 377 (1977) [Sov. Phys. JETP **45**, 199 (1977)].
4. I. I. Balitsky and L. N. Lipatov, Yad. Fiz. **28**, 1597 (1978) [Sov. J. Nucl. Phys. **28**, 822 (1978)].
5. V. S. Fadin and L. N. Lipatov, Phys. Lett. B **429**, 127 (1998); G. Camici and M. Ciafaloni, Phys. Lett. B **430**, 349 (1998).
6. S. J. Brodsky, V. S. Fadin, V. T. Kim, *et al.*, Pis'ma Zh. Éksp. Teor. Fiz. **70**, 161 (1999) [JETP Lett. **70**, 155 (1999)].
7. S. J. Brodsky, G. P. Lepage, and P. B. Mackenzie, Phys. Rev. D **28**, 228 (1983).
8. B. Andersson, G. Gustafson, and J. Samuelsson, Nucl. Phys. B **467**, 443 (1996); M. Ciafaloni, D. Colferai, and G. P. Salam, Phys. Rev. D **60**, 114036 (1999); R. S. Thorne, Phys. Rev. D **60**, 054031 (1999); G. Altarelli, R. D. Ball, and S. Forte, Nucl. Phys. B **599**, 383 (2001).

9. L. N. Lipatov, Zh. Éksp. Teor. Fiz. **90**, 1536 (1986) [Sov. Phys. JETP **63**, 904 (1986)]; Phys. Rep. C **286**, 131 (1997); L. V. Gribov, E. M. Levin, and M. G. Ryskin, Phys. Rep. C **100**, 1 (1983).
10. J. Bartels, A. De Roeck, and H. Lotter, Phys. Lett. B **389**, 742 (1996); A. Białas, W. Czyż, and W. Florkowski, Eur. Phys. J. C **2**, 683 (1998); J. Kwieciński and L. Motyka, Acta Phys. Pol. B **30**, 1817 (1999); Eur. Phys. J. C **18**, 343 (2000); J. Bartels, C. Ewerz, and R. Staritzbichler, Phys. Lett. B **492**, 56 (2000); N. N. Nikolaev, J. Speth, and V. R. Zoller, Zh. Éksp. Teor. Fiz. **93**, 1104 (2001) [JETP **93**, 957 (2001)].
11. S. J. Brodsky, F. Hautmann, and D. E. Soper, Phys. Rev. D **56**, 6957 (1997); Phys. Rev. Lett. **78**, 803 (1997); Erratum: **79**, 3544 (1997).
12. M. Boonekamp, A. De Roeck, C. Royon, and S. Wallon, Nucl. Phys. B **555**, 540 (1999).
13. V. S. Fadin, D. Yu. Ivanov, and M. I. Kotsky, BUDKER-INP-2001-33, DFCAL-TH-01-2 (2001); hep-ph/0106099; J. Bartels, S. Gieseke, and C. F. Qiao, Phys. Rev. D **63**, 056014 (2001); Erratum: **65**, 079902 (2002); J. Bartels, S. Gieseke, and A. Kyrieleis, Phys. Rev. D **65**, 014006 (2002).
14. V. T. Kim, L. N. Lipatov, and G. B. Pivovarov, in *Proceedings of the 29th International Symposium on Multiparticle Dynamics (ISMD99), Providence, 1999*, hep-ph/9911242; in *Proceedings of the 8th Blois Workshop (EDS99), Protvino, Russia, 1999*, hep-ph/9911228; V S. Fadin, V. T. Kim, L. N. Lipatov, and G. B. Pivovarov, in *Proceedings of the XXXV PNPI Winter School, Repino, Russia, 2001*, hep-ph/0207296.
15. S. J. Brodsky, V. S. Fadin, V. T. Kim, *et al.*, presented at PHOTON2001, Ascona, Switzerland, 2001; SLAC-PUB-9069, CERN-TH/2001-341; hep-ph/0111390.
16. G. Abbiendi *et al.* (OPAL Collab.), Eur. Phys. J. C **24**, 17 (2002).
17. P. Achard *et al.* (L3 Collab.), Phys. Lett. B **531**, 39 (2002).
18. G. Prange (ALEPH Collab.), presented at PHOTON2001, Ascona, Switzerland, 2001.
19. M. Cacciari, V. Del Duca, S. Frixione, and Z. Trocsanyi, JHEP **0102**, 029 (2001).
20. M. M. Velasco *et al.*, APS/DPF/DPB Summer Study on the Future of Particle Physics (Snowmass 2001), Snowmass, USA, 2001; hep-ex/0111055; B. Badelek *et al.* (ECFA/DESY Photon Collider Working Group), DESY-TESLA-2001-23, DESY-TESLA-FEL-2001-05 (2001); hep-ex/0108012; J.-P. Delahaye *et al.* (CLIC Study Group), CERN-PS/98-009-LP (1999); Acta Phys. Pol. B **30**, 2029 (1999); K. Abe *et al.* (ACFA Linear Collider Working Group), KEK-REPORT-2001-11 (2001); hep-ph/0109166.
21. A. B. Kaidalov, L. A. Ponomarev, and K. A. Ter-Martirosyan, Yad. Fiz. **44**, 722 (1986) [Sov. J. Nucl. Phys. **44**, 468 (1986)]; M. S. Dubovikov, B. Z. Kopeliovich, L. I. Lapidus, and K. A. Ter-Martirosyan, Nucl. Phys. B **123**, 147 (1977); B. Z. Kopeliovich and L. I. Lapidus, Zh. Éksp. Teor. Fiz. **71**, 61 (1976) [Sov. Phys. JETP **44**, 31 (1976)].
22. J. R. Cudell, V. Ezhela, K. Kang, *et al.*, Phys. Rev. D **61**, 034019 (2000); Erratum: **63**, 059901 (2001); J. R. Cudell, A. Donnachie, and P. V. Landshoff, Phys. Lett. B **448**, 281 (1999); M. M. Block, E. M. Gregores, F. Halzen, and G. Pancheri, Phys. Rev. D **58**, 017503 (1998); P. Gauron and B. Nicolescu, Phys. Lett. B **486**, 71 (2000).

JETP Letters, Vol. 76, No. 5, 2002, pp. 253–257. Translated from Pis'ma v Zhurnal Éksperimental'noĭ i Teoreticheskoĭ Fiziki, Vol. 76, No. 5, 2002, pp. 310–315.

Self-Generation of Spin-Wave Envelope Soliton Trains with Different Periods

B. A. Kalinikos[1, *], N. G. Kovshikov[1], M. P. Kostylev[1], and H. Benner[2]

[1] *St. Petersburg State Electrotechnical University, ul. Popova 5, St. Petersburg, 197376 Russia*

**e-mail: borisk@borisk.usr.etu.spb.ru*

[2] *Technische Universität Darmstadt, D-64289 Darmstadt, Germany*

Received August 2, 2002

The self-generation of periodic spin-wave envelope soliton trains of microwave spin waves in active rings based on ferromagnetic films is studied experimentally. The trains of bright solitons with different periods are self-generated in the same ring due to the frequency-selective control of the attenuation of spin waves circulating in an active ring. © *2002 MAIK "Nauka/Interperiodica"*.

PACS numbers: 75.30.Ds; 75.70.-i

Two types of envelope solitons—bright and dark solitons—can be excited and propagate in nonlinear dispersive media. The properties of these solitons were studied in detail (see, e.g., [1, 2]). Recently, it was suggested using active rings based on nonlinear dispersive media for the self-generation of envelope solitons. In particular, active rings based on ferromagnetic films were used to self-generate envelope solitons of microwave spin waves [3, 4]. In these works, the period T of soliton trains was determined as $T = l/v$, where l is the ring length and v is the soliton velocity. In other words, trains observed in these works can be attributed to the circulation of one soliton in the ring. Similar treatment is applicable to experiments with optical solitons generated in optical fiber rings (see, e.g., [5]).

According to simple physical reasoning, several solitons can generally circulate in a ring. Recently, Carr *et al.* [6, 7] obtained analytical stationary one- and multisoliton solutions for rings based on dispersive media, where nonlinear waves can be described by the one-dimensional nonlinear Schrödinger equation. However, experimental observation of soliton trains self-generated with different periods in the same ring is an open problem.

In this work, the possibility of self-generating periodic trains of bright solitons of microwave spin waves with different periods, i.e., the possibility of controlling the density of nonlinearly generated trains of spin-wave solitons, is investigated experimentally.

The grounds of the experiment are easily presented in spectral terms. Any self-generated periodic train of microwave pulses (solitons in this case) obviously has a discrete frequency spectrum. The period of the train is determined in terms of the frequency spacing between harmonics Δf as $T = 1/\Delta f$ (this was the fact for self-generated dark and bright solitons in [3, 4]). Therefore, increasing the spacing between harmonics forming the train can decrease the period of a generated pulse train. Thus, controlled generation in an active resonant ring can be realized when only selected natural harmonics (resonant modes) are involved in nonlinear self-generation.

Two self-generation regimes were realized for the same ring in this study. The first regime corresponds to the two-soliton circulation mode; i.e., every second ring harmonic is concerned in the generation of bright soliton trains. The second regime corresponds to the one-soliton circulation mode; i.e., all ring harmonics are involved in the generation of bright soliton trains. The initial harmonics (resonant ring modes) were chosen by the frequency-selective control of the attenuation of spin waves circulating in the active ring. As will be shown below, all resonant modes are concerned in generation due to increasing gain, i.e., due to the compensation of attenuation in the ring.

Previous experiments with spin-wave solitons were well described by the nonlinear Schrödinger equation

$$\partial a/\partial t + v_g \partial a/\partial z - iD/2\partial^2 a/\partial z^2 + iN|a|^2 = 0, \quad (1)$$

which indicates that bright envelope solitons can exist in media, when dispersion and nonlinear coefficients of the carrier wave are opposite in sign. This condition is satisfied for so-called backward volume spin waves propagating in an in-plane magnetized ferromagnetic films. The dispersion $\omega(k)$ of this wave is monotonic in the long-wavelength spectral region [8, 9], the dispersion coefficient $D = \partial^2\omega/\partial k^2$ and nonlinear coefficient $N = \partial\omega/\partial|a|^2$ of the wave are positive and negative, respectively. Moreover, the single-mode regime of propagating spin waves is easily realized for this wave [10]. This circumstance is particularly important for excluding undesirable interference effects when studying soliton phenomena. For this reason, a backward

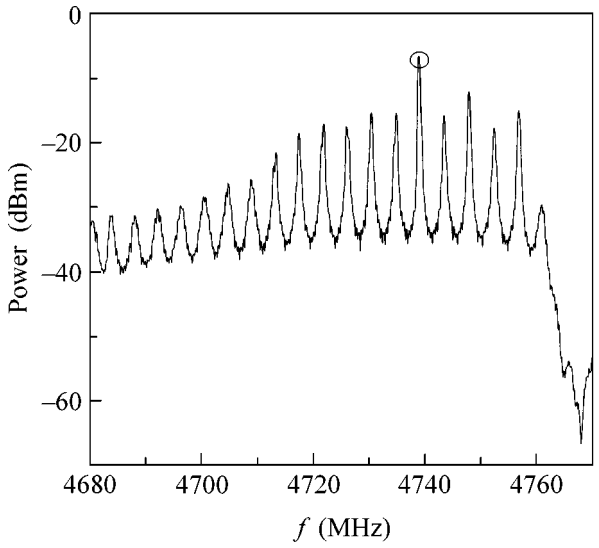

Fig. 1. Frequency response measured for the active YIG film ring near generation threshold for gain $G = -0.2$ dB.

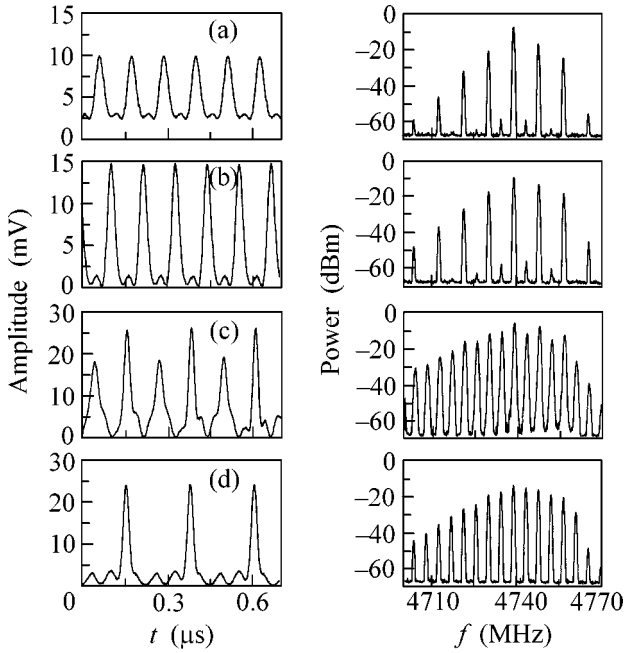

Fig. 2. (Left panels) Envelopes of the self-generated microwave signal circulating in the active ring and (right panels) corresponding frequency spectra as measured for gain G = (a) 0.1, (b) 0.8, (c) 1, and (d) 1.3 dB.

volume spin wave was used as a carrier wave in our experiments.

Experiments were carried out with an active ring involving an yttrium iron garnet (YIG) film, microwave amplifier, and attenuator. We emphasize that the band of amplified frequencies and dynamical range of the amplifier were chosen such that the YIG film determined the nonlinear properties of the ring. The attenuator smoothly controlled attenuation in the ring and switched it to the generation regime. A microwave signal was injected and withdrawn by directed splitters. Experiments were carried out with 2-mm-wide YIG film specimens (spin-wave waveguides), which were cut out of a high-quality single-crystal YIG film 5.2 μm in thickness, which was grown on a substrate of gadolinium gallium garnet with (111) orientation. Microwave spin waves were generated and detected by the ordinary microstrip structure [11, 12], which had short-circuited input and output microstrip antennas, whose width was equal to 50 μm and length, to the width of the film waveguide. According to the condition of obtaining soliton trains with periods of several tens of nanoseconds, the antennas were spaced at 5 mm.

Experiments conventionally involved two stages. The first stage, where the frequency response of the active ring as a ring resonator was controlled and studied, aimed at obtaining the resonator frequency response ensuring minimum losses for several alternate resonant eigenmodes. The lowest losses must be ensured for a resonant mode located deep enough in the spectrum of the backward volume spin waves to keep nonlinearly generated harmonics within this spectrum. Choosing the frequency response of the external part (other than the ferromagnetic film) of the electron microwave section ensures the desired frequency response of the ring. The second stage aimed at self-generating soliton trains of nonlinear pulses of spin waves with different periods.

Figure 1 shows the frequency response of the ring resonator near self-generation threshold for $G = -0.2$ dB and bias field $H = 1020$ Oe. Self-generation threshold $G = 0$ was determined by the onset of the monochromatic generation of a microwave signal in the ring. This generation was detected by the high-sensitive HP70206 spectrum analyzer. The resonant ring eigenmode with the smallest losses, which is indicated by the circle in Fig. 1, was the first mode that reached the self-generation regime for $G \geq 0$ in nonlinear experiments. Thus, this mode was the carrier frequency of the pulse train generated with further increasing gain. We emphasize that the next resonant modes with comparatively small losses are the next nearest modes spaced at $2\Delta f$ from the carrier mode. Losses for nearest modes spaced at $\pm\Delta f$ from the carrier mode were somewhat larger. Due to this relation between attenuations, subsequent to the carrier mode, other resonant modes spaced at $2\Delta f$ were involved in self-generation with increasing gain. Then, as gain increased, all the ring-resonator modes spaced at Δf were concerned in self-generation.

The development of the self-generation process with increasing gain is illustrated in Fig. 2, which shows (left panels) envelopes of the self-generated microwave signal and (right panels) respective frequency spectra. As is seen, single-frequency mono-

chromatic generation is followed by multifrequency generation even at $G = 0.1$ dB, which is slightly above the generation threshold. However, the nonlinear process is insufficiently developed for $G = 0.1$ dB. This conclusion is supported by the presence of the pedestal in Fig. 2a. The self-generated pulse train for $G = 0.8$ dB consists of pronounced knoidal waves (bright soliton train) (Fig. 2b). The period of the train is $T = 1/2\Delta f$, and the FWHM duration of one soliton is $\tau_2 = 29$ ns.

As gain increases further, some nonlinear modes are suppressed, whereas other modes increase (Fig. 2c). The self-generated periodic train for $G = 1.3$ dB again has the form of a stationary soliton train (Fig. 2d), whose period is twice the period of the train shown in Fig. 2b, and the duration of one soliton is equal to $\tau_1 = 27$ ns.[1]

We emphasize that the regime of the self-generation of spin-wave solitons that is shown in Fig. 2b is obtained in this work and corresponds to the simultaneous circulation of two solitons in the ring. The self-generation regime shown in Fig. 2d is similar to the regime described in [4]. Elementary calculations demonstrate that the velocities of solitons coincide in both regimes (Figs. 2b, 2d) and are approximately equal to the group velocity $v_g = 2.4 \times 10^6$ cm/s of the carrier spin wave with a frequency of 4739 MHz and wave number of 80 Rad/cm^{-1}.

The self-generated frequencies of all observed trains coincide with the frequencies of resonant ring eigenmodes (cf. Figs. 1 and 2). Therefore, the observed self-generation process can be treated as modulation instability caused by the four-wave interaction between spin waves corresponding to the resonant modes of the ring.

To check that the observed self-generation of nonlinear-pulse train is the self-generation of solitons, we developed a model of the process and carried out a numerical simulation. In the model, the composite ring is treated as a homogeneous ring resonator of traveling spin waves. The length of this resonator is taken as $l = v_g/T$, where v_g is the group velocity of spin waves at the center frequency of the transmission band in the linear regime. The form of the frequency transmission band can be varied in a numerical simulation.

As is usually done in the theory of envelope solitons, we suppose that spin waves interact though the four-wave interaction. Four-wave processes in an unbounded ferromagnetic medium [13] or in a ferromagnetic film [14] are usually analyzed through the equations of motion in the wave vector space of Fourier components a_k of the spatial variable. In the case under consideration, in order to take into account the resonant properties of the ring, we derive the set for the amplitude of the resonant harmonics a_n of a spin-wave packet that circulates in the ring and has dimensionless scalar envelope $a(z, t)$. Using the formalism developed for nonlinear spin waves [13], we obtain the following equation from the set that consists of the Landau–Lifshitz equation of magnetic-moment motion and magnetostatic equations:

$$\partial a_n/\partial t + i\omega_n a_n + i(N - i\nu) \times \Sigma_{n'}\Sigma_{n''}\Sigma_{n'''} a_{n'} a^*_{n''} a_{n'''} \delta(n' - n'' + n''' - n) = -\gamma_n a_n. \quad (2)$$

Here, $a_n(t)$ and ω_n are, respectively, the dimensionless scalar amplitude and natural frequency of the nth resonant mode of spin waves in the ring resonator; N is the nonlinear coefficient of the four-wave interaction between spin waves; and ν is the nonlinear attenuation parameter of spin waves. Note that, when changing to the equation for the envelopes of a narrow wave packet, set (2) takes the form of the familiar Ginzburg–Landau equation [2] and of nonlinear Schrödinger equation (1) for $\nu = \gamma_n = 0$.

The natural frequencies ω_n of the resonant spin waves in the ferromagnetic film ring are specified by the discrete set of wave numbers $k_n = 2\pi n/l$ determined by the periodic boundary conditions

$$a(z + l, t) = a(z, t), \quad \partial a(z + l, t)/\partial z = \partial a(z, t)/\partial z, \quad (3)$$

i.e., $\omega_n = \omega(k_n)$. Recall that we consider only waves of the lowest thickness mode of the backward volume spin waves whose dispersion $\omega(k)$ is well known [8, 9].

Depending on the frequency, a resonant eigenmode of the ring may be either attenuated or amplified. This fact is taken into account in Eq. (2) through the effective parameter γ_n, which is positive for attenuating resonant modes, is negative for modes beyond self-generation threshold, and is equal to zero for self-generation threshold. The effective parameter γ_n presents losses on the propagation of spin waves in the ferromagnetic film, frequency-dependent losses on the filtration of a signal in the antennas, and frequency-independent amplification of the signal by the microwave amplifier.

Similar to nonlinear optics [2], the attenuation of spin waves is described in Eq. (2) by the frequency-independent phenomenological parameter ν. The measurements in the monochromatic regime of the generation of spin waves in a spin-wave delay line yielded $\nu = 10^9$ s^{-1} for the center (carrier) frequency $f_0 = 4739$ MHz. The nonlinear attenuation of the carrier spin wave, which is comparatively long-wavelength ($k = 80$ Rad/cm^{-1}), can be physically attributed to its scattering into short-wavelength spin waves.

In particular, numerical calculations indicate that the stable self-generation regime for periodic trains of constant-amplitude solitons can be reached only in rings with an asymmetric frequency response. For a symmetric frequency response, the generated-soliton amplitudes oscillate slowly in the stationary regime. This phenomenon must be studied further by computer simulation and, on the basis of the available results, can

[1] With further increasing gain, the ring exhibits chaotic dynamics, which must be studied separately.

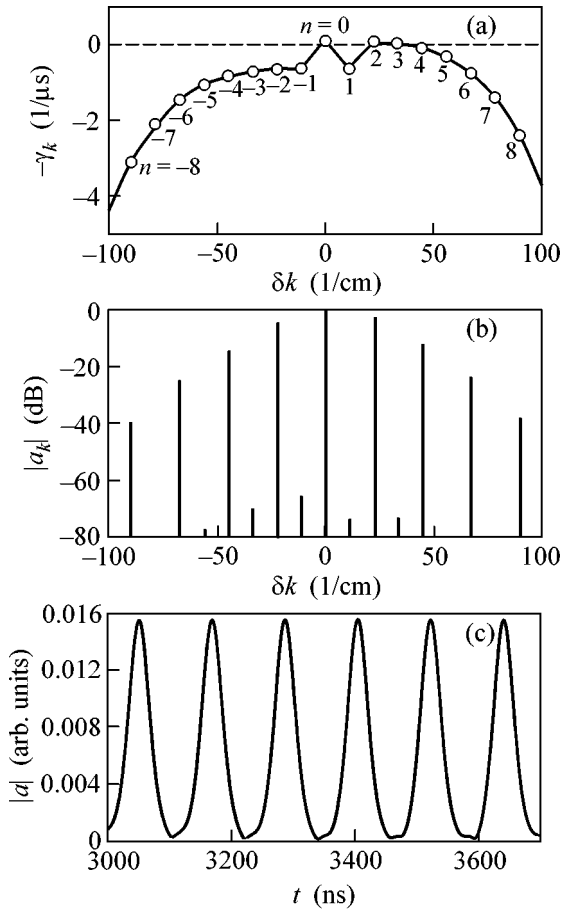

Fig. 3. Results of numerical simulation of the self-generation of soliton pairs in the active ring based on an yttrium iron garnet film: (a) the preset frequency response of the ring, (b) the spectrum of the spatial harmonics of a self-generated periodic train, and (c) the periodic train of self-generated solitons.

be treated as follows. When the frequency response is asymmetric, energy can flow into harmonics having large (given) losses. In this case, the periodic exchange of energy between natural resonant ring harmonics symmetric about the center frequency is suppressed, and the stationary regime of generating a train of solitons of constant amplitude is realized. The frequency response in actual experiments is always asymmetric, so that low-frequency backward volume spin waves are attenuated more strongly than high-frequency waves.

In addition, numerical calculations demonstrated that the stable stationary regime of the self-generation of periodic pulse trains can be reached by increasing losses only in one of ring eigenmodes spaced at $2\Delta f$ from the center mode. In this case, center and next nearest modes that have minimum losses and are spaced at 2Δ serve as initial harmonics whose modulation instability developed with increasing gain is responsible for the generation of a train of solitons.

Figure 3 shows the results of numerical calculations by Eqs. (2). Figure 3a shows the loss characteristic $\gamma_n(k_n)$ of a certain filtering ring, which has an asymmetric frequency response and a locally nonmonotonic transmission band (increase in losses for $n = 1$; n has conventional meaning in Fig. 3). In this case, the harmonics with $n = 0$ and 2 serve as initial harmonics. Figure 3b shows the spectrum of the spatial harmonics of a stationary wave packet formed in this ring. Figure 3c shows the time envelope $|a(z, t)|$ of this packet for a certain point of the ring. As is seen in Fig. 3b, the amplitudes of all odd harmonics are very small compared to the amplitudes of even harmonics including the zeroth harmonic. Therefore, odd harmonics virtually do not contribute to the shape of the spatial envelope of the wave packet, and the envelope of the absolute value of the amplitude of a nonlinearly generated microwave signal has the form of two soliton-like pulses circulating in the ring. The duration of one nonlinear pulse in the periodic train for the stationary regime is equal to 38 ns, which is consistent with the experimental value $\tau_2 = 29$ ns.

Thus, the numerical simulation demonstrates that the control of the frequency response of an active resonant ring can provide the stationary circulation of a wave packet consisting of a pair of pulses. This process is manifested in the time envelope as a train of soliton-like pulses with frequency that is twice the frequency of the wave-packet circulation in the ring.

More detailed experimental results will be reported and compared with theory later.

In conclusion, we emphasize that the above method of controlling the density of nonlinearly self-generated envelope solitons in active ferromagnetic-film rings can be extended to other dispersive ring systems. In such a system, the electric length of a ring must be approximately equal to several or several tens of wavelengths of the wave process in hand in order for the spectrum of its natural resonant frequencies to be discrete despite the losses in the system.

ACKNOWLEDGMENTS

This work was supported by the Russian Foundation for Basic Research (project no. 02-02-16485), by Deutsche Forschungsgemeinschaft (grant no. 436 RUS 113/644/0-1), and by INTAS (grant no. 99-812).

REFERENCES

1. M. Remoissenet, *Waves Called Solitons: Concepts and Experiments* (Springer-Verlag, Berlin, 1996).
2. G. P. Agrawal, *Nonlinear Fiber Optics* (Academic, San Diego, 1995).
3. B. A. Kalinikos, M. M. Scott, and C. E. Patton, Phys. Rev. Lett. **84**, 4697 (2000).
4. M. M. Scott, B. A. Kalinikos, and C. E. Patton, Appl. Phys. Lett. **78**, 970 (2001).

5. F. Gutty, P. Grelu, N. Huot, *et al.*, Electron. Lett. **37**, 745 (2001).
6. L. D. Carr, C. W. Clark, and W. P. Reinhardt, Phys. Rev. A **62**, 063610 (2000).
7. L. D. Carr, C. W. Clark, and W. P. Reinhardt, Phys. Rev. A **62**, 063611 (2000).
8. A. G. Gurevich and G. A. Melkov, *Magnetic Oscillations and Waves* (Nauka, Moscow, 1994).
9. B. A. Kalinikos, in *Linear and Nonlinear Spin Waves in Magnetic Films and Superlattices*, Ed. by M. G. Cottam (World Scientific, Singapore, 1994).
10. V. F. Dmitriev, B. A. Kalinikos, and N. G. Kovshikov, Zh. Tekh. Fiz. **56**, 2169 (1986) [Sov. Phys. Tech. Phys. **31**, 1300 (1986)].
11. B. A. Kalinikos, N. G. Kovshikov, and A. N. Slavin, Zh. Éksp. Teor. Fiz. **94** (2), 159 (1988) [Sov. Phys. JETP **67**, 303 (1988)].
12. M. Chen, M. A. Tsankov, J. M. Nash, and C. E. Patton, Phys. Rev. B **49**, 12773 (1994).
13. V. S. L'vov, *Nonlinear Spin Waves* (Nauka, Moscow, 1987).
14. A. N. Slavin and I. V. Rojdestvenski, IEEE Trans. Magn. **30**, 37 (1994).

Translated by R. Tyapaev

JETP Letters, Vol. 76, No. 5, 2002, pp. 258–263. Translated from Pis'ma v Zhurnal Éksperimental'noĭ i Teoreticheskoĭ Fiziki, Vol. 76, No. 5, 2002, pp. 316–321.

Plateau Effects in the Spectra of Electrons Scattered from Atoms in a Strong Laser Field

N. L. Manakov[1]*, A. F. Starace[2], A. V. Flegel'[1], and M. V. Frolov[2]

[1]*Voronezh State University, Voronezh, 394693 Russia*

**e-mail: manakov@thp.vsu.ru*

[2]*Department of Physics and Astronomy, University of Nebraska, Lincoln, Nebraska 68588-0111, USA*

Received July 16, 2002

An exact quantum solution of the problem of electron scattering from a short-range potential in the presence of a strong elliptically polarized laser field is obtained. The differential scattering cross section as a function of the number of absorbed (or emitted) photons exhibits a plateau caused by the rescattering of electrons from the scattering center. Numerical results for a linearly polarized laser field are presented, and it is shown that the plateau boundaries agree well with classical estimates. © *2002 MAIK "Nauka/Interperiodica".*

PACS numbers: 32.80.Wr; 34.80.Qb; 03.65.Nk

Among the most interesting and extensively studied nonlinear effects involved in above-threshold ionization (ATI) and high-order harmonic generation (HHG) processes are "plateaus" observed in the ATI and HHG spectra. The presence of a plateau implies that the photoelectron yield resulting from n-photon ATI or the intensity of the nth pump laser harmonic depend weakly on the number n of absorbed photons over a broad interval (for $n \lesssim n_{\max}$). Possessing a single-electron character, these effects have been well studied experimentally and described theoretically, both by a direct numerical solution of the nonstationary (time-dependent) Schrödinger equation and within the framework of a quasiclassical approach based on the rescattering concept [1]. According to this concept, a strong oscillating field returns electrons (escaping from atoms due to tunneling ionization events) back to the host ions: rescattering from the ions, the electrons gain additional energy from the pump wave, thus forming a plateau in the ATI spectrum or recombining with the emission of large-n harmonics.

It is interesting to note that the structure of such a plateau depends only weakly on the particular shape of the atomic potential, so that the quasi-classical estimates of the cutoff ($n_{\max}$) values and the structures of the HHG and ATI spectra, calculated in the Keldysh approximation (modified to allow for the rescattering effect) [2] within the framework of a zero-radius three-dimensional potential model, are in perfect qualitative agreement both with the results of exact numerical calculations and with the experimental data for real atoms (see [3] and references therein). Recently [4], it was demonstrated that the appearance of a plateau related to the rescattering effect is also characteristic of a laser-assisted electron–ion recombination process.

A common feature of the aforementioned processes is that an electron in the initial and/or final state is bound to an atom and, hence, is less subject to the action of a laser wave field as compared to electrons in the continuum. This paper presents an example of an exactly solved problem, which shows that plateau effects also accompany free–free electron transitions in a strong laser field (induced multiphoton bremsstrahlung and absorption upon electron scattering from an atom). Therefore, these specific nonlinear effects are inherent in all processes involving the interaction of atomic systems with strong laser fields.

Let us consider the scattering of an electron from a static atomic potential $V(\mathbf{r})$ in the presence of an elliptically polarized laser field with an electric vector $\mathbf{F}(t) = F\mathrm{Re}[\mathbf{e}\exp(-i\omega t)]$, where $\mathbf{e}$ is the unit (complex) vector of polarization: $\mathbf{e}\cdot\mathbf{e}^* = 1$ and $\mathbf{e}\cdot\mathbf{e} = l$ is the degree of linear polarization of the field $\mathbf{F}(t)$ ($0 \le l \le 1$). In a formalism of the quasi-energy states (QES, see, e.g., [5]), the state of an electron with an asymptotic momentum $\mathbf{p}$ in the potential $V(\mathbf{r})$, corresponding to elastic scattering with the energy $E = p^2/2m$ in the absence of the field $\mathbf{F}(t)$, is a periodic function of time which satisfies the following equation:

$$\Phi_{\mathbf{p}}(\mathbf{r}, t) = \chi_{\mathbf{p}}(\mathbf{r}, t) + \Phi_{\mathbf{p}}^{(\mathrm{scatt})}(\mathbf{r}, t) = \chi_{\mathbf{p}}(\mathbf{r}, t) + \int d\mathbf{r}' \int dt' e^{-i\epsilon(t'-t)/\hbar} G^{(+)}(\mathbf{r}, t; \mathbf{r}', t') V(\mathbf{r}') \Phi_{\mathbf{p}}(\mathbf{r}', t'). \quad (1)$$

Here, $\chi_{\mathbf{p}}(\mathbf{r}, t)$ and $G^{(+)}(\mathbf{r}, t; \mathbf{r}', t')$ are the QES wave function and the retarded Green function of the electron in the field $\mathbf{F}(t)$, respectively; $\epsilon = E + U_p$ is the quasi-energy; and $U_p = e^2F^2/4m\omega^2$ is the mean vibrational energy of an electron in the laser field. The scattering

amplitude is determined by the asymptotic behavior of the scattered wave:

$$\Phi_{\mathbf{p}}^{(\mathrm{scatt})}(\mathbf{r}, t)\big|_{r\to\infty} = \sum_{n>-[E/\hbar\omega]+1}^{\infty} \mathcal{A}_n \frac{e^{ip_n r/\hbar - i\omega n t}}{r}, \quad (2)$$

where $p_n = \sqrt{2m(E + n\hbar\omega)}$ is the electron momentum in the channel featuring absorption (for $n > 0$) or emission ($n < 0$) of $|n|$ photons, $\mathcal{A}_n$ is the scattering amplitude in the nth channel, and the sum over n involves all open channels with $E_n = E + n\hbar\omega > 0$.

It is possible to solve Eq. (1) exactly when the atomic potential is modeled by a zero-radius potential (ZRP)

$$V(\mathbf{r}) = \frac{2\pi\hbar^2}{\kappa m}\delta(\mathbf{r})\frac{\partial}{\partial r}r, \quad (3)$$

admitting one weakly bound state $\phi_{E_0}(\mathbf{r})$ with an energy of $E_0 = -\hbar^2\kappa^2/2m$. It should be noted that the use of the ZRP in this problem is much better justified as compared to the cases of ATI or HHG because of the short-range character of the potential of a neutral atom. Below we use dimensionless quantities, whereby the energies (including U_p) are measured in units of $|E_0|$; frequencies, in units of $|E_0|/\hbar$; and the field amplitudes F, in units of $F_0 = \sqrt{2m|E_0|^3}/|e|\hbar$. For example, the scattering on a hydrogen atom is characterized by $|E_0| = 0.754$ eV $= 0.0277$ a.u. (the binding energy of H^-) and $F_0 = 3.362 \times 10^7$ V/cm $= 6.52 \times 10^{-3}$ a.u.

In the ZRP model, the problem reduces to calculation of the Fourier coefficients f_k determining behavior of the scattering wave function $\Phi_{\mathbf{p}}(\mathbf{r}, t)$ at $\mathbf{r} \longrightarrow 0$:

$$\Phi_{\mathbf{p}}(\mathbf{r}, t)\big|_{\mathbf{r}\to 0} = \left(\frac{1}{r} - 1\right) f(t) = \left(\frac{1}{r} - 1\right)\sum_k f_k e^{ik\omega t}. \quad (4)$$

Indeed, using the well-known expression for $G^{(+)}(\mathbf{r}, t; 0, t')$, the amplitude $\mathcal{A}_n$ in Eq. (2) can be represented as (see the results obtained in [6] for a circularly polarized field $\mathbf{F}(t)$)

$$\mathcal{A}_n = \sum_{m,s} i^m e^{im\tilde{\phi}_n} f_{2s-n-m} J_s\left(l\frac{U_p}{2\omega}\right) J_m\left(\frac{2F}{\omega^2}|\mathbf{e}\cdot\mathbf{p}_n|\right),$$
$$e^{i\tilde{\phi}_n} = \frac{\mathbf{e}\cdot\mathbf{p}_n}{|\mathbf{e}\cdot\mathbf{p}_n|}, \quad (5)$$

and the differential scattering cross section is

$$\frac{d\sigma_n}{d\Omega} = \frac{p_n}{p}|\mathcal{A}_n|^2. \quad (6)$$

A system of linear inhomogeneous equations for f_k follows from Eq. (1) with boundary condition (4) (see the analogous calculations in [7] for ionization from the state $\phi_{E_0}(\mathbf{r})$ in the ZRP):

$$(1 + i\sqrt{\mathcal{E}_{n,\delta}} + M_{n,n}(\mathcal{E}_{0,\delta}))f_{2n+\delta} + \sum_{m\neq n} M_{n,m}(\mathcal{E}_{0,\delta}) f_{2m+\delta} = c_{2n+\delta}, \quad (7)$$

where

$$c_k = -i^k \sum_s e^{i(2s+k)\tilde{\phi}} J_s\left(l\frac{U_p}{2\omega}\right) J_{k+2s}\left(\frac{2F}{\omega^2}|\mathbf{e}\cdot\mathbf{p}|\right),$$
$$M_{n,m}(\mathcal{E}_{0,\delta}) = \frac{i^{(m-n)}}{\sqrt{4\pi i}}\int_0^\infty \frac{d\tau}{\tau^{3/2}} e^{i(\mathcal{E}_{0,\delta} - (n+m)\omega)\tau} \times \{e^{iz} J_{n-m}(lz - l(U_p/\omega)\sin\omega\tau) - \delta_{n,m}\}, \quad (8)$$
$$z = \frac{4U_p}{\omega^2\tau}\sin^2\frac{\omega\tau}{2}, \quad e^{i\tilde{\phi}} = \frac{\mathbf{e}\cdot\mathbf{p}}{|\mathbf{e}\cdot\mathbf{p}|},$$

$\mathcal{E}_{n,\delta} = p^2 - (2n + \delta)\omega$, and $\delta = 0(1)$ for even (odd) k values. Note that the coefficients f_k with even and odd numbers are determined independently (for ionization, the incident wave $\chi_{\mathbf{p}}(\mathbf{r}, t)$ in Eq. (1) is absent and the boundary condition (4) contains only the coefficients f_k with even k [7]). Numerical values of f_k are obtained by solving a system of equations (7) "truncated" at n; the rate of convergence with respect to n (the number of coefficients taken into account) depends on F, ω, and p.

The exact relations (5)–(8) admit analytical treatment in some limiting cases. In particular, ignoring nondiagonal matrix elements $M_{n,m}$ in relations (7), we obtain

$$f_{2n+\delta}^{(0)} = \frac{c_{2n+\delta}}{1 + M_{n,n}(\mathcal{E}_{0,\delta}) + i\sqrt{\mathcal{E}_{n,\delta}}}. \quad (9)$$

Note that, in a weak field (i.e., for $F^2 \ll \omega^3$ or $U_p = F^2/2\omega^2 \ll \omega$, we have $M_{m,n} \sim F^{2(|m-n|+\delta_{m,n})}$). For a circularly polarized field $\mathbf{F}(t)$ ($l = 0$), nondiagonal matrix elements are zero and the approximation (9) coincides with the exact expression for f_k; substituting this expression into (5) yields the well-known result for a circularly polarized field [6]. For $0 < l \le 1$, the poles of the coefficients $f_k^{(0)}$ in the complex plane E (i.e., the zeros of the denominator in (9)) give an equation for the complex quasi-energy. The imaginary part of the quasi-energy coincides with the width of level $\phi_{E_0}(\mathbf{r})$ in the Keldysh approximation of multiphoton ionization theory [7].

With neglect of the term $M_{n,n}$ in expression (9), we can obtain simple closed relations for $d\sigma_n/d\Omega$ in the Born and/or low-frequency limits, whereby the term

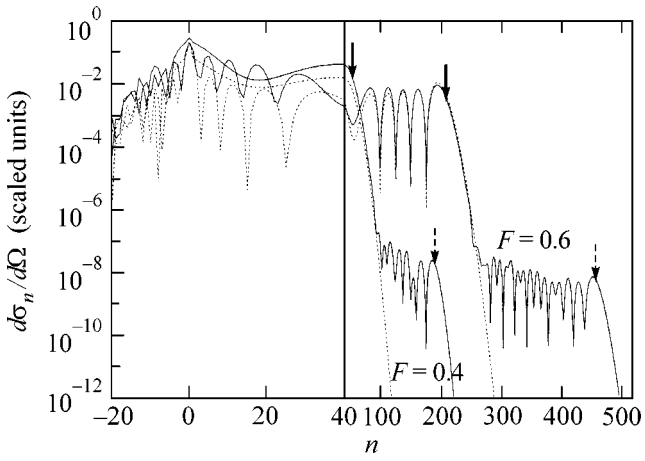

Fig. 1. The differential cross section (in dimensionless units, see the text) of forward scattering ($\theta = 0$) as a function of the number of absorbed (emitted) photons calculated for $\omega = 0.155$, $E = 20.5\omega = 3.1775$, and $F = 0.4$ ($U_p = 3.33 = 21.48\omega$) and 0.6 ($U_p = 7.49 = 48.34\omega$) using the exact equations (solid curves) and the approximate formula (11) (dashed curves). Solid and dashed arrows indicate the K- and R-plateau cutoffs estimated by formulas (15) and (19), respectively.

$(2n + \delta)\omega$ in the relation $\sqrt{\mathscr{E}_{n,\delta}} = \sqrt{p^2 - (2n + \delta)\omega}$ can be omitted. For example, in the low-frequency limit,

$$f_k^{(\mathrm{KW})} = \frac{c_k}{1 + ip}, \tag{10}$$

where $(1 + ip)^{-1}$ is the exact amplitude of elastic scattering in the ZRP model. Substituting (10) into (5) and taking into account orthogonality of the Bessel functions,

$$\sum_{k=-\infty}^{\infty} J_{\nu+k}(u) J_k(u) = \delta_{\nu,0},$$

we arrive at

$$\frac{d\sigma_n^{KW}}{d\Omega} = \frac{p_n}{p(1 + p^2)} J_n^2\left(\frac{2F}{\omega^2}|\mathbf{e} \cdot (\mathbf{p} - \mathbf{p}_n)|\right), \tag{11}$$

which is the Kroll–Watson result [8]. In the case of fast electrons ($p \gg 1$, or $p \gg \sqrt{2m|E_0|}$ in absolute units), we can omit unity in the denominators of (10) and (11), thus obtaining the Bunkin–Fedorov result for the ZRP model [9].

An analysis shows that the main difference of the results [8, 9] from the exact solution is due to neglect of the nondiagonal matrix elements $M_{n,m}$ in expression (9). These elements describe high-order effects (i.e., rescattering effects) of interaction with the atomic potential. In the lowest order, allowance for the rescattering corresponds to an iteration of the system (7) based on the zero approximation (9):

$$f_{2n+\delta}^{(1)} = \frac{c_{2n+\delta} - \sum_{m \neq n} M_{n,m}(\mathscr{E}_{0,\delta}) f_{2m+\delta}^{(0)}}{1 + M_{n,n}(\mathscr{E}_{0,\delta}) + i\sqrt{\mathscr{E}_{n,\delta}}}. \tag{12}$$

In the ZRP model, approximation (12) is equivalent to taking into account the first correction of the atomic potential to the ATI amplitude in the Keldysh approximation. The results of numerical calculations (see below) show that, for frequencies $\omega < 1$, approximation (12) ensures a high accuracy (the difference from the exact results being below 5%) in a broad range of field intensities.

Since the rescattering effects are most significant for a linear polarization of the field $\mathbf{F}(t)$, the numerical results will be presented for the simplest geometry, in which the initial electron momentum is directed along the linear polarization axis and the angular distribution of scattered electrons depends only on the angle θ between $\mathbf{p}$ and $\mathbf{p}_n$. Figure 1 shows the differential forward scattering cross sections ($\theta = 0$) calculated, by approximate formula (11) and by exact formulas (5)–(8), as a function of the number of absorbed (emitted) photons for $\omega = 0.155$; the initial electron energy $E = 20.5\omega$, and two values of the field amplitude, $F = 0.4$ and 0.6. For scattering from a hydrogen atom, these parameters correspond to a CO_2 laser frequency, the initial electron energy $E = 2.4$ eV, and the field intensities $I \approx 2.4 \times 10^{11}$ and 5.4×10^{11} W/cm^2 (in such fields, the probability of tunneling ionization of hydrogen is negligibly small and the effect of ionization of target atoms in the course of scattering can be ignored).

A clearly pronounced feature in Fig. 1 is the presence of two plateaus in the differential scattering cross section as a function of the number of absorbed photons. The first plateau (corresponding to smaller n) is obtained for both exact and approximate calculations and is five-to-six orders of magnitude higher than the second plateau. A fully analogous situation takes place in the ATI spectra (see, e.g., [3]), where the first plateau is well described in the Keldysh approximation (and is referred to below as the K-plateau), while the second is due to the rescattering effects (R-plateau). The results of a numerical analysis show that the lengths of both the K- and R-plateaus for electron scattering at fixed E and ω increase with F, while $n_{\max}^R$ increases much faster than does $n_{\max}^K$. On the contrary, as the electron energy E increases, the length (in the n scale) of both plateaus decreases, the K-plateau contracting much faster than the R- plateau. For example, at $F = 0.4$ and $E = 30.5\omega = 1.42U_p$, the cross section smoothly decays with increasing n unless the R-plateau appears (i.e., the

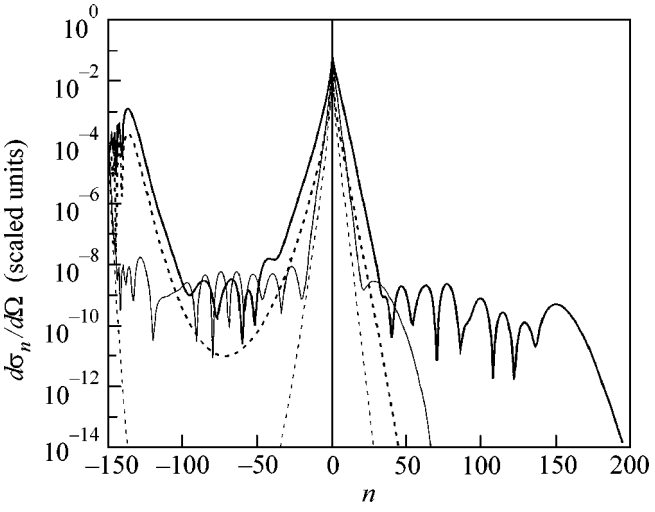

Fig. 2. The same as in Fig. 1, but for $E = 150.5\omega = 23.3275$. Thin and thick solid curves refer to $F = 0.4$ ($U_p = 3.33 = 21.48\omega$) and 0.5 ($U_p = 5.2 = 33.57\omega$), respectively.

K-plateau is virtually absent, while the R-plateau still has a length of $n_{\max}^{R} \approx 100$).

Figure 2 shows the plots of $d\sigma_n/d\Omega$ versus n calculated for the energy $E = 150.5\omega$ and $F = 0.4$ and 0.5 ($U_p = 21.48\omega$ and 33.57ω, respectively). For these parameters, the K-plateau is completely absent and the R-plateau appears only in a sufficiently strong field ($F \gtrsim 0.5$). Another characteristic feature in the high-energy cross section is the appearance of the R-plateau in the process of induced emission ($n < 0$) in a broad range of n (for which the Kroll–Watson and Bunkin–Fedorov approximations give a deep minimum and differ significantly from the exact results).

As the scattering angle θ increases, the structure of the spectrum of scattered electrons significantly changes because the role of rescattering effects decreases. Evolution of the plateau structure is illustrated in Fig. 3. As was noted above for $\theta = 0$, the K-plateau at the E, F, and ω values indicated in Fig. 3 is absent. As the θ value increases, the R-plateau length decreases, while the K-plateau becomes clearly manifested at $\theta \sim \pi/3$, significantly masks the R-plateau at $\theta > \pi/2$, and completely determines the spectrum of scattered electrons for still greater angles of scattering. An analogous situation is also observed for other values of the parameters, so that the scattering by large angles is well described by formula (11). However, it should be pointed out that the interval of small angles $\Delta\theta$, in which approximation (11) is inapplicable (i.e., the region of "critical geometry," where the momentum transfer $\mathbf{p}$–$\mathbf{p}_n$ is perpendicular to the field polarization plane and the argument of the Bessel function in (11) is close to zero), significantly expands with increasing n and may reach up to $\Delta\theta \sim \pi/2$.

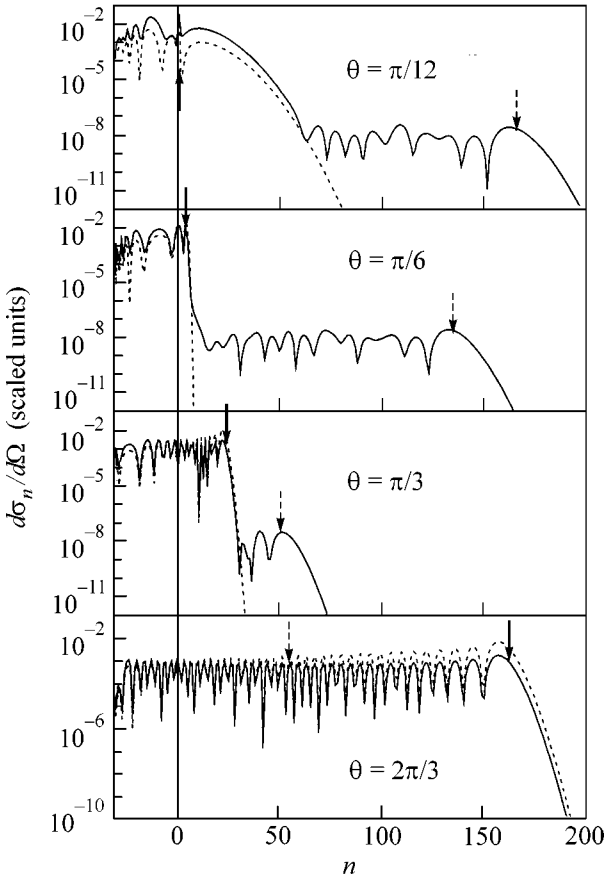

Fig. 3. The plots of $d\sigma_n/d\Omega$ versus n for various scattering angles θ calculated for $F = 0.4$, $\omega = 0.155$, and $E = 30.5\omega$ using the exact equations (solid curves) and approximate formula (11) (dashed curves). Solid and dashed arrows indicate the K- and R-plateau cutoffs according to quasi-classical estimates (see the text).

The above results admit a simple qualitative interpretation within the framework of a quasi-classical approach, by analogy with interpretation of the plateau effects in HHG [2], ATI [10], and electron–ion recombination spectra [4]. The classical equations employed in such an analysis represent the equations for saddle points in the quasi-classical calculation of integrals in the amplitude of the process under consideration (see, e.g., [11]). Restricting our consideration to the case of a one-dimensional motion of the electron along the direction of linear polarization of the field $\mathbf{F}(t)$ (forward scattering and backscattering), the K-plateau cutoff ($n_{\max}^{K}$) can be estimated using an equation expressing the law of conservation of the kinetic energy of the electron in the field upon collision with a scattering center at a time t:

$$\left[p + \frac{1}{c}A(t)\right]^2 = \left[k(t) + \frac{1}{c}A(t)\right]^2, \qquad (13)$$

where $A(t) = -(cF/\omega)\sin\omega t$ is the vector potential, p is the initial momentum, and $k(t)$ is the momentum upon collision. Using a solution to Eq. (13),

$$k(t) = -p - 2\frac{A(t)}{c}, \quad (14)$$

it is possible to calculate the maximum energy gained by the electron as a result of interaction with the scattering center:

$$n^K_{\max}\omega \equiv \max(k(t)^2 - p^2) = 8U_p \mp 4\sqrt{2U_pE}, \quad (15)$$

where the minus and plus signs correspond to forward scattering and backscattering, respectively. Thus, for forward scattering, the K-plateau in the bremsstrahlung absorption spectrum disappears at $E \geq 2U_p$. It should be noted that result (15) can also be obtained more formally, by equating the argument and index of the Bessel function (11), which corresponds to the region of transition from oscillating to decaying behavior of $J_n(x)$. As can be seen from the results of numerical calculations presented in Figs. 1–3, estimate (15) agrees well with the exact quantum-mechanical calculation. The difference in length of the K-plateau for the backscattering and forward scattering is proportional to pF/ω^2 and becomes large in a strong low-frequency field, which explains why backscattering predominates upon absorption of a large number of photons.

The R-plateau cutoff ($n^R_{\max}$) can be estimated within the framework of the rescattering concept, by considering first the collision of an electron with a scattering center at a time instant t, then the motion of the electron in the wave field (over the time interval from t to $t + \tau$) and finally, the repeated scattering (rescattering) at a time instant $t + \tau$. This three-step process is described by the following system of equations:

$$\left[p + \frac{1}{c}A(t)\right]^2 = \left[\tilde{k}(t) + \frac{1}{c}A(t)\right]^2, \quad (16)$$

$$\int_t^{t+\tau}\left[\tilde{k}(t') + \frac{1}{c}A(t')\right]dt' = 0, \quad (17)$$

$$\left[\tilde{k}(t+\tau) + \frac{1}{c}A(t+\tau)\right]^2 = \left[k(t+\tau) + \frac{1}{c}A(t+\tau)\right]^2, \quad (18)$$

where Eqs. (16) and (18) are analogous to Eq. (13) and express the conservation of the kinetic energy of the electron upon collisions at the time instants t and $t + \tau$, while Eq. (17) describes the return of the electron to the scattering center at the time instant of rescattering ($t + \tau$). The joint solution of Eqs. (16)– (18) leads to the following expression for a maximum value of the electron energy ($n^R_{\max}\omega \equiv \max(k(t+\tau)^2 - p^2)$) gained in the course of the "double" scattering:

$$n^R_{\max}\omega = 8U_pK - E, \quad K = \max(g^2_\pm(\tau)), \quad (19)$$

where

$$g_\pm(\tau) = \frac{1}{\zeta^2 + s^2}[a(\zeta^2 - s^2) \pm 2\zeta s\sqrt{\zeta^2 + s^2 - a^2}],$$
$$a = \frac{p\omega}{2F}, \quad \zeta = \frac{s}{\omega\tau} - \cos\frac{\omega\tau}{2}, \quad s = \sin\frac{\omega\tau}{2}. \quad (20)$$

Here, the functions $g_+(\tau)$ and $g_-(\tau)$ correspond to the forward scattering and backscattering, respectively. The coefficient K tends to a maximum ($K_{\max} = 1.25$) for $a \longrightarrow 0$, which corresponds to small primary electron energies and/or superstrong low-frequency fields. In this case, the maximum energy gained by the electron in the field amounts to $10U_p$ (the same maximum energy is gained by the high-energy photoelectrons in the ATI process [10]). In the opposite case, $a \gtrsim 1$ (or $E \gtrsim 8U_p$), the coefficient K is small ($K \lesssim 1$) and rapidly decays with increasing a. Note that the classical equations possess no real solutions for $E > 10U_p$ (the functions $g_\pm(\tau)$ are complex), which corresponds to the absence of rescattering effects: electrons cannot return to the scattering center (see [4] for the electron–ion recombination and [10] for ATI). In the case of backscattering ($\theta = \pi$) of electrons with the energies $E \gtrsim 0.1U_p$, $n^K_{\max} > n^R_{\max}$, the less "intense" R-plateau related to the rescattering is masked by the K-plateau corresponding to a single (direct) scattering (Fig. 3).

The above results show that a correct allowance for the atomic potential essentially determines the pattern of electron scattering from an atom in a strong laser field and accounts for the appearance of plateaus in the spectra of electrons scattered by small angles. The plateau effects observed in induced bremsstrahlung processes are of the same nature as those in other interactions of atoms with intense laser fields.

This study was supported jointly by the U.S. Civilian Research and Development Foundation and the Ministry of Education of the Russian Federation (grant no. VZ-010-0), by the Russian Foundation for Basic Research (project no. 00-02-17843), Center for Competitions of the Ministry of Education of the Russian Federation (project no. E00-3.2-515), and the U.S. National Science Foundation (grant no. PHY-0070980).

REFERENCES

1. M. Yu. Kuchiev, Pis'ma Zh. Éksp. Teor. Fiz. **45**, 319 (1987) [JETP Lett. **45**, 404 (1987)]; K. J. Schafer, B. Yang, L. F. DiMauro, and K. C. Kulander, Phys. Rev. Lett. **70**, 1599 (1993); P. B. Corkum, Phys. Rev. Lett. **71**, 1994 (1993).

2. L. V. Keldysh, Zh. Éksp. Teor. Fiz. **47**, 1945 (1964) [Sov. Phys. JETP **20**, 1307 (1964)].
3. P. Salières, B. Garrè, L. LeDèroff, *et al.*, Science **292**, 902 (2001).
4. D. B. Milošević and F. Ehlotzky, Phys. Rev. A **65**, 042504 (2002).
5. N. L. Manakov, V. D. Ovsiannikov, and L. P. Rapoport, Phys. Rep. **141**, 319 (1986).
6. I. J. Berson, J. Phys. B **8**, 3078 (1975).
7. N. L. Manakov and A. G. Faĭnshteĭn, Zh. Éksp. Teor. Fiz. **79**, 751 (1980) [Sov. Phys. JETP **52**, 382 (1980)].
8. N. M. Kroll and K. M. Watson, Phys. Rev. A **8**, 804 (1973).
9. F. V. Bunkin and M. V. Fedorov, Zh. Éksp. Teor. Fiz. **49**, 1215 (1965) [Sov. Phys. JETP **22**, 844 (1965)].
10. G. G. Paulus, W. Becker, W. Nicklich, and H. Walther, J. Phys. B **27**, L703 (1994).
11. M. Lewenstein, K. C. Kulander, K. J. Schafer, and P. H. Bucksbaum, Phys. Rev. A **51**, 1495 (1995).

Translated by P. Pozdeev

JETP Letters, Vol. 76, No. 5, 2002, pp. 264–269. Translated from Pis'ma v Zhurnal Éksperimental'noĭ i Teoreticheskoĭ Fiziki, Vol. 76, No. 5, 2002, pp. 322–327.

Magnetic Coherence Transfer Induced by Discharge Radiation and the Effect of Radiation Trapping on the Lifetime of the Hidden Alignment of Ne Terms

É. G. Saprykin[1], S. N. Seleznev[2], and V. A. Sorokin[2]

[1] *Novosibirsk State University, Novosibirsk, 630090 Russia*

[2] *Institute of Automation and Electrometry, Russian Academy of Sciences, Siberian Branch, Novosibirsk, 630090 Russia*

Received July 8, 2002

The dichroism of a neon gas discharge plasma in a weak magnetic field is investigated by scanning the $3s_2$–$2p_4$ transition by monochromatic laser radiation. Magneto-optical resonances of the intrinsic macroscopic alignment and hidden alignment of the $2p_4$ level are separated. Against the background of these resonances, resonances attributed to coherence transfer from the $1s_{2,4,5}$ levels and the birefringence of the wings of the nearest absorption lines from the $1s_{4,5}$ levels are observed. A new type of alignment is revealed—integral hidden alignment, whose lifetime, in contrast to the case with macroscopic alignment, increases without bound with increasing radiation trapping. © *2002 MAIK "Nauka/Interperiodica".*

PACS numbers: 33.55.-b; 42.50.Gy

1. The processes of the collisional and radiative transfer of population and coherence play an important role in forming the radiative characteristics of a gas discharge plasma. The possibility of studying them can be substantially extended by using laser radiation. In particular, the laser method was used in [1, 2] to study the population transfer accompanying inelastic collisions with atoms and electrons. The first observation of the collisional transfer of nonlinear resonances [3] indicated that the velocity of atoms can considerably change in their inelastic scattering by electrons. In a gas discharge, radiative transfer processes induced by discharge radiation are of significant importance. The reabsorption of radiation contributes to the decay rate of metastable states and, under certain conditions, is more important than transitions in inelastic collisions with electrons [4]. It should be expected that discharge radiation can also induce the transfer of the coherence of Zeeman sublevels. Coherence transfer from the metastable $1s_5$ level upward to $2p$ Ne levels was tested in experiments [5], in which spontaneous radiation was detected. However, narrow magneto-optical resonances (MORs) were not observed. In this study, we apply the laser method to detect the transfer of magnetic coherence (alignment) of Ne levels.

2. The experiment was described in [6, 7]. A water-cooled gas discharge tube 4 mm in diameter and 40 cm in length with a discharge current of 80 mA was placed in a scanned transverse magnetic field. To detect the alignment of the $2p_4$ level, the $3s_2$–$2p_4$ transition was scanned by weak circularly polarized laser radiation. The dichroism (the difference between the intensities of the linearly polarized laser radiation components parallel and normal to the magnetic field) was measured by the derivation method (the deviation frequency and amplitude being 400 Hz and 0.1 G, respectively) with the signal accumulation over ~15 min. Laboratory magnetic fields were compensated, and their residual effect was taken into account when processing the data obtained. Figures 1 and 2 show the processed spectrograms and the scheme of transitions, respectively.

Visually, the MOR involves narrow and wide components. However, it is formed by numerous factors. First, it is the alignment of the $2p_4$ level by radiation from the $2p_4$–$1s_j$ transitions. Second, it is the induced transfer of alignment from the $1s_{2,4,5}$ levels. Third, the alignment consists of macroscopic alignment (MA), caused by the anisotropy of the aligning radiation, and hidden alignment (HA), associated with anisotropy induced in the reference frame of a moving atom by both the isotropic component of this radiation and anisotropic collisions [8, 9]. MA and HA relax in different ways and, therefore, differently affect the general shape of the MOR. Finally, the birefringence signal falls into the dichroism channel due to the residual parasitic magnetic field (~0.05 Oe) [10].

In our experiment, the contributions P_i from MA ($i = m$) and HA ($i = h$) are described by the same Lorentzian dependence on the magnetic field H, whereas the amplitudes $I_i(\omega)$ as functions of the scanning-radiation frequency ω, as well as relaxation con-

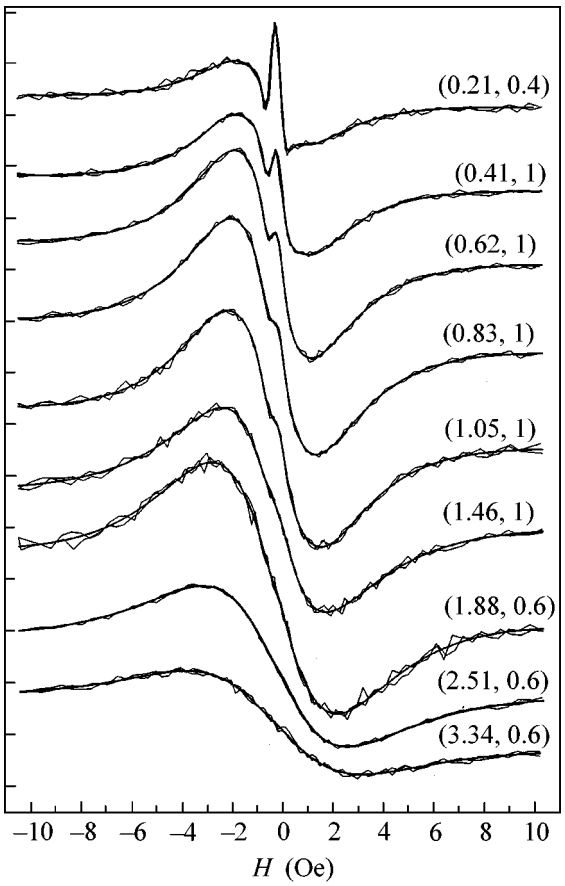

Fig. 1. Typical spectrograms. Numerals by the curves show the pressure (in torr) and the relative scale.

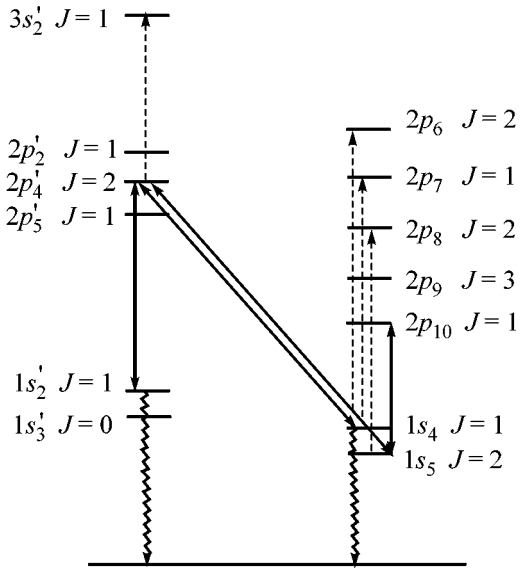

Fig. 2. Level scheme. The dashed straight lines with arrows denote scanning radiation (λ = 6328 Å) that is resonant with the center of the $3s_2$–$2p_4$ transition, blue wings of the $2p_8$–$1s_5$ (6334 Å) and $2p_7$–$1s_4$ (6383 Å) transitions, and the red wing of the $2p_6$–$1s_4$ (6305 Å) transition. The heavy straight lines with arrows are radiation inducing alignment transfer.

stants $\Gamma_{2i}(p)$ as functions of gas pressure p, differ for these two types of alignment:

$$P_i = I_i(\omega)\Gamma_{2i}(p)/[\Gamma_{2i}(p)^2 + (2\mu_B g H)^2], \qquad \Gamma_{2i}(p) = \Gamma_0 k_i + \alpha_2 p, \tag{1}$$

where Γ_0 is the radiative decay probability and k_i is the coefficient dependent on radiation trapping [11] and on the frequency of the induced exchange by alignment with other levels [12]. The function $I_m(\omega)$ repeats the contour of the emission line forming MA, whose lifetime increases with radiation trapping. The function $I_h(\omega)$ is alternating,[1] and the lifetime of HA is independent of radiation trapping [8]. This behavior is due to the absence of the integral spectral component of HA.

The contributions of dichroism and birefringence to the measured signal for varying scanned and parasitic magnetic fields were determined in [10]. The parasitic transverse field H_y is responsible for the term with a parity opposite in sign to the change of the scanned field. This term determines the symmetric structure in curves in Fig. 1 (we recall that the derivative of the MOR signal was recorded). Previously, we attributed this structure to the birefringence of the wing of the absorption line from the $1s_5$ level (the $2p_8$–$1s_5$ transition with a detuning of 16 cm^{-1}, i.e., about one thousand Doppler widths) [13]. In recent experiments, similar MORs with the characteristics of MA and HA of the $1s_4$ level were observed. We attribute these resonances to the birefringence of further absorption lines from the $1s_4$ level: $2p_6$–$1s_4$ (with a detuning of –58.2 cm^{-1}) and $2p_7$–$1s_4$ (with a detuning of +136.1 cm^{-1}). The contribution from the wings was described by three MORs with ω-independent amplitudes.[2] In addition, the structure of the total resonance included five MORs corresponding to the alignment of the $1s_{2,4,5}$ levels.[3] By varying H_y, we demonstrated that these resonances exist even when this field is completely compensated. We attribute them to the induced transfer of alignment.

The longitudinal magnetic field gives rise to additional combinations of contours, which involve, for each MOR, not only ordinary-width Lorentzians, but also double-width Lorentzians described according to [10]. In addition, the model includes shifts along the coordinate axes, the amplitude of the contour associated with the dichroism of the Doppler absorption line, the amplitudes of residual parasitic magnetic fields, and

[1] Its sign coincides with and is opposite to the sign of MA for small and large detunings, respectively.

[2] Numerical estimates of the amplitudes of these contours correspond to their values in the birefringence channel.

[3] Two contours with the same α_2 and different k_i were used to describe the MORs of the HA and MA of the $1s_{2,4}$ levels.

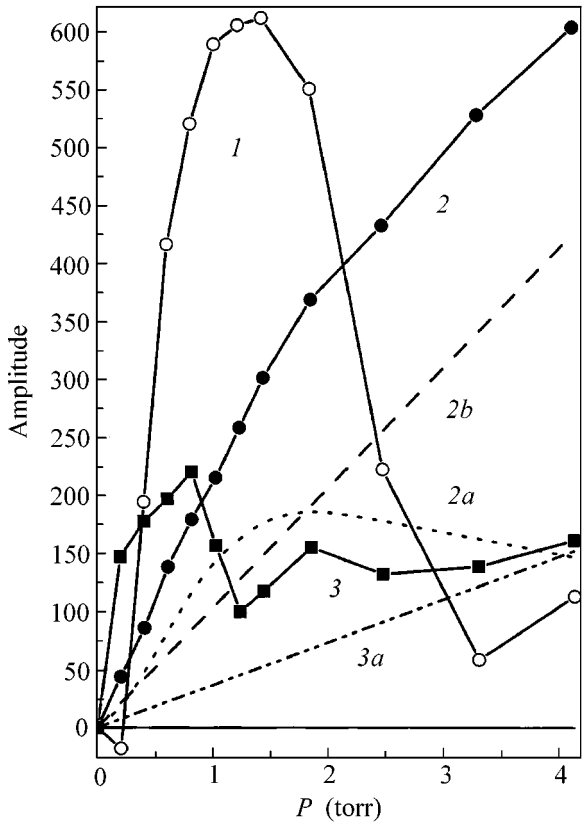

Fig. 3. MOR amplitudes of the $2p_4$ level: (*1*) MA($2p_4$), (*2*) HA($2p_4$), (*2a*) radiation-induced HA($2p_4$), (*2b*) HA($2p_4$) induced by anisotropic collisions, (*3*) IHA($2p_4$), and (*3a*) IHA($2p_4$) induced by anisotropic collisions.

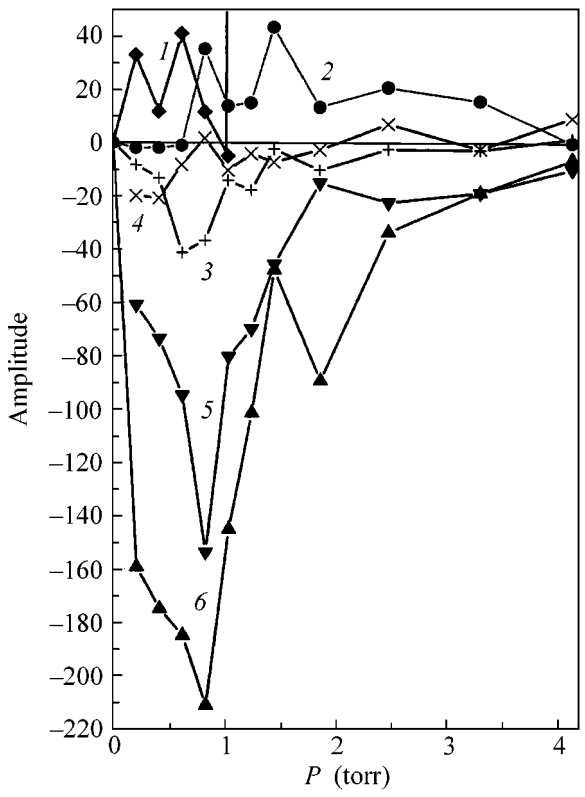

Fig. 4. MOR amplitudes of the HA of the 1*s* levels: (*1*) IHA($1s_2$), (*2*) transfer IHA($1s_4$), (*3*) IHA($1s_5$), (*4*) IHA($1s_5$) in the line wing, (*5*) IHA($1s_4$) in the line wing, and (*6*) IHA($1s_4$).

the parameter of deviation broadening.[4] Such a large number of parameters can only be satisfactorily estimated by simultaneously fitting a set of curves for different pressures (12 curves, each containing 168 points). This fit, which became possible due to increasing computer performance, ensures the use of common parameters and certain physical suppositions, such as the dependence of impact broadening on the gas pressure being linear and identical for different types of alignment of one level and that the dependences are monotonic.

The appearance of HA signals for the $1s_{2,4}$ levels is surprising. As was mentioned above, the function $I_h(\omega)$ is alternating and its integral is equal to zero. Therefore, the spectrally integrated transfer of HA and the HA of the line wings must be absent. However, the experiment indicates the nonzero integral HA (IHA) component, which can be attributed to the fact that slow aligned atoms leave more efficiently hidden aligned levels due to induced transitions. This is possible because the spectral width of the radiation inducing transfer is smaller than or close to the width of the alignment spectrum. In this case, IHA with the alignment sign of fast atoms remains in the original levels, and the lifetime of IHA depends on the degree of radiation trapping. For this reason, we consider k_i for the MOR of IHA of this kind ($i = h_i$) as a varying parameter. Then, this IHA is transferred similar to MA. The exhausted part of HA must have the HA time characteristics (without the effect of radiation trapping on the MOR width), although it acquires integral properties. Such a positive contour with the HA characteristics of the $1s_4$ level really manifests itself in the MOR structure.[5] The HA and IHA of the $2p_4$ level were also allowed.

It is known that the collisional depolarization of the $1s_2$ and $1s_4$ levels in neon is primarily determined by resonant exchange by excitation. In this case, the rate of alignment destruction on the $J = 1 \longrightarrow J = 0$ transition is given by the expression $\alpha_2 p = 0.028\Gamma_0 N\lambda^3$, where N is the atomic density and λ is the wavelength of the resonance transition [14]. For 0°C, we have $\alpha_2(1s_4)/\Gamma_0 = 0.408$ torr^{-1} and $\alpha_2(1s_2)/\Gamma_0 = 0.395$ torr^{-1}. For this reason, the relative collisional broadening of the resonance

[4] The last parameter was determined in a separate experiment with a varying deviation amplitude.

[5] A similar MOR of the $1s_2$ level cannot be separated from other wide MORs, because the scanning range is fairly narrow.

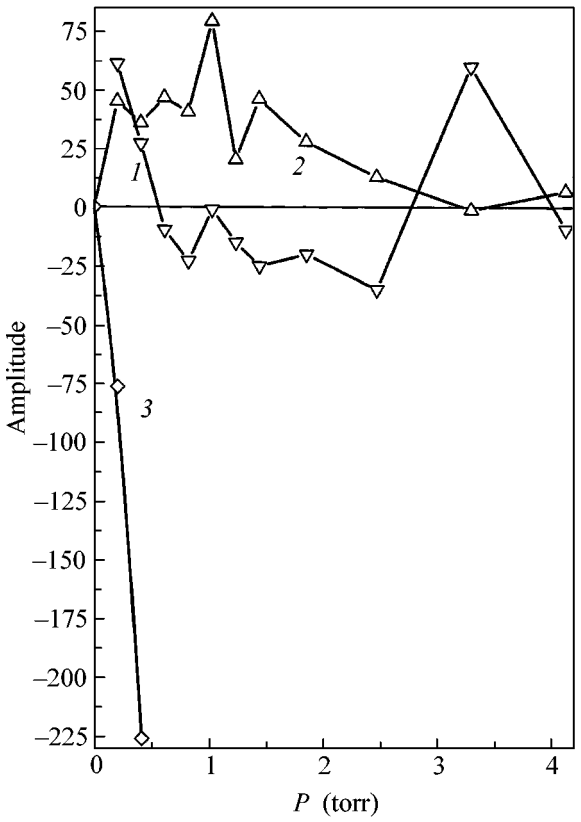

Fig. 5. MOR amplitudes of the MA of the 1*s* levels: (*1*) MA($1s_4$) in the line wing, (*2*) MA($1s_4$), and (*3*) MA($1s_2$).

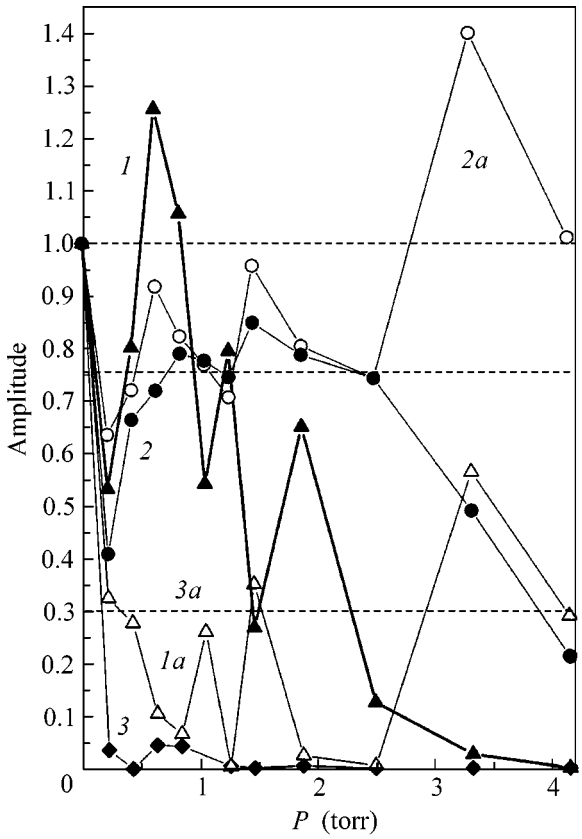

Fig. 6. Variations in the radiative components of the MOR widths: (*1*) $k_{hi}(1s_4)$, (*1a*) $k_m(1s_4)$, (*2*) $k_{hi}(2p_4)$, (*2a*) $k_m(2p_4)$, (*3*) $k_{hi}(1s_2)$, and (*3a*) $k_m(1s_2)$.

levels was described by one variable. In addition, we took $\Gamma_0(1s_2) = 13.3\Gamma_0(1s_4)$.

Figures 3–6 show the amplitudes of intrinsic and "transfer" MORs and k_i values for different types of alignment. The table presents the estimates of the relaxation constants.

The Γ_0 value obtained for the $2p_4$ level is close to measurements [15, 16] and calculation [4], and the collisional damping coefficient α_2 for this level is close to the data of [16]. For MOR($1s_5$), we obtained a negative sign (Fig. 4; curves *3*, *4*),[6] which agrees with the previously determined difference in the alignment signs of the levels $2p_4$ and $1s_5$ [7]. The relaxation constants for this resonance turned out to be close to the data of [7], whereas $\Gamma_0(1s_4)$ and α_2 appeared to be close to the data of [4, 5, 17] and [14, 17, 18], respectively. For the MORs of MA($1s_4$) (Fig. 5; curves *1*, *2*) and IHA($1s_4$) (Fig. 4; curves *5*, *6*), we obtained positive and negative signs, respectively. According to [5], the alignment of the $1s_4$ level also consists of two contours of different signs: a wide contour associated with HA and a narrow contour, which is, in our opinion, the MA contour narrowed by trapping.[7] The signs of the corresponding MORs from the $1s_2$ level turned out to be opposite (Fig. 4, curve *1* and Fig. 5, curve *3*). However, this is due to the difference in the widths (rather than the signs) of the level alignments. The spontaneous or induced alignment transfer induces two MORs in the final level, the first and second of which have the initial-level and final-level widths, respectively. These resonances have opposite signs and equal squares [12]. The narrow resonance has the sign of the original MOR and determines the sign of alignment for zero magnetic field. For the $1s_2$ level, the MOR($2p_4$) has the original sign, whereas the MOR($1s_2$) has the opposite sign.

3. Thus, the decomposition of the total MOR of the alignment of the $2p_4$ level into Lorentzians reveals contours with the characteristics (widths and signs) of the alignment of the 1*s* levels, which indicates the transfer of the alignment of these levels upward to the 2*p* levels.

In our opinion, in this study, the narrowing of MORs associated with radiation trapping was detected for the first time by using monochromatic radiation. Although a similar narrowing was observed for the first time by

[6] The alignment of the $2p_4$ level is taken as positive, which corresponds to MA at the $J = 1 \longrightarrow J = 0$ transition.

[7] In contrast, in [5], the narrow contour was attributed to the transfer of alignment from the $1s_5$ level.

Table

Level *g*-factor	Γ_0, MHz		α_2/Γ_0, torr^{-1}	
	Estimate	Ref.	Estimate	Ref.
$2p_4$	8.3	8.3 [15]	0.43	0.48 [16]
1.301		8.47 [4]		0.43 [7]
		7.31 [7]		
$1s_5$	1.3	1.14 [7]	0.8	0.83 [7]
1.503				
$1s_4$	6.6	6.3 [17]	0.35	0.34 (325 K) [14]
1.464		6.4 [5]		0.32 [17]
		6.64 [4]		0.35 (340 K) [18]
				0.203 [5]
$2p_0$		6.8 [4]		0.01 (315 K) [18]
1.984				

Lukomskiĭ *et al.* [5], they attributed it to the alignment transfer from the $1s_5$ level. At the same time, this phenomenon is not extraordinary. Indeed, the alignment lifetime is determined by the integral spectral processes of radiation reabsorption in a discharge, whereas the MOR shape, reflecting these processes, is determined by the destruction of alignment by a magnetic field. For this reason, the spectrum of scanning radiation is of minor importance.

The $k_m(1s_4)$ value (Fig. 6, curve *1a*) falls below the complete-trapping limit (0.3 for the $J = 1 \longrightarrow J = 0$ transition [11]). According to [12], this can result from the induced exchange of alignment with wider $2p_j$ levels, whose MORs must be widened in this case. However, the $2p_{10}$ level stands out among them, because it is the narrowest, has the maximum *g* factor, and is only slightly broadened by collisions and because its MOR width of MA for pressures near 3.3 torr becomes comparable to or smaller than the MOR width of the MA of the $1s_4$ level.[8] Seemingly, the increase in the MOR width of MA($1s_4$) at this pressure (Fig. 6, curve *1a*) can be attributed to the exchange by MA with the $2p_{10}$ level. The pressure dependence of $k_m(2p_4)$is nonmonotonic (Fig. 6, curve *2a*), which can also be associated with the exchange processes.

However, the trapping-induced decrease in k_{hi} (Fig. 6, curves *1*–*3*) is greater than the theoretical predictions for MA [11] and cannot be attributed to the exchange processes. The cause can be the fact that the original distribution of the alignment axis directions for individual atoms for IHA (as well as for HA) is isotropic. Therefore, although reemission somewhat reduces original anisotropy and limits the increase in the lifetime of MA under complete trapping, it does not affect the increase in the "trapped" lifetime of IHA. For the same reason, disordering collisions should not destroy IHA. In view of this circumstance, it is possible that IHA can be formed when inelastic atomic collisions transfer IHA and HA of fast atoms from the $1s_4$ to $1s_5$ level. The effect of the cell temperature on the characteristics of the MOR($1s_5$) testifies to this phenomenon [13]. The peaks in curve *1* in Fig. 6 seemingly result from transfer of IHA between the $1s_4$ and $2p_{10}$ levels. On the left side of the first peak, the MOR width of IHA($1s_4$) is larger than that of IHA($2p_{10}$) and increases as the exchange rate rises and as the MOR widths approach each other. On the right side, the trapped MOR width of IHA($1s_4$) is equal to or less than that of IHA($2p_{10}$). In this case, the MOR of IHA($1s_4$) narrows sharply. Then, the large collisional broadening of the $1s_4$ level compensates for the trapping-induced narrowing and again results both in the prevalence of the MOR width of IHA($1s_4$) and in the appearance of an additional peak. MORs with the characteristics of the $2p_{10}$ level were not included into the processing algorithm, and variations in their characteristics manifest themselves as distortions (nonmonotonicity) of the amplitudes and widths of the other resonances in the pressure range 1–1.5 torr and near 3.3 torr.

The irradiation anisotropy on the discharge axis at the center of the line for the $1s_{2,4}$ levels is small for the pressures in use. MA in the line wing (Fig. 5, curve *1*) is obviously formed by atoms that have high transverse (with respect to the cell axis) velocities. Since the density of these atoms is low, the photon free path is longer than the cell diameter. The change in the sign of this MOR with increasing pressure can be attributed to the spontaneous transfer of negative MA from the $2p_6$ level. For transfer MORs (Fig. 5, curve *2*), the contribution of anisotropy near the tube wall is more substantial,[9] and the sign of the MOR is conserved. MA of the $1s_5$ level can be formed due to radiation-induced transfer from the 2*p* levels (rather than spontaneous decay, which is absent in this case). For this reason, radiation is not trapped, and the MOR widths of IHA and MA, which are described by one contour with the width depending linearly on pressure, are indistinguishable. Possible variations induced in the MOR width by exchange processes can affect the estimates of other parameters.

The peak in the MOR amplitude of MA($2p_4$) (Fig. 3, curve *1*) is caused by the $2p_4$–$1s_{2,4}$ ($\Delta J = 1$) transitions with the maximum oscillator strengths (0.249 and 0.173, respectively), whereas the dip is caused by emission from the $2p_4$–$1s_5$ transition, where $\Delta J = 0$ and, therefore, the sign of this MOR is negative. In this case, the oscillator strength is noticeably smaller (0.074), and MA is maximum at higher pressures. Similar to [8], the

[8] According to [12], the effect of changing the MOR widths is maximum when the MOR widths of levels exchanging by alignment are close to each other and depends on the sign of the difference of these widths.

[9] The signal in the wings corresponds to the tube axis, whereas the transfer signal is integral over the tube cross section.

MOR of HA($2p_4$) (Fig. 3, curve *2*) involves not only the contribution proportional to the radiation intensity (Fig. 3, curve *2a*),[10] but also the contribution from anisotropic collisions, which is proportional to the atomic density (Fig. 3, curve *2b*). The MOR of IHA($2p_4$) has positive sign (Fig. 3, curve *3*), which is possible if IHA is induced by transfer from the $1s_4$ level.[11] Indeed, curve *3*, disregarding the slope proportional to the atomic density (straight line *3a*), is similar to the MOR amplitude (taken with the opposite sign) of the IHA from this level (see Fig. 4). The fraction of IHA that increases linearly with pressure is likely formed by HA($2p_4$), which is induced by anisotropic collisions (as a result of transitions of fast atoms to other 2*p* levels due to inelastic atomic collisions).

In this brief communication, we cannot discuss in detail all the features of the complex interaction between the 2*p* and 1*s* levels. We only point to the presence of transfer MORs and nonzero IHA, emphasize that the dependence of the radiative component of the MOR widths of IHA on the neon pressure differs from the dependence predicted for MA under the conditions of radiation trapping, and call attention to the dependence of the MOR widths on the frequencies of induced alignment exchange. Since all the parameters are interrelated, the quantitative estimates can be insufficiently accurate; hence, more precise measurements and a more complete processing algorithm are required.

We are grateful to S.G. Rautian for stimulating discussions and S.N. Kobtsev for technical support. This work was supported by the Program "Universities of Russia" (project no. 01.01.054) and by the Russian Foundation for Basic Research (project no. 02-02-17923).

REFERENCES

1. J. H. Parks and A. Javan, Phys. Rev. A **139**, 1351 (1965).
2. A. S. Khaĭkin, Zh. Éksp. Teor. Fiz. **54**, 52 (1968) [Sov. Phys. JETP **27**, 28 (1968)].
3. S. N. Atutov, A. G. Nikitenko, S. G. Rautian, *et al.*, Pis'ma Zh. Éksp. Teor. Fiz. **13**, 232 (1971) [JETP Lett. **13**, 163 (1971)].
4. L. A. Vaĭnshteĭn, V. R. Mironenko, S. G. Rautian, *et al.*, Opt. Spektrosk. **87**, 372 (1999) [Opt. Spectrosc. **87**, 341 (1999)].
5. N. G. Lukomskiĭ, V. A. Polishchuk, and M. P. Chaĭka, Opt. Spektrosk. **71**, 46 (1991) [Opt. Spectrosc. **71**, 25 (1991)].
6. É. G. Saprykin, S. N. Seleznev, and V. A. Sorokin, Pis'ma Zh. Éksp. Teor. Fiz. **50**, 316 (1989) [JETP Lett. **50**, 351 (1989)].
7. É. G. Saprykin, S. N. Seleznev, and V. A. Sorokin, Zh. Éksp. Teor. Fiz. **102**, 14 (1992) [Sov. Phys. JETP **75**, 8 (1992)].
8. M. P. Chaĭka, *Interference of Degenerate States* (Leningr. Gos. Univ., Leningrad, 1975).
9. G. N. Nikolaev, G. D. Rodionov, S. G. Rautian, *et al.*, Opt. Spektrosk. **60**, 244 (1986) [Opt. Spectrosc. **60**, 149 (1986)].
10. É. G. Saprykin, S. N. Seleznev, and V. A. Sorokin, Opt. Spektrosk. **91**, 313 (2001) [Opt. Spectrosc. **91**, 288 (2001)].
11. M. I. D'yakonov and V. I. Perel', Zh. Éksp. Teor. Fiz. **47**, 1483 (1964) [Sov. Phys. JETP **20**, 997 (1964)].
12. S. G. Rautian and É. G. Saprykin, Opt. Spektrosk. **92**, 385 (2002) [Opt. Spectrosc. **92**, 342 (2002)].
13. É. G. Saprykin, S. N. Seleznev, and V. A. Sorokin, Opt. Spektrosk. **85**, 721 (1998) [Opt. Spectrosc. **85**, 658 (1998)].
14. M. I. D'yakonov and V. I. Perel', Zh. Éksp. Teor. Fiz. **48**, 345 (1965) [Sov. Phys. JETP **21**, 227 (1965)].
15. W. R. Bennett, Jr. and P. J. Kindlmann, Phys. Rev. **149**, 38 (1966).
16. Im Tkhek-de, S. G. Rautian, É. G. Saprykin, *et al.*, Opt. Spektrosk. **49**, 438 (1980) [Opt. Spectrosc. **49**, 240 (1980)].
17. Im Tkhek-de, É. G. Saprykin, and A. M. Shalagin, Opt. Spektrosk. **35**, 202 (1973).
18. S. A. Kazantsev, Usp. Fiz. Nauk **139**, 621 (1983) [Sov. Phys. Usp. **26**, 328 (1983)].

Translated by R. Tyapaev

[10] In the first approximation, curve *2a*, which is proportional to the absorption of laser radiation, describes the dependence of the aligning radiation intensity on the gas pressure.

[11] We recall that transfer MORs acquire the negative sign of the IHA of these levels, whereas the MOR with the characteristics of the $2p_4$ level gains positive sign.

JETP Letters, Vol. 76, No. 5, 2002, pp. 270–274. Translated from Pis'ma v Zhurnal Éksperimental'noĭ i Teoreticheskoĭ Fiziki, Vol. 76, No. 5, 2002, pp. 328–332.

Confinement of Atoms with Nondegenerate Ground States in a Three-Dimensional Dissipative Optical Superlattice

I. V. Krasnov* and S. P. Polyutov

Institute for Computational Modeling, Russian Academy of Sciences, Siberian Division, Krasnoyarsk, 660036 Russia

**e-mail: krasn@icm.krasn.ru*

Received July 15, 2002

Based on the developed kinetic theory of rectified radiative forces, we found sufficient conditions for purely optical (nonmagnetic) three-dimensional confinement and cooling of atoms with the $J = 0 \longrightarrow J = 1$ quantum transition in a weak field of mutually orthogonal bichromatic standing waves. We show that a deep stable atom localization of atoms in the cells of an effective light superlattice (with a spacing much larger than the light wavelength) can be achieved by controlling the phase shifts (time-difference phase) of the temporal oscillations in orthogonally polarized field components and by specially choosing the field parameters. The proposed scheme of purely optical confinement can be directly used for a large group of atoms like Yb isotopes and alkali-earth elements with even–even nuclei. © *2002 MAIK "Nauka/Interperiodica".*

PACS numbers: 32.80.Pj; 42.50.Vk

Because of its unique physical applications, the optical localization of atoms is an extremely important trend in current studies of resonant light pressure [1–3].

One of the most successful and fruitful solutions to this problem is the confinement of atoms in a magneto-optical trap (MOT)[1] [4]. A nonuniform magnetic field is an integral MOT element, because it allows the Earnshaw optical theorem (EOT) [5] to be circumvented. This theorem states that a stable localization of atoms by spontaneous light pressure forces in a weak (unsaturating the quantum transition) resonant field is not possible. Bouyer *et al.* [6] showed how the EOT could be circumvented by purely optical (nonmagnetic) methods using optical pumping of atoms with degenerate ground states. This scheme does not work for atoms with the ground-state angular momentum $J_g = 0$.

Meanwhile, the EOT was proved [5] (see also [6] for a discussion) precisely for atoms with scalar linear polarizability, which the atoms with the $J_g = 0 \longrightarrow J_e = 1$ quantum transition are. The principal possibility of overcoming the fundamental EOT constraints (without applying a magnetic field) for such atoms using the so-called rectified radiative forces (RRFs) in weak[2] bichromatic fields was pointed out in [7] (2D localization) and [8] (3D localization). However, the final solution of the problem and the elucidation of specific practical conditions for the achievement of dissipative optical confinement by this method requires a mandatory allowance for quantum RRF fluctuations and for the effect of field phases on the RRF spatial structure.

Here, these factors are simultaneously taken into account in the Wigner atomic density matrix formalism for a simple field model in the form of mutually orthogonal bichromatic standing waves. We found sufficient conditions (imposed on the relative initial phase shifts and on the wave parameters) that provide a deep stable 3D localization of atoms and, thereby, ensure that the EOT constraints (i.e., suppression of the vortex RRF component and long-term particle confinement in ultradeep light-induced potential wells) are overcome.

The problem under study also has an interesting research-and-application aspect, because it is directly related to the purely optical confinement of a large group of atoms like odd–odd Yb isotopes and alkali-earth elements with the $J_g = 0 \longrightarrow J_e = 1$ quantum transition (strong singlet, ${}^1S_0$–${}^1P_1$, and intercombination, ${}^1S_0$–${}^3P_1$, transitions of this type were effectively used in MOT experiments [10–12]). These atoms are believed to be very promising objects for carrying out new fundamental cold-particle experiments (see [10–13] and references therein). We emphasize that the presence of a magnetic field (as in MOTs) is undesirable for several important physical applications of the optical confinement of atoms [6, 9].

Consider an ensemble of atoms in a bichromatic field with a complex amplitude,

$$\mathbf{E} = \mathbf{E}_0(\mathbf{r})e^{-i\Delta_0 t} + \mathbf{E}_1(\mathbf{r})e^{-i\Delta_1 t}, \qquad (1)$$

where Δ_0 and Δ_1 are the frequency detunings of the fields $\mathbf{E}_0$ and $\mathbf{E}_1$ from the frequency $\omega_0 \gg |\Delta_0|, |\Delta_1|$ of

[1] By its nature, a MOT is a dissipative optical trap, because the particles are simultaneously cooled and confined in it.

[2] Here, we do not consider the use of rectified gradient (dipole) forces in strong bichromatic fields [7, 9] for the localization of atoms.

the quantum transition between the ground (with angular momentum $J_g = 0$) and excited (with angular momentum $J_e = 1$) atomic states.

As was shown in [7, 8], zero total radiation flux densities for each field mode frequency are a necessary condition for stable confinement of atoms with the type of transition under consideration in weak biharmonic fields (it predetermines the suppression of the principal, quadratic (in field) vortex RRF component):

$$\sum_j \langle \mathbf{J}_{j\alpha} \rangle = 0, \quad j = x, y, z, \quad \alpha = 0, 1,$$

where $\mathbf{J}_{j\alpha}$ is the energy flux density of the field components in superposition (1) that are polarized along the unit vector $\mathbf{e}_j$ of a Cartesian coordinate system and that have the frequency detuning Δ_α; the angular brackets denote averaging over microscopic spatial oscillations with a period of the order of the light wavelength. The field model in the form of a superposition of mutually orthogonal standing waves satisfies this condition:

$$\begin{aligned} V_{x\alpha}(\mathbf{r}) &= V_\alpha e^{i\xi_{z\alpha}} \cos(k_\alpha z + \varphi_z), \\ V_{y\alpha}(\mathbf{r}) &= V_\alpha e^{i\xi_{x\alpha}} \cos(k_\alpha x + \varphi_x), \\ V_{z\alpha}(\mathbf{r}) &= V_\alpha e^{i\xi_{y\alpha}} \cos(k_\alpha y + \varphi_y), \end{aligned} \tag{2}$$

where $V_{j\alpha}(\mathbf{r}) = d(\mathbf{e}_j \mathbf{E}_\alpha(\mathbf{r}))/\hbar$ are the local Rabi frequencies, $d = \|d\|/\sqrt{3}$, $\|d\|$ is the reduced matrix element of the transition dipole moment, $k_\alpha = (\omega_0 + \Delta_\alpha)/c$ are the wave numbers, $\xi_{j\alpha}$ and φ_j are the phases of the temporal and spatial oscillations in the field components, and V_α are their real amplitudes. Note that the phase shifts of the spatial oscillations in the complex field amplitudes that have identical polarizations but belong to different frequency modes can always be made equal by appropriately choosing the coordinate system. Therefore, the phases φ_j in expression (2) do not depend on α.

We describe the state of the atoms interacting with a resonant optical field by using the Wigner matrix of density $\rho(\mathbf{r}, \mathbf{v}, t)$ [1, 2]. In the quasi-classical limit $\hbar k_\alpha \ll mv$ (v and m are the characteristic atomic velocity and mass, respectively) and in interaction representation, this matrix satisfies the kinetic equation

$$\left(\frac{\partial}{\partial t} + \mathbf{v}\frac{\partial}{\partial \mathbf{r}} + \hat{\gamma}\right)\hat{\rho} = -i[\hat{V}\hat{\rho}] + \frac{1}{2m}\left\{\frac{\partial \hat{V}}{\partial \mathbf{r}}\frac{\partial \hat{\rho}}{\partial \mathbf{v}}\right\}, \tag{3}$$

where $\hbar\hat{V}$ is the dipole atom-field interaction operator; $\hat{\gamma}$ is the relaxation operator that includes the recoil effect during spontaneous transitions [1, 2]; and the square brackets and braces denote the commutator and anticommutator, respectively. Below, it is convenient for our analysis to consider $\hat{\rho}$ in Cartesian representation [8], i.e., in the representation of basis wave functions (intra-atomic motion) for the ground (φ^g) and excited (φ_j^e) states, in which the matrix elements of the transition dipole moment $\hat{\mathbf{d}}$ are directed along the unit vectors of the Cartesian coordinate system:

$$\langle \varphi_j^e | \hat{\mathbf{d}} | \varphi^g \rangle = \mathbf{e}_j d.$$

In the resonance approximation, the system of equations (3) can then be represented as

$$\begin{aligned} i\left(\frac{d}{dt} + \gamma_\perp\right)\rho_i &= \sum_j q_{ij} V_j \\ &- \frac{\hbar i}{2m}\sum_{j \neq i}\frac{\partial q_{ij}}{\partial \mathbf{v}}\frac{\partial V_j}{\partial \mathbf{r}} - \frac{\hbar i}{4m}\frac{\partial Q_i}{\partial \mathbf{v}}\frac{\partial V_i}{\partial \mathbf{r}}, \\ \frac{d}{dt} &= \frac{\partial}{\partial t} + \mathbf{v}\frac{\partial}{\partial \mathbf{r}}, \quad Q_i = f + q_{ii} - \sum_{l \neq i} q_{ll}, \end{aligned} \tag{4}$$

$$\begin{aligned} i\left(\frac{d}{dt} + \gamma\right)q_{ij} &= -i\gamma f \delta_{ij} + (\rho_i V_j^* - V_i \rho_j^*) \\ &- \delta_{ij}\left(\sum_{l = x, y, z} \rho_l^* V_l - \text{c.c.}\right) + \delta_{ij}\frac{\hbar i}{2m}\sum_l \left(\frac{\partial \rho_l}{\partial \mathbf{v}}\frac{\partial V_l^*}{\partial \mathbf{r}} + \text{c.c.}\right) \\ &- \frac{\hbar i}{2m}\left(\frac{\partial \rho_i}{\partial \mathbf{v}}\frac{\partial V_j^*}{\partial \mathbf{r}} + \frac{\partial V_i}{\partial \mathbf{r}}\frac{\partial \rho_j^*}{\partial \mathbf{v}}\right), \\ \frac{df}{dt} + \left(\frac{\hbar}{m}\right)\sum_j \left(\frac{\partial \rho_j}{\partial \mathbf{v}}\frac{\partial V_j^*}{\partial \mathbf{r}} + \text{c.c.}\right) &= D(\hat{\rho}), \end{aligned} \tag{5}$$

where γ is the decay rate of the excited state, $\gamma_\perp = \gamma/2$, $f(\mathbf{r}, \mathbf{v}, t) = \text{Sp}(\hat{\rho})$ is the Wigner particle distribution function in phase space $(\mathbf{r}, \mathbf{v})$, $q_{ii}(\mathbf{r}, \mathbf{v}, t)$ and $\rho_i(\mathbf{r}, \mathbf{v}, t)$ mean the densities of the distributions of the population difference and the projections of the complex amplitude of the induced dipole moment onto the axes of the Cartesian coordinate system, the functions $q_{ij}(\mathbf{r}, \mathbf{v}, t)$ for $i \neq j$ describe the coherence between the excited atomic states, and the term $\hat{D}(\rho)$ on the right-hand side of Eq. (5) describes the recoil effect during spontaneous transitions in the quasi-classical limit:

$$\hat{D}(\hat{\rho}) = \frac{\hbar^2 k^2}{5m^2}\gamma\sum_{i,j}\left(\delta_{ij}\frac{\partial^2}{\partial \mathbf{v}^2} - \frac{1}{2}\frac{\partial^2}{\partial \mathbf{v}_i \partial \mathbf{v}_j}\right)\rho_{ij},$$

$$\rho_{ij} = q_{ij} + (\delta_{ij}/4)\left(f - \sum_l q_{ll}\right).$$

Let the resonant fields be weak and the frequency detunings Δ_0 and Δ_1 be not very close to each other:

$$\left|\frac{V_{j\alpha}}{\nu_\alpha}\right|^2, \quad \left|\frac{V_{j\alpha}^2}{\nu_1\nu_0}\right|, \quad \left|\frac{V_{j\alpha}^2}{\nu_\alpha\gamma}\right| \le g \ll 1, \qquad (6)$$
$$\delta = |\Delta_1 - \Delta_0| \gg g|\nu_\alpha|,$$

where $\nu_\alpha = \Delta_\alpha + i\gamma_\perp$.

In that case, the excited-state populations and the Stark energy-level shifts are small [8] and the distribution function (DF) can be represented as the sum of a slowly varying [on time scales $t > \tau = (\omega_R g)^{-1}$, $\omega_R = \hbar k^2/2m$, $k = \omega_0/c$] principal component $\bar{f}$ and a small rapidly oscillating (with characteristic frequencies $\Omega_1 \gg \tau^{-1}$) addition to it $\tilde{f}$ (cf. [14]):

$$f = \bar{f} + \tilde{f}, \quad |\tilde{f}/\bar{f}| \ll \frac{\hbar k}{mv} \lesssim \sqrt{\frac{\omega_R}{\gamma}} \ll 1. \qquad (7)$$

The density matrix elements that describe the light-induced internal motions in the atom can be eliminated from the system of equations (4) and (5) by the expansion of the field in powers (actually in the parameter $g \ll 1$) of the following structure:

$$\rho_j = \rho_j^{(1)}(\mathbf{r}, \mathbf{v}, t|\bar{f}(\mathbf{r}, \mathbf{v}, t)) + \rho^{(3)}(\mathbf{r}, \mathbf{v}, t|\bar{f}(\mathbf{r}, \mathbf{v}, t)) + \ldots, \qquad (8)$$
$$q_{ij} = -\delta_{ij}\bar{f} + \bar{q}_{ij}^{(2)}(\mathbf{r}, \mathbf{v}, t|\bar{f}(\mathbf{r}, \mathbf{v}, t)) + \ldots,$$

where $\rho_j^{(\sigma)}$ and $q_{ij}^{(\sigma)}$ are the linear differential operators acting on $\bar{f}$ and the superscript denotes the order of smallness of the corresponding terms in $g \ll 1$.

Below, we restrict our analysis to slow atoms ($kv \ll \gamma$) and take into account the fact that in our problem (as we will see), the atomic temperature T (in energy units) that corresponds to the Doppler cooling limit is always much higher than the depth of the microscopic potential wells produced by rapidly oscillating (with a period of ~1/k) gradient forces,

$$T \gg U_g \sim \hbar\gamma g, \qquad (9)$$

because $T \gtrsim \hbar\gamma/2$. Using the expansion (8) and additional averaging of the DF over small-scale spatial oscillations with a period of the order of the light wavelength [valid under the condition (9)], we obtain the following Fokker–Planck equation for the DF (for the averaged DF, we retain the original designation):

$$\frac{df}{dt} + \frac{1}{m}\frac{\partial}{\partial \mathbf{v}}(\mathbf{F}_{1R} + \mathbf{F}_R)f = \sum_{ij} D_{ij}\frac{\partial^2 f}{\partial v_i \partial v_j}, \qquad (10)$$

where the linear (in velocity) force $\mathbf{F}_{1R}$ and the RRF $\mathbf{F}_R$, respectively, match the general formulas (11) and (12) from [8] derived in a simple model of preset motion and the velocity diffusion tensor D_{ij}, in the second order of smallness in the field, is given by the formula ($r_i = \mathbf{re}_i$)

$$D_{ij} = \frac{\hbar^2\gamma}{5}\left\langle \sum_{\alpha=0}^{1}\left\{\frac{5}{2}\sum_l \frac{1}{|\nu_\alpha|^2}\frac{\partial V_{l\alpha}^*}{\partial r_i}\frac{\partial V_{l\alpha}}{\partial r_j} - \frac{k^2}{2}\frac{V_{i\alpha}V_{j\alpha}^*}{|\nu_\alpha|^2} + \frac{k^2}{2}\delta_{ij}\left(\frac{|V_{i\alpha}|^2}{|\nu_\alpha|^2} + 2\sum_l \frac{|V_{l\alpha}|^2}{|\nu_\alpha|^2}\right)\right\}\right\rangle.$$

For our case of the fields (2), we have

$$\mathbf{F}_{1R} = -m\kappa\mathbf{v}, \quad \kappa = -\frac{\hbar k^2\gamma}{m}\left[\frac{V_0^2\Delta_0}{|\nu_0|^4} + \frac{V_1^2\Delta_1}{|\nu_1|^4}\right], \qquad (11)$$

$$\mathbf{F}_R = -\nabla U + \mathrm{curl}\,\mathbf{A}, \qquad (12)$$

$$D_{ij} = D\delta_{ij}, \quad D = \left(\frac{\hbar k}{m}\right)^2\frac{\gamma}{2}\left(\frac{V_0^2}{|\nu_0|^2} + \frac{V_1^2}{|\nu_1|^2}\right), \qquad (13)$$

where the scalar, $U(\mathbf{r})$, and vector, $\mathbf{A}(\mathbf{r})$, RRF potentials are defined by the expressions

$$U = -\frac{\hbar k\Gamma_1 V_0^2 V_1^2}{4\delta k|\nu_0|^2|\nu_1|^2}\left\{\sum_j \cos(2\delta k\mathbf{e}_j\mathbf{r}) + \frac{1}{2}\sum_{i\neq j}\cos\Psi_{ij}(\cos[\delta k(\mathbf{e}_i - \mathbf{e}_j)\mathbf{r}] + \cos[\delta k(\mathbf{e}_i + \mathbf{e}_j)\mathbf{r}])\right\},$$

$$\mathbf{A} = -\frac{\hbar k\Gamma V_0^2 V_1^2}{2\delta k|\nu_0|^2|\nu_1|^2} \times \{\mathbf{e}_y\sin\Psi_{zx}(\cos[\delta k(z-x)] - \cos[\delta k(z+x)]) + \mathbf{e}_x\sin\Psi_{yz}(\cos[\delta k(y-z)] - \cos[\delta k(y+z)]) + \mathbf{e}_z\sin\Psi_{xy}(\cos[\delta k(x-y)] - \cos[\delta k(x+y)])\}, \qquad (14)$$

$$\delta k = k_1 - k_0, \quad \Psi_{ji} = (\xi_{j1} - \xi_{i1}) - (\xi_{j0} - \xi_{i0}),$$

$$\Gamma_1 = \gamma\gamma_\perp(\Delta_1 - \Delta_0)\left(\frac{1}{|\nu_1|^2} + \frac{1}{|\nu_0|^2}\right),$$

$$\Gamma = (\Delta_1\Delta_0 + \gamma_\perp^2)\left(\frac{\gamma}{|\nu_1|^2} + \frac{\gamma}{|\nu_0|^2}\right).$$

Thus, the quadratic (in field) force $\mathbf{F}_{1R}$ is the friction force and the RRF $\mathbf{F}_R$, which arises in the fourth order of smallness in the field, is generally a potential-vortex force in nature. The latter is attributable to interference effects in the resonant light pressure [7, 8], which, in particular, shows up in the dependence of its spatial structure on the relative phase shifts of the standing waves: $(\xi_{j\alpha} - \xi_{i\alpha})$. In this case, the vortex RRF component is determined by the correlators (of the fourth order of smallness in the field) of the mixed products of

the projections of the field amplitudes and their derivatives that refer to standing waves of different frequency modes and different polarizations (in the notation of [8], the terms in the expression for the RRF $\propto \langle \mathbf{J}_\alpha^{jl} I_{\alpha'}^{lj} \rangle$, $\alpha \neq \alpha'$, $j \neq l$).

Even for overdamped motion, where $\Omega^2/\kappa^2 = \varepsilon \sim \gamma\delta k/\omega_R k \ll 1$ ($\Omega^2 \sim F\delta k/m$), the vortex RRF component curl$\mathbf{A}$ can result in unstable motion (the EOT manifestation mechanism!) and hamper particle localization [7, 8]. Let us show that by controlling the relative phase shifts $\xi_{j\alpha} - \xi_{i\alpha}$ of bichromatic fields of the form (2), we can successfully solve this problem. Note that for two intersecting monochromatic standing waves (polarized along the same direction), control of the spatial radiative-force structure by varying the relative phase shifts of the waves was convincingly demonstrated in experiments [15].

Let the phase shifts of the bichromatic field components satisfy the condition (n_1 and n_2 are arbitrary integers)

$$\Psi_{zx} = 2\pi n_1, \quad \Psi_{yz} = 2\pi n_2. \tag{15}$$

In particular, this condition is always satisfied if the phase differences between orthogonally polarized waves, $\xi_{j\alpha} - \xi_{i\alpha}$, are multiples of π: $\xi_{j\alpha} - \xi_{i\alpha} = \pi m_{ij}$, where m_{ij} are arbitrary integers of the same parity. In that case, $\sin\Psi_{ij} = 0$, $\cos\Psi_{ij} = 1$, and, as follows from (12) and (14), the RRF is a purely potential ($\mathbf{A} = 0$) force. For $\kappa > 0$, it can generate a body-centered cubic superlattice (with spacing $L = \pi/\delta k \gg \lambda = 2\pi/k$) of atoms localized in potential wells with the characteristic depth

$$U_0 \cong \frac{\hbar\omega_0}{2}\left(\frac{\gamma^2}{|\nu_1|^2} + \frac{\gamma^2}{|\nu_0|^2}\right)\frac{V_1^2 V_0^2}{|\nu_1|^2|\nu_0|^2}. \tag{16}$$

Indeed, in this case, the Fokker–Planck equation (10) for $\kappa > 0$ admits a steady-state solution of the Boltzmann form:

$$f(\mathbf{r}, \mathbf{v}) \propto e^{-E(\mathbf{r})/T}, \quad E(\mathbf{r}) = \frac{m\mathbf{v}^2}{2} + U(\mathbf{r}),$$

$$T = \frac{mD}{\kappa} = -\frac{\hbar}{2}(g_0 + g_1)/\left(\frac{g_0\Delta_0}{|\nu_0|^2} + \frac{g_1\Delta_1}{|\nu_1|^2}\right), \tag{17}$$

$$g_\alpha = V_\alpha^2/|\nu_\alpha|^2.$$

The condition for deep localization of atoms in superlattice cells follows from Eqs. (17):

$$\eta = U_0/T \gg 1.$$

If this condition is satisfied, the sizes of the localized bunches of atoms are estimated as $r_0 \sim 1/\delta k\eta^{1/2} \ll 1/\delta k \sim L$. Thus, the localization parameter η is a complicated function of the field amplitudes and frequency detunings: $\eta = \eta(\Delta_1, \Delta_2, V_1, V_2)$. The stability of deep ($\eta \gg 1$) atom localization is characterized by the mean lifetime of an atom in an individual superlattice cell (determined by the time of particle diffusion from one well into another). The latter is estimated as

$$\tau > \tau_0 \frac{\pi^{5/2}}{8}\left(\frac{1}{\eta}\right)^{3/2} e^\eta, \quad \tau_0 = (4D_s\delta k^2)^{-1}, \tag{18}$$

where $D_s \simeq D/\kappa^2$ is the coefficient of spatial diffusion of the atoms in the field of radiative forces and τ_0 has the meaning of the particle lifetime in the so-called optical molasses with sizes $L/2$ (see, e.g., [2]). The estimate (18) was obtained from (10) in the limit ($\varepsilon \ll 1$) of overdamped particle motion (which is reached in most real situations [8]) based on the approximation of the boundary of the region of attraction of a stable RRF node by an atom-absorbing sphere of radius $L/2$. Clearly, it makes sense to speak about stable localization of atoms in the superlattice if τ is much longer than the lifetime of viscous confinement, i.e., when $(1/\eta)^{3/2}e^\eta \gg 1$.

To obtain specific estimates showing the real possibility of deep atom localization, we choose field frequencies and amplitudes to satisfy the conditions

$$\Delta_0 = -\frac{\gamma}{2}, \quad |\Delta_1| \gg \gamma,$$
$$|V_{j1}|^2/|\nu_1\nu_0| \sim |V_{j0}/\nu_0|^2 \sim g \simeq 2 \times 10^{-2} \ll 1. \tag{19}$$

In that case, only the field $\mathbf{E}_0$ is responsible for cooling (because $g_1 \ll g_0$), $T \simeq \hbar\gamma/2$, the frequency detuning Δ_1 of the field $\mathbf{E}_1$ determines the superlattice spacing (because $\delta k \simeq \Delta_1/c$), and all conditions (6) for the application of perturbation theory ($\left|\rho_j^{(3)}/\rho^{(1)}\right| \sim 0.1$) are satisfied. The atom localization parameter η is determined only by the ratio of the transition frequency to the detuning Δ_1,

$$\eta \simeq \frac{\omega_0}{|\Delta_1|} \times 6 \times 10^{-4},$$

and the field intensities J_α with the frequency detuning Δ_α required for particle localization are related to the radiation intensity saturating the quantum transition, J_s, by simple formulas, $J_0 = J_s \times 10^{-2}$ and $J_1 = \sqrt{2} \times 10^{-2}$ $(|\Delta_1|/\gamma)J_s$. For example, for the $^1S_0$–$^1P_1$ singlet transition of the ytterbium atom with $\lambda = 398.8$ nm, $\gamma = 1.8 \times 10^8$ s^{-1}, and detuning $|\Delta_1| \sim 2 \times 10^{11}$ s^{-1}, we have the following estimates: $L \simeq 0.5$ cm, $\eta = 14$, $r_0 \sim 0.1$ cm, $\tau_0 \simeq 0.01$ s, $\tau \sim 250$ s, $T = 7.2 \times 10^{-4}$ K, $J_0 \sim 0.6$ mW cm^{-2}, and $J_1 \simeq 0.8$ W cm^{-2}. For the same detuning Δ_1 of the quasi-resonant field and for the $^1S_0$–$^3P_1$ intercombination transition [11] with $\lambda = 555.6$ nm and $\gamma \sim 1.2 \times 10^6$ s^{-1}, we have $L \simeq 0.5$ cm, $\eta \sim 10$, $r_0 \sim 0.1$ cm, $\tau_0 \simeq 1$ s, $\tau \sim 250$ s, $T = 5$ μK (!), $J_0 \sim 1.4 \times 10^{-6}$ W/cm^2, and $J_1 \simeq 280$ mW/cm^2.

Thus, the atom localization conditions are satisfied for extremely low intensities. By decreasing the detuning $|\Delta_1|$, we can increase the localization parameter η and decrease the quasi-resonant field intensity J_1. In this case, the confinement of atoms may require increasing the cross-sectional laser-beam sizes R because of the condition $R > 1/\delta k$.

In conclusion, note that the vortex RRF component of atoms in a bichromatic field of the form (2) for arbitrary relative phase shifts of the standing waves can be suppressed by a purposeful choice of field detunings [see expressions (12) and (14)]: $\Delta_1\Delta_0 = -\gamma_\perp^2$. In such a situation, however, the stability condition ($\eta \gg 1$) is very difficult to satisfy for realistic superlattice parameters, because the field frequency detunings are "rigidly" related to each other. In particular, the regime of atom confinement that corresponds to the conditions (19) cannot be achieved; in this regime, cooling to limiting temperatures $\sim\hbar\gamma$ is combined with stable deep localization and a relatively small ($L < 1$ cm) adjustable superlattice spacing.

The vortex RRF component is also suppressed for uncorrelated fluctuating phases of orthogonally polarized standing waves [in superposition (2)], which can be produced, for example, by using independent sources of laser radiation. In this case, the localization conditions deteriorate, because the depths of the light-induced potential wells decrease and the relative phase shifts of the waves completely lose their role of controlling parameters.

ACKNOWLEDGMENTS

This study was supported by the Krasnoyarsk Science Foundation (project no. 11F0036C).

REFERENCES

1. V. G. Minogin and V. S. Letokhov, *The Pressure of Laser Radiation on Atoms* (Nauka, Moscow, 1986).
2. A. P. Kazantsev, G. I. Surdutovich, and V. P. Yakovlev, *The Mechanical Action of Light on Atoms* (Nauka, Moscow, 1991).
3. V. I. Balykin, V. G. Minogin, and V. S. Letokhov, Rep. Prog. Phys. **63**, 1429 (2000).
4. E. Raab, M. Prentiss, S. Chu, and D. Pritchhard, Phys. Rev. Lett. **59**, 2631 (1987).
5. A. Ashkin and J. P. Gordon, Opt. Lett. **8**, 511 (1983).
6. P. Bouyer, P. Lemonde, M. Ben Dahan, *et al.*, Europhys. Lett. **27**, 569 (1994).
7. A. P. Kazantsev and I. V. Krasnov, J. Opt. Soc. Am. B **6**, 2140 (1989).
8. S. A. Gavrilyuk, I. V. Krasnov, and S. P. Polyutov, Zh. Éksp. Teor. Fiz. **120**, 1135 (2001) [JETP **93**, 985 (2001)].
9. G. Wasik and R. Grimm, Opt. Commun. **137**, 406 (1997).
10. K. Honda, Y. Takahasi, T. Kuwamoto, *et al.*, Phys. Rev. A **59**, R934 (1999).
11. T. Kuwamoto, K. Honda, Y. Takahashi, and T. Yabuzaki, Phys. Rev. A **60**, R745 (1999).
12. J. Grunert and A. Hemmerich, Phys. Rev. A **65**, 041401(R) (2002).
13. E. A. Curtis, C. W. Oates, and L. Holberg, Phys. Rev. A **64**, 031403 (2001).
14. I. V. Krasnov, Laser Phys. **4**, 906 (1994).
15. A. Hemmerich, D. Schropp, and T. W. Hansh, Phys. Rev. A **44**, 1910 (1991).

Translated by V. Astakhov

JETP Letters, Vol. 76, No. 5, 2002, pp. 275–278. Translated from Pis'ma v Zhurnal Éksperimental'noĭ i Teoreticheskoĭ Fiziki, Vol. 76, No. 5, 2002, pp. 333–336.

The Formation of a Light Field with Suppressed Photon Fluctuations by Nonlinear Optical Methods

A. V. Nikandrov[1] and A. S. Chirkin[2]

Moscow State University, Vorob'evy gory, Moscow, 119992 Russia

[1] *e-mail: avn@squeez.phys.msu.su*

[2] *e-mail: chirkin@squeez.phys.msu.su*

Received July 30, 2002

A quantum theory is developed to describe optical parametric amplification under low-frequency pumping, which is observed in nonlinear photonic crystals in sequential interactions of light waves with multiple frequencies. Spatial variations of the mean number of photons and the Fano factor at signal and additional frequencies are analyzed. It is shown that a field with a sub-Poisson statistics of photons can be formed at a signal frequency which is 1.5 times higher than the frequency of pumping. © *2002 MAIK "Nauka/Interperiodica".*

PACS numbers: 42.50.Dv; 42.65.Ky; 42.65.Yj

The goal of this letter is to call attention to the possibility of applying nonlinear optical methods to create fields with a level of photon fluctuations below that for coherent radiation. This is achieved without the use of feedback and is observed in light field at the exit from a nonlinear optical crystal. The case in point is sequential three-frequency interactions of light waves with multiple frequencies ω, 2ω, and 3ω in nonlinear photonic crystals (NPCs), that is, in optical crystals with periodic modulation of only nonlinear susceptibility (see review [1]). Such a nonlinear lattice is, for instance, created in nonlinear optical crystals with a regular domain structure or in periodically polarized crystals.

It is well known [2, 3] that light attenuation and amplification (in a laser or an optical parametric amplifier at low-frequency pumping) either occur with the conservation of the statistics of photons or are accompanied by an increase in the level of photon fluctuations. In the nonlinear optical method considered below, which uses phase sensitivity of the parametric process under low-frequency pumping conditions, a decrease in the number of signal-wave photons is accompanied by the suppression of signal photon fluctuations. This radically distinguishes the parametric process under consideration from the traditional parametric process under high-frequency pumping conditions.

Consider the sequential interaction of light waves with multiple frequencies ω, 2ω, and 3ω in an NPC. We assume that the intense pumping and signal waves have the frequencies 2ω and 3ω, respectively (Fig. 1). Let one of the nonlinear optical processes be the parametric frequency conversion downward

$$2\omega \longrightarrow \omega + \omega, \tag{1}$$

and let the other process be the mixing of optical frequencies

$$\omega + 2\omega \longrightarrow 3\omega. \tag{2}$$

The phase detunings for Eqs. (1) and (2)

$$\Delta k_2 = k_2 - 2k_1, \quad \Delta k_3 = k_3 - k_2 - k_1 \tag{3}$$

in an NPC, for instance, in lithium niobate [1], can be balanced by the vector of the reciprocal nonlinear "lattice" (collinear quasi-phase-matching conditions)

$$\Delta k_2 = 2\pi m_2/\Lambda, \quad \Delta k_3 = 2\pi m_3/\Lambda, \tag{4}$$

where $k_j = k(j\omega)$ is the wave number at the frequency $j\omega$; the $m_j = \pm 1, \pm 3, \ldots$ numbers characterize the order of quasi-phase-matching; and Λ is the modulation period of nonlinear susceptibility. If conditions (4) are satisfied, a parametric process occurs under low-frequency pumping conditions in the sequential interactions that we are considering [4]. Note that sequential

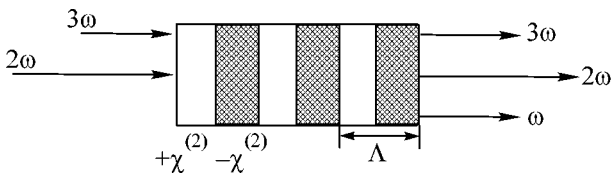

Fig. 1. Schematic drawing of optical parametric amplification at low-frequency NPC pumping. Pumping wave frequency is 2ω, and signal wave frequency is 3ω ($\chi^{(2)}$ is quadratic nonlinearity). In addition to pumping and signal waves, a wave with frequency ω appears at the crystal output.

0021-3640/02/7605-0275$22.00

interactions have been observed in KTP (potassium titanyl phosphate $KTiOPO_4$) and $LiNbO_3$ crystals [1].

We will show that a signal with a sub-Poisson statistics of photons can be obtained if a coherent signal of the frequency 3ω is fed to the entrance of an NPC. A quantum description of nonlinear optical processes in space requires the use of the field momentum operator [5]. In the approximation of a given classical pumping field, the momentum operator for processes (1) and (2) has the form [6]

$$G_I = \hbar[\beta_2 a_1^{+2} + \beta_2^* a_1^2 + \beta_3 a_3^+ a_1 + \beta_3^* a_3 a_1^+], \quad (5)$$

where a_j, a_j^+ are the photon annihilation and creation operators with the commutation relations $[a_j, a_k^+] = \delta_{jk}$, $[a_j, a_k] = 0$ and β_j is the effective nonlinear wave coupling coefficient ($j = 1, 3$). Equation (5) for an NPC is valid under the conditions of weak amplification at length Λ, $\beta_2\Lambda \approx \beta_3\Lambda \ll 1$.

The dynamics of the a_j operators in the interaction representation is given by the Heisenberg equation

$$i\hbar\frac{da_j}{dz} = [G_I, a_j] \quad (j = 1, 3). \quad (6)$$

Our major interest is the wave with the frequency 3ω. We will therefore consider the case $|\beta_3| > |\beta_2|$, for which the solution to Eq. (6) is

$$\begin{aligned} a_3(z) &= u_-(z)a_{30} - ie^{3i\varphi}F_-(z)a_{30}^+ \\ &\quad - ie^{i\varphi}G_+(z)a_{10} - e^{2i\varphi}G_-(z)a_{10}^+, \\ a_1(z) &= -e^{-i\varphi}G_+(z)a_{30} + e^{2i\varphi}G_-(z)a_{30}^+ \\ &\quad + u_+(z)a_{10} - ie^{i\varphi}F_+(z)a_{10}^+. \end{aligned} \quad (7)$$

The values of the a_{j0} and a_{j0}^+ operators correspond to the entrance of the nonlinear medium, $\varphi = \arg\beta_2 = \arg\beta_3$ is the pumping phase, and the functions in Eq. (7) are given by the equations

$$\begin{aligned} u_\pm(z) &= \cosh(|\beta_2|z)\cos(\gamma z) \pm \kappa\varepsilon\sinh(|\beta_2|z)\sin(\gamma z), \\ F_\pm(z) &= \pm\sinh(|\beta_2|z)\cos(\gamma z) \\ &\quad + \kappa\varepsilon\cosh(|\beta_2|z)\sin(\gamma z), \\ G_\pm(z) &= 0.5\kappa[e^{(|\beta_2|z)} \pm e^{-(|\beta_2|z)}]\sin(\gamma z), \end{aligned} \quad (8)$$

where $\kappa = 1/\sqrt{1-\varepsilon^2}$, $\varepsilon = |\beta_2/\beta_3|$, and $\gamma = \sqrt{|\beta_3|^2 - |\beta_2|^2}$.

The initial condition of our problem is field at frequency ω in the vacuum state $|0\rangle_1$ and field at frequency 3ω in the coherent state $|\alpha\rangle_3$; that is, the quantum field state at the entrance of an NPC has the form $|\psi(0)\rangle = |0\rangle_1|\alpha\rangle_3$, $\alpha = |\alpha|e^{i\varphi_{30}}$, and $|\alpha| = \sqrt{\langle n_{30}\rangle}$, where $\langle n_{30}\rangle$ is the mean number of signal photons and φ_{30} is the signal-wave phase.

The dynamics of the mean number of photons in an NPC is determined by the equations

$$\begin{aligned} \langle n_1\rangle &= \langle n_{30}\rangle(G_+^2 + G_-^2 - 2G_+G_-\sin(3\varphi - 2\varphi_{30})) \\ &\quad + G_-^2 + F_+^2, \\ \langle n_3\rangle &= \langle n_{30}\rangle(u_-^2 + F_-^2 + 2u_-F_-\sin(3\varphi - 2\varphi_{30})) \\ &\quad + G_+^2 + F_-^2. \end{aligned} \quad (9)$$

The terms outside parentheses in Eq. (9) are related to vacuum fluctuations, and their contribution decreases as $\langle n_{30}\rangle$ grows. Equation (9) shows that the mean numbers of photons depend on the ratio between the pumping φ and signal φ_{30} phases; that is, the process under consideration possesses phase sensitivity. If the G_+G_- and u_-F_- products have the same sign, the mean numbers of photons at frequencies ω and 3ω vary in antiphase as functions of the $(3\varphi - 2\varphi_{30})$ phase relation; that is, a maximum of $\langle n_1\rangle$ corresponds to the minimum of $\langle n_3\rangle$ and vice versa. As $G_+G_- > 0$ always, the behavior of the mean number of photons depends on the sign of u_-F_-. According to Eq. (8), $u_-F_- > 0$ at small $|\beta_2|z$ parameter values.

The nonmonotonic dependences of the mean numbers of photons $\langle n_1\rangle$ and $\langle n_3\rangle$ on interaction length at $(3\varphi - 2\varphi_{30}) = \pi/2$, where $\langle n_1\rangle$ and $\langle n_3\rangle$ have extrema, are shown in Fig. 2. It follows from Fig. 2b that the mean number of photons at the frequency 3ω first decreases as interaction length increases and then, at $|\beta_2|z \gtrsim 1.5$, grows. The behavior of the mean number of photons at the frequency ω is more complex (Fig. 2a). Curves *1* and *2* show that the mean number of photons first increases, decreases at interaction lengths $|\beta_2|z \gtrsim 0.5$, and then again increases.

We arrive at the conclusion that, at small interaction lengths $|\beta_2|z \lesssim 1.5$, signal "damping" rather than amplification occurs in the process under consideration. This damping is related to the conversion of signal photons into photons with frequency ω; that is, the difference frequency is generated ($3\omega - 2\omega \longrightarrow \omega$). Signal amplification at this frequency occurs when the process of parametric frequency conversion downward (Eq. (1)) accompanied by mixing of optical frequencies (Eq. (2)) becomes substantial. The competition of these two processes can, we believe, somewhat decrease the level of photon fluctuations at the frequency 3ω (see below).

The $(3\varphi - 2\varphi_{30}) = \pi/2$ phase relation also deserves attention because maximum photon fluctuation sup-

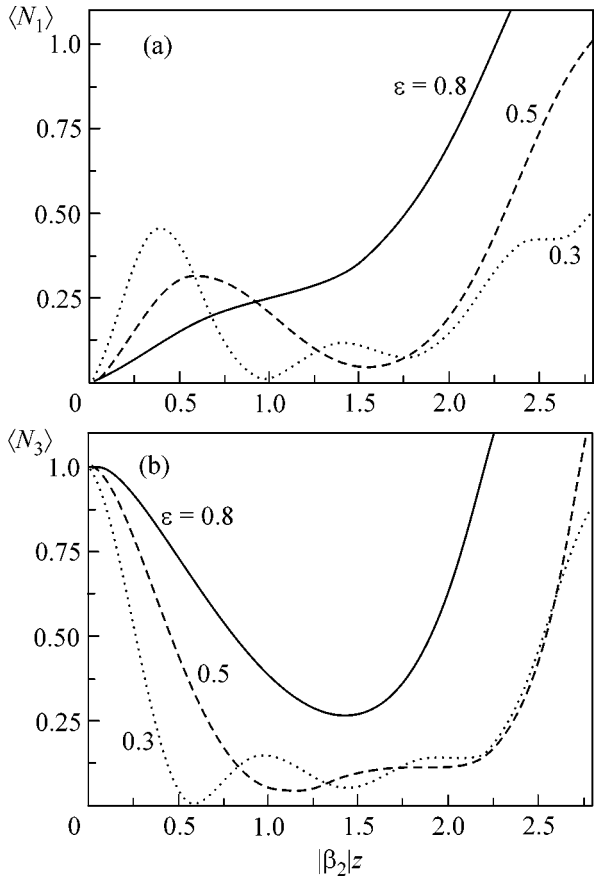

Fig. 2. Dependences of normalized mean numbers of photons (a) $\langle N_1 \rangle$ and (b) $\langle N_3 \rangle$ at frequencies ω and 3ω, respectively, on reduced interaction length $|\beta_2|z$ for various $\varepsilon = |\beta_2/\beta_3|$ values. The curves were calculated and the mean numbers of photons normalized for the initial mean number of signal photons $\langle n_{30} \rangle = 100$, $\langle N_j \rangle = \langle n_j \rangle / \langle n_{30} \rangle$.

pression is then observed at the frequency 3ω. The Fano factor then takes the form

$$\mathcal{F}_3 = \frac{1}{\langle n_3 \rangle}\{\langle n_{30} \rangle (u_- + F_-)^2 [(G_+ - G_-)^2 + (u_- - F_-)^2) + 4u_- F_-] + 2u_-^2 F_-^2 + 2G_-^2 G_+^2 + (F_- G_+ - u_- G_-)^2\}. \quad (10)$$

The dependences of the Fano factor (Eq. (10)) on the interaction length are shown in Fig. 3. According to these plots, there is a region of $|\beta_2|z$ values, which depends on the ratio between the nonlinear coupling coefficients $\varepsilon = |\beta_2/\beta_3|$, where a sub-Poisson statistics of photon fluctuations is observed ($\mathcal{F}_3 < 1$); for the problem parameters under consideration, the minimum Fano factor value is $\mathcal{F}_3 \approx 0.6$. An analysis shows that the statistics of photons at the frequency ω is then super-Poisson ($\mathcal{F}_1 > 1$) irrespective of the $(3\varphi - 2\varphi_{30})$ value. Note that if no signal wave is fed to the entrance

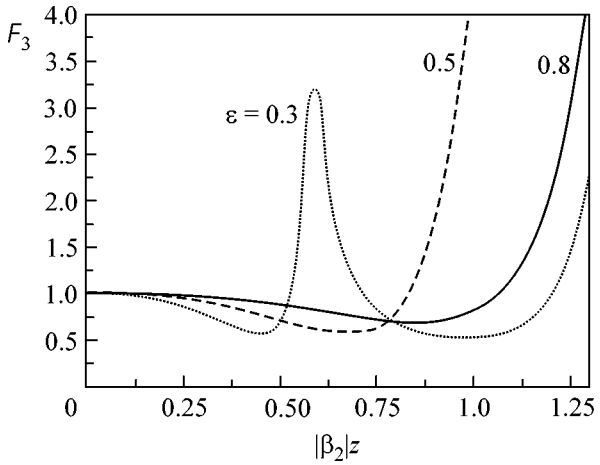

Fig. 3. Dependence of the Fano factor $\mathcal{F}_3$ at the frequency 3ω on reduced interaction length $|\beta_2|z$ for various $\varepsilon = |\beta_2/\beta_3|$ values. The curves were obtained for $\langle n_{30} \rangle = 100$.

of an NPC ($\langle n_{30} \rangle = 0$), the statistics of photons at the frequencies ω and 3ω at the output is super-Poisson [7].

The most important result of this work is the development of a quantum theory of the process observed in sequential wave interactions in which an intense pumping wave parametrically interacts with a signal wave whose frequency is 1.5 times higher than that of pumping. We can then obtain radiation with a sub-Poisson statistics of photons at the output of an NPC under signal attenuation conditions.

According to the theory developed, fields with a sub-Poisson statistics of photons can form at $|\beta_2|z \approx 1$ (see Fig. 3). Let us estimate the intensity of pumping at which this condition is satisfied, for instance, for the $LiNbO_3$ NPC, when all interacting waves are extraordinary. The nonlinear β_2 coefficient is then given by $\beta_2 = 8\pi\chi^{(2)}|A_2|/\lambda n m_2$, where $\chi^{(2)} = d_{33} = 34$ pm/V is the quadratic susceptibility tensor; A_2 and λ are the pumping amplitude and wavelength, respectively; and n is the refractive index at wavelength λ. Put $\lambda = 0.5$ μm, $m_2 = 3$, and $z = 1$ cm. We then have $|A_2| \approx 3 \times 10^3$ V/cm and an intensity of pumping $I_2 \approx 10^4$ W/cm^2, which is quite attainable in experiments. As to the ratio between the nonlinear coupling coefficients $\varepsilon = |\beta_2/\beta_3|$, it is virtually determined by the ratio between the quasi-phase-matching orders $\varepsilon \approx m_2/m_3$.

Our analysis therefore shows that the suggested nonlinear optical method for creating fields with a sub-Poisson statistics of photons can be implemented experimentally.

Note in conclusion that the method under consideration augments the laser method for generating radiation with a sub-Poisson statistics of photons (see [8, 9] and the references cited therein). The suggested source of nonclassical light can be of interest for high-preci-

sion measurements and for quantum communication purposes.

The authors thank G.D. Laptev and A.A. Novikov for useful discussions. This work was financially supported by the Russian Foundation for Basic Research (project nos. 01-02-16311 and 02-02-06418) and INTAS (grant no. 2001-2097).

REFERENCES

1. A. S. Chirkin, V. V. Volkov, G. D. Laptev, and E. Yu. Morozov, Kvantovaya Élektron. (Moscow) **30**, 847 (2000).
2. D. F. Walls and G. J. Milburn, *Quantum Optics* (Springer-Verlag, Berlin, 1995).
3. L. Mandel and E. Wolf, *Optical Coherence and Quantum Optics* (Cambridge Univ. Press, Cambridge, 1995; Fizmatlit, Moscow, 2000).
4. V. V. Volkov and A. S. Chirkin, Kvantovaya Élektron. (Moscow) **25**, 101 (1998).
5. J. Fiurasek and J. Perina, in *Coherence and Statistics Photons and Atoms*, Ed. by J. Perina (Wiley, New York, 2001), p. 65.
6. A. S. Chirkin, Opt. Spektrosk. **87**, 627 (1999) [Opt. Spectrosc. **87**, 575 (1999)].
7. A. S. Chirkin, J. Opt. B **4**, S91 (2002).
8. Ya. A. Fofanov and I. V. Sokolov, Opt. Spektrosk. **91**, 550 (2001) [Opt. Spectrosc. **91**, 519 (2001)].
9. J.-P. Hermier, M. I. Kolobov, I. Maurin, and E. Giacobino, Phys. Rev. A **65**, 053825 (2002).

Translated by V. Sipachev

JETP Letters, Vol. 76, No. 5, 2002, pp. 279–282. Translated from Pis'ma v Zhurnal Éksperimental'noĭ i Teoreticheskoĭ Fiziki, Vol. 76, No. 5, 2002, pp. 337–340.

Multiple Scattering Effect on the Line Width of Parametric X-Ray Relativistic Electron Radiation in a Crystal

N. F. Shul'ga[1, *] and M. Tabrizi[2]

[1] *Institute for Theoretical Physics, National Science Center Kharkov Institute of Physics and Technology, Kharkov, 61108 Ukraine*

** e-mail: shulga@kipt.kharkov.ua*

[2] *Kharkov National University, Kharkov, 61077 Ukraine*

Received August 5, 2002

It is shown that multiple scattering is of significant importance in the formation of the line width of parametric X-ray "backward" radiation of relativistic electrons in a crystal. A theory of the line width of this radiation based on the functional integration method is suggested. The problem of multiple scattering effects on parametric X-ray radiation is shown to be similar to the problem of the Landau–Pomeranchuk–Migdal multiple scattering effect on the bremsstrahlung of high-energy electrons in an amorphous medium. © *2002 MAIK "Nauka/Interperiodica".*

PACS numbers: 79.20.Kz; 61.14.Dc

1. Parametric X-ray radiation of relativistic electrons is observed when particles fall at a small incidence angle with respect to one of the crystallographic planes of crystal atoms (see recent reviews [1, 2] and references therein). This radiation is largely concentrated in directions close to the Bragg angles of particle field reflection from such planes. Of special interest is parametric X-ray radiation "backward" when particles fall onto a crystal at a small angle with respect to one of its crystallographic axes (axis z), because the contributions of other kinds of radiation such as bremsstrahlung and coherent radiation are then considerably suppressed. Narrow lines then appear in the spectral angular radiation density as a result of the interference of waves reflected from crystallographic atomic planes oriented normally to axis z. The natural width of these lines is determined by the number of crystal atom planes with which an electron interacts. Experimental studies of the line widths of parametric X-ray radiation backward have recently been performed on an MAMI accelerator (Mainz, Germany) at electron energies of 855 MeV [3]. The measured line widths were, however, much larger than the natural line width of parametric X-ray radiation.

In this work, we show that multiple scattering of particles in a crystal is of significant importance in the formation of the line width of parametric X-ray radiation. Equations that describe the multiple scattering effect on the line width of parametric X-ray radiation are obtained. The spectral-angular density of parametric X-ray radiation is averaged using the functional integration method. It is shown that, mathematically, this problem is similar to the problem of the Landau–Pomeranchuk–Migdal effect of multiple scattering on bremsstrahlung of ultrahigh-energy electrons in an amorphous medium.

2. The determination of the spectral-angular radiation density of a relativistic electron that moves along the $\mathbf{r}(t)$ trajectory in a medium with nonuniform permittivity $\epsilon_\omega(\mathbf{r}) = 1 + \epsilon'_\omega(\mathbf{r})$ requires knowledge of the time Fourier component of the particle electric field vector $\mathbf{E}_\omega(\mathbf{r})$. This value is determined by the equation [4]

$$\begin{aligned}(\Delta + \omega^2)E_{\omega,i} - \nabla_i \nabla_k E_{\omega,k} \\ = -4\pi i\omega j_{\omega,i} - \omega^2 \epsilon'_\omega(\mathbf{r}) E_{\omega,i},\end{aligned} \tag{1}$$

where $\mathbf{j}_\omega(\mathbf{r})$ is the Fourier component of the particle current density vector,

$$\mathbf{j}_\omega(\mathbf{r}) = e\int_{-\infty}^{\infty} dt e^{i\omega t}\mathbf{v}(t)\delta(\mathbf{r} - \mathbf{r}(t)), \tag{2}$$

and $\mathbf{v}(t)$ is the velocity of the particle.

The method of Green's functions can be used to show that the spectral-angular radiation density has the form

$$\frac{dE}{d\omega do} \frac{1}{4\pi^2}\left|\mathbf{k}\times\int d^3 r e^{-i\mathbf{kr}}(4\pi i\mathbf{j}_\omega(\mathbf{r}) + \omega\epsilon'_\omega(\mathbf{r})\mathbf{E}_\omega(\mathbf{r}))\right|^2, \tag{3}$$

0021-3640/02/7605-0279$22.00

where $\mathbf{k}$ is the wave vector in the direction of radiation ($|\mathbf{k}| = \omega$) (we use units in which the velocity of light is equal to one).

The first term in Eq. (3) determines the contribution to the radiation of changes in the trajectory of the particle in an external field. This term does not depend on $\epsilon'_\omega(\mathbf{r})$. For a relativistic electron, this term makes a major contribution in the region of radiation angles close to the direction of particle velocity $\mathbf{v}(t)$. The contribution of this term to parametric X-ray radiation backward can be ignored. The second term in Eq. (3) is only nonzero in the region of coordinates where the $\varepsilon_\omega(\mathbf{r})$ value is nonzero. For this reason, the determination of the contribution to radiation caused by nonuniformity of medium permittivity only requires knowledge of field $\mathbf{E}_\omega(\mathbf{r})$ in the region where $\epsilon'_\omega(r) \neq 0$. In the simplest situation of a small $\epsilon'_\omega(\mathbf{r})$ value, a solution to Eq. (1) can be sought in the form of the expansion in powers of $\epsilon'_\omega(\mathbf{r})$. The first term of this expansion is independent of $\epsilon'_\omega(\mathbf{r})$ and is the $\mathbf{E}^0_\omega(\mathbf{r})$ field of the particle moving in the vacuum along the $\mathbf{r}(t)$ trajectory. Substituting this expression for $\mathbf{E}^0_\omega(\mathbf{r})$ into Eq. (3) and using the Fourier expansion of $\mathbf{E}^0_\omega(\mathbf{r})$ and $\epsilon'_\omega(\mathbf{r})$, we obtain the following equation for the spectral-angular density of radiation:

$$\frac{dE}{d\omega do} = \frac{e^2\omega^4}{4\pi^2}\left|\mathbf{k}\times\int\frac{d^3q}{(2\pi)^3}\frac{\epsilon'_{\omega,\mathbf{q}}}{\omega^2-(\mathbf{k}-\mathbf{q})^2}\right.$$
$$\left.\times\left\{\mathbf{j}_{\omega,\mathbf{k}-\mathbf{q}}-\frac{1}{\omega^2}(\mathbf{k}-\mathbf{q})[(\mathbf{k}-\mathbf{q})\cdot\mathbf{j}_{\omega,\mathbf{k}-\mathbf{q}}]\right\}\right|^2, \quad (4)$$

where $\mathbf{j}_{\omega,\mathbf{k}-\mathbf{q}}$ is the coordinate Fourier component of the particle current density vector,

$$\mathbf{j}_{\omega,q} = e\int_{-\infty}^{\infty} dt\mathbf{v}(t)\exp[i(\omega t-\mathbf{q}\mathbf{r}(t))]. \quad (5)$$

When a relativistic electron falls onto a crystal at a small angle ψ to one of the crystallographic axes (axis z), the major contribution to parametric X-ray radiation backward is made by the $q_x = q_y = 0$ components. Permittivity nonuniformity along the x and y axes normal to z is then inessential to radiation. Taking into account the periodicity of permittivity along the z axis, the radiation intensity can be found using the following expression for $\epsilon'_{\omega,\mathbf{q}}$:

$$\epsilon'_{\omega,\mathbf{q}} = (2\pi)^2\delta(\mathbf{q}_\perp)\epsilon_{\omega,q_z}\frac{1-\exp(-iNaq_z)}{1-\exp(-iaq_z)}, \quad (6)$$

where $\delta(\mathbf{q}_\perp)$ is the two-dimensional delta function, $\mathbf{q}_\perp = (q_x, q_y)$; a is the distance between crystallographic atomic planes along the z axis; N is the number of such planes; and

$$\epsilon_{\omega,q_z} = \int_0^a dz\epsilon_\omega(z)\exp(-iq_z z). \quad (7)$$

Function (6) has sharp maxima at $q_z = g$, where $g = 2\pi n/a$ and n are integers. For $N \longrightarrow \infty$ and rectilinear particle movement in a crystal, these g values correspond to the parametric X-ray radiation lines $\omega_n = \nu g\cos\psi(1+\nu\cos\theta)^{-1}$, where $\psi = (\psi_x, 0)$ is the angle between $(-\mathbf{v})$ and $\mathbf{g}$ and $\boldsymbol{\theta} = (\theta_x, 0)$ is the angle at which radiation occurs [we are interested in radiation in the (x, z) plane in the region of θ_x angles close to the direction of Bragg reflection of waves].

Multiple scattering results in small deviations of the particle velocity vector from the initial direction $\mathbf{v}$. Taking these small deviations into account, the $\mathbf{v}(t)$ velocity vector can be written as

$$\mathbf{v}(t) \approx \mathbf{v}\left(1-\frac{\mathbf{v}_\perp^2(t)}{2}\right)+\mathbf{v}_\perp(t), \quad (8)$$

where $\mathbf{v}_\perp(t)\cdot\mathbf{v} = 0$ and $|\mathbf{v}_\perp| \ll |\mathbf{v}|$. The mean distance covered by a particle between its sequential collisions with crystal atomic planes then changes, which in turn causes changes in the line width of parametric X-ray radiation. The finite number of crystal atomic planes that interact with the particle also causes line broadening.

Consider radiation close to one of the parametric X-ray radiation lines $\omega = \omega_n$, taking into consideration the influence of crystal thickness $L = Na$ and multiple particle scattering in a crystal on the line width. After substituting the $q_z \longrightarrow g + q'_z$ variable into Eq. (4), it is easy to see that the characteristic q'_z values that make the major contribution to parametric X-ray radiation near the line of interest are close in order of magnitude to $q'_{z\text{eff}} \sim 1/Na$. To within terms of the order of $1/N$, the spectral-angular density of parametric X-ray radiation close to the line with frequency ω_n is given by the equation

$$\frac{dE}{d\omega do} = \frac{e^2\omega_n^2}{4\pi^2a^2}\left|\epsilon_{\omega_n,g}\right|^2$$
$$\times\left|\int_0^L dt e^{2i(\omega-\omega_n)t}\frac{\boldsymbol{\theta}-\boldsymbol{\psi}-\frac{\partial}{\partial\boldsymbol{\mu}}}{\gamma^{-2}+(\boldsymbol{\theta}-\boldsymbol{\psi})^2-\frac{2i}{\omega_n}\frac{\partial}{\partial t}}\Phi(\mathbf{v}_\perp(t))\right|^2_{\mu\to 0}, \quad (9)$$

where $\Phi(\mathbf{v}_\perp(t))$ is the function that determines the influence of multiple scattering on parametric X-ray radiation,

$$\Phi(\mathbf{v}_\perp(t)) = \exp\left\{\boldsymbol{\mu}\mathbf{v}_\perp(t) + \frac{i\omega_n}{2}\int_0^t dt'\mathbf{v}_\perp^2(t') - i\omega_n(\boldsymbol{\theta}-\boldsymbol{\psi})\int_0^t dt'\mathbf{v}_\perp(t')\right\}. \quad (10)$$

The $\mathbf{v}_\perp(t)$ value in Eq. (10) is a random particle scattering angle value at time t related to multiple scattering of the particle in the crystal. Equation (9) should be averaged over these random scattering angle values. An important property of relativistic electron scattering in a crystal when a beam falls at a small angle ψ to crystallographic axis z is scattering of particles largely along azimuthal angle φ in the plane orthogonal to the z axis [5]. A redistribution of particles over this angle occurs as a result of multiple scattering by crystal atom chains oriented parallel to the z axis. If $\psi \gg \psi_c$, where ψ_c is the critical angle of axial channeling, multiple scattering by crystal atom chains is a Gaussian process with the mean square of multiple scattering angles $\overline{\vartheta^2} = qL$. This differs from the mean square of multiple scattering angles of particles in an amorphous medium by a factor of the order of $R/4\psi d$, where R is the Thomas–Fermi radius of screening of the potential of a separate crystal atom and d is the interatomic distance along axis z [5]. Functional (9), which should be averaged, also has Gaussian form, and averaging can therefore be performed by the functional integration method [6]. In the simplest situation of $(\theta - \psi)^2 \gg qL$, the dependence of the preexponential factor on random value $\nu_\perp(t)$ can be ignored in Eq. (9). This dependence appears as a result of the action of differential operators on the $\Phi(\mathbf{v}_\perp(t))$ functional. Separating out the part of Eq. (9) subject to averaging and taking into account that particle scattering in the problem under consideration largely occurs along axis y, we obtain the following equation for the spectral angular density of parametric X-ray radiation backward:

$$\frac{dE}{d\omega do} = \frac{e^2\omega_n^2\left|\epsilon_{\omega_n, g}\right|^2}{4\pi^2 a^2}\frac{(\theta-\psi)^2}{[\gamma^{-2}+(\theta-\psi)^2]^2}L^2F(L, \omega-\omega_n), \quad (11)$$

where

$$F = (L, \omega-\omega_n) = \frac{2}{L^2}\mathrm{Re}\int_0^L dt\int_0^t dt' e^{2i(\omega-\omega_n)(t-t')}\langle\Phi(\nu_\perp(t))\Phi^*(\nu_\perp(t'))\rangle, \quad (12)$$

$$\langle\Phi(\nu_\perp(t))\Phi^*(\nu_\perp(t'))\rangle = \lim_{N\to\infty}\int\ldots\int\frac{d\nu_1\ldots d\nu_N}{(\pi q\Delta)^{N/2}}\exp\left\{-\frac{\nu_1^2}{q\Delta}-\ldots - \frac{(\nu_N-\nu_{N-1})^2}{q\Delta}+\frac{i\nu g\Delta}{4}\sum_{n=k}^N\nu_n^2\right\}. \quad (13)$$

Here, $t = N\Delta$, $t' = k\Delta$, and ν_n is the scattering angle at time $t_n = n\Delta$.

Functional integral (13) has the same structure as the corresponding integral in the theory of the Landau–Pomeranchuk–Migdal multiple scattering effect on bremsstrahlung of high-energy electrons in an amorphous medium [7, 8]. Integral (13) can therefore be calculated by the method developed in [7] to describe the Landau–Pomeranchuk–Migdal effect. This gives

$$\langle\Phi(\nu_\perp(t))\Phi^*(\nu_\perp(t'))\rangle = \left(1-\frac{i\omega_n(t-t')qt'}{2}+\frac{\omega_n^2q^2(t-t')^3t'}{12}\right)^{-1/2}. \quad (14)$$

Separating out dimensional values in Eqs. (12) and (14), we can write function F in the form

$$F = 2\mathrm{Re}\int_0^1 dx\int_0^x du e^{2iL(\omega-\omega_n)u}\times\left(1-\left(i\sigma u(x-u)+\frac{\sigma^2}{3}u^3(x-u)\right)\right)^{-1/2}, \quad (15)$$

where $\sigma \equiv \omega_n qL^2/2$, $x = t/L$, and $u = (t - t')/L$. This formula shows that the influence of multiple scattering on parametric X-ray radiation backward is determined by the σ parameter. If $\sigma \ll 1$, the influence of multiple scattering on parametric X-ray radiation can be ignored. The $F = F_0$ function then determines the natural line width of parametric X-ray scattering,

$$F_0 = \frac{\sin^2(\omega-\omega_n)L}{((\omega-\omega_n)L)^2}. \quad (16)$$

According to Eq. (16), the line width is given by $\Delta\omega \sim 1/L$ to within an order of magnitude.

If $\sigma \gg 1$, the characteristic u_{eff} values in Eq. (15) have the order of magnitude $u_{\mathrm{eff}} \sim (3/\sigma^2)^{1/3}$. The line width is then determined by the equation

$$\Delta\omega \sim \frac{1}{L}\left(\frac{\sigma^2}{3}\right)^{1/3}. \quad (17)$$

It follows that multiple scattering at $\sigma \gg 1$ causes substantial broadening of parametric X-ray radiation lines compared with their natural widths. Under the conditions of experiments performed in [3], in which electrons with an energy of 855 MeV fell on a silicon

crystal 525 μm thick at an angle of $\psi = 5$ mrad to the $\langle 111 \rangle$ axis, the σ value for the line corresponding to $g = 2\pi/a$ was $\sigma \sim 75$. Multiple scattering in these experiments caused substantial (larger than an order of magnitude) line broadening compared with the natural line width of parametric X-ray radiation.

N.F.Sh. thanks Professor H. Backe of the University of Mainz for discussions of measurements and interpretation of ultranarrow parametric X-ray radiation lines.

REFERENCES

1. M. L. Ter-Mikaelyan, Usp. Fiz. Nauk **171**, 579 (2001).
2. P. Rullhusen, X. Artru, and P. Dhez, *Novel Radiation Sources Using Relativistic Electrons* (World Scientific, Singapore, 1998).
3. H. Backe, G. Kube, and W. Lanth, *Electron-Photon Interaction in Dense Media*, Ed. by H. Wiedemann (Kluwer, Dordrecht, 2001), pp. 153–181.
4. G. M. Garibyan and Yan Shi, *X-ray Transient Radiation* (Akad. Nauk Arm. SSR, Yerevan, 1983).
5. A. I. Akhiezer and N. F. Shul'ga, *Electrodynamics of High Energies in Matter* (Nauka, Moscow, 1993).
6. I. M. Gel'fand and A. M. Yaglom, Usp. Mat. Nauk **11**, 77 (1956).
7. N. V. Laskin, A. S. Mazmanishvili, N. N. Nasonov, and N. F. Shul'ga, Zh. Éksp. Teor. Fiz. **89**, 763 (1985) [Sov. Phys. JETP **62**, 438 (1985)].
8. N. V. Laskin and A. I. Zhukov, Zh. Éksp. Teor. Fiz. **98**, 571 (1990) [Sov. Phys. JETP **71**, 318 (1990)].

Translated by V. Sipachev

JETP Letters, Vol. 76, No. 5, 2002, pp. 283–286. Translated from Pis'ma v Zhurnal Éksperimental'noĭ i Teoreticheskoĭ Fiziki, Vol. 76, No. 5, 2002, pp. 341–344.

Generating Intense Beams of Low-Energy Molecules

G. N. Makarov

Institute of Spectroscopy, Russian Academy of Sciences, Troitsk, Moscow region, 142190 Russia
e-mail: g.makarov@isan.troitsk.ru

Received July 31, 2002

A method for obtaining intense pulsed beams of molecules possessing low kinetic energies is proposed. The method is based on the formation of a cold pressure shock (shock wave) in an intense pulsed molecular beam interacting with a solid surface, which serves as a source of the secondary beam of low-energy molecules. The proposed method was successfully used to obtain intense beams of H_2, He, CH_4, and Kr molecules with kinetic energies not exceeding 10 meV, and H_2/Kr and He/Kr beams with kinetic energies of H_2 and He molecules below 1 meV. © *2002 MAIK "Nauka/Interperiodica".*

PACS numbers: 07.77.Gx; 79.20.Rf

1. Introduction. Intense molecular beams with a particle flux density of $\geq 10^{20}$ (sr s)$^{-1}$ and a kinetic energy in the interval from a few units to several tens of millielectronvolts are required for the experimental investigation of chemical reactions, elastic and inelastic collisions, and interactions of molecules with surfaces [1]. In recent years, such beams were also employed in experiments on the confinement of molecules in traps [2, 3].

A method most widely used for the obtaining of intense molecular beams is based on their separation by skimmers from gasdynamically cooled streams emitted by pulsed nozzles [4]. The kinetic energy of molecules in a beam is determined by the gas temperature T_0 reached before expansion through the nozzle:

$$\frac{1}{2}mv^2 = \frac{\gamma}{\gamma - 1}k(T_0 - T), \qquad (1)$$

where v is the established gas flow rate, m is the molecular mass, $\gamma = c_p/c_v$ is the ratio of specific heats, k is the Boltzmann constant, and T is the established temperature. For a gas at room temperature in the source, the kinetic energy of molecules in the beam varies, depending on the γ value, from ≅50–60 meV (for monoatomic gases) to ≥150–200 meV (for polyatomic molecules).

According to Eq. (1), obtaining low-energy molecular beams requires a gas in the source to be cooled. However, cooling the pulsed sources of molecular beams down to low temperatures is a difficult problem because the materials employed (in particular, plastics and elastomers) lose their elastic and plastic properties. Moreover, a decrease in the temperature leads to a significant drop in the gas pressure, which complicates the formation of gasdynamically cooled intense streams.

The beams of molecules possessing low kinetic energies (≤50 meV) are usually obtained with effusion sources either operating at room temperature or employing a gas cooled to liquid nitrogen temperature (for helium beams, down to liquid helium temperature) [1, 5]. The kinetic energy of molecules in such a beam is determined by the gas temperature in the effusion source ($E_{\text{kin}} \cong kT_0$). However, intensities of the molecular beams obtained by this method are relatively low (not exceeding 10^{16}–10^{17} (sr s)$^{-1}$). In addition, the velocities of molecules in such beams exhibit considerable scatter. Therefore, it is necessary to separate a low-energy component, which still reduces the beam intensity.

In this paper, a relatively simple method is proposed for obtaining intense pulsed beams of molecules with a kinetic energy variable from about 1 meV to several tens of millielectronvolts.

2. Description of method and experiment. According to the proposed method, low-energy pulsed molecular beams are produced using a pressure shock (shock wave) [6–8] generated as a result of interaction of an intense, gasdynamically cooled, pulsed molecular beam (or stream) with a solid surface. The essence of the process is illustrated in Fig. 1. In the experiment, an intense ($\geq 10^{21}$ (sr s)$^{-1}$), wide-aperture (divergence, $\omega \cong 0.05$ sr), pulsed molecular beam was incident onto a liquid-nitrogen-cooled copper heat exchanger, to which a duralumin multichannel metal plate with a thickness of $L = 4$ mm was fastened. The plate contained channels with a diameter of $d_0 = 0.5$ mm, arranged in a close-package pattern with a distance of 0.75 mm between the hole centers. The 8-mm-thick heat exchanger had a through channel of a converging cone shape, with input and output diameters of 11 and 9 mm, respectively. The distance from the nozzle outlet edge to the front surface of the multichannel plate was about 70 mm. In order to exclude the multichannel plate operation in the "transparency" mode, the plate was tilted relative to the beam axis by a small angle of $\alpha \cong d_0/L \cong 7°$.

0021-3640/02/7605-0283$22.00

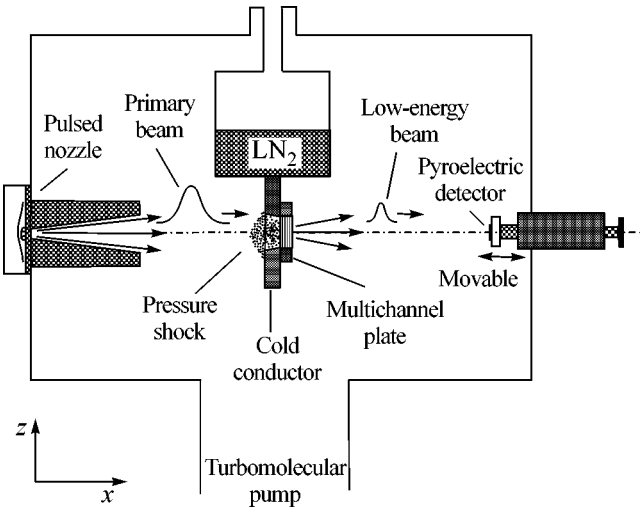

Fig. 1. Schematic diagram of the experimental setup.

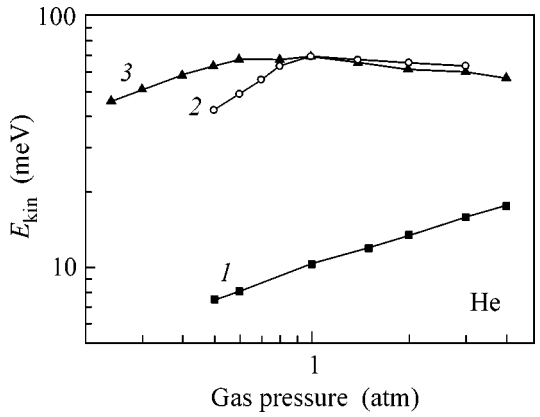

Fig. 2. Plots of the kinetic energy of molecules in a low-energy beam of He versus gas pressure in the nozzle (*1*) for a gasdynamically cooled beam, (*2*) for the absence of gas cooling in the shock wave region, and (*3*) for the primary molecular beam.

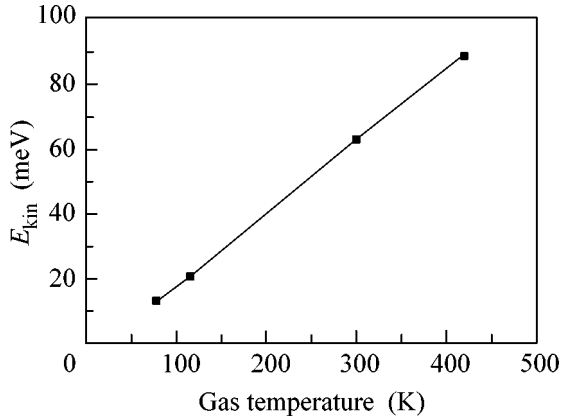

Fig. 3. Plot of the kinetic energy of molecules in a low-energy molecular beam of He versus gas temperature in the pressure shock region (He pressure in the nozzle, 2 atm).

When an intense supersonic molecular beam strikes the cooled plates, a cold pressure shock is formed in front of the plates and inside the channels [9, 10]. The characteristic size of this pressure shock region is on the order of the mean free path of molecules Λ [7, 8]. For $\Lambda_{eff} \geq d_0$ ($\Lambda_{eff} > \Lambda$ is the effective mean free path of molecules in the channels [1]), the gas inside the channels cools down to the wall temperature (i.e., approximately to liquid nitrogen temperature), so that the pressure shock generates a beam of low-energy molecules. The condition of $\Lambda_{eff} \geq d_0$ was nearly always realized under the experimental conditions studied. As a result, intense gasdynamically cooled molecular beams were obtained, with the kinetic energy of molecules determined by gas temperature in the pressure shock region (~77 K) according to formula (1). At a low pressure in the shock wave, when the gasdynamic flow conditions were not obeyed, the system operates in the effusion mode and the average velocity of molecules in the beam is close to the value for a gas at liquid nitrogen temperature (naturally, with an increased scatter of the velocities of molecules in the beam).

The experiments were performed using a pulsed nozzle of the current loop type [11] with an output diameter of 0.75 mm. The time of nozzle opening (pulse width at half-height) varied within ~70–100 μs, depending on the gas pressure and composition. The gas pressure in the nozzle was varied in the range from ≅ 0.1 to 7 at. The nozzle outlet had the shape of a cone with a total opening angle of 15° and a length of 35 mm. The molecular beam was formed in a vacuum chamber evacuated to a residual pressure of $\sim 1 \times 10^{-6}$ Torr by a turbomolecular pump. The number of molecules ejected from the nozzle per pulse depended on the gas pressure in the nozzle and varied from $\sim 8 \times 10^{15}$ to 2×10^{18}. A method for determining this value is described in detail elsewhere [12, 13].

The intensity and the velocity of molecules in the low-energy beams were experimentally studied as functions of the intensity and velocity of an incident beam and the gas temperature in the pressure shock region. The scatter of particle velocities (the degree of gas cooling) was determined in both incident and output beams. These measurements were performed by a time-of-flight (TOF) technique using a pyroelectric detector with a time resolution of ~3–5 μs [14, 15]. The TOF spectra of molecules, recorded at various distances from the nozzle, were used to determine the particle velocity and its scatter in the molecular beams.

3. Results and discussion. The experiments were performed with the molecular beams of H_2, He, CH_4, and Kr. In all cases, the above source generated the beams of molecules possessing low velocities. Figure 2 shows a plot of the kinetic energy of He molecules in a low-energy molecular beam versus gas pressure in the nozzle (curve *1*) in comparison to the analogous plots for the secondary beam measured in cases when the gas in the shock wave was not cooled ($T_0 \sim 300$ K) and for

Data on the velocities and energies of molecular beams

Gas composition and pressure (atm) in the nozzle		Primary beam		Low-energy beam	
		v, m/s	E_{kin}, meV	v, m/s	E_{kin}, meV
H_2	1.9	2950	91.7	1050	11.6
	0.6	2620	72.4	810	6.9
CH_4	2.0	1330	149.2	450	17.1
	0.6	1250	131.8	370	11.5
Kr	2.0	385	62.5	168	11.9
	1.0	360	54.7	130	7.1

the initial (primary) beam (curves *2* and *3*, respectively). As the intensity of the primary beam (i.e., the gas pressure in the nozzle) is reduced, the energy of molecules in the secondary (low-energy) beam significantly decreases, approaching the mean energy of He atoms at $T \cong 77$ K (~6.6 meV).

Figure 3 shows a plot of the kinetic energy of molecules in a He beam versus the gas temperature in the pressure shock, which was measured at a helium pressure of 2 atm in the nozzle. Note that, in the given temperature interval, the kinetic energy of molecules decreases somewhat more rapidly as compared to the linear law. This behavior is related to the fact that, under the experimental conditions studied, a decrease in the temperature was accompanied by a decrease in the gas pressure in the shock wave (i.e., in the source of the low-energy beam), which additionally decreased the secondary beam velocity.

The results of measurements of the average velocity and energy of molecules in the low-energy beams of H_2, CH_4, and Kr are presented in the table, in comparison to the analogous data for the initial (primary) beam. As can be seen, experiments under the conditions described above allowed the molecular beams of H_2 to be obtained with a kinetic energy of $E_{kin} \le 6.9$ meV, and the beams of CH_4 and Kr, with $E_{kin} \le 11.5$ and 7.1 meV, respectively. Note that the mean velocity of Kr atoms in such a beam is $v \cong 130$ m/s.

The experiments were also performed with mixed molecular beams of the H_2/Kr and He/Kr types (at a partial pressure ratio of 1:5 in both cases). At a gas pressure of 0.8 atm in the nozzle and a temperature of ≅77 K in the shock wave, the molecular beam velocity (~165 m/s) corresponded to kinetic energies of ≤0.3 and 0.6 meV for H_2 and He molecules in the beams, respectively.

Let us estimate the intensities of low-energy beams obtained by the proposed method, using the results of measurements for the molecular beams of He. According to the amount of gas consumed for a series of n pulses ejected from the nozzle (see, e.g., [12, 13]), the total number of He atoms emitted per pulse at a gas pressure of 2 atm in the nozzle is $\cong 7 \times 10^{17}$. Since the initial molecular beam pulse duration was ~100 μs and the beam divergence was $\omega \cong 0.05$ sr, the beam intensity was $I_1 \cong 1.4 \times 10^{23}$ (sr s)$^{-1}$. The low-energy molecular beam intensity was lower by a factor of 30–50 and amounted to $I_2 \ge 10^{21}$ (sr s)$^{-1}$. Therefore, intensities of the molecular beams obtained were four to five orders of magnitude greater as compared to those of the "standard" effusion beams. The concentrations of helium atoms in the initial beam and in the shock wave, estimated as described in [12, 13], were $N_1 \cong 2.5 \times 10^{16}$ cm^{-3} and $N_2 \cong 1 \times 10^{17}$ cm^{-3}.

Thus, the proposed method allows intense pulsed molecular beams to be obtained, with the kinetic energies of molecules in the range from 1 meV to several tens of millielectronvolts. It was demonstrated that the energy of molecules in such beams can be controlled by varying the initial (primary) beam intensity or the gas temperature in the shock wave. For the obtaining of low-energy molecular beams of He and H_2, a deeper gas cooling in the pressure shock regions can be achieved by using liquid helium. It should be noted that, using Kr as the carrier gas, it is possible to obtain beams of CO, N_2, NO, and O_2 molecules with energies not exceeding 2–3 meV.

The author is grateful to V.M. Apatin and A.N. Petin for technical assistance.

This study was partly supported by the Russian Foundation for Basic Research, project no. 00-03-33003.

REFERENCES

1. *Atomic and Molecular Beam Methods*, Ed. by G. Scoles (Oxford Univ. Press, New York, 1988).
2. S. K. Sekatskiĭ, Pis'ma Zh. Éksp. Teor. Fiz. **62**, 900 (1995) [JETP Lett. **62**, 916 (1995)].
3. R. T. Jongma, G. von Helden, G. Berden, and G. Meijer, Chem. Phys. Lett. **270**, 304 (1997).
4. W. R. Gentry, in *Atomic and Molecular Beam Methods*, Ed. by G. Scoles (Oxford Univ. Press, New York, 1988).
5. R. Feltgen, H. Kirst, K. A. Kohler, and H. Pauly, J. Chem. Phys. **76**, 2360 (1982).

6. Ya. B. Zel'dovich and Yu. P. Raizer, *Physics of Shock Waves and High-Temperature Hydrodynamic Phenomena* (Nauka, Moscow, 1966; Academic, New York, 1966).
7. L. D. Landau and E. M. Lifshitz, *Course of Theoretical Physics*, Vol. 6: *Fluid Mechanics* (Nauka, Moscow, 1986; Pergamon, New York, 1987).
8. G. N. Abramovich, *Applied Gas Dynamics* (Nauka, Moscow, 1991), Part 1.
9. G. N. Makarov and A. N. Petin, Pis'ma Zh. Éksp. Teor. Fiz. **71**, 583 (2000) [JETP Lett. **71**, 399 (2000)].
10. G. N. Makarov and A. N. Petin, Chem. Phys. Lett. **323**, 345 (2000).
11. W. R. Gentry and C. F. Giese, Rev. Sci. Instrum. **49**, 595 (1978).
12. G. N. Makarov and A. N. Petin, Zh. Éksp. Teor. Fiz. **119**, 5 (2001) [JETP **92**, 1 (2001)].
13. G. N. Makarov and A. N. Petin, Chem. Phys. **266**, 125 (2001).
14. V. M. Apatin, L. M. Dorozhkin, G. N. Makarov, and L. M. Pleshkov, Appl. Phys. B **29**, 273 (1982).
15. V. M. Apatin and G. N. Makarov, Zh. Éksp. Teor. Fiz. **84**, 15 (1983) [Sov. Phys. JETP **57**, 8 (1983)].

Translated by P. Pozdeev

JETP Letters, Vol. 76, No. 5, 2002, pp. 287–290. From Pis'ma v Zhurnal Éksperimental'noĭ i Teoreticheskoĭ Fiziki, Vol. 76, No. 5, 2002, pp. 345–348.

Coulomb Singularity Effects in the Tunneling Spectroscopy of Individual Impurities¶

P. I. Arseyev, N. S. Maslova, V. I. Panov, and S. V. Savinov

Department of Physics, Moscow State University, Moscow, 119899 Russia

Received June 7, 2002; in final form, July 4, 2002

Nonequilibrium Coulomb effects in resonant tunneling through deep impurity states are analyzed. It is shown that Coulomb vertex corrections to the tunneling transfer amplitude lead to power law singularity in the current–voltage characteristics. © *2002 MAIK "Nauka/Interperiodica".*

PACS numbers: 73.40.Gk

Localized states of individual impurity atoms and interacting impurity clusters can play the key role in tunneling processes in small size junctions and often determine the behavior of tunneling characteristics in STM/STS contacts. Now it is evident that in tunneling junctions of nanometer scale there exists nonequilibrium distribution of tunneling electrons which changes local density of states and tunneling conductivity spectra. Some interesting effects, such as resonance structure of tunneling conductivity inside the semiconductor band gap, the increased value of the observed band gap and nonequilibrium interaction of neighboring impurity atoms have been recently investigated experimentally and theoretically analyzed [1–4]. But all these effects are caused by local changes of the initial density of states in the contact area due to interactions of nonequilibrium particles. The modification of tunneling amplitude by the Coulomb interaction of conduction electrons in a metallic tip with nonequilibrium localized charges was ignored. It is shown in the present paper that corrections to the tunneling vertex caused by the Coulomb potential can also result in nontrivial behavior of tunneling characteristics and should be taken into account. One encounters effects similar to the Mahan edge singularities in the problem of X-ray absorption spectra in metals [5]. The effect is well pronounced if the tunneling rate from a deep impurity level to metallic tip γ_t is much larger than relaxation rate γ of nonequilibrium electron distribution at a localized state. This condition can be realized experimentally for a deep impurity state in the semiconductor gap. Direct tunneling from such states to semiconductor continuum states is strongly reduced due to the wide barrier formed by surface-band bending. The relaxation rate connected with electron–phonon interaction can be estimated to be of the order 10^8–10^{10} 1/s at low temperatures [6]. As to γ_t it is a parameter which can be varied in STM/STS experiments changing tip-sample separation. Since tip-sample separation is comparable with atomic scale, γ_t often exceeds the relaxation rate for deep impurity states. The typical experimental value of tunneling current 1 nA corresponds to $\gamma_t \simeq 10^{11}$–10^{12} 1/s [3]. As will be shown below for $\gamma_t \gg \gamma$, the impurity level becomes nearly empty when the value of applied bias voltage approaches the impurity energy. So the core hole Coulomb potential is suddenly switched on and the tunneling amplitude is changed. One might expect in this situation a power-law singularity in the current–voltage characteristics near the threshold voltage.

The system semiconductor—impurity state—metallic tip can be described by the Hamiltonian $\hat{H}$:

$$\hat{H} = \hat{H}_L + \hat{H}_R + \hat{H}_{\text{imp}} + \hat{H}_T + \hat{H}_{\text{int}}, \tag{1}$$

where

$$\hat{H}_R = \sum_{k\sigma} (\varepsilon_k - \mu) c^+_{k\sigma} c_{k\sigma},$$
$$\hat{H}_L = \sum_{p\sigma} (\varepsilon_p - \mu - eV) c^+_{p\sigma} c_{p\sigma} \tag{2}$$

describes the electron states in the metallic tip and the semiconductor, respectively; $c^+_{k\sigma}(c_{k\sigma})$ and $c^+_{p\sigma}(c_{p\sigma})$ describe creation (annihilation) of electron in states $(k\sigma)$ and $(p\sigma)$ in each bank of the contact.

$$\hat{H}_{\text{imp}} = \sum_{d\sigma} \varepsilon_d c^+_{d\sigma} c_{d\sigma} + U n_{d\sigma} n_{d-\sigma} \tag{3}$$

corresponds to a localized impurity state. We consider "one electron neutral impurity"—the impurity level is singly occupied at zero applied voltage due to the on-site Coulomb interaction. But in the case of large tunneling rate to the metallic tip, the on-site Coulomb repulsion of localized electrons can be omitted if we

¶This article was submitted by the authors in English.

analyze the behavior of tunneling current at the applied voltage close to the impurity energy ε_d, because in this situation the impurity state becomes nearly empty above the threshold value of the applied bias. Let us also point out that the Kondo regime is destroyed at Anderson impurity for the values of applied bias near the threshold [7, 8]. In this case the Kendo effect is not responsible for any unusual features of the tunneling characteristics.

Tunneling transitions from the impurity state to the semiconductor and the metal are described by the part

$$\hat{H}_T = \sum_{kp} (T_{kd} c^+_{k\sigma} c_{d\sigma} + T_{pd} c^+_{p\sigma} c_{d\sigma}) + \text{h.c.} \qquad (4)$$

Finally, part H_{int} includes the Coulomb interaction of the core (impurity) hole with conduction electrons in the metal:

$$\hat{H}_{\text{int}} = \sum_{kk'\sigma\sigma'} W_{kk'} c^+_{k\sigma} c_{k'\sigma} (1 - c^+_{d\sigma'} c_{d\sigma'}). \qquad (5)$$

Hamiltonian H_{int} appears as a many-particle interaction and describes rearrangement of conduction electrons in the potential of the hole, suddenly switched on by tunneling transition of the impurity electron. Since we are far from the Kondo regime it is sufficient to consider tunneling current in the lowest order in the tunneling amplitude T_{kd}. Scattering by the impurity hole Coulomb potential does not change electron spin. Thus, in the lowest order in T_{kd} we can consider renormalization of the tunneling amplitude independently for each spin—the same one for conduction and impurity electrons. It is also reasonable to use for simplicity an averaged value of screened Coulomb interaction describing *s*-wave scattering of conduction electrons by a deep hole $W_{kk'} = W$.

Edge singularities in the tunneling current can be analyzed by means of diagram technique for nonequilibrium processes. Using Keldysh functions $G^<$, the tunneling current can be determined as (we set charge $e = 1$)

$$I(V) = \text{Im}(J(V)), \quad J(V) = i \sum_{k,\sigma} \int d\omega T_{kd} G^{\sigma <}_{kd}, \quad (6)$$

where we have defined tunneling "response function" $J(V)$. If the Coulomb interaction is neglected, one can obtain the usual expression for this response function in the lowest order in T_{kd}:

$$J^0(V) = i \sum_{k,\sigma} \int d\omega T^2_{kd} (G^{\sigma <}_{kk} G^{\sigma A}_{dd} + G^{\sigma R}_{kk} G^{\sigma <}_{dd}). \qquad (7)$$

Substituting the corresponding expressions for the Keldysh functions [4] and performing integration over k we get

$$J^0(V) = \gamma_t \int d\omega \left[\frac{n^0_k(\omega)}{\omega + eV - \varepsilon_d + i(\gamma + \gamma_t)} + \frac{n_d(\omega)(-i(\gamma + \gamma_t))}{(\omega + eV - \varepsilon_d)^2 + (\gamma + \gamma_t)^2} \right], \qquad (8)$$

where the tunneling rate $\gamma_t = T^2_{kd} \nu$ and ν is the unperturbed density of states in the metallic tip. Kinetic parameter γ corresponds to relaxation rate of electron distribution at the localized state. In the suggested microscopic picture (Eq. (4)), this relaxation rate is determined by sufficiently small electron tunneling transitions from the impurity to the semiconductor continuum states $\gamma = T^2_{pd} \nu_p$. (In general γ can include different types of relaxation processes.)

Nonequilibrium impurity filling numbers $n_d(\omega)$ are determined from kinetic equations for the Keldysh functions $G^<$:

$$n_d(\omega) = \frac{\gamma n^0_p(\omega) + \gamma_t n^0_k(\omega)}{\gamma + \gamma_t}. \qquad (9)$$

As was explained in the Introduction for a deep impurity level, the relation $\gamma_t \gg \gamma$ is quite possible. Then $n^0_p(\varepsilon_d) = 1$, while $n_d(\varepsilon_d) \ll 1$ and there is actually a core hole in the impurity state. Thus, for low temperatures one can obtain from Eq. (8)

$$J^0(V) = \gamma_t \ln(|X|) + i \frac{\gamma_t \gamma}{\gamma + \gamma_t} \times \left[\text{arccot}\left(\frac{eV - \varepsilon_d}{\gamma + \gamma_t} \right) - \text{arccot}\left(\frac{-\varepsilon_d}{\gamma + \gamma_t} \right) \right], \qquad (10)$$

where

$$X = (eV - \varepsilon_d + i(\gamma + \gamma_t))/D) \qquad (11)$$

and D is the band width for electrons in metal.

The usual form of the tunneling current is of course reproduced from Eqs. (6), (8), (10).

Now let us consider renormalization of the tunneling amplitude and vertex corrections to the tunneling current caused by the Coulomb interaction between the impurity core hole and electrons in the metal. The many-particle picture strongly differs from the single-particle one near the threshold voltage. First-order corrections due to the Coulomb interaction (the first graph in Fig. 1a) have a logarithmic divergence at the thresh-

old voltage $eV = \varepsilon_d$, which is cut off by the finite relaxation and tunneling rates:

$$J^1(V) = i\sum_{k,\sigma}\int d\omega T_{kd}(-G_{kk}^{\sigma<}G_{dd}^{\sigma A}T_{kd}^{1++} + G_{kk}^{\sigma R}G_{dd}^{\sigma<}T_{kd}^{1--}). \quad (12)$$

Tunneling matrix elements are changed by the Coulomb interaction:

$$T_{kd}^{1--} = \sum_{k,\sigma}\int d\omega T_{kd}W(G_{kk}^{\sigma<}G_{dd}^{\sigma A} + G_{kk}^{\sigma R}G_{dd}^{\sigma<}). \quad (13)$$

If we look at Eqs. (7), (8), it becomes clear that logarithmic contribution comes from the first combination of the Green functions: $G_{kk}^{\sigma<}G_{dd}^{\sigma A}$. In what follows we retain only logarithmically large parts, assuming that $|\ln((\gamma + \gamma_t)/D)| \gg 1$, so only these combinations of the Green functions are the most important in perturbation series. Then from Eq. (13) we obtain that the tunneling amplitude contains logarithmic correction: $T_{kd}^{1--} = -T_{kd}L$, $T_{kd}^{1++} = -T_{kd}^{1--}$, where factor L is

$$L = (W\nu)\ln(X). \quad (14)$$

In high orders of perturbation, the expansion ladder graphs (Fig. 1a) are the simplest "maximally singular" graphs. But this is not the only relevant kind of graphs. If we look at the first graph in Fig. 1b, we notice, that a new type of "bubble" appears, which is logarithmically large for small "total" energy $(\omega + \omega_1)$. The important point is that the relevant region of integration over ω and ω_1 is the region of small ω. It is just this region which gives the essential contribution to logarithmic factor L in any other pair of $G_{kk}^{<}G_{dd}^{A(R)}$.

This means that the central bubble also contributes an additional logarithmic factor to the total result. In this situation, which is not new in physics, one should retain in the nth order of perturbation expansion the most divergent terms proportional to $(W\nu)^nL^{n+1}$. For the first time such a method was developed by Dyatlov *et al.* [9]. It was shown that for a proper treatment of this problem one should write down integral equations for the so-called parquet graphs (Fig. 1b), which are constructed by successive substitution of the simple Coulomb vertex for the two types of bubbles in perturbation series. These equations represent some extension of the ordinary Bethe–Salpeter equation and describe multiple scattering of conduction electrons by the core hole Coulomb potential in the two "most singular" channels. The integral equations can be solved with logarithmic accuracy, as was done, for example, by Nozieres [10, 11] for edge singularities in X-ray absorption spectra in metals.

The solution of the "parquet" equations contains nothing new in our problem. So we present the result

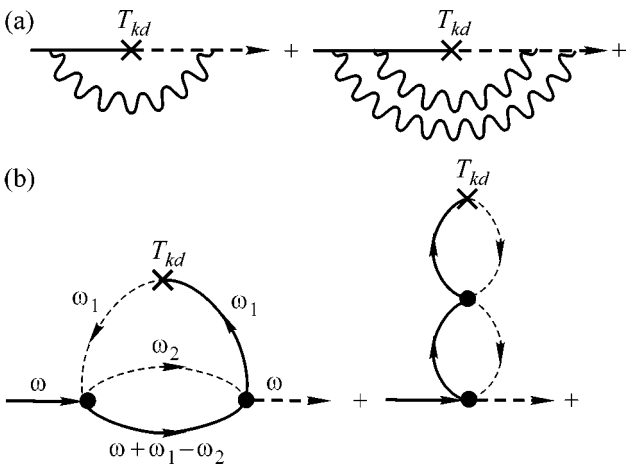

Fig. 1. Coulomb corrections to T_{kd}. Solid lines represent G_k and dashed lines, G_d. (a) Ladder approximation, (b) parquet graphs (Coulomb wavy lines are overdrawn as black circle vertexes).

without going into technical details. Summing up the most divergent graphs with logarithmic accuracy, one can obtain the following singular part of the response function [10]:

$$J(V) = \frac{\gamma_t(1 - \exp(-2L))}{2W\nu}. \quad (15)$$

Then the tunneling current near the threshold voltage can be expressed as

$$I(V) = \frac{\gamma_t}{2W\nu}\left[\frac{D^2}{(eV - \varepsilon_d)^2 + (\gamma_t + \gamma)^2}\right]^{W\nu}\sin(2W\nu\phi), \quad (16)$$

where $\phi = \operatorname{arccot}((eV - \varepsilon_d)/(\gamma + \gamma_t))$. If we consider a deep impurity state in the gap of the semiconductor (below the Fermi level) and positive tip bias voltage, then $\varepsilon_d < 0$, $eV < 0$. So, phase ϕ is a steplike function varying approximately from 0 to π, when the applied bias crosses the threshold $eV = \varepsilon_d$. Since we retain only the most logarithmically large terms in the tunneling current, Eq. (16) is valid only if $|eV - \varepsilon_d| \ll D$. In the absence of the Coulomb interaction (W = 0), this singular part reduces to the usual first-order contribution arising from the first term in Eqs. (7), (8).

In summary, if the tunneling rate to the metallic tip exceeds the relaxation rate of localized electrons, the Coulomb interaction of the core hole and the conduction electrons in the metal strongly modifies the tunneling transition amplitude and leads to (i) nonmonotonic behavior of the current–voltage characteristics; (ii) power-law singularity of the tunneling current and conductivity when the value of the applied voltage approaches the impurity level energy; (iii) the possibility of the current–voltage characteristics being rather

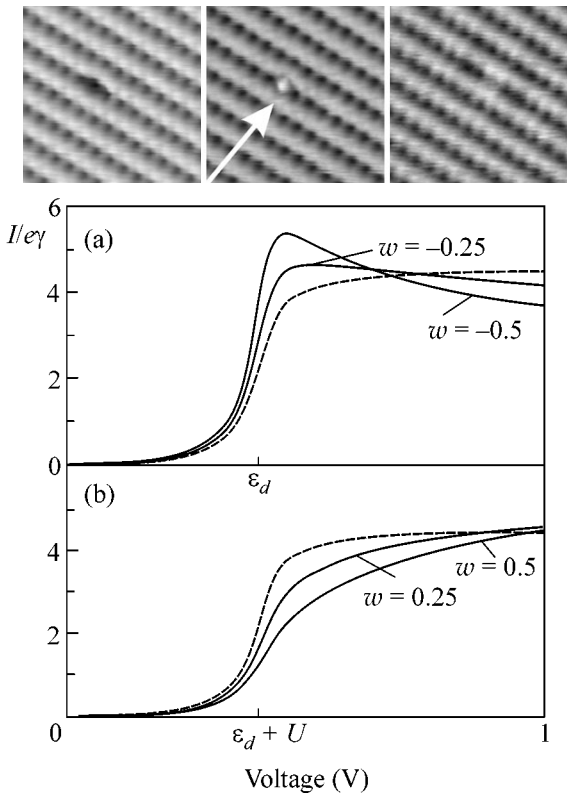

Fig. 2. Current–voltage curves for typical values of dimensionless Coulomb and kinetic parameters. Current is measured in dimensionless units $I/e\gamma$. (a) $w = W\nu < 0$, $\varepsilon_d = 0.4$ eV, (b) $w = W\nu > 0$, $\varepsilon_d + U = 0.4$ eV, $\gamma_t/\gamma = 3$, $\varepsilon_d/\gamma = 40$. Dashed lines correspond to W = 0. The experimental STM image of Cr impurity on the InAs (110) surface is shown in the inset for V = 0, V = 0.5(V), V = 1.5(V) in sequence.

asymmetric, because of different dependence of phase factor ϕ on the applied bias below and above the threshold value. Power law singular behavior of the tunneling current is sensitive to the values of the tunneling and relaxation rates, as well as to the value of the Coulomb interaction *W*. So, different exponents in power dependences of the tunneling current on the applied voltage can appear with changing tip-sample separation. Some current–voltage characteristics obtained for typical values of parameters are shown in Fig. 2.

It seems also possible to set up an experiment with negative impurity charge and negative tip voltage close to the value $\varepsilon_d + U$. In this case, $W > 0$ and the Coulomb corrections to the tunneling amplitude result in power-law behavior of the tunneling current with the opposite sign exponent in Eq. (16). The tunneling current is suppressed near the threshold, compared to the noninteracting case. This behavior is shown in Fig. 2b.

Experimental STM/STS investigations of deep impurity levels on semiconductor surfaces give evidence of the existence of the described effects. Some STM images demonstrate nonmonotonic dependence of tunneling current on applied bias voltage [1]. With increasing bias voltage, the impurity atom is "switched on" in the STM image—it appears as a bright spot. But further increase of the tunneling bias "extinguishes" the brightness of the impurity atom and it is seen as a dark spot in the STM image (see inset in Fig. 2). According to the present model, it can be explained by a decrease in the tunneling current caused by the Coulomb vertex corrections to the tunneling amplitude for some types of impurities.

We thank L.V. Keldysh for helpful discussions. This work was supported by the Russian Foundation for Basic Research, project nos. 00-15-96558 and 00-02-17759, and by the Nanostructure program.

REFERENCES

1. N. S. Maslova, V. I. Panov, V. V. Rakov, *et al.*, Appl. Phys. A **66**, 171 (1998).
2. N. S. Maslova, V. I. Panov, S. V. Savinov, *et al.*, Phys. Rev. B **60**, 2619 (1999).
3. P. I. Arseyev, N. S. Maslova, and S. V. Savinov, Pis'ma Zh. Éksp. Teor. Fiz. **68**, 299 (1998) [JETP Lett. **68**, 320 (1998)].
4. P. I. Arseev, N. S. Maslova, V. I. Panov, and S. V. Savinov, Zh. Éksp. Teor. Fiz. **121**, 225 (2002) [JETP **94**, 191 (2002)].
5. G. D. Mahan, Phys. Rev. **163**, 612 (1967).
6. O. Agam, N. S. Wingreen, and B. L. Altshuler, Phys. Rev. Lett. **78**, 1956 (1997).
7. Y. Goldin and Y. Avishai, Phys. Rev. B **61**, 16750 (2000).
8. A. Rosch, J. Kroha, and P. Wolfle, Phys. Rev. Lett. **87**, 156802 (2001).
9. I. T. Diatlov, V. V. Sudakov, and K. A. Ter-Martirosian, Zh. Éksp. Teor. Fiz. **32**, 767 (1957) [Sov. Phys. JETP **5**, 631 (1957)].
10. B. Roulet, J. Gavoret, and P. Nozieres, Phys. Rev. **178**, 1072 (1969).
11. P. Nozieres and C. de Dominicis, Phys. Rev. **178**, 1097 (1969).

JETP Letters, Vol. 76, No. 5, 2002, pp. 291–294. Translated from Pis'ma v Zhurnal Éksperimental'noĭ i Teoreticheskoĭ Fiziki, Vol. 76, No. 5, 2002, pp. 349–352.

Instability of the Magnetization Reversal Front in Superconductors with a Nonlinear Anisotropic Current–Voltage Characteristic

A. L. Rakhmanov[1], L. M. Fisher[2,*], A. A. Levchenko[3], V. A. Yampol'skii[3], M. Baziljevich[4], and T. H. Johansen[4]

[1] *Institute of Theoretical and Applied Electrodynamics, Russian Academy of Sciences, Moscow, 125412 Russia*
[2] *State Scientific Center GUP "All-Russia Electrotechnical Institute," Moscow, 111116 Russia*
* *e-mail: fisher@vei.ru*
[3] *Usikov Institute of Radiophysics and Electronics, National Academy of Sciences of Ukraine, Kharkov, 61085 Ukraine*
[4] *Faculty of Physics, University of Oslo, 0316 Oslo, Norway*

Received July 11, 2002

The instability of a magnetic flux flow in a system of vortices and antivortices in superconductors with a power (exponent m) anisotropic current–voltage characteristic was studied theoretically. It was shown that instability arose even at a comparatively weak anisotropy of the current-carrying properties of a superconductor if $m \gg 1$. The dispersion equation determining the dependence of the increment of instability growth on the wave number was derived and analyzed. © *2002 MAIK "Nauka/Interperiodica".*

PACS numbers: 74.25.Ha; 75.60.Jk; 74.60.Ec; 74.60.Ge

One of the most striking effects in the dynamics of vortex systems in second-kind superconductors discovered some ten years ago was the observation of a macroturbulent magnetic flux behavior at the magnetization reversal front, which separated regions with opposite directions of Abrikosov vortices [1–3]. In some interval of magnetic field and temperature values, the stationary picture of the distribution of vortices and antivortices became unstable. A disordered magnetic flux motion arose at the magnetization reversal front. This process rapidly developed in time and was accompanied by the appearance of channels of antivortex penetration into the region occupied by vortices. The annihilation of vortices and antivortices occurred at the front, and the process of macroturbulence soon ended with the complete disappearance of vortices. This phenomenon has an obvious analogy with turbulence in hydrodynamics, and its interpretation is therefore of general interest for physics.

An attempt at explaining macroturbulence was made in [4]. The instability was related to a heat wave, which was generated at the magnetization reversal front because of energy release in the annihilation of vortices and antivortices. Unfortunately, this mechanism can hardly be responsible for macroturbulence [5], because energy released in the annihilation of vortices in high-T_c superconductors is too low to cause noticeable heating.

A different instability mechanism suggested in [5] related its nature to well-defined anisotropy of the current-carrying properties of samples in the **ab** plane. The matter is that macroturbulence is only formed in $YBa_2Cu_3O_{7-\delta}$ single crystals and other 1–2–3 systems in which twin boundaries are always present. In our view, precisely this circumstance is of key importance for solving the problem of the nature of macroturbulence. Because of the presence of twin boundaries, vortices and antivortices move under the action of Lorentz forces along these "guiding" boundaries (the so-called guiding effect) toward each other at an angle of about 45° with respect to the magnetization reversal front. As a result, the tangential component of the velocity of vortices experiences discontinuity at the interface. As is known from classical hydrodynamics, the presence of tangential velocity discontinuities causes instability of liquid flow. This approach allowed certain macroturbulence peculiarities observed in experiments to be explained.

The hydrodynamic approximation taking into account anisotropy of viscous flow of vortices provides a basis for understanding macroturbulence [5]. The analysis performed in [5] was, however, based on the simplest approximation of a linear relation between the Lorentz force that acted on vortices and the velocity of vortices. This approximation corresponded to a linear current–voltage characteristic of the sample, which only existed in superconductors in the region of strong currents. It turned out that instability only arose at a very strong anisotropy of the viscosity coefficient. Clearly, a more correct description of instability required using a more realistic model of the viscous flow of vortices based on a nonlinear current–voltage

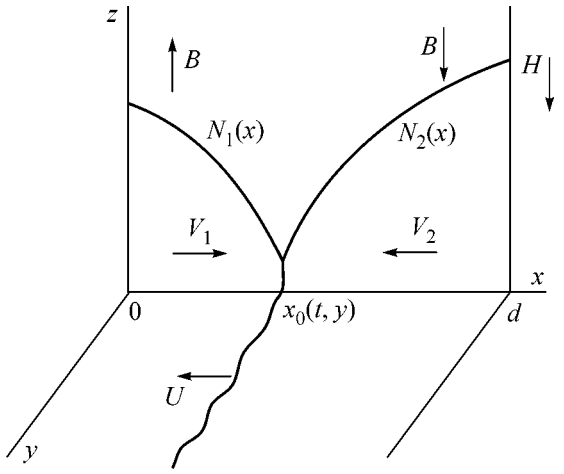

Fig. 1. Density distributions of vortices ($N_1(x)$) and antivortices ($N_2(x)$) in the right half of the plate ($0 < x \le d$).

characteristic. In this work, we theoretically studied the instability of the magnetization reversal front on the assumption that the current–voltage characteristic was a power function with exponent $m \ge 1$. We showed that, even at a comparatively weak anisotropy of the current–voltage characteristic, the flow of a system of vortices and antivortices in a superconductor became unstable.

Consider an infinite superconducting plate of thickness $2d$ placed into external magnetic field H oriented parallel to the sample surface along the z axis. The x axis is directed normally to the plate, and the origin $x = 0$ is situated in the center of the plate. Let magnetic field **H** first increase to the extent that the magnetic flux in the form of vortices completely fills the sample. Further, let this field decrease, pass through zero, and assume some negative value. Vortices with opposite magnetic flux directions (antivortices) then penetrate into the surface regions of the plate on both its sides. It is clear from the problem symmetry that it suffices to consider one (e.g., the right, $0 < x < d$) half of the sample. The geometry of the problem is schematically shown in Fig. 1.

Thermal activation causes slow magnetic flux flow. The annihilation of vortices and antivortices at the $x = x_0$ boundary separating the regions of their existence (see Fig. 1) results in additional penetration of antivortices from the plate surface in a constant magnetic field **H**. As a result, the total number of vortices in the center of the sample decreases, and the $x = x_0$ boundary slowly moves at rate U deeper into the sample (Fig. 1).

Let us denote the densities of vortices and antivortices by $N_1(x)$ and $N_2(x)$, respectively. The relation between vortex density $N_\alpha(x, y)$ ($\alpha = 1, 2$) and magnetic induction $B(x, y)$ in the corresponding superconductor region is obvious, $N_\alpha(x, y) = s_\alpha B(x, y)/\Phi_0$, where $s_1 = 1$ and $s_2 = -1$. The densities of vortices and antivortices should satisfy the continuity equation

$$\partial N_\alpha/\partial t + \mathrm{div}(N_\alpha \mathbf{V}_\alpha) = 0, \tag{1}$$

where $\mathbf{V}_\alpha$ are the hydrodynamic velocities of vortices and antivortices. The second equation for vortex densities $\mathbf{N}_\alpha$ and velocities $\mathbf{V}_\alpha$ is found using the current–voltage characteristic of the sample, which can be written as

$$J_X = \frac{1}{\varepsilon} J_c\left(\left|\frac{E_X}{E_0}\right|\right)^{1/m} \mathrm{sgn}\left(\frac{E_X}{E_0}\right),$$
$$J_Y = J_c\left(\left|\frac{E_Y}{E_0}\right|\right)^{1/m} \mathrm{sgn}\left(\frac{E_Y}{E_0}\right). \tag{2}$$

Here, **J** is the current density; **E** is the electric field; J_c is the critical current density, which is determined as J_Y at $E_Y = E_0$ (usually, E_0 is set equal to 1 μV/cm); $\varepsilon < 1$ (anisotropy parameter); and axes X and Y correspond to directions along and across twin boundaries (further, it is assumed that these boundaries make angles of 45° with axes x and y). The magnetic field dependence of the critical current density will be taken into account in the simplest form, namely, $J_c = A/N_\alpha$. The current density and electric field values are related to $\mathbf{N}_\alpha$ and $\mathbf{V}_\alpha$ by the known equations

$$\mathbf{J} = \frac{c s_\alpha}{4\pi} \mathrm{curl}\mathbf{N}_\alpha, \tag{3}$$

$$E_x = -\frac{N_\alpha s_\alpha \Phi_0}{c} V_{\alpha y}, \quad E_y = \frac{N_\alpha s_\alpha \Phi_0}{c} V_{\alpha x}. \tag{4}$$

Let us formulate the boundary conditions at the magnetization reversal front, which moves at rate **U**. According to the first condition, vortex and antivortex fluxes normal to the boundary are equal in magnitude but have opposite signs in a frame of reference that moves together with the front, that is,

$$N_1(\mathbf{V}_1 - \mathbf{U})_n + N_2(\mathbf{V}_2 - \mathbf{U})_n = 0. \tag{5}$$

The second condition takes into account the annihilation of vortices and antivortices. We assume that the rate of annihilation is proportional to the product of vortex densities,

$$N_1(\mathbf{V}_1 - \mathbf{U})_n = R N_1 N_2. \tag{6}$$

Lastly, the mean magnetic induction in the vicinity of the interface is set to zero,

$$N_1 = N_2. \tag{7}$$

This equality directly follows from Eq. (1) and from the observation that condition (7) is fulfilled at the initial time of the penetration of antivortices into the sample (at this time, $N_1 = N_2 = 0$).

To study the instability of the system under consideration, we must first determine the unperturbed (base)

distribution profiles $N_1(x)$ and $N_2(x)$. A simple analysis shows that, unfortunately, the problem does not have self-similar solutions corresponding to plane front motion $x = x_0(t)$ at a constant rate $U = \text{const} \neq 0$. We first find the stationary solution corresponding to zero velocity $U = 0$. Putting $\partial N_\alpha/\partial t = 0$ in Eq. (1) and using boundary conditions (5)–(7), we obtain

$$N_\alpha(x) = N_0\sqrt{1 + s_\alpha C(x_0 - x)/d},$$
$$C = \frac{8\pi\sqrt{2}dA}{c\Phi_0 N_0^2}\left[\frac{\sqrt{2}\Phi_0 R N_0^2}{cE_0(1+\varepsilon^m)}\right]^{1/m}. \quad (8)$$

In what follows, the constant C is assumed to be much larger than unity for the vortex density at the front, N_0, to be much lower than that at the boundary of the sample. Ignoring unity under the square root in Eq. (8) and using the boundary condition for the induction at the sample boundary, $N_2(d) = H/\Phi_0$, we obtain the following estimate for vortex density N_0:

$$N_0 = N_\alpha(x = x_0) \sim \left(\frac{H}{H_p}\right)\left(\frac{cE_0}{2^{(m+1)/2}\Phi_0 R}\right)^{1/2}, \quad (9)$$
$$H_p = (8\pi dA\Phi_0 R/c)^{1/2}.$$

Base profile (9) is observed if the front of magnetization reversal is immobile. In our problem, the interface moves. This movement changes the base profile. We will, however, assume that the rate of front movement is fairly low, $U \ll V_\alpha$, and that the base profile only slightly differs from Eq. (9).

The stability of the front can conveniently be analyzed using the dimensionless variables

$$n_\alpha = N_\alpha/N_0, \quad \tau = t/t_0, \quad t_0 = \frac{\Phi_0^2 N_0^3}{8\pi A E_0}, \quad (10)$$
$$\xi = x/L, \quad \zeta = y/L, \quad L = \frac{c\Phi_0 N_0^2}{4\pi\sqrt{2}A}, \quad r = \frac{RN_0^2\Phi_0}{\sqrt{2}cE_0}.$$

The normalization with respect to the time-dependent value $N_0 = N_\alpha(x_0(t))$ is admissible, because we assume the time of instability development to be small compared with the characteristic time of base profile changes.

The perturbed vortex density will be sought in the form

$$n_\alpha = n_\alpha^{(0)} + f_\alpha \exp[\lambda\tau + ik\zeta + p_\alpha(\xi - \xi_0(\tau))]. \quad (11)$$

The linearized boundary conditions are written at the perturbed front,

$$\xi = \xi_0(\zeta, \tau) = \xi_0(\tau) + \delta\xi \exp(ik\zeta + \lambda\tau), \quad (12)$$

with the unit normal vector $\mathbf{\nu} = (1, -ik\delta\xi(\zeta, \tau))$. It follows from boundary condition (7) that $\delta\xi = (f_1 - f_2)/2$.

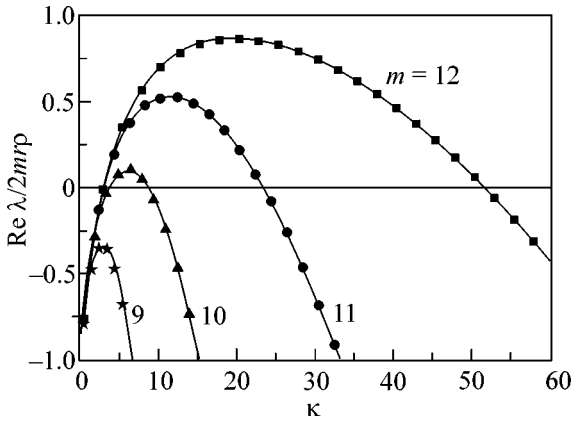

Fig. 2. $\mathrm{Re}\lambda(\kappa)$ dependence at $\varepsilon = 0.2$, $(u/r)^2 = 0.02$, and various parameter m values.

Equation (1) gives expressions for the p_1 and p_2 parameters. Substituting them and Eq. (11) into Eqs. (5) and (6) yields a system of two linear homogeneous algebraic equations for the f_1 and f_2 fluctuation amplitudes. Equating the determinant of the system to zero and ignoring the terms quadratic in velocity U, we obtain the dispersion equation for the dependence of increment λ on wave number k,

$$\lambda = mr\rho(\Omega^2 + 2i\kappa - 2 - \epsilon\kappa^2),$$
$$\kappa = k|u|/2mr\rho, \quad u = Ut_0/L, \quad (13)$$
$$\rho = (2r)^{1/m}, \quad \epsilon = \varepsilon^m(4mr/u)^2.$$

The Ω value is the root with $\mathrm{Re}\,\Omega > 0$ of the following algebraic equation:

$$\Omega^4 + \frac{m+2}{m}\Omega^3 - 2\frac{m-1}{m}\Omega^2 - \frac{4}{m}\Omega + i\kappa\left(\frac{m-1}{m}\Omega^2 + \Omega + 2\right) - \epsilon\kappa^2\left(\Omega^2 + \frac{2}{m}\Omega - i\kappa\frac{m-1}{m}\right) = 0. \quad (14)$$

The dispersion equation is written in the $\varepsilon \ll 1$ limit. Equations (13) and (14) only contain the ε anisotropy parameter raised to a power of m. Typical of 1–2–3 high-T_c superconductors far from T_c are the $\varepsilon \sim 0.1$–0.2 and $m \sim 10$ values.

Consider the solution of the dispersion equation. At $m = 1$, we obtain the same result as in [5], that is, if $\epsilon < \epsilon_c$ $(m = 1) \approx 0.0045$, the solutions to problem (13), (14) include $\lambda(\kappa)$ such that $\mathrm{Re}\,\lambda > 0$. The increment of instability increase $\mathrm{Re}\,\lambda$ then reaches a maximum at finite wave number k values. Clearly, this corresponds to breaking the magnetization reversal front with a characteristic spatial scale $\sim k^{-1}$. At $m > 1$, the behavior of the increment of instability growth is qualitatively similar. The dependences of $\mathrm{Re}\,\lambda$ on κ at various m values

and the characteristic anisotropy parameter value $\epsilon = 0.2$ are shown in Fig. 2 by way of illustration. For definiteness, the $(u/r)^2$ ratio (which should, according to the assumptions made above, be small) was set equal to 0.02. The figure shows that the spectrum of perturbations depends strongly on the exponent of the current–voltage characteristic. Instability is observed at $m > 10$; that is, $\mathrm{Re}\lambda > 0$ solutions that reach maxima at finite k values exist at fairly large m.

The results obtained in [5] were based on the model of linear viscosity anisotropy, which was not very realistic. In that model, instability began to develop only when fairly stringent requirements on the anisotropy parameter value were met. In the more realistic model used in this work, instability developed virtually irrespective of the anisotropy parameter ε value if the current–voltage characteristic of the superconductor was fairly steep; that is, if $m \gg 1$. The use of this model should allow theory to be quantitatively compared with the results of magnetooptical measurements and the experimental current–voltage characteristics of samples.

This work was financially supported by the Russian Federal Program on Superconductivity (contract 40.012.1.1.11.46), INTAS (project no. 01-2282), the Russian Foundation for Basic Research (projects nos. 00-02-17145 and 00-02-18032), and the Research Council of Norway.

REFERENCES

1. V. K. Vlasko-Vlasov, V. I. Nikitenko, A. A. Polyanskii, *et al.*, Physica C (Amsterdam) **222**, 361 (1994).
2. M. V. Indenbom, Th. Schuster, M. R. Koblischka, *et al.*, Physica C (Amsterdam) **209**, 259 (1993).
3. T. Frello, M. Baziljevich, T. H. Johansen, *et al.*, Phys. Rev. B **59**, R6639 (1999).
4. F. Bass, B. Ya. Shapiro, I. Shapiro, and M. Shvartser, Phys. Rev. B **58**, 2878 (1998).
5. L. M. Fisher, P. E. Goa, M. Baziljevich, *et al.*, Phys. Rev. Lett. **87**, 247005 (2001).

Translated by V. Sipachev

JETP Letters, Vol. 76, No. 5, 2002, pp. 295–298. Translated from Pis'ma v Zhurnal Éksperimental'noĭ i Teoreticheskoĭ Fiziki, Vol. 76, No. 5, 2002, pp. 353–356.

The Special Features of the Ground State in $CeAl_3$

V. N. Lazukov[1, *], P. A. Alekseev[1], N. N. Tiden[1], K. Bek[2], E. S. Klement'ev[1, 2], and I. P. Sadikov[1]

[1] *Russian Research Centre Kurchatov Institute, pl. Akademika Kurchatova 1, Moscow, 123182 Russia*

* *e-mail: lvn@isssph.kiae.ru*

[2] *Laboratory of Neutron Scattering, ETHZ, Villigen, PSI, Switzerland*

Received July 12, 2002

The temperature (3–60 K) and transferred momentum (0.3–2.3 $Å^{-1}$) dependences of the intensity of quasi-elastic magnetic neutron scattering were studied for the polycrystalline heavy-fermion $CeAl_3$ compound to elucidate the special features of its ground state. Transferred momentum variations caused oscillations of the intensity of quasi-elastic magnetic neutron scattering, which was evidence of magnetic correlations in the *f*-electron subsystem occurring in a fairly wide temperature range. *© 2002 MAIK "Nauka/Interperiodica".*

PACS numbers: 71.27.+a

The scale of interactions between 4*f* electrons and the crystal electric field in heavy-fermion compounds as a rule noticeably exceeds that of hybridization with conduction electrons. It is therefore usually assumed that hybridization only enhances the relaxation of crystal electric field excitations and manifests itself in physical properties only at low temperatures comparable to the Kondo temperature (T_K). For instance, according to the recent work [1], the crystal field effects on the spectrum of magnetic excitations are limited to the situations when the crystal electric field splitting $-\Delta_{CF}$ is smaller than or equal to T_K. If $\Delta_{CF} > T_K$, the only energy scale is T_K; that is, the role played by the crystal field effects then reduces to changes in the degree of degeneracy of the ground state. A detailed study of the spectra of magnetic excitations of $CeAl_3$ ($T_K \approx 0.5$ meV) [2] (where we have $\Delta_{CF} \gg T_K$) at low temperatures by inelastic neutron scattering, however, gave evidence of strong changes in both the intensity and energy of the transition between the ground and the first excited levels of the ground multiplet, which was split in the crystal electric field. It was found that the transition energy ($E \approx 6$ meV) began to gradually grow as temperature decreased below the Δ_{CF} scale value. A further increase in temperature to $T \sim T_K$ accelerated this growth. The intensity of the transition remained approximately constant and even decreased at $T \sim T_K$ in spite of an obvious increase in the population of the ground state, which accompanied temperature decrease.

Another peculiarity of the spectra of magnetic excitations of $CeAl_3$ was the presence of noticeable quasi-elastic scattering at low temperatures [3], although the ground state of $CeAl_3$ in the crystal electric field was the $|\pm 3/2\rangle$ doublet, in which quasi-elastic transitions were forbidden in the dipole approximation. The quasi-elastic signal observed at $T < T_K$ in heavy-fermion systems is usually treated as a consequence of the relaxation of 4*f* electron spins on conduction electrons caused by the Kondo effect. That is, the conclusion can be drawn that quasi-elastic scattering at $T < T_K$ reflects the properties of the new, so-called Kondo, ground state rather than being related to magnetic dipole transitions between 4*f* electron states in the crystal electric field. Nevertheless, the deviations from the single-ion behavior specified above were observed in [2] at substantially higher temperatures, that is, starting with $T \sim \Delta_{CF}$, although the quasi-elastic signal proper was not studied in detail.

To summarize, the experimental results described above contradict the fairly popular description of the special features of the spectrum of magnetic excitations in heavy-fermion systems in which a single characteristic energy scale ($\sim T_K$) is used. This prompted us to undertake a detailed study of the temperature and momentum transfer dependences of the intensity of quasi-elastic magnetic neutron scattering in the temperature range $T_K \le T \le \Delta_{CF}$. Our goal was to shed light on the roles played by Kondo scattering and crystal field effects in the formation of the ground state of heavy-fermion systems.

We used the same polycrystalline $CeAl_3$ and $LaAl_3$ samples as in [2]. The quasi-elastic magnetic neutron scattering spectra of polycrystalline $CeAl_3$ were measured on a FOCUS time-of-flight spectrometer with the use of a SINQ source of neutrons (Paul Scherrer Institute, Switzerland) in the temperature range 3–60 K. The initial neutron energy was $E = 3.1$ meV, and the resolution at the elastic line was $\Delta E = 0.06$ meV. The interval of neutron scattering angles (2θ) was 10°–130°, which corresponded to ~0.3–2.3 $Å^{-1}$ momenta transferred by neutrons. Each sample weighed ~20 g. The transmission of $CeAl_3$ was higher than 90%. The characteristic

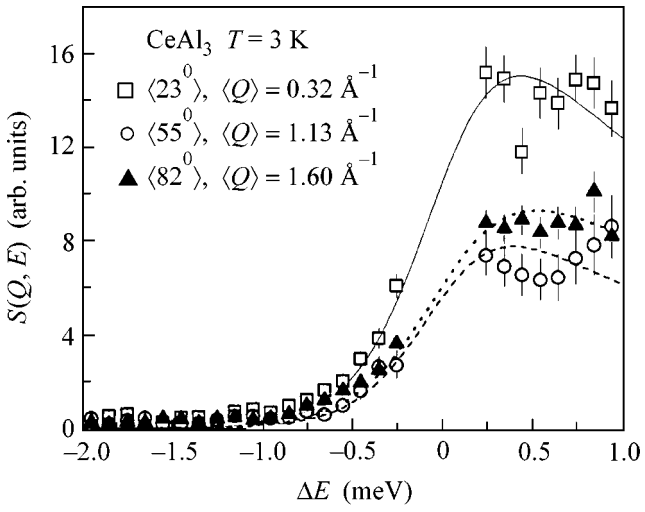

Fig. 1. Quasi-elastic magnetic neutron scattering spectra of $CeAl_3$ at $T = 3$ K for mean transferred momenta (Q) □, 0.32; ○, 1.13; and ▲, 1.60 Å^{-1}. Lines are fitted curves.

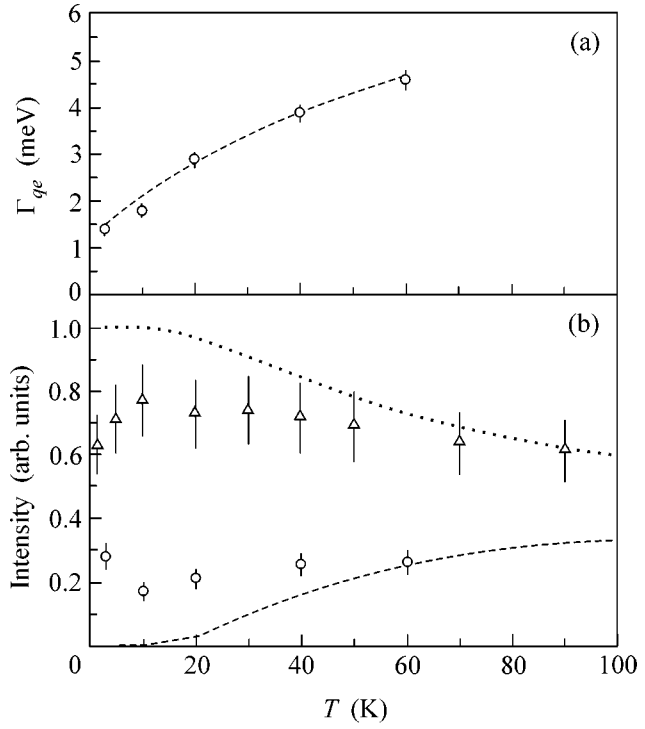

Fig. 2. (a) Temperature dependences of the FWHM (Γ_{qe}) of quasi-elastic magnetic neutron scattering by $CeAl_3$: open circles (this work) and dashed line (data from [3]). (b) Integral intensity of ○, quasi-elastic magnetic neutron scattering and △, inelastic magnetic neutron scattering [2]. The dashed and dotted lines in Fig. 2b are the calculated results obtained in the single-ion approximation; see text for details.

time of measurements at one temperature was ~20 h. Measurements on $LaAl_3$ were used to estimate phonon scattering and background. A comparison of the neutron spectra of $CeAl_3$ and $LaAl_3$ showed that the phonon component in the spectrum of $CeAl_3$ was much weaker than the contribution of magnetic scattering under our experimental conditions; this component was therefore ignored in the further analysis. The effectiveness of detectors was calibrated against a vanadium reference.

Some of the experimental spectra obtained at $T = 3$ K are shown in Fig. 1. The mean angle values (transferred momenta) in this figure were found by averaging over a ±5° (±0.1 Å^{-1}) interval. Note that the intensity of quasi-elastic magnetic neutron scattering varied nonmonotonically as the transferred momentum increased (compare Q = 1.13 and 1.60 Å^{-1}). The temperature dependence of quasi-elastic magnetic neutron scattering was obtained by summing the spectra recorded at all angles. The shape of the quasi-elastic magnetic neutron scattering spectrum line was approximated by a Lorentz function multiplied by a temperature factor. The experimental data on the temperature dependence of the width of quasi-elastic scattering closely coincided with those obtained in [3] (Fig. 2a).

The integral intensity of quasi-elastic magnetic neutron scattering was calculated from the experimental width and the amplitude of the Lorentz function. The width of quasi-elastic magnetic neutron scattering changed as temperature varied, and the integral intensity was therefore obtained by integrating the spectrum in the energy range of –2 meV to $E = 10\Gamma(T)$ [where $\Gamma(T)$ is the width of the spectrum at half-height], that is, to E of 15 to 40 meV depending on temperature. The temperature dependence obtained is shown in Fig. 2b. The same figure contains the data from [2] on the intensity of the $|\pm 3/2\rangle \longrightarrow |\pm 1/2\rangle$ transition and the calculated temperature dependences of the intensities of the inelastic and quasi-elastic peaks. These dependences were obtained for the single-ion model of crystal electric field effects taking into account the probabilities of transitions and changes in level populations under temperature variations. The experimental spectra were not absolutized, and the data from [2] were therefore compared with the experimental values by referencing the latter to the calculated results. The referencing was performed for the data obtained at the highest temperature ($T = 60$ K for quasi-elastic magnetic neutron scattering).

Note that the deviations from the single-ion calculations of both inelastic and quasi-elastic components are observed at temperatures commensurate with Δ_{CF} and noticeably increase at about $2T_K$. Importantly, the intensity of the quasi-elastic component decreases; that is, a new ground state is formed. The conclusion can be drawn that the formation of this new ground state begins at $T \sim \Delta_{CF} \gg T_K$ rather than at $T \sim T_K$.

The anomalies observed in the temperature dependence of the intensity of the $|\pm 3/2\rangle \longrightarrow |\pm 1/2\rangle$ transition were explained in [4] by strong anisotropic exchange interaction specific to the Kondo systems. This interaction decreases the lattice symmetry because of a dynamic distortion of the environment of the rare-earth metal ion and therefore changes the symmetry of the *f*-electron ground state Hamiltonian. As a result, the "pure" states in the crystal electric field transform into mixed states; for instance, the $|\pm 3/2\rangle$ state transforms into $\alpha|\pm 3/2\rangle + \beta|\pm 1/2\rangle$, which decreases the intensity of the transition under consideration. The anomalous temperature dependence of quasi-elastic magnetic neutron scattering can, we believe, be explained in a similar way (by the $|\pm 1/2\rangle$ "impurity" state).

The momentum transfer dependence of the intensity of quasi-elastic magnetic neutron scattering was studied for the spectra recorded at $T = 3$, 10, and 40 K, see Fig. 3. The form factor of the Ce^{3+} ion is shown by the dashed line in this figure. At $T = 3$ K, the intensity oscillates as a function of the transferred momentum with a period of ~1.0 ± 0.2 Å. The amplitude of oscillations noticeably decreases as temperature increases (T = 10 K), and, at $T = 40$ K, this amplitude becomes comparable with measurement errors. It follows that we obtained experimental evidence of the existence of *f*–*f* correlations in a fairly wide temperature range. As concerns the single-ion behavior, it is established for Ce ions at temperatures close to or higher than ~40 K, which is much higher than T_K. Note that the temperature range of intensity (that is, form factor) oscillations coincides with the temperature range of deviations from the "single-ion" inelastic peak parameters.

One of the possible approaches to describing the ground state of a heavy-fermion system is in treating this state as a spin liquid-type state with resonating valence bonds [5, 6]. The main property of such a state is the fact that the system of localized spins transforms at low temperatures to a half-filled band of spin excitations with a width of order T_K with the excitations of the spin liquid described by the Fermi statistics [7]. The calculated results obtained using this model [7] predict the appearance of oscillations in the dependence of the intensity of quasi-elastic magnetic neutron scattering on the transferred momentum. These oscillations "survive" even in polycrystalline samples. According to the model, the period of oscillations is related to the distance between cerium ions ($\kappa = 2\pi/d$, where κ is the period of oscillations and d is the distance between the ions that form resonating valence bonds). The approximation of the experimental data by the equations from [7] showed that the best description of these data was attained at $d = (6.5 \pm 1.3)$ Å (see Fig. 3, solid line), which coincided with the distance between Ce ions, that is, the lattice parameter **a**. This means that the model suggested in [7] predicts ions with resonating valence bonds to be situated at hexagonal lattice sites along axis **a**.

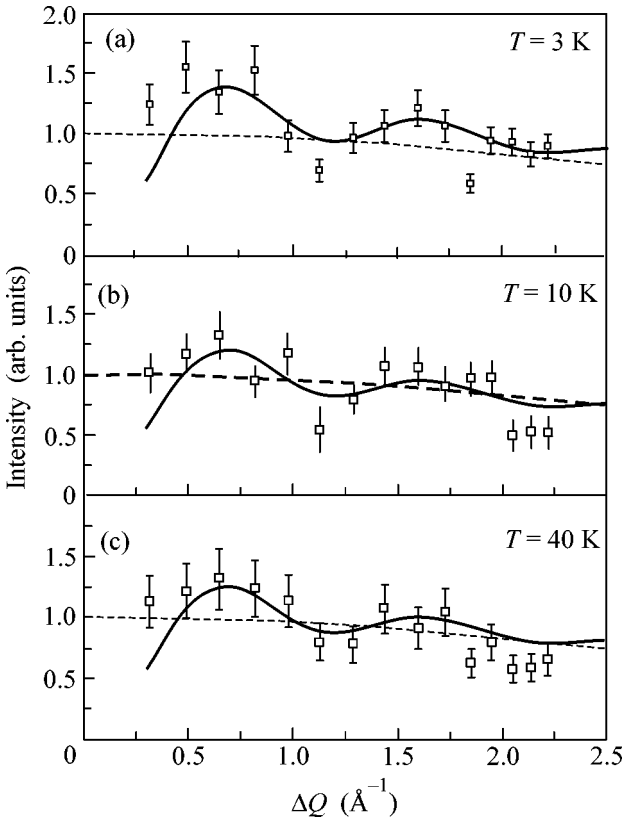

Fig. 3. Momentum transfer dependences of the intensity of quasi-elastic magnetic neutron scattering by $CeAl_3$ obtained at $T = 3$, 10, and 40 K. The form factor of Ce^{3+} is shown by the dashed lines. The solid lines were obtained in calculations by the model suggested in [7] with distance d = 6.55 Å between Ce ions.

To summarize, the most important results of this work are as follows. First, we observed interrelation between variations in the intensity of the inelastic and quasi-elastic components of the spectrum of magnetic excitations. Secondly, we showed the existence of spin correlation effects in heavy-fermion compounds in a fairly wide temperature range ($\sim\Delta_{CF}$); these effects became noticeably stronger at temperatures of about T_K. This led us to conclude that the temperature evolution of the spectrum of magnetic excitations in a heavy-fermion system was determined by two rather than one physically significant energy parameters, namely, T_K and Δ_{CF}. Note that the results obtained do not contradict the description of the ground state of a heavy-fermion system as a spin liquid-type state with resonating valence bonds and the spectrum of spin-liquid excitations that obeys the Fermi statistics [6].

The authors thank A.S. Mishchenko for fruitful discussions and valuable comments and D. Rubio for help with measurements. This work was financially supported by the Russian Foundation for Basic Research

(project no. 00-15-96712) and the State Scientific-Technical Program "Topical Areas in the Physics of Condensed Matter."

REFERENCES

1. A. Tomiyama, S. Suga, and A. Okiji, Phys. Rev. B **63**, 024407 (2001).
2. P. A. Alekseev, W. Buhrer, V. N. Lazukov, *et al.*, Physica B (Amsterdam) **217**, 2416 (1996).
3. A. P. Murani, K. Knorr, K. H. J. Buschow, *et al.*, Solid State Commun. **36**, 523 (1980).
4. A. S. Mishchenko, Pis'ma Zh. Éksp. Teor. Fiz. **66**, 460 (1997) [JETP Lett. **66**, 487 (1997)].
5. G. Baskaran, Z. Zou, and P. W. Anderson, Solid State Commun. **63**, 973 (1987).
6. K. A. Kikoin, M. N. Kiselev, and A. S. Mischenko, Zh. Éksp. Teor. Fiz. **112**, 729 (1997) [JETP **85**, 399 (1997)].
7. A. S. Mishchenko, Pis'ma Zh. Éksp. Teor. Fiz. **68**, 480 (1998) [JETP Lett. **68**, 514 (1998)].

Translated by V. Sipachev

JETP Letters, Vol. 76, No. 5, 2002, pp. 299–301. Translated from Pis'ma v Zhurnal Éksperimental'noĭ i Teoreticheskoĭ Fiziki, Vol. 76, No. 5, 2002, pp. 357–360.

Temperature-Induced Orientational Transition of Nematics on the Surface of a Ferroelectric Crystal

A. M. Parshin*, V. A. Gunyakov, and V. F. Shabanov

Kirenskii Institute of Physics, Siberian Division, Russian Academy of Sciences, Krasnoyarsk, 660036 Russia

**e-mail: parshin@akadem.ru*

Received July 10, 2002

A temperature-induced orientational transition is investigated in a mixture of nematic liquid crystals on the surface of a cleavage of a ferroelectric triglycine sulfate crystal. The transition has been observed by the variation of the polarized absorbance components of a dye introduced into the nematic matrix with increasing temperature. The reorientation of molecules in the liquid crystal volume confined by solid walls is due to competition between dispersion and polar forces at the surface and the decrease in the electric field of the substrate up to its complete disappearance at the ferroelectric Curie point. © *2002 MAIK "Nauka/Interperiodica".*

PACS numbers: 61.30.Gd; 64.70.Md; 77.84.Nh

The alignment of liquid crystal molecules confined by solid walls can be due to the competition of two or more independent factors favorable to homeotropic or planar texture [1]. If the competing factors differ in their temperature dependence, an orientational transition from one texture to the other can take place. A transition from planar to homeotropic alignment with varying temperature under conditions of a competition between van der Waals and short-range anchoring forces on the surface was observed previously [2]. The competition of polar and dispersion van der Waals forces of the substrate also favors the orientational transition [3]. At the same time, the electric field of the substrate substantially affects the alignment of the liquid crystal because of its dielectric anisotropy and enhances the polar effects at the confining surfaces [4]. The competing effect of dielectric, polar, and dispersion forces can be effectively observed on the orienting surfaces of ferroelectrics. The spontaneous polarization field of a ferroelectric single crystal depends on temperature and vanishes at the point of its phase transition to a nonpolar state. If the liquid crystal is chosen so that its temperature of the transition to an isotropic liquid is above the Curie point, the alignment of the nematic can be traced until the electric field of the substrate completely disappears. The polar and surface polarization effects on the energy of nematic anchoring to the ferroelectric surface were discovered recently [5].

In this work the behavior of a mixture of nematic liquid crystals is studied on the surface of a cleavage of a ferroelectric triglycine sulfate (TGS) crystal. An orientational transition in the bulk of the liquid crystal layer due to variations of the competing forces at the surface with temperature is reported.

Polar and nonpolar substrates were used in the experiment for orienting liquid crystals. Areas of TGS cleavages containing "–" domains served as polar substrates. A liquid crystal was placed in the space between two coaxially oriented cleavages [6] separated by wire spacers 20 μm in diameter. Mixture B ((2/3) MBBA + (1/3) EBBA) was used as the liquid crystal in order to extend the temperature range of the existence of the mesophase [7]. An observation using a polarization microscope demonstrated that the mixture existed as a nematic phase up to 51.5°C, that is, above the ferroelectric phase transition temperature (49°C). With the aim of visualizing the orientational effects under conditions of the intrinsic birefringence of the substrates, the anthraquinone dye KD-10 [6] was added to the mixture in the amount of 0.3 wt %, whose absorption band maximum coincided with the He–Ne laser wavelength (λ = 632.8 nm). Observations by polarization microscopy led to the conclusion that the nematic mixture is in a planar alignment along the crystallographic axis *c* of TGS. Absorption spectra $D_\parallel$ and $D_\perp$ of the KD-10 dye in the nematic phase of mixture B at a fixed temperature (23°C) are presented in Fig. 1. The large value of the dichroic ratio $D_\parallel/D_\perp = 7$ at the He–Ne laser wavelength provides the possibility of reliably observing the orientational effects. TGS cleavage plates made a small contribution to polarized absorbance components. This contribution was determined in samples that did not contain a liquid-crystal mixture and a dye and was taken into account in the experiment. The spectrum was obtained on an SF-20 spectrophotometer connected to a computer. Nonpolar substrates were glass plates treated by depositing a polymer film of poly(vinyl alcohol) on them. It is known [8] that such a treatment gives a nonpolar surface layer and provides a homogeneous alignment of nematics. The substrates were oriented uniaxially (that is, the directions of their easy orientation axes coincided) and were separated by Teflon spacers 20 μm thick. Mixture B with the KD-10 dye was poured in the gap between the substrates in the isotropic phase.

0021-3640/02/7605-0299$22.00

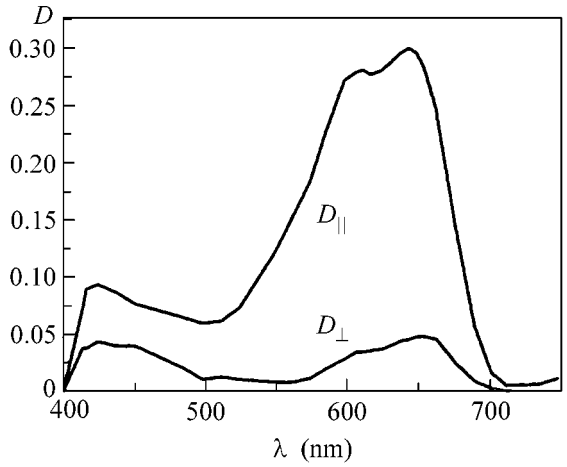

Fig. 1. Polarized absorption spectra $D_\parallel$ and $D_\perp$ of the KD-10 dye in nematic mixture B between TGS cleavages in a 20-μm gap at a temperature of 23°C.

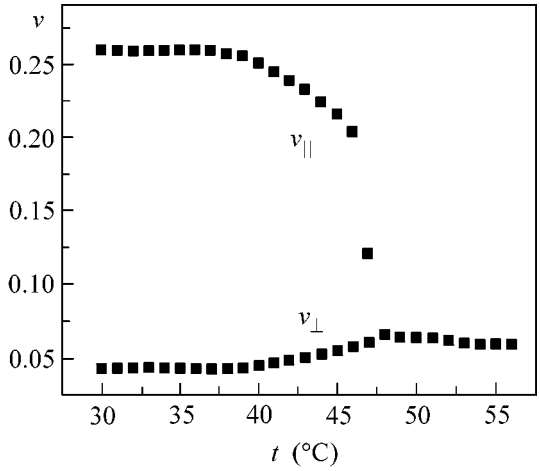

Fig. 2. Absorbance components $\nu_\parallel$ and $\nu_\perp$ of the KD-10 dye at the He–Ne laser wavelength in nematic mixture B between two polar surfaces of TGS cleavages in a 20-μm gap as functions of temperature.

The orientational texture of the liquid crystal mixture was studied by placing the samples in a thermostated cell. The temperature was scanned by a thermostat and was measured by a copper–constantan thermocouple. A He–Ne laser beam passed through the sample so that the direction of its polarization coincided with the director *n* of the nematic mixture and the crystallographic axes of the TGS plates. The intensity $I_\parallel$ of the modulated signal was taken from a photodiode and was measured by a selective nanovoltmeter. Next, the sample was rotated around the laser beam through 90°, and the temperature dependence of $I_\perp$ was recorded. The magnitude of I_0 corresponded to the intensity of the laser radiation passed through the sample area free of the liquid crystal mixture. The experimental procedure with the use of laser radiation allowed the state of a sample to be controlled by a polarization microscope while scanning the temperature so as to exclude the possible motion of domain walls on TGS cleavage surfaces [9]. The mixture absorbance components corresponding to the dye absorption band maximum for the light polarization directions parallel and perpendicular to the director were calculated by the equations $\nu_\parallel = \log(I_0/I_\parallel)$ and $\nu_\perp = \log(I_0/I_\perp)$ [7].

The absorbance components $\nu_\parallel$ and $\nu_\perp$ of the dye at the He–Ne laser wavelength are given in Fig. 2 as functions of temperature for nematic mixture B on polar surfaces. The experimental data in Fig. 2 demonstrate a significant decrease in $\nu_\parallel$ and an insignificant increase in $\nu_\perp$ in the vicinity of the ferroelectric phase transition. The components become equal on the transition of TGS to the nonpolar state (49°C). The temperature dependence of $\nu_\parallel$ and $\nu_\perp$ is shown in Fig. 3 for mixture B on nonpolar substrates. The curves draw closer together up to the point of the phase transition of the nematic mixture to the isotropic liquid (51.5°C). The difference in the run of the polarized absorbance components on polar and nonpolar surfaces points to an orientational effect, which accompanies the decrease in the order parameter of the liquid crystal with increasing temperature. The $\nu_\parallel$ and $\nu_\perp$ components on polar substrates are equal to each other above the point of the phase transition of the ferroelectric to the nonpolar state, in which the electric field of the substrate disappears, but below the point of the phase transition of the nematic mixture to the isotropic liquid, up to which this mixture retains its liquid crystal properties. This fact allows the conclusion that the nematics undergo an orientational transition from the planar to homeotropic texture.

In order to analyze the experimental data, let us consider processes at the boundary of the liquid crystal layer. On the TGS cleavage surface, the electric field of the spontaneous polarization of the ferroelectric "packs" the molecules of the nematic mixture, because of its negative dielectric anisotropy, in the substrate plane [9]. The field may turn out to be nonuniform across the thickness of the polarized layer of the liquid crystal λ_D with the average dielectric constant ε and to make a contribution to the surface energy proportional to the quadrupole density *q* [9] and the density σ of charges adsorbed on the surface [4]. The total contribution of the electric field to the surface energy, depending on the deflection angle θ of the liquid crystal director from the normal to the surface, was $f_e = (-\pi\Delta\varepsilon\sigma\lambda_D/\varepsilon^2 + 4\pi q/\varepsilon)\cos^2\theta) = w_e\cos^2\theta$ [4]. Van der Waals dispersion forces of the substrate favors the planar texture, because these forces are responsible for the difference in the alignment of nematics on the "+" and "–" domains of TGS [9]. The anisotropic part of the surface energy for dispersion forces, without taking into account correlations between molecular orientations and assuming the equality of the order parameter in the bulk and at the surface of the liquid crystal cell, can be represented in the form $f_d = w_d\cos^2\theta$ [3]. Thus,

the contributions of the electric field and dispersion forces to the surface energy of nematics have the same angular dependences. In addition, these forces give rise to unidirectional moments on the surface. The temperature dependences of the spontaneous polarization vector of the ferroelectric [10] and the order parameter of nematics on glass surfaces [11] qualitatively coincide and cannot generate the reorientation threshold of the liquid crystal [1]. These features allow us not to consider the competition of the given factors in our experiment. At the same time, the asymmetric action of the liquid crystal–solid interface and the character of the interaction of the ends of molecules with the TGS cleavage surface [9] may give rise to a polar moment favorable to the homeotropic alignment of nematics. The surface induces a polar order parameter, which contributes to the surface energy $f_p = -w_p \cos\theta$ [3]. The coefficient w_p also takes into account surface polarization. This polarization is due to ordering of molecular dipoles and interacts with the electric field of the substrate [12]. Competition between the polar f_p and dispersion f_d factors leads to a temperature-induced orientational transition in nematics [13]. The minimization of the free energy carried out in [3] gave $\cos\theta = 1$ if $w_p > w_d$ and $\cos\theta = w_p/w_d$ at $w_p < w_d$. Because the temperature dependences of w_p and w_d are different, an orientational transition may occur from planar to homeotropic texture. Suppose that in our case $w_p < w_d$. Polar moments favor homeotropic alignment. However, both the electric field and surface dispersion forces tend to orient the director of nematics in the planar geometry. As the electric field of the ferroelectric decreases with increasing temperature and completely disappears above the Curie point, the competition of dispersion and polar forces lead to the homeotropic texture. Another contribution to the surface energy should also be taken into account. This contribution is due to the gradient of the scalar order parameter of the liquid crystal at the surface, which can be represented in the form $f_q = w_q \cos\theta^4$ [14]. The coefficients w_p and w_d differ in their temperature dependence, and an orientational transition of the nematic is possible. However, the contribution of f_q commonly turns out to be small [4]. It was this instance that did not allow the significant difference in the anchoring coefficients of MBBA on the TGS cleavage surfaces for the planar and homeotropic alignments to be explained using this mechanism [5, 15].

Thus, an orientational transition of nematic mixture B from the planar texture to the homeotropic one was observed. The alignment was a consequence of the competition of three contending factors: the electric field of the ferroelectric tends to "lay" liquid crystal molecules in the substrate plane and the van der Waals anchoring forces favor the planar alignment, whereas the polar effects give rise to the homeotropic texture. The transition is due to a difference in the temperature dependence of the competing factors and a decrease in the electric field of the substrate down to its complete disappearance at the Curie point of the ferroelectric.

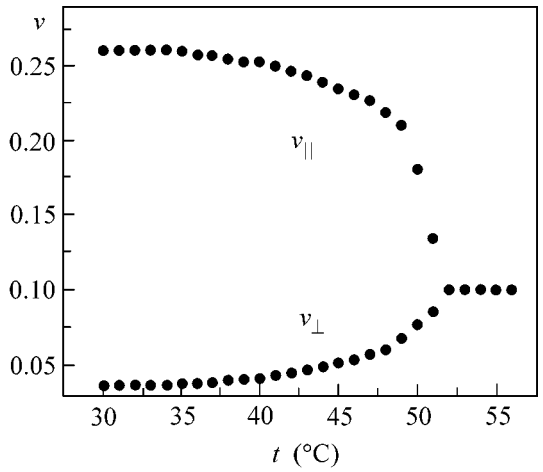

Fig. 3. Absorbance components $\nu_{||}$ and $\nu_\perp$ of the KD-10 dye at the He–Ne laser wavelength in nematic mixture B between two nonpolar glass surfaces in a 20-μm gap as functions of temperature.

REFERENCES

1. E. Dubois-Violette, J. Phys. Lett. **36**, L255 (1975).
2. G. Ryshenkov and M. Kleman, J. Chem. Phys. **64**, 404 (1976).
3. J. D. Parsons, Phys. Rev. Lett. **41**, 877 (1978).
4. G. Barbero and G. Durand, *Liquid Crystals in Complex Geometries*, Ed. by G. Ph. Crawford and S. Zumer (Taylor and Francis, London, 1996).
5. V. A. Gunyakov, A. M. Parshin, and V. F. Shabanov, Solid State Commun. **105**, 761 (1998).
6. V. A. Gunyakov, A. M. Parshin, B. P. Khrustalev, *et al.*, Solid State Commun. **87**, 751 (1993).
7. L. M. Blinov, *Electro-Optical and Magneto-Optical Properties of Liquid Crystals* (Nauka, Moscow, 1978; Wiley, New York, 1983).
8. W. H. de Jeu, *Physical Properties of Liquid Crystalline Materials* (Gordon and Breach, New York, 1980; Mir, Moscow, 1982).
9. N. A. Tikhomirova, L. I. Dontsova, S. A. Pikin, *et al.*, Kristallografiya **23**, 1239 (1978) [Sov. Phys. Crystallogr. **23**, 701 (1978)].
10. S. Hoshino, T. Mitsui, F. Jona, *et al.*, Phys. Rev. **107**, 1255 (1957).
11. L. M. Blinov, V. A. Kizel', V. G. Rumyantsev, *et al.*, Kristallografiya **20**, 1245 (1975) [Sov. Phys. Crystallogr. **20**, 750 (1975)].
12. A. G. Petrov and A. Derzhanski, Mol. Cryst. Liq. Cryst., Lett. Sect. **41**, 41 (1977).
13. G. A. Di Lisi and C. Rosenblatt, Liq. Cryst. **7**, 353 (1990).
14. G. Barbero, Z. Gabbasova, and M. A. Osipov, J. Phys. II **1**, 691 (1991).
15. M. Glogarova and G. Durand, J. Phys. (Paris) **49**, 1575 (1988).

Translated by A. Bagatur'yants

JETP Letters, Vol. 76, No. 5, 2002, pp. 302–306. From Pis'ma v Zhurnal Éksperimental'noĭ i Teoreticheskoĭ Fiziki, Vol. 76, No. 5, 2002, pp. 361–365.

Non-BCS Pairing in Anisotropic Strongly Correlated Electron Systems in Solids¶

V. A. Khodel[1] and J. W. Clark[2]

[1] *Russian Research Centre Kurchatov Institute, Moscow, 123182 Russia*

[2] *McDonnell Center for the Space Sciences and Department of Physics, Washington University, MO 63130, USA*

Received July 30, 2002

The problem of pairing in anisotropic electronic systems possessing patches of fermion condensate in the vicinity of the Van Hove points is analyzed. Attention is directed to opportunities for the occurrence of non-BCS pairing correlations between the states belonging to the fermion condensate. It is shown that the physical emergence of such pairing correlations would drastically alter the behavior of the single-particle Green function, the canonical pole of Fermi-liquid theory being replaced by a branch point. © *2002 MAIK "Nauka/Interperiodica".*

PACS numbers: 74.20.Mn

The ground state of conventional superconductors at zero temperature is known to be a condensate of Cooper pairs with total momentum $\mathbf{P} = 0$. In Fermi-liquid theory, the familiar BCS structure of the ground state is associated with the logarithmic divergence of the particle–particle propagator at $\mathbf{P} = 0$ and is independent of the details of the pairing interaction. However, a markedly different situation can exist in strongly correlated systems in which the necessary stability condition for the Landau state is violated and the Landau quasiparticle momentum distribution suffers a rearrangement. Under certain conditions, this rearrangement leads to a fermion condensate (FC): a continuum of dispersionless single-particle (sp) states whose energy $\epsilon(\mathbf{p})$ coincides with the chemical potential μ over a finite (and, in general, disconnected) domain $\mathbf{p} \in \mathcal{F}$ in the momentum space [1–6]. In such a case, the preference for pairing with $\mathbf{P} = 0$ comes into question because of the degeneracy of the FC sp spectrum, and the nature of pairing depends on the configuration assumed by the FC.

Here we study a two-dimensional square-lattice system having lattice constant l, in which the FC is situated in domains adjacent to four Van Hove points with coordinates $(\pm\pi/l, 0)$ and $(0, \pm\pi/l)$, while the sp states with ordinary dispersion are concentrated around diagonals of the Brillouin zone [2, 5]. To proceed efficiently, we shall focus on the nature of particle–particle correlations in the FC subsystem and ignore contributions from the sp states with nonzero dispersion. It is assumed that all the particle–hole contributions have already been taken into account in terms of an effective single-particle Hamiltonian with sp spectrum $\xi(\mathbf{p}) = \epsilon(\mathbf{p}) - \mu$. Accordingly, only pairing contributions should be incorporated in the equation for the Green function $G_{\alpha\beta}(x, x') = -i\langle T\psi_\alpha(x)\psi^\dagger_\beta(x')\rangle$. For simplicity, spin indices α, β, etc., will henceforth be omitted. The Green function is then expressed as $G(\mathbf{p}, \varepsilon) = [G_o^{-1}(\mathbf{p}, \varepsilon) - \Sigma(\mathbf{p}, \varepsilon)]^{-1}$ in terms of the free Green function $G_o^{-1}(\mathbf{p}, \varepsilon) = \varepsilon - \xi(\mathbf{p})$ and a self-energy or mass operator $\Sigma(\mathbf{p}, \varepsilon)$. In superfluid electron systems with an FC, the familiar Cooper pair ("C-pair") of BCS theory, which by definition has momentum $\mathbf{P} = 0$, can form only from sp states of diagonally opposite patches of the FC. The electron mass operator Σ is given by the usual formula $\Sigma = -\Delta G_o^- \Delta$, where $G_o^-(\mathbf{p}, \varepsilon) = -[\varepsilon + \xi(\mathbf{p})]^{-1}$ and Δ is the amplitude associated with generation of the BCS pair. In this case the electron Green function G has the conventional pole, and the sp spectrum, given by $E(\mathbf{p}) = [\xi^2(\mathbf{p}) + \Delta^2]^{1/2}$, possesses a gap specified by Δ.

In anisotropic electron systems inhabiting crystalline materials that exhibit fermion condensation, all FC patches should in principle be treated on an equal footing. It follows that pairing correlations affecting sp states located in neighboring FC patches may become important. Since the fraction of the Brillouin zone occupied by the FC is small, these correlations are specified by the antiferromagnetic vector $\mathbf{Q} = (\pi/l, \pi/l)$. In the conventional situation, the BCS coupling constant prevails, and the formation of "Q-pairs" having momentum $\mathbf{Q}$ is irrelevant. However, in the antiferromagnetic scenario for fermion condensation [5], wherein the scattering amplitude Γ is approximated by the well-known spin-fluctuation-exchange term [7]

$$N_0\Gamma(\mathbf{q} \longrightarrow \mathbf{Q}, \omega) = -\frac{\boldsymbol{\sigma}_1 \cdot \boldsymbol{\sigma}_2}{\kappa^2 p_F^{-2}(\mathbf{q} - \mathbf{Q})^2 + \beta^2 + i\omega/\omega_0}, \quad (1)$$

the constant λ_C associated with C-pair formation coincides with the Q-pair coupling constant λ_Q. Upon sup-

¶This article was submitted by the authors in English.

plementing Eq. (1) by regular terms, the ratio λ_Q/λ_C may vary in either direction. This prompts us to investigate the condition for stability of the BCS state against perturbations Δ' of the BCS gap function characterized by vectors close to **Q** (see below).

If this condition is violated, then Q-pairs must enter the picture. The most likely outcome is the Larkin–Ovchinnikov–Fulde–Ferrell (LOFF) [8, 9] scenario, in which the Q-pair condensate simply replaces the C-pair condensate of the BCS description. In the LOFF scenario, the new ground state usually ceases to be homogeneous. However, in the present case involving the single commensurate vector **Q**, the system remains homogeneous. Another possibility is that the new ground state becomes a "cocktail" composed of C- and Q-condensates. In this nonabelian exemplar of the pairing problem, the whole band of many-particle–many-hole states, envisioned as a conglomerate of C- and Q-pairs, comes into play. A similar situation occurs in the microscopic theory of rotation treated as a collective excitation [10].

To gain insight into the problem, let us represent the relevant mass operator Σ in terms of Feynman diagrams, as illustrated in the figure. The propagator of a C-pair is depicted by a double solid line; the propagator of a Q-pair, by a double dashed line; and that of an electron, by a single solid line. The open circle stands for the usual block of the Feynman diagrams representing the amplitude Δ for generation of a C-pair, while the solid circle stands for the block D of similar diagrams describing generation of a Q-pair. Within a BCS-like approximation, only diagrams (a) and (b) are relevant, as in the conventional case of interband transitions.

In drawing more complicated diagrams contributing to the mass operator, these restrictions must be obeyed:

(i) Emission of a pair of either type (C or Q) must be compensated by its absorption, ensuring particle conservation. In fact, pair emission and pair absorption must alternate from left to right in any diagram.

(ii) The direction of the single electron line reverses upon passing through a circle, whether open or solid.

(iii) The first (leftmost) and the last (rightmost) circles must be of the same type.

(iv) The first two circles cannot be of the same type; otherwise the diagram is reducible. Likewise, the last two circles cannot be of the same type.

With these restrictions, the equation for the mass operator Σ can be expressed in closed form, since only two different degrees of freedom are involved. We obtain a system of three equations,

$$\begin{aligned} \Sigma &= -\Delta^+ G_C^- \Delta - D^+ G_Q^- D, \\ G_C &= G_o - G_o D^+ G_Q^- D G_C, \\ G_Q &= G_o - G_o \Delta^+ G_C^- \Delta G_Q. \end{aligned} \tag{2}$$

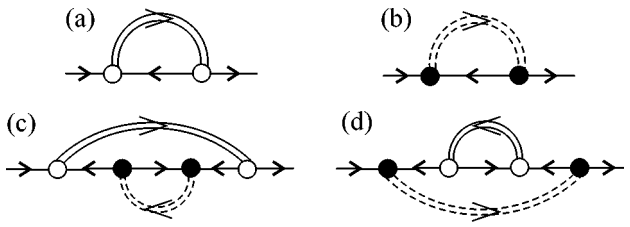

Diagrammatic representation of contributions to the mass operator Σ.

Upon introducing the dimensionless quantities $X_C = G_C/G_o$, $X_Q = G_Q/G_o$, and

$$\begin{aligned} K_C &= G_o \Delta^+ G_o^- \Delta, \\ K_Q &= G_o D^+ G_o^- D, \end{aligned} \tag{3}$$

this system can be conveniently rewritten

$$\begin{aligned} \Sigma G_o &= -K_C X_C - K_Q X_Q, \\ X_C &= 1 - K_Q X_C X_Q^-, \\ X_Q^- &= 1 - K_C X_C X_Q^-. \end{aligned} \tag{4}$$

The second of Eqs. (4) gives $X_C X_Q^- = (1 - X_C)/K_Q$; insertion of this relation into the third equation of the set leads to $K_C X_C^2 + (K_Q - K_C + 1)X_C - 1 = 0$. Analogous operations yield $K_Q X_Q^2 + (K_C - K_Q + 1)X_Q - 1 = 0$. These quadratic equations have respective solutions

$$\begin{aligned} X_C &= \frac{K_C - 1 - K_Q + [(K_C - 1 - K_Q)^2 + 4K_C]^{1/2}}{2K_C}, \\ X_Q &= \frac{K_Q - 1 - K_C + [(K_Q - 1 - K_C)^2 + 4K_Q]^{1/2}}{2K_Q}. \end{aligned} \tag{5}$$

The Green function G is now easily evaluated from the first of Eqs. (4), with the result

$$G = \frac{G_o}{[(K_C - K_Q + 1)^2 + 4K_Q]^{1/2}}. \tag{6}$$

The same result may be derived from the equations of motion [11]. We observe that the conventional Fermi-liquid-theory pole has been replaced by a branch point. The new Green function (6) possesses a nonzero imaginary part over a finite interval in ε delimited by the two zeros $E_\pm$ of the denominator of G. This is our primary result.

For the sake of clarity, let us neglect the inclination of the FC plateau in the spectrum of the sp excitations

due to pairing and set $\xi(\mathbf{p} \in F) \equiv 0$, just as in the system with an FC present but without pairing. We then find

$$[(K_C - K_Q + 1)^2 + 4K_Q]^{1/2} = \varepsilon^{-2}[(\varepsilon^2 - E_+^2)(\varepsilon^2 - E_-^2)]^{1/2}, \quad (7)$$

where $E_\pm(\Delta \pm D)^2$, and Eq. (6) takes the form

$$G(\varepsilon) = \frac{\varepsilon}{[(\varepsilon^2 - E_+^2)(\varepsilon^2 - E_-^2)]^{1/2}}, \quad \mathbf{p} \in \mathcal{F}. \quad (8)$$

Another interesting result concerns the topological charge N introduced by Volovik [2] to analyze the structure of the sp Green function of Fermi systems. Suppressing a trace over spin and band indices, this quantity is given by

$$N = \oint_C \frac{dl}{2\pi i} G(\omega, \mathbf{p}) \partial_l G^{-1}(\Omega, \mathbf{p}), \quad (9)$$

where the behavior of G is considered on an imaginary semiaxis of frequencies $\varepsilon = i\Omega$ and the integral is evaluated along an arbitrary contour C in the space $(\Omega, \mathbf{p})$ enclosing the singularity (a linear singularity—the Fermi line—occurring at $\Omega = 0$). The topological charge has the value $N = 1$ for a normal Fermi liquid and remains unchanged for marginal and Luttinger Fermi liquids. However, when a fermion condensate is present, its value shrinks to $N = 1/2$ [2]. If we now generalize the definition of N to apply to superfluid systems, asserting simply that the integration contour embraces the singularity of G, the topological charge evaluated for the Green function (8) is again $N = 1/2$, since the full variation of the argument of G over the contour amounts only to π. We conclude that the topological charge is conserved in the superfluid phase transition induced by non-BCS pairing.

Beyond these formal results, there is the pivotal question of whether non-BCS pairing of the kind described here can, in reality, win the contest with ordinary BCS pairing when the effective interaction Γ takes the form (1) and therefore entails comparable values of the two coupling constants λ_C and λ_Q. Resolution of this issue requires knowledge of the actual gap functions Δ and D. Generalized gap equations determining the two gap functions may be derived by summation of the appropriate diagrams of the scattering amplitude in the particle–particle channel, as is done in the diagrammatic foundation of BCS theory. Explicitly, these equations read

$$\Delta(\mathbf{p}) = -\int \mathcal{V}(\mathbf{p}, \mathbf{p}_1, \mathbf{P} = 0) G_C^-(\mathbf{p}_1, \varepsilon) \times \Delta(\mathbf{p}_1) G(\mathbf{p}_1, \varepsilon) dV_{\mathbf{p}_1} \frac{d\varepsilon}{2\pi i},$$
$$D(\mathbf{p}) = -\int \mathcal{V}(\mathbf{p}, \mathbf{p}_1, \mathbf{P} = \mathbf{Q}) G_Q^-(\mathbf{p}_1 + \mathbf{Q}, \varepsilon) \times D(\mathbf{p}_1) G(\mathbf{p}_1, \varepsilon) dV_{\mathbf{p}_1} \frac{d\varepsilon}{2\pi i}, \quad (10)$$

where $\mathcal{V}(\mathbf{p}, \mathbf{p}_1, \mathbf{P} = 0)$ and $\mathcal{V}(\mathbf{p}, \mathbf{p}_1, \mathbf{P} = \mathbf{Q})$ are the respective blocks of scattering-amplitude diagrams irreducible in the particle–particle channel and specified by pair momenta 0 and $\mathbf{Q}$, while $dV_\mathbf{p}$ denotes the FC momentum-space volume element. At nonzero temperature T, the usual factor $\tanh(\varepsilon/2T)$ is to be inserted in the integrands of Eqs. (10).

In the familiar case with $D = 0$, the second equation in the set (10) disappears, and we are left with the single gap equation of BCS theory. Conversely, if $\Delta = 0$, only the second equation in (10) survives, and we are led to the LOFF type of pairing. A third possibility is the emergence of a "cocktail" with both $\Delta \neq 0$ and $D \neq 0$. To decide which of the competing scenarios prevails in a given case, we should compare the respective superfluid corrections δE_N and δE_{BCS} to the ground-state energy (i.e., we should compare the condensation energies for the different pairing alternatives, where N labels one or another non-BCS scenario).

It is instructive to treat a simple model in which the blocks $\mathcal{V}(\mathbf{p}, \mathbf{p}_1, \mathbf{P} = 0)$ and $\mathcal{V}(\mathbf{p}, \mathbf{p}_1, \mathbf{P} = \mathbf{Q})$ are approximated by respective constants λ_C and λ_Q in the FC region, while vanishing outside. The solutions Δ and D of Eqs. (10) are then also constants in this domain and zero outside. The non-BCS condensation energy is given by the formula

$$\delta E_N(\lambda) = -\int_0^\lambda \frac{\Delta^2 + D^2}{\lambda_1^2} d\lambda_1, \quad (11)$$

which may be derived in the same manner as the analogous formula for δE_{BCS} appearing in the Landau–Lifshitz textbook [12]. In obtaining this result, the ratio λ_Q/λ_C has been fixed.

A comprehensive study of the problem requires a knowledge of the sp spectrum $\xi(\mathbf{p}) = \epsilon(\mathbf{p}) - \mu$, since when pairing occurs, $\xi(\mathbf{p})$ necessarily differs from zero even in the momentum region $\mathcal{F}$ occupied by the FC [1]. In evaluating $\xi(\mathbf{p})$, one can employ the standard relation

$$\delta\epsilon(\mathbf{p}) = \int f(\mathbf{p}, \mathbf{p}_1) \delta n(\mathbf{p}_1) dV_{\mathbf{p}_1}, \quad \mathbf{p} \in \mathcal{F}, \quad (12)$$

where $\delta n = n - n_0$ is the difference between the momentum distributions for the superfluid and nonsuperfluid states of the system *with* the fermion condensate present, $\delta\epsilon$ is the corresponding difference in the sp spectra, and f is the effective interaction in the particle–hole channel.

In analyzing the problem, we exploit the fact that the strength f of the effective interaction $f(\mathbf{p}, \mathbf{p}_1)$ in the particle–hole channel exceeds its strength in the particle–particle channel. This allows one to expand $\xi(\mathbf{p})$ as given by Eq. (12) in a Taylor series with respect to the

order parameter Δ and evaluate the coefficients of the expansion by equating terms of the same power in this parameter. To illustrate the procedure, consider the situation in which the ordinary C-pairing of BCS theory prevails. In this case,

$$\Delta = -\lambda_C \int_{\mathscr{F}} n(\mathbf{p})(1-n(\mathbf{p}))dV_{\mathbf{p}}, \tag{13}$$

where

$$n(\mathbf{p}) = \frac{E(\mathbf{p})-\xi(\mathbf{p})}{2E(\mathbf{p})} \tag{14}$$

and $E(\mathbf{p}) = [\xi^2(\mathbf{p}) + \Delta^2]^{1/2}$. Let us now insert the expansion

$$\xi(\mathbf{p}) = \xi_1(\mathbf{p})\Delta + \xi_2(\mathbf{p})\Delta^2 + \ldots, \quad \mathbf{p} \in \mathscr{F} \tag{15}$$

first into Eq. (14) and then into Eq. (12), thereby obtaining

$$\xi_1(\mathbf{p})\Delta + \xi_2(\mathbf{p})\Delta^2 + \ldots = \int_{\mathscr{F}} f(\mathbf{p}_1, \mathbf{p}_1) \times \left[\frac{1}{2} - \frac{\xi_1(\mathbf{p}_1) + \xi_2(\mathbf{p}_1)\Delta + \ldots}{2[((\xi_1(\mathbf{p}_1) + \xi_2(\mathbf{p}_1)\Delta + \ldots)^2 + 1]} - n_0(\mathbf{p}_1)\right] \times dV_{\mathbf{p}_1}. \tag{16}$$

Here we have neglected an insignificant variation of the chemical potential of order Δ^2. Since the gap value Δ is small, one can expand the right-hand-side of Eq. (16) into a Taylor series in Δ. Every term of the latter expansion must necessarily coincide with the respective term of the Taylor expansion on the left-hand-side of the equation. Focusing on the terms of zeroth power in Δ, which are absent from the left-hand-side of Eq. (16), this fact is seen to require that the term $1 - \xi_1(p)/[\xi_1^2(p) + 1]^{1/2} - 2n_0(p)$ on the right-hand-side is identically zero, which in turn yields

$$\xi_1(\mathbf{p}) = \frac{(1-2n_0(\mathbf{p}))]}{2[n_0(\mathbf{p})(1-n_0(\mathbf{p}))]^{1/2}},$$
$$E_1(\mathbf{p}) = \frac{\Delta}{2[n_0(\mathbf{p})(1-n_0(\mathbf{p}))]^{1/2}}, \quad \mathbf{p} \in \mathscr{F}. \tag{17}$$

These conditions are virtually equivalent to the coincidence of $n_0(\mathbf{p})$ in the FC region, in the limit $\Delta \longrightarrow 0$. Equating the terms linear in Δ on the left and right of Eq. (16), one can find the quantity ξ_2, and so on to higher orders as needed. The analysis shows that the dimensionless ratio $\xi_2(\mathbf{p})\Delta/\xi_1(\mathbf{p})$, which is proportional to the ratio $(\mathscr{V}/f) \sim (T_c/T_f)$ of the critical temperature T_c of the pairing transition to the characteristic temperature T_f of fermion condensation, always remains rather small because the interaction f must be very strong for a fermion condensate to form. It is thus a reasonable approximation to retain only the term ξ_1 in expansion (15).

One can proceed analogously in the general case with $D \neq 0$. The same argumentation can in fact be applied to evaluate the variation of the FC spectrum with T in the normal state at temperatures near T_c. The result becomes especially transparent if one may ignore damping effects, in which case the standard formula $n(\mathbf{p}, T) = [1 + \exp(\xi(\mathbf{p}, T)/T)]^{-1}$ may be employed in Eq. (12) to obtain [1, 3]

$$\xi(\mathbf{p}, T) = T\ln\frac{1-n_0(\mathbf{p})}{n_0(\mathbf{p})}, \quad \mathbf{p} \in \mathscr{F}. \tag{18}$$

The key equations (10) and (12) are cumbersome to analyze and solve. However, their treatment is facilitated if we work in the temperature region close to the critical temperature T_c, since one of the gap functions Δ or D vanishes, while the other satisfies a linear equation yielding the corresponding critical temperature, T_{c1} (for $\Delta \equiv 0$) or T_{c2} (for $D \equiv 0$). If BCS pairing is victorious, this equation takes the customary form [13]

$$1 = -\lambda_C \int \frac{1-2n(\mathbf{p}, T_{c1})}{2\xi(\mathbf{p}, T_{c1})} dV_{\mathbf{p}}. \tag{19}$$

Suppressing an insignificant variation of the momentum distribution $n(\mathbf{p}, T)$ with T and inserting $\xi(\mathbf{p}, T)$ from Eq. (18), we arrive at the relation

$$T_{c1} = -\frac{\lambda_C}{2}\int \frac{1-2n_0(\mathbf{p})}{\ln[1-n_0(\mathbf{p})] - \ln n_0(\mathbf{p})} dV_{\mathbf{p}}, \tag{20}$$

which determines T_{c1}. In the opposite case, for which the Q-condensate disappears at $T_{c2} > T_{c1}$, the analog of Eq. (20) is found to be

$$T_{c2} = -\lambda_Q \int_{\mathscr{F}} \frac{1-n_0(\mathbf{p})-n_0(\mathbf{p}+\mathbf{Q})}{\ln(1-n_0(\mathbf{p})) - \ln n_0(\mathbf{p}) + \ln(1-n_0(\mathbf{p}+\mathbf{Q})) - \ln n_0(\mathbf{p}+\mathbf{Q})} dV_{\mathbf{p}}. \tag{21}$$

We see that the outcome of the contest between C- and Q-condensates at sufficiently high temperatures depends crucially on the arrangement of the FC.

What conditions ensure the occurrence of the cocktail solution of the gap equations (10)? We answer this question for the case $T = 0$ by considering the stability condition

$$\Delta'(\mathbf{k}, \omega) \equiv -(\mathscr{V}F') = -\int \mathscr{V}[G^-(\mathbf{p}, \varepsilon)G(\mathbf{p}+\mathbf{k}, \varepsilon+\omega) \tag{22}$$

$$+ F(\mathbf{p}, \varepsilon)F(\mathbf{p}+\mathbf{k}, \varepsilon+\omega)]\Delta'(\mathbf{k}, \omega)dv_{\mathbf{p}}\frac{d\varepsilon}{2\pi i}$$

for the BCS state in the particle–particle channel, derived from the first of Eqs. (10) with D set identically to zero. Violation of stability is signaled by the emergence of imaginary frequencies $\omega(\mathbf{k})$ in solutions of this equation. In the most dangerous case, the wave vector $\mathbf{k}$ associated with the perturbation Δ' coincides with $\mathbf{Q}$ and involves the block $\mathcal{V}(\mathbf{p}, \mathbf{p}_1, \mathbf{Q})$, which we treat as a parameter λ_Q. The stability condition is violated if the coupling constant λ_Q exceeds a critical value λ_Q^{cr}. The equation fixing λ_Q^{cr} is

$$1 = -\lambda_Q^{\mathrm{cr}}\int_{\mathcal{F}}[G(\mathbf{p}, \varepsilon)G(\mathbf{Q}-\mathbf{p}, -\varepsilon) + F(\mathbf{p}, \varepsilon)F(\mathbf{Q}-\mathbf{p}, -\varepsilon)]dv_{\mathbf{p}}\frac{d\varepsilon}{2\pi i}, \quad (23)$$

where G and F are the pair of Green functions entering the system of Gor'kov equations. Upon substituting the explicit forms for these functions, Eq. (23) may be converted into

$$1 = -\lambda_Q^{\mathrm{cr}}\int_{\mathcal{F}}\frac{E(\mathbf{p})E(\mathbf{p}+\mathbf{Q}) + \xi(\mathbf{p})\xi(\mathbf{p}+\mathbf{Q}) + \Delta^2}{2E(\mathbf{p})E(\mathbf{p}+\mathbf{Q})[E(\mathbf{p}) + E(\mathbf{p}+\mathbf{Q})]}dv_{\mathbf{p}}, \quad (24)$$

the gap $\Delta(\lambda_C)$ and the spectra $E(\mathbf{p}, \lambda_C)$ and $\xi(\mathbf{p}, \lambda_C)$ being given by Eqs. (13) and (17). Equation (24) serves to determine the critical constant λ_Q^{cr} for given λ_C, and the pure BCS vacuum is destroyed if $\lambda_Q > \lambda_Q^{\mathrm{cr}}$.

Violation of the stability condition for the state with a pure Q-condensate may be analyzed along the same lines. In this case, one employs the second of Eqs. (10) with Δ set identically zero and determines the critical constant λ_C^{cr} responsible for destroying the pure Q-pairing state as a function of λ_Q. Now, suppose that the two curves $\lambda_C^{\mathrm{cr}}(\lambda_Q)$ and $\lambda_Q^{\mathrm{cr}}(\lambda_C)$ are plotted on the plane (λ_C, λ_Q). If a region is found in which *both* the C- and Q-condensates lose their stability, then the cocktail solution of Eqs. (10) must prevail throughout that region.

Finally, we turn briefly to possible experimental consequences of non-BCS pairing. In conventional superconductors, the linewidth is known to be very narrow, but this would not be the case if non-BCS pairing were to occur (see Eq. (8)). A significant broadening of the sp line is predicted to accompany the cocktail solution. Such a spectral broadening would affect many prominent experimental signatures of pairing, notably the falloff of the specific heat $C(T)$ as $T \longrightarrow 0$ (slower than in the BCS case), the dependence of the gap value on T, and the behavior of the penetration depth. Another specific feature of the non-BCS solutions is related to possible violation of the property of time-reversal invariance. This property is of course intrinsic to BCS theory, since the ground state is time-reversal invariant by construction. However, if the total momentum $\mathbf{P}$ of the pairs involved differs from zero, special restrictions are needed to maintain the invariance.

We are indebted to G.E. Volovik and M.V. Zverev for numerous valuable discussions. This research was supported in part by NSF Grant no. PHY-9900713, by the McDonnell Center for the Space Sciences, and by the Russian Foundation for Basic Research, grant no. 00-15-96590.

REFERENCES

1. V. A. Khodel and V. R. Shaginyan, Pis'ma Zh. Éksp. Teor. Fiz. **51**, 488 (1990) [JETP Lett. **51**, 553 (1990)]; Condens. Matter Theor. **12**, 222 (1997).
2. G. E. Volovik, Pis'ma Zh. Éksp. Teor. Fiz. **53**, 208 (1991) [JETP Lett. **53**, 222 (1991)]; Pis'ma Zh. Éksp. Teor. Fiz. **59**, 798 (1994) [JETP Lett. **59**, 830 (1994)].
3. P. Nozières, J. Phys. I **2**, 443 (1992).
4. M. R. Norman, in *High Temperature Superconductivity*, Ed. by S. E. Barnes, J. Ashkenazi, J. L. Cohn, and F. Zuo (American Inst. of Physics, Woodbury, 1999), p. 298.
5. M. V. Zverev, V. A. Khodel, and J. W. Clark, Pis'ma Zh. Éksp. Teor. Fiz. **74**, 48 (2001) [JETP Lett. **74**, 46 (2001)].
6. V. Yu. Irkhin, A. A. Katanin, and M. I. Katsnelson, cond-mat/0110516.
7. A. J. Millis, H. Monien, and D. Pines, Phys. Rev. B **42**, 167 (1990).
8. A. I. Larkin and Yu. N. Ovchinnikov, Zh. Éksp. Teor. Fiz. **47**, 1136 (1964) [Sov. Phys. JETP **20**, 762 (1965)].
9. P. Fulde and R. A. Ferrell, Phys. Rev. **135**, A550 (1964).
10. S. T. Belyaev and V. G. Zelevinski, Yad. Fiz. **11**, 741 (1970) [Sov. J. Nucl. Phys. **11**, 416 (1970)].
11. V. A. Khodel and J. W. Clark, cond-mat/0112059.
12. L. D. Landau and E. M. Lifshitz, *Course of Theoretical Physics*, Vol. 5: *Statistical Physics* (Nauka, Moscow, 1995; Pergamon, Oxford, 1980), Part 1.
13. A. A. Abrikosov, L. P. Gor'kov, and I. E. Dzyaloshinskii, *Methods of Quantum Field Theory in Statistical Physics* (Fizmatgiz, Moscow, 1962; Prentice-Hall, Englewood Cliffs, 1965), p. 172.

JETP Letters, Vol. 76, No. 5, 2002, pp. 307–311. Translated from Pis'ma v Zhurnal Éksperimental'noĭ i Teoreticheskoĭ Fiziki, Vol. 76, No. 5, 2002, pp. 366–370.

Magnetic Field Effect on the Photoluminescence of an Eu Impurity during Its Aggregation in NaCl Crystals

R. B. Morgunov, S. Z. Shmurak, B. K. Ponomarev, A. A. Baskakov, and V. I. Kulakov

Institute of Solid-State Physics, Russian Academy of Sciences, Chernogolovka, Moscow region, 142432 Russia

e-mail: morgunov@issp.ac.ru

Received July 30, 2002

It is found that a magnetic field up to 20 T affects photoluminescence absorption spectra in NaCl:Eu crystals in the process of impurity aggregation into complexes. The spectral changes are irreversible and are observed after quenching the crystals at the early stages of the formation of small metastable complexes containing impurity–vacancy Eu^{2+}–V dipoles. Emporal correlations revealed between the occurrence of the magnetoplastic effect and a change in the optical properties of the crystals in a magnetic field. © *2002 MAIK "Nauka/Interperiodica".*

PACS numbers: 75.80.+q; 78.55.Hx; 61.72.Hh

The discovery of magnetoplastic effects in ionic crystals [1–10] and the experimental corroboration of spin-dependent mechanisms of the magnetic field effects on plasticity [11, 12] revealed new aspects of the physics of structural defects and posed numerous problems in this area. Notwithstanding abundant evidence of the existence of magnetoplastic effects in dielectrics [1–12], metals [13–15], and semiconductors [16–20], comprehensively justified models of such phenomena have not been proposed so far. The main obstacles are, first, the absence of convincing data on the type of atoms of which the defects that determine the occurrence of magnetoplastic effects are composed and, second, the absence of direct methods for measuring the amount of elementary spin-dependent events in a magnetic field. Indirect information on such events obtained in studying the mobility of individual dislocations and other characteristics of plasticity gives no way of unambiguously determining microscopic parameters of the defects under study.

The aim of this work is to create experimental conditions for observing the magnetic field effect on photoluminscencve excitation spectra of ionic crystals in which magnetoplastic effects is observed.

Procedure. NaCl:Eu crystals (~0.01 at. %) were chosen for the investigation because (1) magnetoplastic effects are observed in these crystals and arise, according to suggestions made in [10, 11], because of the structural rearrangement of complexes of impurity–vacancy dipoles (Eu^{2+} ion + cation vacancy V), which are stoppers for dislocations; (2) magnetic properties of Eu^{2+} ions and some of their large complexes are well known (see reviews [21, 22]); and (3) Eu^{2+}–V centers in ionic crystals give intense photoluminescence whose excitation spectrum is sensitive to the aggregation of single impurity–vacancy dipoles into complexes [21, 22].

Magnetic field pulses of 10-ms duration and amplitude B up to 20 T were generated in a short solenoid by a discharge of a condenser battery. The magnetic field with induction $B \sim 10$ T is "weak" for the system of paramagnetic defects at hand, because the energy $\mu B \sim 10^{-3}$ eV, which it can impart to an Eu^{2+} ion with a magnetic moment μ ($\mu \sim \mu_B$, μ_B is the Bohr magneton) is an order of magnitude less than the mean energy of thermal fluctuations $kT \sim 10^{-2}$ eV at $T \sim 300$ K. Hence, the presence of nonequilibrium defects is of principal importance for observing the effect of a weak magnetic field on the physical properties of crystals [11]. In our experiments, the magnetic field effect on photoluminescence spectra was sought in quenched crystals. These crystals contained nonequilibrium complexes of impurity–vacancy dipoles and exhibited a magnetoplastic effect within ~ 50 h after quenching [10].

The quenching of crystals was carried out after their heating for 1–2 h at a temperature of 770 K by cooling on a copper plate to a temperature of 293 K with an average rate of ~ 5 K/s. To prevent the diffusion deleted of oxygen, hydroxyl groups, etc., into the crystals, the thermal treatment was performed in a He or Ar atmosphere.

The luminescence of crystals was excited by the ultraviolet light of a DKCSh-120 lamp passed through an MDR-4 monochromator and was measured with a second MDR-6 monochromator and an FÉU-106 photomultiplier. All spectra were obtained at room temperature.

0021-3640/02/7605-0307$22.00

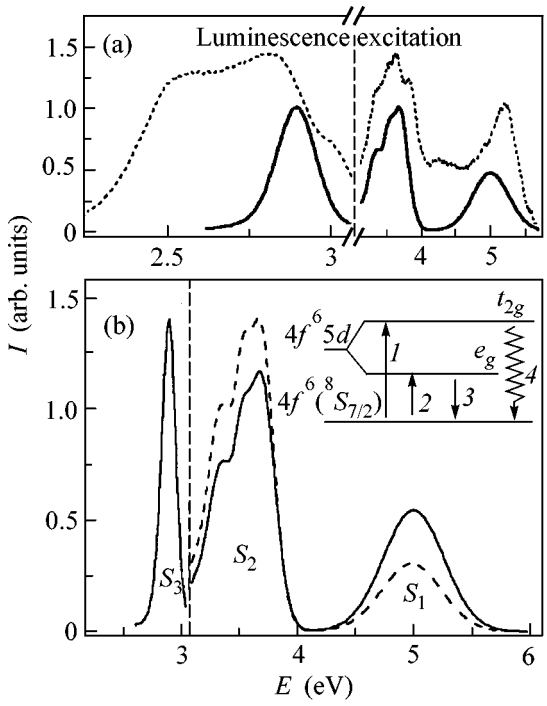

Fig. 1. Photoluminescence excitation spectrum (on the right) recorded at 428 nm (E_{lum} = 2.9 eV) and a luminescence spectrum (on the left) excited by light with a wavelength of 350 nm (E_{ex} = 3.7 eV) of NaCl:Eu single crystals: (a) before (dashed line) and after (solid line) quenching and (b) before (solid line) and after (dashed line) exposure of the quenched crystals in a magnetic field with B = 20 T. The inset in Fig. 1b demonstrates the system of Eu^{2+} ions electronic levels split by the crystal field, between which transitions take place under the action of light. The numbering of transitions *1*, *2*, and *3* coincides with the numbering of bands S_1, S_2, and S_3. Radiationless transitions are designated by wavy line *4*.

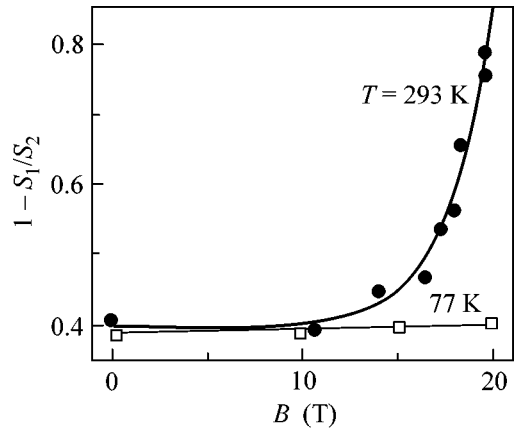

Fig. 2. Dependence of the value of $(1 - S_1/S_2)$ (relative difference in integral intensities of the S_1 and S_2 bands of the luminescence excitation spectrum) on the magnitude B of the magnetic field pulse.

Results and discussion. Quenching causes the dissolution of large complexes of impurity–vacancy dipoles (precipitates) [21, 22]. The corresponding changes in the photoluminescence spectrum due to the quenching of crystals are in the disappearance of bands assigned to the glow of precipitates of three types: (1) ordered aggregates of impurity–vacancy dipoles along the (301) planes (at the emitted light quantum energy E_{lum} = 2.56 eV), (2) ordered aggregates of impurity–vacancy dipoles along the (111) planes (E_{lum} = 2.83 eV), and (3) the $EuCl_2$ Suzuki phase (E_{lum} = 3.03 eV) [21]. The bands that remained after quenching in the luminescence spectrum (at E_{lum} = 2.90 eV) and in the luminescence excitation spectrum (Fig. 1a) correspond to impurity–vacancy dipoles and their small (undetectable by x-ray methods) nonequilibrium complexes of unknown structure [21]. The sensitivity of optical properties of these complexes to a magnetic field was the subject of investigation.

In order to provide a way for complexes of various atomic configurations to form, each sample after quenching was held during a certain time t (from 10 min to 2 months) at room temperature. After that, the photoluminescence excitation spectrum of the sample was measured, which served for determining the initial state of the impurity before the exposure of the sample to a magnetic field. Next, the sample was exposed to a magnetic field, and the photoluminescence excitation spectrum was measured again. Subsequently, we compared the spectra obtained before and after the exposure of the sample to a magnetic field; that is, we attempted to detect the residual changes induced by the field.

It was found that exposure of a crystal to a magnetic field with B = 20 T at T = 293 K gave rise to a change in the ratio of intensities in the S_1 and S_2 bands of the photoluminescence excitation spectrum recorded at 428 nm (E_{lum} = 2.90 eV) (Fig. 1b). The quantity $1 - S_1/S_2$, which expressed the relative difference in the emitted energies at the same (in terms of the photon flux) excitation for the S_1 and S_2 bands, was chosen as characteristic of the residual changes of the excitation spectrum after the exposure of a crystal to a magnetic field. As the magnetic field induction increased, a monotonic increase in the value of $1 - S_1/S_2$ was observed at T = 293 K (Fig. 2).

The magnetic field effect on the optical properties of crystals can be observed only in the samples that were held after quenching at room temperature for 15 h < t < 100 h. At different t that fall outside this range, no change in the value of $1 - S_1/S_2$ action was observed under exposure to magnetic field; that is, $\Delta(1 - S_1/S_2) = 0$ (Fig. 3a). This is in good agreement with the results obtained in [10], where a change in the microhardness ΔH of NaCl:Eu crystals was observed after their exposure to a magnetic field with B = 6 T at 30 h < t < 80 h (Fig. 3a). Correlation is also observed between the variations of the absolute value of the microhardness H and

the quantity S_1/S_2 with time after the quenching of crystals (Fig. 3b).

If, after the first exposure of a crystal to a magnetic field with $B = 20$ T and the recording of the changes in its excitation spectrum, the crystal was exposed to the field several more times, no additional changes were observed (Fig. 4a). This fact was verified within both several hours and several days after the first exposure of a crystal to a magnetic field. Hence, a single magnetic field pulse leads to a complete and irreversible transformation of all the magnetically sensitive defects occurring in the crystal. Nevertheless, it was possible to observe the magnetic field effect on the photoluminescence excitation spectrum in the same sample up to three times if the crystal was previously quenched and held at $T = 293$ K during ~ 50 h at each such attempt (Fig. 4b).

Another type of changes induced by a magnetic field in the photoluminescence excitation spectrum represents a change in the fine structure of the S_2 band (see inset in Fig. 5a). This band consists of several components (Fig. 5a), the position of whose centers was found by the twofold differentiation of the excitation spectrum and was fixed when the procedure of decomposition was carried out. The best fit of the spectrum is achieved with the use of five Gaussian lines (Fig. 5a). In spite of the fact that these lines have not been assigned to certain small complexes of impurity–vacancy dipoles so far, their existence has been long known and their positions in our experiments agree well (to 1 nm) with the data obtained in [23]. Assuming that $S_2 = 1$, we investigated the integral intensity (area) of each of the four lines σ_i ($i = 1, 2, 3, 4$) as a function of the induction of the applied magnetic field. It was found that σ_1 and σ_3 remain virtually unchanged after exposure of the crystal to a magnetic field, whereas σ_2 increases, and σ_4 decreases with increasing B, so that the sum $\sigma_2 + \sigma_4$ remains constant (Fig. 5b). In studying the dependences $\sigma_i(t)$, where t is the time elapsed after quenching, it was found that it was lines *2* and *4*, which are sensitive to the magnetic field, that exhibited the greatest changes during the pause between quenching and exposure to magnetic field (Fig. 5c).

The experimental conditions created in this work allowed us to observe the effect of a "weak" magnetic field on the photoluminescence of point defects composed of a small number of reliably identified centers, which represent Eu^{2+}–V impurity–vacancy dipoles. It is known that light excitation of the Eu^{2+} ions entering the composition of such centers initiates transitions from the $4f^7$ level to the $4f^6\,5d$ level, which is split in the crystal field into two sublevels, t_{2g} and e_g, differing in symmetry [21, 22] (see inset in Fig. 1b). The radiative relaxation of excited ions proceeds from the state of the e_g symmetry with an overwhelmingly high probability (~99%), whereas the transition from the t_{2g} state can proceed in two ways: either through multiphonon, fully

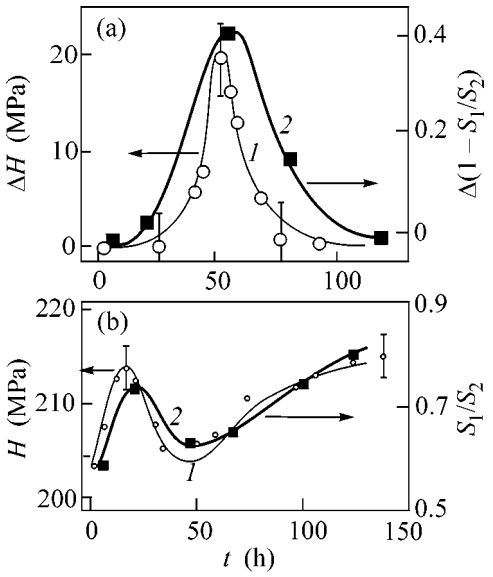

Fig. 3. Variations of the spectral properties and microhardness of crystals: (a) (*1*) the increment of the value of $(1 - S_1/S_2)$ after a magnetic field pulse with $B = 20$ T and (*2*) the change in the microhardness of crystals ΔH under the action of a magnetic field pulse with $B = 6$ T [10] as functions of the time t passed after the quenching of crystals; (b) (*1*) the value of S_1/S_2 and (*2*) the microhardness of crystals H [10] as functions of the time t passed after the quenching of crystals.

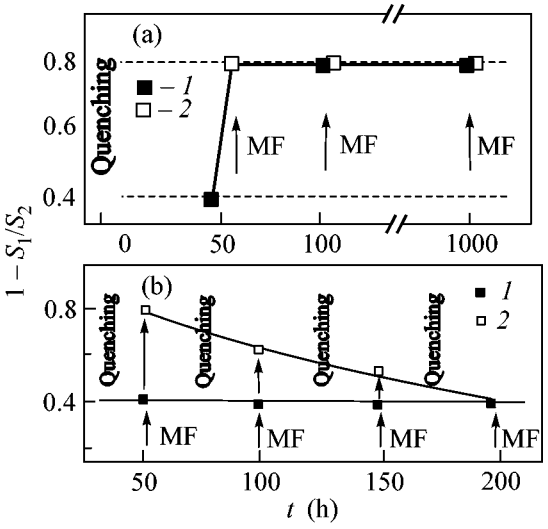

Fig. 4. Distribution of intensities in the luminescence excitation spectrum $(1 - S_1/S_2)$ as a function of current time t: (a) under the action of repeated magnetic field pulses with $B = 20$ T at single quenching of a crystal ((*1*) before and (*2*) after exposure to magnetic field); (b) the same as (a) at multiple quenching of a crystal 50 h prior to each exposure to magnetic field.

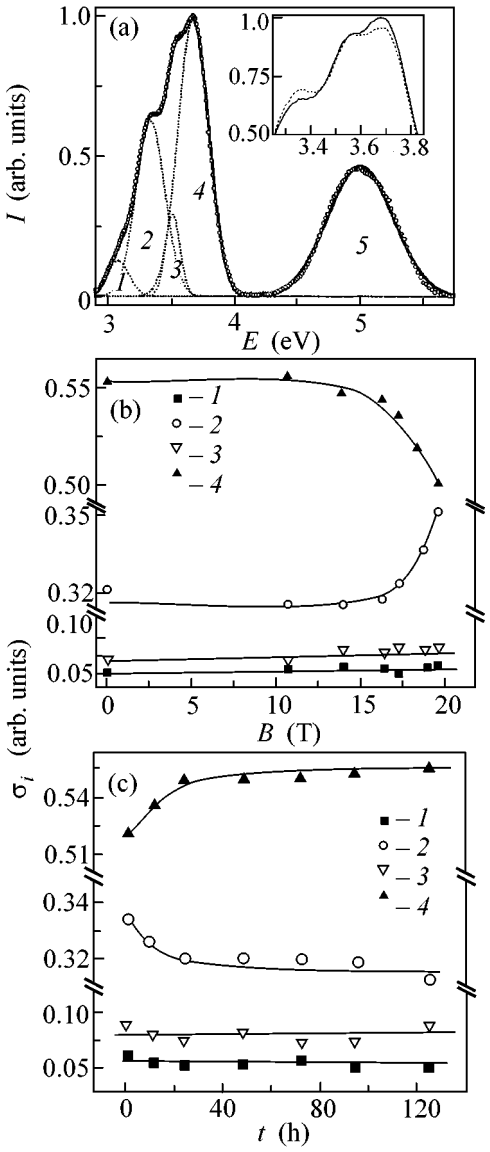

Fig. 5. (a) Decomposition of the photoluminescence excitation spectrum of quenched crystals into Gaussian components (curves *1–5*); (b) and (c) areas of components σ_i designated in Fig. 5a by numbers (i = 1, 2, 3, and 4) as functions of (b) the magnitude B of the magnetic field pulse and (c) the time t passed after the quenching of crystals. The total area $S_2 = \sum\sigma_i = 1$ is assumed to be constant. The inset in Fig. 5a demonstrates a fragment of the excitation spectrum in the S_2 band before (solid line) and after (dashed line) the exposure of a crystal to a magnetic field.

radiationless relaxation or through radiationless transition to the e_g level followed by emission with the transition from the e_g level to the $4f^7$ ground state [21, 22]. The change in the ratio of the integral intensities of the S_1 and S_2 bands after exposure of the crystal to a magnetic field (Fig. 1b) can be due to an increase in the fraction of the defects characterized by a high probability of radiationless relaxation. It was reported in [24] that such complexes were found in NaCl:Eu.

The disappearance of the magnetic field effect on the photoluminescence excitation spectrum as the temperature at which the crystal was exposed to a magnetic field decreased (Fig. 2) points to a significant role of thermal fluctuations, which initiate the transitions of metastable complexes to short-lived, magnetically sensitive states. This is in agreement with the results obtained in [11] in an investigation of magnetoplastic effects. The dependence of $1 - S_1/S_2$ on B obtained in this work exhibits a similarity to the dependence of the dislocation path on the magnetic field induction [25].

A gradual decrease in the effect of sensitization of the optical properties of crystals with respect to exposure to a magnetic field after multiply repeated quenching procedures (Fig. 4b) indicates that the magnetic field changes the probability of the formation of complexes of impurity–vacancy dipoles to the benefit of the stable configurations such that they are poorly "dissolved" in the next thermal treatments. Therefore, quenching ceases to sensitize the crystals with respect to exposure to a magnetic field after several cycles.

The areas under individual lines σ_i (Fig. 5) characterize the amount of complexes of defects excited by light of corresponding energy. Therefore, the mutually compensating changes in σ_2 and σ_4 induced by the magnetic field (Fig. 5b) can be interpreted as a transformation of complexes from one type to another. The variation of the areas of these lines with the time after quenching (Fig. 5c) indicates that the magnetically sensitive complexes consist of several impurity–vacancy dipoles rather than one.

Because the magnetic field effect on both plasticity and photoluminescence excitation spectra reaches a maximum within ~50 h after quenching (Fig. 3), it can be suggested that the transformation of the same defects in a magnetic field makes a contribution to the change in both optical and mechanical properties of crystals.

Conclusions. It was found that the magnetic field exerts effect on the photoluminescence excitation spectrum in NaCl:Eu crystals in the process of Eu impurity aggregation after quenching. The change of optical properties of crystals is due to transformation of the structure of nonequilibrium, intermediate, small Eu^{2+} impurity–vacancy dipole complexes in a magnetic field.

It is revealed that the magnetic field effect on complexes of point defects is irreversible. This indicates that the role of magnetic field consists in initiating the relaxation of metastable states of complexes. Repeated thermal treatments, which lead to the nucleation of metastable complexes of defects, partially sensitize the crystal with respect to the action of a magnetic field.

It is hoped that the results obtained will replenish the lack of information on the initial stages of the formation of small clusters and nuclei of growth for various nano- and microsamples (nanotubes, precipitates and second phase formations in electronic materials,

etc.). In addition, the possibility of controlling spin-dependent stages of the impurity aggregation process using a magnetic field extends the range of nonthermal methods for changing the atomic structure of defects and the corresponding structure-sensitive crystal properties. The latter is of special importance for understanding physical processes in Eu^{2+}-doped dielectrics, which find wider and wider technical applications as elements of optical sensors and dosimeters [23, 26–29].

This work was supported by the Russian Foundation for Basic Research, project nos. 02-02-99302, 02-15-96703, and 01-02-97029.

REFERENCES

1. V. I. Al'shits, E. V. Darinskaya, T. M. Perekalina, and A. A. Urusovskaya, Fiz. Tverd. Tela (Leningrad) **29**, 467 (1987) [Sov. Phys. Solid State **29**, 265 (1987)].
2. V. I. Al'shits, E. V. Darinskaya, and O. L. Kazakova, Pis'ma Zh. Éksp. Teor. Fiz. **62**, 352 (1995) [JETP Lett. **62**, 375 (1995)].
3. V. I. Al'shits, E. V. Darinskaya, and O. L. Kazakova, Zh. Éksp. Teor. Fiz. **111**, 615 (1997) [JETP **84**, 338 (1997)].
4. Yu. I. Golovin and R. B. Morgunov, Pis'ma Zh. Éksp. Teor. Fiz. **61**, 583 (1995) [JETP Lett. **61**, 596 (1995)].
5. A. A. Urusovskaya, V. I. Al'shits, A. E. Smirnov, and N. N. Bekkauer, Pis'ma Zh. Éksp. Teor. Fiz. **65**, 470 (1997) [JETP Lett. **65**, 497 (1997)].
6. V. I. Al'shits, N. N. Bekkauér, A. E. Smirnov, and A. A. Urusovskaya, Zh. Éksp. Teor. Fiz. **115**, 951 (1999) [JETP **88**, 523 (1999)].
7. N. A. Tyapunina, V. L. Krasnikov, and É. P. Belozerova, Fiz. Tverd. Tela (St. Petersburg) **41**, 1035 (1999) [Phys. Solid State **41**, 942 (1999)].
8. B. I. Smirnov, N. N. Peschanskaya, and V. I. Nikolaev, Fiz. Tverd. Tela (St. Petersburg) **43**, 2154 (2001) [Phys. Solid State **43**, 2250 (2001)].
9. V. I. Al'shits, E. V. Darinskaya, and E. A. Petrzhik, Fiz. Tverd. Tela (Leningrad) **33**, 3001 (1991) [Sov. Phys. Solid State **33**, 1694 (1991)].
10. R. B. Morgunov and A. A. Baskakov, Fiz. Tverd. Tela (St. Petersburg) **43**, 1632 (2001) [Phys. Solid State **43**, 1700 (2001)].
11. Yu. I. Golovin, R. B. Morgunov, V. E. Ivanov, and A. A. Dmitrievskiĭ, Zh. Éksp. Teor. Fiz. **117**, 1080 (2000) [JETP **90**, 939 (2000)].
12. V. I. Al'shits and E. V. Darinskaya, Pis'ma Zh. Éksp. Teor. Fiz. **70**, 749 (1999) [JETP Lett. **70**, 761 (1999)].
13. V. I. Al'shits, E. V. Darinskaya, I. V. Gektina, and F. F. Lavrent'ev, Kristallografiya **35**, 1014 (1990) [Sov. Phys. Crystallogr. **35**, 597 (1990)].
14. O. I. Datsko and V. I. Alekseenko, Fiz. Tverd. Tela (St. Petersburg) **39**, 1234 (1997) [Phys. Solid State **39**, 1094 (1997)].
15. M. I. Molotskii and V. N. Fleurov, Phys. Rev. B **52**, 15829 (1995).
16. S. A. Dembovskiĭ, E. A. Chechetkina, and S. A. Kozyukhin, Pis'ma Zh. Éksp. Teor. Fiz. **41**, 74 (1985) [JETP Lett. **41**, 88 (1985)].
17. E. V. Darinskaya, E. A. Petrzhik, S. A. Erofeeva, and V. P. Kisel', Pis'ma Zh. Éksp. Teor. Fiz. **70**, 298 (1999) [JETP Lett. **70**, 309 (1999)].
18. Yu. I. Golovin, R. B. Morgunov, A. A. Baskakov, *et al.*, Pis'ma Zh. Éksp. Teor. Fiz. **69**, 114 (1999) [JETP Lett. **69**, 127 (1999)].
19. A. A. Skvortsov, A. M. Orlov, and L. I. Gonchar, Zh. Éksp. Teor. Fiz. **120**, 134 (2001) [JETP **93**, 117 (2001)].
20. Yu. A. Osip'yan, Yu. I. Golovin, R. B. Morgunov, *et al.*, Pis'ma Zh. Éksp. Teor. Fiz. **69**, 110 (1999) [JETP Lett. **69**, 123 (1999)].
21. P. W. M. Jacobs, J. Phys. Chem. Solids **51**, 35 (1990).
22. J. E. Munoz-Santiuste and J. Garcia Sole, Phys. Rev. B **38**, 10874 (1988).
23. J. Qi, M. Tanaka, J. S. Ahn, and Y. Masumoto, J. Lumin. **87–89**, 1102 (2000).
24. V. Chernov, V. Melendrez Ao, T. Piters, and M. Barboza Flores, Radiat. Meas. **33**, 797 (2001).
25. Yu. I. Golovin, R. B. Morgunov, S. E. Zhulikov, and D. Yu. Golovin, Fiz. Tverd. Tela (St. Petersburg) **38**, 3047 (1996) [Phys. Solid State **38**, 1666 (1996)].
26. H. Nanto, Y. Hirai, M. Ikeda, *et al.*, Sens. Actuators A **53**, 223 (1996).
27. A. Lobnik, N. Majcen, K. Niederreiter, *et al.*, Sens. Actuators B **74**, 200 (2001).
28. S. Cordoba-Jabonero, I. Aguirre de Carser, M. Barboza-Flores, and F. Jaque, J. Alloys Compd. **323–324**, 847 (2001).
29. R. Akimoto, M. Kobayashi, and T. Suzuki, J. Phys. Soc. Jpn. **63**, 4616 (1994).

Translated by A. Bagatur'yants

JETP Letters, Vol. 76, No. 5, 2002, pp. 312–317. Translated from Pis'ma v Zhurnal Éksperimental'noĭ i Teoreticheskoĭ Fiziki, Vol. 76, No. 5, 2002, pp. 371–376.

Nonlinear NMR in a Superfluid B Phase of ^{3}He in Aerogel

V. V. Dmitriev[1, *], V. V. Zavjalov[1], D. E. Zmeev[1], I. V. Kosarev[1], and N. Mulders[2]

[1] *Kapitza Institute of Physical Problems, Russian Academy of Sciences, Moscow, 119334 Russia*

** e-mail: dmitriev@kapitza.ras.ru*

[2] *Department of Physics and Astronomy, University of Delaware, Newark, Delaware 19716, USA*

Received August 1, 2002

The properties of liquid ^{3}He in a low-density aerogel preliminarily covered with a few monolayers of ^{4}He were studied by pulsed and nonlinear CW NMR techniques. It was found that an NMR frequency shift from the Larmor value exhibits a sharp increase at a magnetization tilting angle exceeding 104°. Nonlinear CW NMR signals related to the formation of a macroscopic region featuring homogeneous precession of the magnetization (homogeneous precession domain) were observed. The experimental results confirm that the low-temperature superfluid ^{3}He phase in the aerogel is analogous to the B-phase in bulk ^{3}He and indicate that the spin supercurrents play an important role in the spin dynamics of superfluid ^{3}He in aerogel. © *2002 MAIK "Nauka/Interperiodica".*

PACS numbers: 67.57.Lm; 76.60.-k

1. Introduction. The theory of superfluid ^{3}He phases is well developed and in most cases shows a quantitative agreement with experiment. For this reason, superfluid ^{3}He is an ideal object for verification of the theoretical models of systems with nontrivial Cooper spin pairing. Presently, an important problem is to study the influence of impurities on such an object. Such a possibility was offered by development of the technology of low-density aerogels. An aerogel represents a "mop" consisting of SiO_2 strands with a diameter on the order of 30 Å, while the characteristic distance between strands amounts to 500–1000 Å (we imply so-called 98% aerogel, in which 98% of the volume is free, employed in most experiments with ^{3}He). Since the coherence length of superfluid ^{3}He (amounting to several hundreds of Angströms) significantly exceeds the diameter of strands, the strands play the role of impurities in ^{3}He.

The superfluidity of ^{3}He in aerogel was discovered several years ago [1, 2]. At present, it is known that the presence of strands leads to a small (20–30%) depression of the superfluid transition temperature in ^{3}He and that two superfluid ^{3}He phases, analogous to the superfluid A and B phases in bulk ^{3}He, may exist in the aerogel [3, 4]. However, the phase diagram of superfluid ^{3}He in aerogel exhibits qualitative differences from that of bulk ^{3}He. In particular, the region of existence of the equilibrium A-like phase is much smaller (even at large pressures and in strong magnetic fields) as compared to that of bulk ^{3}He; however, the A-like phase remains stable in a sufficiently wide temperature interval in a supercooled state.

Experiments in aerogel can be performed both with pure ^{3}He and in the presence of a small admixture of ^{4}He. In the former case, the NMR spectrum is significantly influenced by the paramagnetic solid ^{3}He, which a high magnetic susceptibility at low temperatures and whose two monolayers cover the surface of strands. Upon the introduction of ^{4}He, solid ^{3}He is replaced by nonmagnetic ^{4}He and the NMR response is fully determined by the liquid ^{3}He.

2. NMR in bulk ^{3}He-B. In the superfluid B phase of bulk ^{3}He, the frequency of linear (at small excitation amplitudes) CW NMR is determined by the angle ψ between the direction of external magnetic field **H** and the order parameter vector **n**: $\omega \approx \omega_L + \frac{\Omega_B^2}{2\omega_L}\sin^2\psi$, where Ω_B is the temperature-dependent longitudinal resonance frequency (Leggett frequency) for ^{3}He-B and $\omega_L = \gamma H$ is the Larmor frequency. Far from the cell walls, $\mathbf{n} \parallel \mathbf{H}$ and $\omega = \omega_L$. Near the wall, $\psi \approx 63°$ for **H** parallel to the wall plane, which leads to a shift of the frequency. As a result, the absorption line in the linear CW NMR spectrum become asymmetric, comprising a peak at the Larmor frequency and a long "tail" extended toward high frequencies and determined by a spatial distribution (texture) of the order parameter.

In the case of a pulsed NMR measured for sufficiently large magnetization tilting angles β, the system exhibits a texture transition and the **M** and **n** vectors exhibit precession as if the walls were absent (the Brinkman–Smith mode) [5]. The frequency of precession is ω_L if the β value does not exceed Θ_0 =

$\arccos(-1/4) \approx 104°$. For $\beta > \Theta_0$, the precession frequency varies by the law

$$\omega = \omega_L - \frac{4\Omega_B^2}{5\omega_L}(1 + 4\cos\beta)$$

The presence of spatial inhomogeneities of the precessing magnetization (e.g., due to a gradient of the field H) leads to the appearance of spin supercurrents carrying the longitudinal magnetization component. As a result, a homogeneously precessing two-domain structure (homogeneous precession domain, HPD [6]) may form in a closed ^{3}He-B volume. One of these domains represents a region of virtually equilibrium magnetization; in the other, the magnetization vector is rotated by an angle close to Θ_0 and exhibits in-phase precession at a Larmor frequency at the interdomain wall, the characteristic thickness of which usually amounts to 0.2–0.3 mm. The spin supercurrents also play an important role in determining the stability of an HPD: spatial inhomogeneities give rise to currents which tend to restore homogeneous precession.

Under CW NMR conditions, when a homogeneous magnetic field gradient (parallel to **H** and directed in the z axis) is applied to a sample and the RF field frequency ω_{rf} is fixed, an HPD is formed in the course of a gradual decrease of the homogeneous component of the external magnetic field H_0 (the RF field amplitude must be sufficiently large) [7]. The HPD begins to form when the coordinate z (determined by the condition $\omega_{rf} = \gamma H(z)$) reaches the cell boundary (z_c). Owing to the spin supercurrents, the magnetization tilting angle in this region may reach and exceed the Θ_0 value. When the field H_0 decreases, this region of the cell keeps in resonance with the RF field (due to the fact that β slightly exceeds Θ_0, which leads to a positive frequency shift). As a result, the HPD size increases and the spatial distribution of β is determined by the condition that the frequency of precession is equal to that of the RF field; the domain wall coordinate (z_0) is determined by the resonance condition $\omega_{rf} = \gamma H(z_0)$. The absorbed RF power is determined by a phase difference between the precessing magnetization and the RF field. This difference is established on a level such that the absorbed power equals the power dissipated within the HPD via the magnetic relaxation processes. The dissipation increases with the HPD size. As H_0 keeps decreasing, the HPD breaks (and is not restored when H_0 is scanned in the reverse direction). If the RF field is switched off in the presence of an HPD, the domain will retain its homogeneity and the magnetic relaxation will only reduce the HPD size: the domain wall moves and the frequency of a long- lived induction signal (the duration of which is significantly greater than the characteristic time of dephasing in an inhomogeneous magnetic field—$\tau = (\gamma\nabla HL)^{-1}$, where L is the cell length) gradually decreases from ω_{rf} to $\gamma H(z_c)$.

If the order parameter of a low-temperature superfluid ^{3}He phase in aerogel corresponds to that of the B phase in bulk ^{3}He, the NMR behavior in this system must be similar to that observed in bulk ^{3}He-B. Accordingly, it is natural to expect that the dependence of ω on β for nonlinear NMR would exhibit a feature at $\beta \approx 104°$. It can be also suggested that the spin supercurrents in the ^{3}He B-like phase in aerogel are qualitatively similar to those in bulk ^{3}He-B and can lead to HPD formation. However, until now the NMR investigations of ^{3}He in aerogel were mostly restricted to linear CW NMR response. These experiments showed that the NMR behavior of the ^{3}He B-like phase in aerogel is in fact like that of bulk ^{3}He-B: the NMR line exhibits broadening toward high frequencies (while a quantity analogous to the Leggett frequency is several times smaller in aerogel than in bulk ^{3}He-B) and the decrease of magnetic susceptibility with decreasing temperature is similar to that observed in bulk ^{3}He-B.

Until the present, pulsed NMR measurements were performed either for pure ^{3}He in aerogel (whereas no features in dependence of the NMR frequency on β were found near $\beta \approx \Theta_0$) or at small magnetization tilting angles [2, 8]. Recently, a study of the nonlinear CW NMR in superfluid ^{3}He B-like phase in aerogel was reported by the Grenoble group [9]. The NMR signal characteristics (dependence on the scan direction and the field gradient) reported in [9] corresponded to the behavior typical of the HPD. However, the region of existence and the amplitude of the signal observed in [9] were smaller than one may expect from an HPD with the length significantly exceeding the domain wall thickness. Thus, the question concerning the possible HPD formation in the B-like phase of ^{3}He in aerogel did not receive an unambiguous answer.

The aim of our experiments was to study the nonlinear NMR (in both pulsed and continuous modes) in superfluid B-like phase of ^{3}He in aerogel. The experiments, discussed below, were conducted in an aerogel with the surface covered with two monolayers (calculated estimate) of ^{4}He.

3. Experimental. The experiments were performed at a pressure of 25.5 bar in a magnetic field varied from 284 to 1082 Oe (which corresponded to NMR frequencies from 922 kHz to 3.51 MHz). The experimental chamber (Fig. 1), mounted on a nuclear demagnetization stage, comprised two similar cells of the same cylindrical shape (diameter, 5.3 mm; height, 5.6 mm) made of a Stycast-1266 epoxy resin. Each cell was surrounded by NMR coils (thermally insulated from the cell body). The first cell (cell 1) was almost completely filled with 98% aerogel (except for 0.15-mm gaps between the aerogel and internal wall surface). The second cell (cell 2) contained aerogel in the form of a disk with a thickness of ~2.4 mm, which was situated in the middle part of the sample volume. The required temperature was provided by a nuclear demagnetization

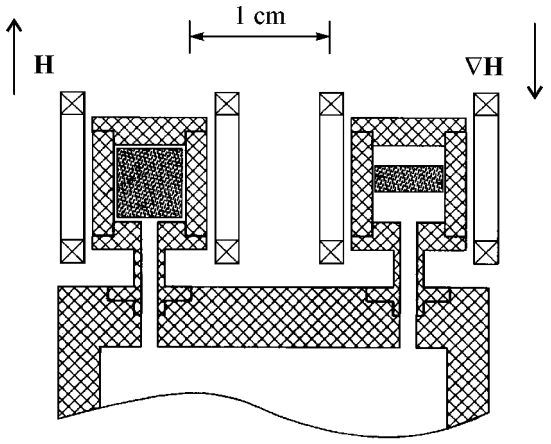

Fig. 1. Schematic diagram of the experimental chamber (see the text for explanations).

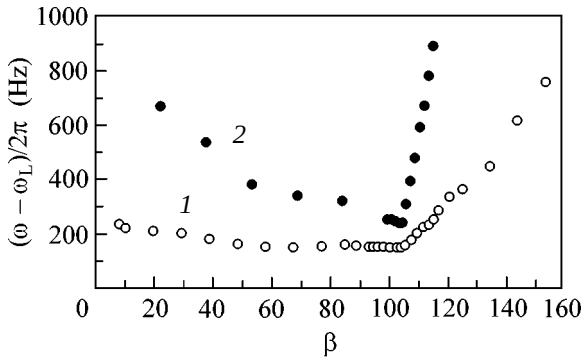

Fig. 2. Initial frequency of induction signal in ^{3}He-B in aerogel vs. the tilting angle of magnetization. (*1*) H = 1.01 kOe, $T \approx 0.83\,T_c^a$ and (*2*) H = 285 Oe, $T \approx 0.78\,T_c^a$.

cryostat and monitored by a platinum NMR thermometer gauge located in a special volume below the experimental cells.

4. Pulsed NMR of ^{3}He-B in aerogel. The pulsed NMR measurements were conducted only with cell 1. The sample was exposed to magnetization-tipping RF pulses at the NMR frequency. The free precession (induction) response signals were recorded in the memory of a computer and processed to determine the time dependence of the frequency and the signal amplitude.

The phase transitions in ^{3}He in aerogel were manifested by changes in the frequency, amplitude, and duration of the free induction signal in response to application of the small RF pulses (corresponding to the angles of magnetization deflection less than ~20°). Upon cooling below the superfluid transition temperature of ^{3}He in aerogel ($T_c^a \approx 0.76T_c$, where T_c = 2.37 mK is the superfluid transition temperature for bulk ^{3}He under the given conditions), the system exhibited two sequential transitions. First, there appeared and increased a negative shift of the NMR frequency relative to the Larmor value, which was related to the transition to a supercooled ^{3}He A-like phase in aerogel. Then, at a certain temperature of about $\approx 0.85\,T_c^a$, the sample converted into a B-like phase whereby the frequency shift became positive and increased with further decrease in the temperature [10]. On heating from the B-like phase, the shift decreased in proportion to $(1 - T)/T_c^a$ and vanished (being always positive) at $T = T_c^a$. These results agree with the recent experiments [4], where a similar behavior was observed by a CW NMR technique.

It was established that the free induction signal at large magnetization tilting angles significantly varies with time. For determining the dependence of ω on β, the time variation of the induction signal was extrapolated to the initial time instant (it should be noted that the results remain qualitatively the same for any reasonable method of determining the characteristic frequency at a given β, for example, by taking the average frequency of the Fourier transform of the frequency of the induction signal). Figure 2 shows a plot of the induction signal frequency versus initial magnetization deflection angle for the ^{3}He B phase in aerogel. As can be seen, the experimental curves exhibit a feature at $\beta \approx 104°$ whereby the signal frequency begins to grow sharply with β, as should be expected for the B phase. At the same time, we observed no signs of a textural transition to the Brinkman–Smith precession mode. As can be seen, the precession frequency at any magnetization tilting angle below 104° is significantly shifted from the Larmor value, while still varies depending on β. This result indicates that the texture of the order parameter is determined by the aerogel volume (and, probably, by the aerogel density inhomogeneities over distances much shorter than the characteristic cell size), rather than by the walls of the experimental cell.

5. HPD in ^{3}He-B in aerogel. Experiments devoted to determining the possibility of HPD formation in aerogel were performed with both cells. Figure 3 shows the CW NMR signal profiles measured in cell 1 on decreasing H_0 for various RF field amplitudes. The abscissa axis in Fig. 3 (and in the other plots of CW NMR signals) shows the homogeneous component of the applied magnetic field recalculated into a coordinate by the formula $z = (\gamma H - \omega_{rf})/\gamma\nabla H$. The point $z = 0$ corresponds to the validity of the resonance condition for bulk ^{3}He at the top of the cell, and z = –5.6 mm, at the bottom of the cell. When the domain wall occurs inside the cell, the resonance condition is obeyed at the middle of the wall (this is true for bulk ^{3}He-B and will be shown below to hold for an HPD in aerogel as well), and the abscissa in fact indicates the domain wall position.

The signal observed for a pumping field amplitude of ~0.02 Oe (Fig. 3b) is significantly higher than the signals measured at smaller amplitudes of pumping, which corresponds to HPD formation, growth (whereby the HPD occupies the entire cell), and breakage (for $z \approx -9.4$ mm). Upon breakage, no HPD is formed during the reverse scan. Our calibration of the NMR spectrometer showed that the NMR signal amplitude (Fig. 3b) corresponds to within 10% to the amplitude of the NMR signal anticipated from the HPD.

Figure 4 shows variation of the induction signal amplitude and frequency with time after the HPD was "grown" as described above and the RF field was switched off. As can be seen, the signal amplitude exhibits oscillations (rather than smoothly decaying to zero as in the case of bulk ^{3}He [7]), although the characteristic signal duration is large and the time dependence of frequency on average agrees well with that expected for a slow relaxation of the HPD. A total change of the induction signal frequency amounts to ≈1590 Hz, which coincides to a good accuracy with the frequency change calculated by the formula $\delta\omega = \gamma\nabla H L_0$ (where L_0 is the HPD length immediately before switching off the RF field), as it has to be in the case of HPD formation. Oscillations of the induction signal amplitude may be caused by spatial inhomogeneities (or anisotropy) of the aerogel density. These would result in inhomogeneities within the HPD and in a nonuniform magnetic dissipation over the HPD volume. This would lead to inhomogeneous β distribution over the sample and to dephasing of the precession in various parts of the aerogel. Spin supercurrents will tend to restore the homogeneous precession, thus giving rise oscillations in the precession phase distribution, analogous to the torsional HPD oscillations observed in bulk ^{3}He-B [11].

It should be noted that the magnetic dissipation may give rise, due to a low thermal conductivity of ^{3}He in aerogel, to significant temperature nonuniformities and resulting HPD inhomogeneities. In our experiments with CW NMR, HPD formation in cell 1 was accompanied by an increase in the temperature of ^{3}He in aerogel because of magnetic relaxation leading to energy dissipation. When the H_0 variation was stopped (i.e., the HPD length was fixed), the sample temperature continued to grow at a time constant on the order of one minute (estimates obtained from the data [12] on the thermal conductivity of ^{3}He in aerogel show that overheating may reach up to $0.1–0.2\,T_c^a$ at a characteristic power of several nanowatts, dissipated in the aerogel). The magnetic relaxation rate increases with temperature, and the HPD breaks within several minutes, since the dissipated power exceeds the maximum possible value of the absorbed power at a given RF field amplitude.

The overheating effects were barely manifested in cell 2, where the maximum distance from the aerogel center to bulk ^{3}He was several times smaller than in cell 1. In cell 2, the HPD initially formed, as a rule, in the volume free of aerogel. As the HPD length increased, it penetrated the aerogel and eventually filled the entire cell. Figure 5 shows the absorption and dispersion profiles measured during HPD formation in cell 2. Here (as well as in Fig. 3) the value $z = 0$ on the abscissa axis corresponds to the validity of the resonance condition

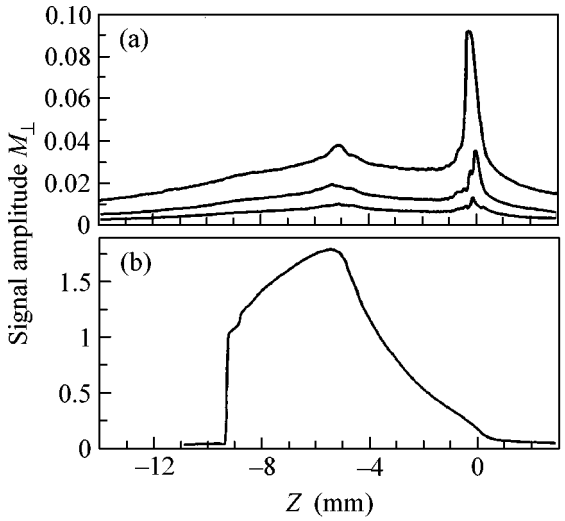

Fig. 3. Transverse magnetization amplitude profiles (i.e., the square root of the sum of squared absorption and dispersion signal intensities) measured at ∇H = 284 Oe/cm, $T \sim 0.67\,T_c^a$ and various RF field amplitudes: (a) 0.002, 0.005, and 0.01 Oe, in the order or increasing average signal intensity; (b) 0.02 Oe.

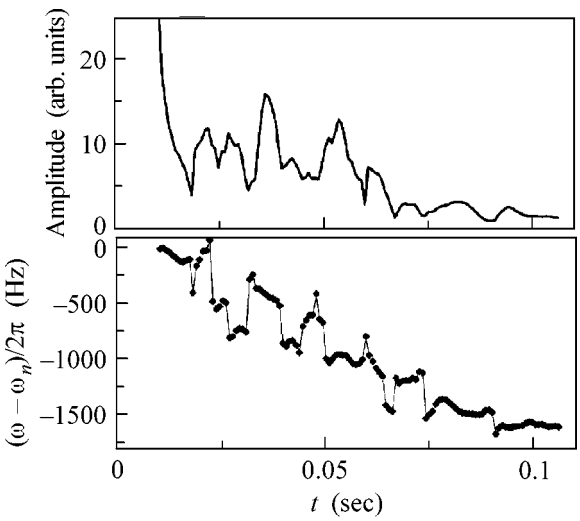

Fig. 4. Time variation of the amplitude and frequency of a long-lived NMR induction signal after switching off the RF field at an HPD length of ~4.9 mm in cell 1. The experimental conditions are the same as indicated for Fig. 3b.

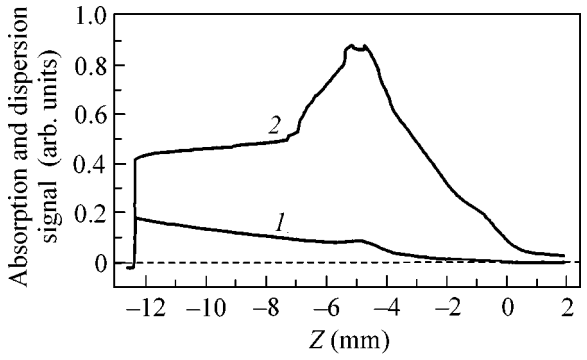

Fig. 5. Profiles of the (*1*) NMR absorption and (*2*) dispersion signals during the HPD formation in cell 2 for H = 284 Oe, ∇H = 0.94 Oe/cm, $T \sim 0.66\,T_c^a$, an RF field amplitude of ~0.01 Oe.

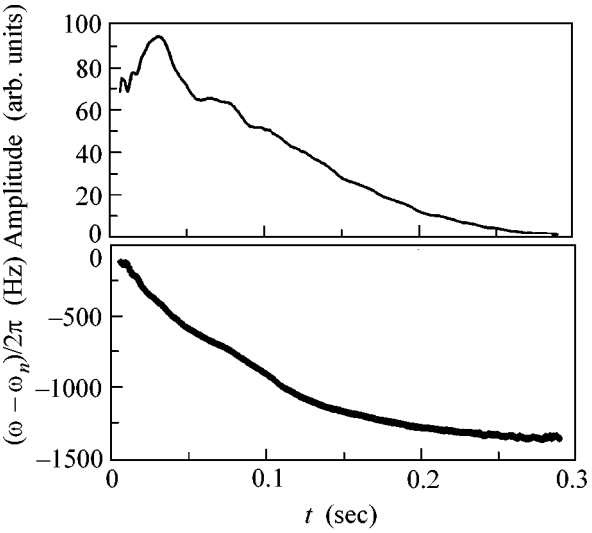

Fig. 6. Time variation of the amplitude and frequency of a long-lived induction signal after switching off the RF field at an HPD length of ~4.7 mm in cell 2. The experimental conditions are the same as indicated for Fig. 5.

for bulk ^{3}He at the top of the cell, the value of z = –5.6 mm implies the same at the bottom of the cell, while z = –1.5 and –3.9 mm correspond to the aerogel–bulk ^{3}He boundaries.

As can be seen from Fig. 5, the NMR absorption both in bulk ^{3}He and in aerogel monotonically increases with the HPD length (a faster signal buildup in the initial HPD growth stage is related to domain wall formation). Note that no sharp features are observed when the domain wall crosses the aerogel–bulk ^{3}He interface. Previously, we repeatedly observed the growth of the HPD absorption by a nearly linear law (over the HPD length) for bulk ^{3}He (unpublished data of many experiments performed in the past years). A mechanism of this absorption still remains unclear and requires further investigation. Here, we will only note that this mechanism is effective in aerogel as well. It was found (in this study, as well as in the preceding experiments with bulk ^{3}He) that the absorption increases with the temperature and is virtually independent of the external magnetic field gradient.

In contrast to the results of experiments in cell 1, the amplitude and frequency of the induction signal from the HPD, measured after switching off the RF field, varied in a smooth manner, which was indicative of homogeneity of the HPD retained in the course of the relaxation process (Fig. 6). No distinguishable features were observed at the frequency of the induction signal corresponding to a moment of the domain wall crossing the aerogel–bulk ^{3}He boundary (for a current coordinate determined by the signal frequency).

Using the sample in cell 2, we also studied the temperature dependence of the HPD formation process. It was established that the HPD did not penetrate the aerogel at a temperature slightly below T_c^a (usually, on the order of $0.9\,T_c^a$), although an HPD in the upper aerogel-free volume part of the cell forms at temperatures up to that corresponding to the transition of bulk ^{3}He into the A-phase ($T_{AB} \approx 1.2\,T_c^a$). On the other hand, an inverse pattern was observed at a sufficiently low temperature: the HPD formation in the bulk (aerogel-free) part of cell 2 took place at greater RF field amplitudes as compared to those in aerogel. As a result, there was a certain interval of the RF field amplitudes in which it was possible to form an HPD only in aerogel in the absence of HPD in bulk ^{3}He. Figure 7 shows two NMR signal profiles measured at $T \lesssim 0.65\,T_c^a$ for different amplitudes of the RF field (curve *1* corresponds to the case of HPD formation in aerogel only). The fact that the abscissa corresponding to the signal growth onset (curve *1*) is close to the coordinate of the aerogel–bulk ^{3}He interface shows that the NMR frequency in the domain wall is close to the Larmor value; this is probably indicative of a texture transition of the Brinkman–Smith type in the case of the HPD formation in aerogel under CW NMR conditions. In contrast to the pulsed NMR data (Fig. 2), this results in an almost zero shift of the precession frequency from the Larmor value at magnetization tilting angles close to Θ_0 (otherwise, the HPD signal growth onset would be shifted to the left by a value corresponding to the frequency shift from the Larmor value, which amounts to not less than 1 mm in the z scale).

6. Conclusion. The results of our investigation leave no doubt that a low-temperature superfluid ^{3}He phase in aerogel is analogous to the B phase of bulk ^{3}He. It was demonstrated that the spin supercurrents play an important role in the spin dynamics of ^{3}He-B in aerogel, as well as in bulk ^{3}He-B, and can lead to the formation of

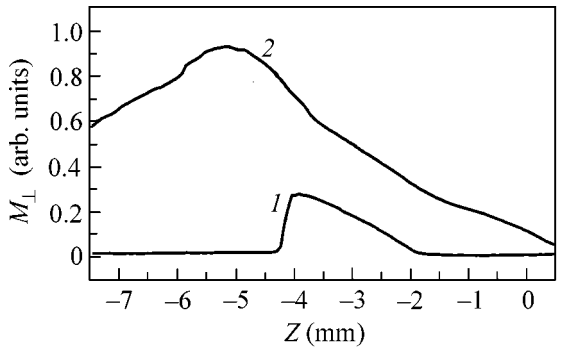

Fig. 7. Transverse magnetization amplitude profiles (i.e., the square root of the sum of squared absorption and dispersion signal intensities), measured at H = 284 Oe, ∇H = 0.94 Oe/cm, $T \lesssim 0.65 T_c^a$ and an RF field amplitude of (*1*) 0.02 and (*2*) 0.04 Oe.

a homogeneously precessing domain. Similar to the case of bulk ^{3}He-B, HPD formation can be used as a probe for studying the superfluid ^{3}He-B phase in aerogel. In particular, it would be very interesting to elucidate questions concerning the observation and study of the "catastrophic" relaxation of ^{3}He in aerogel, by analogy with the phenomenon taking place in bulk ^{3}He-B at temperatures on the order of $0.4T_c$ [13], the nature of which is still unclear.

The authors are grateful to J. Parpia who suggested the idea of using cell partly filled with aerogel for the experiments, and to I. Fomin for fruitful discussions. This study was supported by the U.S. Civilian Research and Development Foundation (grant no. RP1-2098), by the Russian Foundation for Basic Research (project nos. 00-02-17514 and 00-15-96574), and by the Ministry of Industry, Science, and Technology of the Russian Federation.

REFERENCES

1. J. V. Porto and J. M. Parpia, Phys. Rev. Lett. **74**, 4667 (1995).
2. D. T. Sprague, T. M. Haard, J. B. Kycia, *et al.*, Phys. Rev. Lett. **75**, 661 (1995).
3. G. Gervais, T. M. Haard, R. Nomura, *et al.*, Phys. Rev. Lett. **87**, 035701 (2001).
4. B. I. Barker, Y. Lee, L. Polukhina, *et al.*, Phys. Rev. Lett. **85**, 2148 (2000).
5. A. S. Borovik-Romanov, Yu. M. Bun'kov, V. V. Dmitriev, and Yu. M. Mukharskiĭ, Pis'ma Zh. Éksp. Teor. Fiz. **37**, 600 (1983) [JETP Lett. **37**, 716 (1983)]; V. L. Golo, A. A. Leman, and I. A. Fomin, Pis'ma Zh. Éksp. Teor. Fiz. **38**, 123 (1983) [JETP Lett. **38**, 146 (1983)].
6. A. S. Borovik-Romanov, Yu. M. Bun'kov, V. V. Dmitriev, *et al.*, Zh. Éksp. Teor. Fiz. **88**, 2025 (1985) [Sov. Phys. JETP **61**, 1199 (1985)]; I. A. Fomin, Zh. Éksp. Teor. Fiz. **88**, 2039 (1985) [Sov. Phys. JETP **61**, 1207 (1985)].
7. A. S. Borovik-Romanov, Yu. M. Bun'kov, V. V. Dmitriev, *et al.*, Zh. Éksp. Teor. Fiz. **96**, 956 (1989) [Sov. Phys. JETP **69**, 542 (1989)].
8. D. T. Sprague, T. M. Haard, J. B. Kycia, *et al.*, Phys. Rev. Lett. **77**, 4568 (1996).
9. Yu. M. Bun'kov, in *Proceedings of Seminar of the Institute of Physical Problems, Russian Academy of Sciences, 2001*; Yu. Bunkov, E. Collin, H. Godfrin, and R. Harakaly, in *Proceedings of 23rd International Conference on Low Temperature Physics, LT23, Hiroshima, 2002*, submitted to Physica B.
10. V. V. Dmitriev, I. V. Kosarev, N. Mulders, *et al.*, in *Proceedings of 23rd International Conference on Low Temperature Physics, LT23, Hiroshima, 2002*, submitted to Physica B.
11. Yu. M. Bun'kov, V. V. Dmitriev, and Yu. M. Mukharskiĭ, Pis'ma Zh. Éksp. Teor. Fiz. **43**, 131 (1986) [JETP Lett. **43**, 168 (1986)]; I. A. Fomin, Pis'ma Zh. Éksp. Teor. Fiz. **43**, 134 (1986) [JETP Lett. **43**, 171 (1986)].
12. B. I. Barker, L. Polukhina, J. F. Poko, *et al.*, J. Low Temp. Phys. **113**, 635 (1998).
13. Yu. M. Bunkov, V. V. Dmitriev, J. Nyeki, *et al.*, Physica B (Amsterdam) **165–166**, 675 (1990); Yu. M. Bunkov, S. N. Fisher, A. M. Guenault, *et al.*, Phys. Rev. Lett. **68**, 600 (1992).

Translated by P. Pozdeev

JETP Letters, Vol. 76, No. 5, 2002, pp. 318–320. Translated from Pis'ma v Zhurnal Éksperimental'noĭ i Teoreticheskoĭ Fiziki, Vol. 76, No. 5, 2002, pp. 377–379.

Hydrogen Tunneling Modes in α-Mn Suppressed by Elastic Stresses

V. E. Antonov[1], V. P. Glazkov[2, *], D. P. Kozlenko[3], B. N. Savenko[3], V. A. Somenkov[2], and V. K. Fedotov[1]

[1] *Institute of Solid State Physics, Russian Academy of Sciences, Chernogolovka, Moscow region, 142432 Russia*
[2] *Russian Research Centre Kurchatov Institute, Moscow, 123182 Russia*
* *e-mail: glazkov@isssph.kiae.ru*
[3] *Laboratory of Neutron Physics, Joint Institute for Nuclear Research, Dubna, Moscow region, 141980 Russia*
Received August 6, 2002

Behavior of the tunneling mode of hydrogen in $MnH_{0.04}$ and $MnH_{0.07}$ under high pressures in sapphire anvils was studied by the method of incoherent inelastic neutron scattering (INS). It is established that the INS peak corresponding to the hydrogen tunneling in a double-well potential disappears at a pressure of 0.8 GPa in a quasi-hydrostatic regime, while being retained without visible changes under pure hydrostatic conditions. An analogous, albeit weaker, suppression of the tunneling mode takes place upon grinding of a freshly prepared sample. The effect of suppression of the hydrogen tunneling modes by applied inhomogeneous elastic stresses is explained by a shift of the energy levels in the adjacent wells caused by the static displacements. © *2002 MAIK "Nauka/Interperiodica".*

PACS numbers: 62.50.+p; 61.12.Ex

Recent experiments [1–3] on the neutron diffraction and inelastic neutron scattering (INS) from solid solutions of hydrogen in α-Mn revealed the effect of hydrogen tunneling at relatively high temperatures (up to about 90 K). The effect was manifested by the appearance of a temperature-dependent intense narrow peak at 6.3 meV in the INS spectra, which was explained by splitting of the ground vibrational state as a result of the tunneling of hydrogen atoms between adjacent closely spaced 12e positions. The energy of the observed tunneling modes was about 30 times that for the other quantum systems [4, 5].

The nature of the observed effect is probably related to the fact that hydrogen atoms incorporated into complex Bravais lattices (such as those of α- and β-Mn) occur in positions spaced much more closely as compared to the case of hydrogen solutions in other metals possessing simple lattices. For example, the neutron diffraction data [2] showed that hydrogen atoms in α-Mn randomly occupy 12e dumb-bell positions in the space group $I43m$, the distance between which (0.68 Å) is much shorter than that typical of the hydrogen atoms dissolved in bcc metals (2.2 Å). It was natural to suggest that a decrease in volume, leading to a reduction of the distances between possible positions of hydrogen atoms and to a change in the shape of the double-well potential, may significantly influence the tunneling of hydrogen. In connection with this, we studied the effect of high pressures on the effect of hydrogen tunneling in α-Mn by method of incoherent INS.

The experiments were performed on the $MnH_{0.04}$ and $MnH_{0.07}$ samples prepared as described previously [6]. The powder of α-Mn was saturated with hydrogen (generated via decomposition of aluminum hydride) in a high-pressure chamber. The hydrogenation process was conducted at a pressure of 0.85 GPa and a temperature of 623 K for 4 h, followed by rapid cooling to room temperature. The content of dissolved hydrogen was determined by hot extraction into a calibrated volume.

The neutron scattering measurements were performed in a temperature interval from 15 to 100 K on a DN-12 spectrometer operating in the INS mode [7] using an IBR-2 reactor of the Laboratory of Neutron Physics (JINR). For this purpose, a ring-shaped pyrolytic graphite analyzer was placed between the samples and a ring detector composed of 16 ^{3}He counters of the SNM-31 type, so that the scattering angle was $2\theta = 90°$ and the energy analyzed was 14.9 meV.

High pressures were applied to the samples placed into special cells with sapphire anvils [8]. Samples with a volume of ~2 mm^3 were loaded at a pressure of up to 20 kbar in a quasi-hydrostatic regime. Purely hydrostatic conditions were created by filling anvils with a special fluid (Fluorinert). Samples in a high-pressure chamber were cooled using a special cryogenic refrigerator.

The INS spectra of freshly prepared samples (Fig. 1a) showed that a decrease in temperature below 100 K leads to the appearance of a sharp resonance

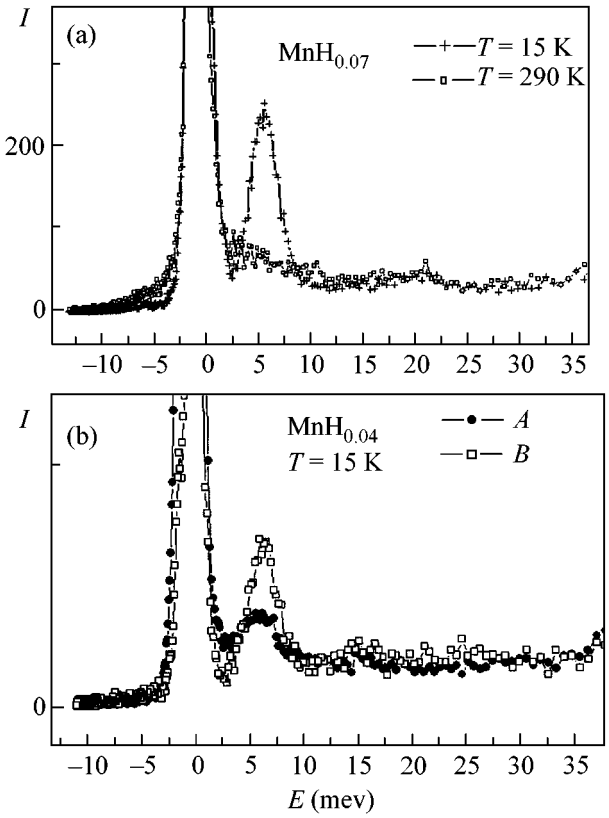

Fig. 1. INS spectra measured on a DN-12 spectrometer (a) for $MnH_{0.07}$ at different temperatures and (b) for freshly prepared and triturated $MnH_{0.04}$ samples.

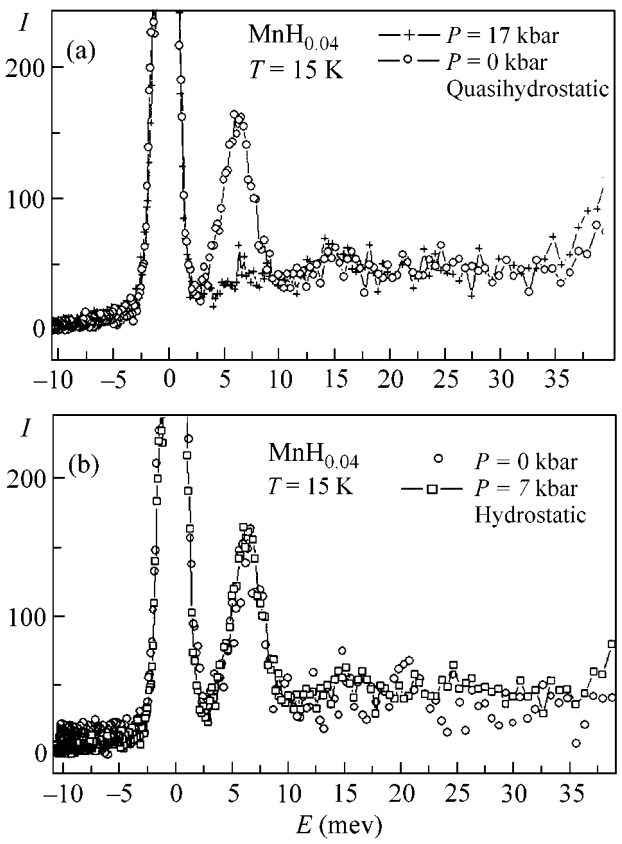

Fig. 2. INS spectra measured on $MnH_{0.04}$ samples loaded by different pressures in sapphire anvils under (a) quasi-hydrostatic and (b) purely hydrostatic conditions.

peak at 6.4 meV, which agrees with the previous results [3] and corresponds to the tunneling motion of hydrogen atoms in the double-well potential. The peak amplitude significantly decreases upon dry or wet (ethanol) trituration of the samples (Fig. 1b). Upon loading in a quasi-hydrostatic mode in sapphire anvils, the INS spectrum exhibits a dramatic change: the peak at 6.4 meV disappears already at a pressure of about 8 kbar and is restored neither at higher pressures (17 kbar) nor upon unloading (Fig. 2a). Since the phenomenon is observed in both $MnH_{0.04}$ and $MnH_{0.07}$ samples, the effect of pressure is independent of (or weakly dependent on) the hydrogen concentration.

The above results suggest that the effect of suppression of the hydrogen tunneling states is related to the residual elastic stresses (or defects) arising in the samples as a result of nonhydrostatic loading or grinding, while the contribution of homogeneous compression is small. In order to verify this assumption, we conducted experiments under hydrostatic conditions, using freshly prepared samples loaded in anvils filled with Fluorinert. In this case, no significant changes in the INS peak at 6.4 meV were observed: the intensity and the width and position of the peak remained virtually the same upon hydrostatic loading (Fig. 2b).

Thus, changes in intensity of the INS peak related to hydrogen tunneling are caused by the local elastic stresses in the sample, either induced by inhomogeneous pressure or produced by grinding, rather than by applied pressure as such.

The probability of tunneling in a defect-free crystal is determined as

$$W \approx \Delta^2/\omega,$$

where Δ is the tunneling bandwidth and ω is the characteristic frequency of the dynamic displacements caused by the interaction with lattice vibrations [9, 10]. The probability of tunneling in a crystal strained by elastic stresses must be significantly decreased by a shift δ between the energy levels:

$$W \approx \Delta^2 \frac{\omega}{\omega^2 + \delta^2}.$$

In the absence of local stresses, a shift of levels arises due to the dynamic displacements and determines the temperature dependence of the tunneling probability. In our experiments, the shift of levels is determined by static (rather than dynamic) displacements. The large magnitude of this shift is explained by the elastic mod-

uli of the metal matrix being much higher as compared to those of a quantum crystal [11]. Analogous manifestations of the tunneling modes suppressed by local elastic stresses should probably be observed in other quantum systems as well, albeit being less pronounced in cases of lower elastic moduli.

The authors are grateful to L.A. Maksimov for fruitful discussions and valuable remarks, and to Yu.M. Kagan and E.G. Ponyatovskiĭ for discussion of the results.

This study was supported by the Russian Foundation for Basic Research (project nos. 00-02-17077 and 99-02-17299) and by the Federal Program "Leading Scientific Schools" (project no. 00-15-96712).

REFERENCES

1. V. E. Antonov, T. E. Antonova, N. A. Chirin, *et al.*, Scr. Mater. **34**, 1331 (1996).
2. V. K. Fedotov, V. E. Antonov, K. Comell, *et al.*, J. Phys.: Condens. Matter **10**, 5255 (1998).
3. A. I. Kolesnikov, V. E. Antonov, S. M. Bennington, *et al.*, Physica B (Amsterdam) **263–264**, 421 (1999).
4. T. Springer, in *Dynamics of Solids and Liquids by Neutron Scattering* (Springer-Verlag, Berlin, 1977), p. 380.
5. H. Wipf, in *Hydrogen in Metals III*, Ed. by H. Wipf (Springer-Verlag, Berlin, 1997), p. 51.
6. E. G. Ponyatovsky, V. E. Antonov, and I. T. Belash, in *Problems in Solid State Physics*, Ed. by A. M. Prohorov and A. S. Prohorov (Mir, Moscow, 1984), p. 109.
7. V. L. Aksenov, A. M. Balagurov, S. L. Platonov, *et al.*, High Press. Res. **14**, 181 (1995).
8. V. P. Glazkov and I. N. Goncharenko, Sov. Phys. Tech. High Press. **1**, 56 (1991).
9. Yu. M. Kagan and L. A. Maksimov, Zh. Éksp. Teor. Fiz. **79**, 1363 (1980) [Sov. Phys. JETP **52**, 688 (1980)].
10. Yu. M. Kagan, L. A. Maksimov, and N. F. Prokof'ev, Pis'ma Zh. Éksp. Teor. Fiz. **36**, 204 (1982) [JETP Lett. **36**, 253 (1982)].
11. A. F. Andreev, Usp. Fiz. Nauk **118**, 251 (1976) [Sov. Phys. Usp. **19**, 137 (1976)].

Translated by P. Pozdeev

JETP Letters, Vol. 76, No. 5, 2002, pp. 321–325. Translated from Pis'ma v Zhurnal Éksperimental'noĭ i Teoreticheskoĭ Fiziki, Vol. 76, No. 5, 2002, pp. 380–384.

Critical Current in a System of Two Superconductors Connected by a Short Small-Diameter Normal Metal Bridge

Yu. N. Ovchinnikov[1, 2] and A. I. Larkin[1, 3]

[1] *Landau Institute for Theoretical Physics, Russian Academy of Sciences, Moscow, 117940 Russia*

[2] *Max-Planck Institute for Physics of Complex System, D-01187 Dresden, Germany*

[3] *Theoretical Physical Institute, University of Minnesota, Minneapolis, Minnesota 55455, USA*

Received July 31, 2002; in final form, August 6, 2002

It is shown that states with phase increments $\delta\varphi > \pi$ can form in superconductor–narrowing (normal metal)–superconductor systems. If the conditions $a \ll l \ll \xi(0)$, where a is the cross-sectional size of the narrowing, l is the length of narrowing, and $\xi(0)$ is the correlation radius at zero temperature, are satisfied, there is a region of parameters (a, l, $\xi(0)$, T) in which the critical current is attained in solutions with a phase difference $\delta\varphi > \pi$. © *2002 MAIK "Nauka/Interperiodica".*

PACS numbers: 74.50.+r; 74.60.Jg

Superconducting systems with a "bottleneck" to current passage have been studied in many works [1–6]. The simplest systems of this kind are SIS systems (superconductor–insulator–superconductor). Such systems (Josephson contacts) have been used extensively, and the theory of both stationary and nonstationary phenomena in them has been developed as early as the late 1960s [1–5]. Superconductor–narrowing (normal metal)–superconductor systems are more complicated, and the theory of nonstationary phenomena in them cannot be considered complete. We will show for the simplest example of a superconductor–short "impure" normal metal bridge–superconductor system that even the critical current problem has not been solved correctly. This circumstance is, we believe, in part related to advances in the theory of SIS systems. One of the first works on an S–normal metal narrowing–S system dates back to 1975 [7]. A superconductor–narrowing of the same material–superconductor system was considered in [8]. In particular, current was found to be a function of phase difference in the $[-\pi, \pi]$ interval in both works. Below, we analyze superconductor–impure-normal-metal narrowing–superconductor systems and determine the dependence of current on the phase difference in a wide range of phase difference values. We show that the situation in which critical current is attained at a phase difference much larger than π in the $(\xi(0)/l)\,(\Delta/T_c)$ parameter, where l is the bridge length, a is the cross-sectional bridge size, and Δ is the order parameter in the superconductor, is quite realistic. The bridge length is assumed to be much smaller than $(D/\pi T_c)^{1/2}$, where T_c is the transition temperature in superconducting beaches. It is assumed for simplicity that the contact is symmetrical and the transparency at the SN boundary is equal to one, which allows the simplest boundary conditions to be used, namely, those of the continuity of Green functions and their derivatives at interfaces. In the "impure" limit, the equations for the Green functions α and β for a superconductor have the form [9, 10]

$$\alpha\Delta - \beta\omega + \frac{D}{2}\left(\alpha\partial_-^2\beta - \beta\frac{\partial^2\alpha}{\partial r^2}\right) = \alpha\beta\Gamma, \qquad \alpha^2 + \beta\beta^* = 1, \tag{1}$$

where $D = vl_{tr}/3$ is the diffusion coefficient, $\partial_- = \partial/\partial\mathbf{r} - 2ie\mathbf{A}$, $\mathbf{A}$ is the vector potential, and $\Gamma = \tau_s^{-1}$ is the electron time of travel with spin flip.

The coupling constant in the bridge is zero; therefore, $\Delta = 0$. It is also assumed that $\Gamma = 0$ and $\mathbf{A} = 0$. Current density j is expressed through the β Green function as

$$j = -ie\nu D 2\pi T \sum_{\omega > 0} (\beta^*\partial_-\beta - \beta\partial_+\beta^*), \tag{2}$$

where $\nu = mp/2\pi^2$ is the density of states on the Fermi surface. Set

$$\alpha = \sin\theta, \quad \beta = \cos\theta\exp(i\varphi). \tag{3}$$

Within a normal metal bridge, Eq. (1) reduces to a system of two equations, one of which,

$$\frac{\partial}{\partial x}\left(\frac{\partial\varphi}{\partial x}\cos^2\theta\right) = 0, \tag{4}$$

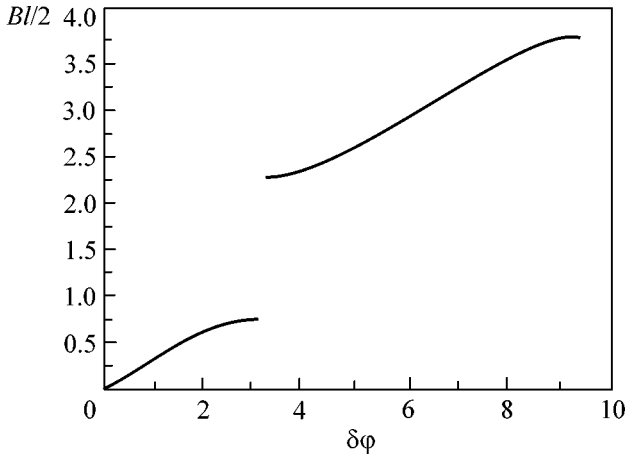

Dependence of the $Bl/2$ value on phase difference $\delta\varphi$.

is a corollary to the law of current conservation. The solution to Eq. (4) is

$$\frac{\partial\varphi}{\partial x} = \frac{A}{\cos^2\theta}, \tag{5}$$

where $A \equiv A(\omega)$ is the constant of integration. Using Eq. (4) allows the second equation to be transformed as

$$\frac{\partial}{\partial x}\left\{\omega\sin\theta + \frac{D}{4}\left[\left(\frac{\partial\theta}{\partial x}\right)^2 + \frac{A^2}{\cos^2\theta}\right]\right\} = 0. \tag{6}$$

This means that system (1) has two integrals of motion. Equation (6) gives

$$\frac{\partial\sin\theta}{\partial x} = \pm\left\{\left[B^2 - A^2 - \frac{4\omega}{D}\sin\theta\right] - \left(B^2 - \frac{4\omega}{D}\sin\theta\right)\sin^2\theta\right\}^{1/2}, \tag{7}$$

where B is the second constant of integration. Generally, Eq. (7) is solved in elliptical functions. In our problem with a short bridge, the $\{A, B\}$ values are large. We use Eq. (7) to find the $\sin\theta$ function,

$$\sin\theta = \pm\sqrt{1 - Z^2}\cos\left(Bx - \frac{Bl}{2} + \gamma\right), \tag{8}$$

where $Z = A/B$ and γ is the constant of integration. For a symmetrical contact,

$$\gamma = 0. \tag{9}$$

Under the assumption that only the bottleneck region is important, the phase difference $\delta\varphi$ between two superconductors is obtained from Eq. (5) in the form

$$\delta\varphi = A\int_0^l \frac{dx}{\cos^2\theta} = Z\int_0^{2Bl} \frac{dy}{(1+Z^2) - (1-Z^2)\cos(y - Bl)}. \tag{10}$$

The Bl value is a function of two variables, $(\delta\varphi, Z)$. At a fixed Z value, Eq. (10) yields

$$\frac{\partial(Bl)}{\partial(\delta\varphi)} = \frac{(1+Z^2) - (1-Z^2)\cos(Bl)}{2Z}. \tag{11}$$

It follows from this equation that the Bl value at a fixed Z value is an unambiguous monotonically increasing function of $\delta\varphi$.

The integration in Eq. (10) yields

$$\delta\varphi = 2\arctan\left[\frac{1}{Z}\tan\left(\frac{Bl}{2}\right)\right]. \tag{12}$$

In the region of phase gradients, as long as the current density is not too high, we can use the boundary condition of continuity of function α at the superconductor–normal metal interface using the unperturbed superconductor α value,

$$\frac{\omega}{\sqrt{\omega^2 + \Delta^2}} = \pm\sqrt{1 - Z^2}\cos\left(\frac{Bl}{2}\right). \tag{13}$$

Equations (12) and (13) give

$$Z = \frac{\Delta}{(\omega^2 + \Delta^2)^{1/2}} \frac{\left|\cos\left(\frac{\delta\varphi}{2}\right)\right|}{\left(1 - \frac{\Delta^2}{\omega^2 + \Delta^2}\sin^2\left(\frac{\delta\varphi}{2}\right)\right)^{1/2}}, \tag{14}$$

$$\cos\left(\frac{Bl}{2}\right) = \pm\left(1 - \frac{\Delta^2}{\omega^2 + \Delta^2}\sin^2\left(\frac{\delta\varphi}{2}\right)\right)^{1/2}. \tag{15}$$

As phase difference $\delta\varphi$ passes points $\pi(2N + 1)$ (N is an integer), the Bl function has discontinuities. The $\delta(Bl/2)$ jump value is

$$\delta\left(\frac{Bl}{2}\right) = 2\left(\frac{\pi}{2} - \arccos\left(\frac{\omega}{\sqrt{\omega^2 + \Delta^2}}\right)\right). \tag{16}$$

The Bl value is an odd function of phase difference $\delta\varphi$. The dependence of $Bl/2$ on $\delta\varphi$ is schematically shown in the figure. The general solution to Eq. (10) for the $Bl/2$ value can be written in the form

$$\frac{Bl}{2} = \pi N + \arctan\left(Z\tan\left(\frac{\delta\varphi}{2}\right)\right), \tag{17}$$

where N is the jump number.

The current density at the contact is determined by Eq. (2):

$$j = \frac{e\nu D}{l} 8\pi T \sum_{\omega > 0} \Delta \frac{\left|\cos\left(\frac{\delta\varphi}{2}\right)\right|}{\left(\omega^2 + \Delta^2 \cos^2\left(\frac{\delta\varphi}{2}\right)\right)^{1/2}} \times \left[\pi N + \arctan\left(\frac{\Delta\left|\cos\left(\frac{\delta\varphi}{2}\right)\right|}{\left(\omega^2 + \Delta^2 \cos^2\left(\frac{\delta\varphi}{2}\right)\right)^{1/2}} \tan\left(\frac{\delta\varphi}{2}\right)\right)\right]. \quad (18)$$

At $N \neq 0$, the major contribution to current density is made by the first term in square brackets in Eq. (18). At $N \neq 0$, the equation

$$j = \frac{8\pi e\nu D}{l} N\Delta \left|\cos\left(\frac{\Delta\varphi}{2}\right)\right| \ln\left(\frac{\pi^2 N^2 D}{l^2 \max(\pi T, \Delta)}\right) \quad (19)$$

has logarithmic accuracy. Impure metal conductivity σ is

$$\sigma = 2\nu D e^2. \quad (20)$$

Using Eq. (20), total current I through the contact can be written as

$$I = \frac{2\pi}{eR} \Delta N \left|\cos\left(\frac{\delta\varphi}{2}\right)\right| \ln\left(\frac{\pi^2 N^2 D}{l^2 \max(\pi T, \Delta)}\right), \quad (21)$$

where R is the resistance of the narrowing in the normal state. An increase in current through the bottleneck causes an increase in N up to N_{cr}. The critical N_{cr} value is found from the condition that current density is large to the extent that the Δ superconductor order parameter is suppressed near the bottleneck. At $N \sim N_{cr}$, Eq. (21) for the current through the contact ceases to be valid.

Let us find N_{cr} and the current through the contact at $N \sim N_{cr}$. We will use a simpler model in which a weak connection is the neck of the hyperboloid of revolution [8]. The coordinates of hyperboloid points are given by the orthogonal curvilinear coordinates $\{u, v, \psi\}$ [11]

$$\begin{aligned} x &= a \sin u \cosh v \cos\psi, \\ y &= a \sin u \cosh v \sin\psi, \\ z &= a \cos u \sinh v, \end{aligned} \quad (22)$$

where $0 \leq u < u_s$. As follows from Eq. (22), the surface of the hyperboloid is given by the equation

$$u = u_s. \quad (23)$$

Suppose that the mean free path of electrons is $l_{tr} \ll a u_s$, where $a \ll \xi(0)$. If these conditions are met, the $\{\theta, \varphi\}$ functions only depend on one coordinate v. We find from Eq. (1) that

$$\frac{\partial}{\partial \mathbf{r}}\left(\frac{\partial\varphi}{\partial \mathbf{r}} \cos^2\theta\right) = \frac{1}{a^2 \cosh v (\cos^2 u \cosh^2 v + \sin^2 u \cosh^2 v)} \times \frac{\partial}{\partial v}\left(\cosh v \cos^2\theta \frac{\partial\varphi}{\partial v}\right) = 0. \quad (24)$$

The solution to Eq. (24) is

$$\frac{\partial\varphi}{\partial v} = \frac{A}{\cosh v \cos^2\theta}, \quad (25)$$

where A is the constant of integration. Using Eq. (25) and the condition $a \ll \xi(0)$, we transform Eq. (1) for the θ function to the form valid at all v values,

$$\frac{\partial}{\partial v}\left[\cosh^2 v \left(\frac{\partial\theta}{\partial v}\right)^2 + \frac{A^2}{\cos^2\theta}\right] + \frac{4a^2}{D} \cosh^4 v \left[\omega \frac{\partial \sin\theta}{\partial v} + \Delta \frac{\partial \cos\theta}{\partial v}\right] = 0. \quad (26)$$

In the region of large gradient terms, only the first term in Eq. (26) should be retained. This equation is easily solved, and, taking into account $v \longrightarrow -v$ symmetry, the solution has the form

$$\sin\theta = \pm\sqrt{1 - \frac{A^2}{B^2}} \cos[B(\arctan(e^v) - \arctan(e^{-v}))]. \quad (27)$$

Phase change $\delta\varphi$ in passing through the neck of the hyperboloid is determined by the equation

$$\delta\varphi = 2A \int_0^\infty \frac{dv}{\cosh v \left[1 - \left(1 - \frac{A^2}{B^2}\right) \cos^2(B(\arctan(e^v) - \arctan(e^{-v})))\right]} = 2\arctan\left(\frac{B}{A} \tan\left(\frac{\pi B}{2}\right)\right). \quad (28)$$

The solution to Eq. (28) can be written in the form

$$\frac{\pi B}{2} = \pi N + \arctan\left(\frac{A}{B}\tan\left(\frac{\delta\varphi}{2}\right)\right). \quad (29)$$

In the $v \gg 1$ region, we can conveniently pass to spherical coordinates by setting

$$\rho = a\cosh v. \quad (30)$$

Equation (26) then takes the form

$$\frac{1}{\rho^2}\frac{\partial}{\partial\rho}\left(\rho^2\frac{\partial\theta}{\partial\rho}\right) + \frac{2}{D}(\omega\cos\theta - \Delta\sin\theta) = 0, \quad (31)$$

$\rho \gg a$, Eq. (31) can be solved by perturbation theory methods. We assume in this region that

$$\theta = \theta_0 + \theta_1; \quad \Delta = \Delta_0 + \Delta_1, \quad (32)$$

where Δ_0 is the superconductor order parameter at large distances from the narrowing and $\sin\theta_0 = \omega(\omega^2 + \Delta_0^2)^{-1/2}$. The θ_1 value satisfies the equation

$$\frac{\partial^2\theta_1}{\partial\rho^2} + \frac{2}{\rho}\frac{\partial\theta_1}{\partial\rho} - \frac{2}{D}\sqrt{\omega^2 + \Delta_0^2}\,\theta_1 - \frac{2}{D}\frac{\omega}{\sqrt{\omega^2 + \Delta_0^2}}\Delta_1 = 0. \quad (33)$$

Setting

$$\theta_1 = \Phi/\rho, \quad (34)$$

we can rewrite Eq. (33) in the form

$$\frac{\partial^2\Phi}{\partial\rho^2} - \kappa^2\Phi = \frac{2}{D}\frac{\omega\rho}{\sqrt{\omega^2 + \Delta_0^2}}\Delta_1, \quad (35)$$

where

$$\kappa = \left(\frac{2}{D}\sqrt{\omega^2 + \Delta_0^2}\right)^{1/2}. \quad (36)$$

The solution to Eq. (35) satisfying the boundary conditions as $\rho \longrightarrow \infty$ has the form

$$\Phi = -\frac{\omega}{\kappa D\sqrt{\omega^2 + \Delta_0^2}}\exp(\kappa\rho) \times \int_\rho^\infty d\rho_1\rho_1\Delta_1(\rho_1)\exp(-\kappa\rho_1) - \exp(-\kappa\rho) \times \left[C_2 + \frac{\omega}{\kappa D\sqrt{\omega^2 + \Delta_0^2}}\int_a^\rho d\rho_1\rho_1\Delta_1(\rho_1)exo(\kappa\rho_1)\right], \quad (37)$$

where C_2 is the constant of integration.

Sewing together the solutions to Eqs. (27), (31), and (34) in the intermediate region $a \ll \rho \ll \xi$, we find the C_2 coefficient and one equation for the free parameters of Eq. (27),

$$C_2 = -\frac{\omega}{2\Delta_0\kappa} \pm \frac{\sqrt{\omega^2 + \Delta_0^2}}{2\Delta_0\kappa}\sqrt{1 - \frac{A^2}{B^2}} \times \left[\cos\left(\frac{\pi B}{2}\right) - \kappa aB\sin\left(\frac{\pi B}{2}\right)\right], \pm\sqrt{1 - \frac{A^2}{B^2}}\left[\cos\left(\frac{\pi B}{2}\right) + \kappa aB\sin\left(\frac{\pi B}{2}\right)\right] = \frac{\omega}{\sqrt{\omega^2 + \Delta_0^2}} - \frac{2\Delta_0\omega}{D(\omega^2 + \Delta_0^2)}\int_0^\infty d\rho_1\rho_1\Delta_1(\rho_1)e^{-\kappa\rho_1}. \quad (38)$$

Equations (38) were obtained with the use of the expression for the $\sin\theta$ function in the region $a \ll \rho \ll \xi$, which follows from Eq. (27),

$$\sin\theta = \pm\sqrt{1 - \frac{A^2}{B^2}}\cos\left(\frac{\pi B}{2} - \frac{aB}{\rho}\right). \quad (39)$$

Correction Δ_1 to the order parameter satisfies the equation

$$2\pi T\sum_{\omega>0}\left(\frac{\Delta_1}{\sqrt{\omega^2 + \Delta_0^2}} + \frac{\omega}{\sqrt{\omega^2 + \Delta_0^2}}\frac{\Phi}{\rho}\right) = 0. \quad (40)$$

The current density in the hyperboloid is determined by the equation

$$j = ev D4\pi T\sum_{\omega>0}\cos^2\theta\frac{\partial\varphi}{\partial r} = ev D4\pi T\sum_{\omega>0}\frac{A}{a\cos u}. \quad (41)$$

The integration of Eq. (41) over the surface $\{v = 0, u < u_s\}$ yields the total current I through the contact,

$$I = \frac{2\pi^2}{eR}T\sum_{\omega>0}A(\omega), \quad (42)$$

where R is the resistance of the hyperboloid in the normal state,

$$R = \frac{1}{4a\sigma\sin^2(u_s/2)}. \quad (43)$$

At $N = 0$, Eqs. (29), (38), and (42) give the result obtained in [12]. The critical current at $a \ll \xi$ is, however, attained at N values larger than 0 rather than at $N = 0$. In the region $N \geq 1$, Eqs. (29) and (38) give

$$A = 2NZ, \quad Z = \frac{\Delta_0}{\omega}\left|\cos\left(\frac{\delta\varphi}{2}\right)\right|, \quad (44)$$

where frequency ω lies in the interval

$$\Delta_0 < \omega < \omega_{cr}(N). \quad (45)$$

The $\omega_{cr}(N)$ limiting frequency value can be estimated by Eq. (38) from the condition that correction terms have values of the same order of magnitude as the principal terms,

$$\omega_{cr}(N) \approx \Delta_0 \left(\frac{1}{aN\left|\cos\left(\frac{\delta\varphi}{2}\right)\right|} \sqrt{\frac{D}{\Delta_0}} \right)^{2/3}. \quad (46)$$

Equations (42), (43), and (45) can be used to find the total current through the narrowing as a function of parameter N,

$$I = \frac{4\pi\Delta_0 N}{3eR} \times \left|\cos\left(\frac{\delta\varphi}{2}\right)\right| \ln\left[\left(\frac{\Delta_0}{\pi T_c}\right)^{3/2} \sqrt{\frac{D}{\Delta_0}} \frac{1}{aN\left|\cos\left(\frac{\delta\varphi}{2}\right)\right|} \right]. \quad (47)$$

Equation (47) allows the critical current I_{cr} value to be determined up to a factor of the order of one,

$$I_{cr} = \frac{\Delta_0}{eRa} \sqrt{\frac{D}{\Delta_0}} \left(\frac{\Delta_0}{\pi T_c}\right)^{3/2}. \quad (48)$$

This critical current I_{cr} exceeds the value obtained in [12] in the $\xi(0)/a$ parameter.

In deriving Eq. (48) for the critical contact current, we used the strong dirt approximation. This means that the l_{tr} electron mean free path should be shorter than all characteristic lengths of the problem. In particular, the conditions

$$l_{tr} \ll a u_s, \quad l_{tr} < \frac{\pi a}{N_{cr}}, \quad (49)$$

where

$$N_{cr} = \frac{\xi(0)}{a}\left(\frac{\Delta_0}{\pi T_c}\right), \quad \xi(0) = \sqrt{\frac{D}{\pi T_c}} \quad (50)$$

should be met. If the second condition in Eq. (49) is not satisfied, Eq. (47) for the current can, in any event, be used up to N values of the order of N_1, where

$$N_1 = \frac{\pi a}{2 l_{tr}}. \quad (51)$$

To study the region of N values $N > N_1$, we must use more general equations valid at arbitrary electron mean free path values [13, 14]. This problem requires separate consideration and will be considered in a detailed communication.

The goal of this work was to demonstrate the existence of solutions in the region of large gradients of the order parameter phase, which are capable of carrying currents that substantially exceed current values when the phase difference changes in the $(-\pi, \pi)$ interval.

One of us (Yu.N.O.) thanks the Russian Foundation for Basic Research (project no. 17729) and the Ministry of Science of the Russian Federation for financial support; A.I.L. thanks NSF (grant no. 0120702).

REFERENCES

1. M. Cohen, L. Falicov, and J. Phillips. Phys. Rev. Lett. **8**, 316 (1962).
2. B. D. Josephson, Phys. Lett. **1**, 251 (1962).
3. A. I. Larkin and Yu. N. Ovchinnikov, Zh. Éksp. Teor. Fiz. **51**, 1535 (1966) [Sov. Phys. JETP **24**, 1035 (1967)].
4. N. R. Werthamer, Phys. Rev. **147**, 235 (1966).
5. V. Ambegaokar and A. Baratoff, Phys. Rev. Lett. **10**, 486 (1963).
6. L. G. Aslamazov, A. I. Larkin, and Yu. N. Ovchinnikov, Zh. Éksp. Teor. Fiz. **55**, 323 (1968) [Sov. Phys. JETP **28**, 171 (1969)].
7. I. O. Kulik and A. N. Omel'yanchuk, Pis'ma Zh. Éksp. Teor. Fiz. **21**, 216 (1975) [JETP Lett. **21**, 96 (1975)].
8. L. G. Aslamazov and A. I. Larkin, Pis'ma Zh. Éksp. Teor. Fiz. **9**, 150 (1969) [JETP Lett. **9**, 87 (1969)].
9. K. D. Usadel, Phys. Rev. Lett. **25**, 507 (1970).
10. A. I. Larkin and Yu. N. Ovchinnikov, Zh. Éksp. Teor. Fiz. **64**, 1096 (1973) [Sov. Phys. JETP **37**, 557 (1973)].
11. L. D. Landau and E. M. Lifshitz, *Course of Theoretical Physics*, Vol. 8: *Electrodynamics of Continuous Media* (Fizmatgiz, Moscow, 1959; Pergamon, New York, 1984).
12. I. O. Kulik and A. N. Omel'yanchuk, Fiz. Nizk. Temp. **4**, 296 (1978) [Sov. J. Low Temp. Phys. **4**, 142 (1978)].
13. G. Eilenberger, Z. Phys. **214**, 195 (1968).
14. A. I. Larkin and Yu. N. Ovchinnikov, Zh. Éksp. Teor. Fiz. **55**, 2262 (1968) [Sov. Phys. JETP **28**, 1200 (1969)].

Translated by V. Sipachev